Universidad de Granada

Facultad de Ciencias

Departamento de Electrónica y Tecnología de Computadores

Tesis doctoral

RESISTIVE MEMORIES SIMULATION BASED ON THE KINETIC MONTE CARLO ALGORITHM

Programa de Doctorado en Tecnologías de la Información y la Comunicación

Doctorando:
Samuel Aldana Delgado

Directores:
Juan Bautista Roldán Aranda
Francisco Jiménez Molinos

Granada 2020

Editor: Universidad de Granada. Tesis Doctorales
Autor: Samuel Aldana Delgado
ISBN: 978-84-1306-673-8
URI: http://hdl.handle.net/10481/64065

A mi familia, que ha estado siempre ahí y ha sido un gran apoyo emocional. Porque nunca faltó la paciencia y la comprensión.

A mis hermanos, que me han aguantado y me han obligado a distraerme cuando hacía falta.

A mi padre por su apoyo incondicional y los largos debates que me han hecho evolucionar en mi manera de pensar. A mi madre que, aunque ya no esté, es imprescindible para entender a donde he llegado y lo que soy ahora.

A mis amigos, que tienen la paciencia de esperarme cuando no estoy y de recibirme como si no pasase el tiempo cuando estoy. Aquellos con los que tantas veces he debatido, me han hecho desarrollarme como persona y ver el mundo con otros ojos.

Agradecimientos

Me gustaría agradecer en primer lugar la labor y dedicación de Dr. Juan Bautista Roldán Aranda y Dr. Francisco Jiménez Molinos como directores y tutores. Por la continua labor de asesoramiento, corrección y orientación. Labor indispensable para el correcto desarrollo de esta tesis doctoral.

Agradecer también la colaboración de los miembros del grupo de investigación Nanoestructuras, propiedades cuánticas y aplicaciones tecnológicas" y del Departamento de Electrónica y Tecnología de Computadores de la Universidad de Granada, especialmente a Dr. Pedro García Fernández y Francisco Manuel Gómez Campos, por la participación en los artículos [Aldana2017, Aldana2018, Aldana2018b, Aldana2018c, Aldana2020].

Agradecer a Dra. Rocío Celeste Romero Zaliz del Departamento de Ciencias de la Computación e Inteligencia Artificial, por la realización de algoritmos necesarios para el desarrollo de los diferentes simuladores [Aldana2017, Aldana2018, Aldana2018b, Aldana2018c, Aldana2020].

Agradecer la participación de diferentes grupos de investigación pertenecientes a otras universidades y entidades:

- Dra. Francesca Campabadal Segura y Dra. Mireia Bargalló González, del Institut de Microelectrònica de Barcelona IMB-CNM (CSIC) Bellaterra en España, por las muestras y medidas de los dispositivos TiN/Ti/HfO_2/W y Ni/HfO_2/Si-n^{++}, y la colaboración en la redacción y revisión de los artículos [Aldana2017, Aldana2020].
- Dr. Jordi Suñé Tarruella y Dr. Alberto Rodríguez Fernández del Departament d'Enginyeria Electrònica de la Universitat Autònoma de Barcelona, por la colaboración y revisión de los artículos [Aldana2018] y [Aldana2017] respectivamente.
- Dr. Shibing Long, Lab of Nanofabrication and Novel Device Integration, Institute of Microelectronics, Chinese Academy of Sciences en Beijing, y el Dr. Maochuan Liu, School of Mechano-Electronic Engineering, Xidian University, por facilitar las muestras del dispositivo Cu/HfOx/Pt, realizar las medidas y su colaboración en la revisión del artículo [Aldana2018].
- Dr. Eduardo Pérez del IHP-Leibniz-Institut für innovative Mikroelektronik en Frankfurt (Oder), Germany por la fabricación y las medidas del dispositivo TiN/Ti/Al: HfO_2/TiN que se han utilizado en la sección **4.3**.

Agradecer la financiación ofrecida por el Ministerio de Economía y Competitividad de España, con fondos de la Unión Europea del programa FEDER a través de los proyectos TEC2014-52152-C3-2-R y TEC2017-84321-C4-3-R.

A la red española ICTS MICRONANOFABS, por la fabricación de algunos de los dispositivos empleados en esta tesis.

S. Aldana Delgado

Granada, a 7 de septiembre de 2020

Index

List of Figures

List of abbreviations

Abbreviation	Description
RRAM	Resistive Random Access Memory
CBRAM	Conductive Bridge Random Access Memory
EMC	Electrochemical Metallization Cells
VCM	Valence Change Memories
NVM	Non-Volatile Memories
KMC	Kinetic Monte Carlo
FEM	Finite Element Method
FDM	Finite Difference Method
FVM	Finite Volume Method
IoT	Internet of Things
SSD	Solid-State Drives
BEOL	Back-End-Of-Line
SRAM	Static Random-Access Memory
DRAM	Dynamic Random-Access Memory
PCM	Phase Change Memories
STT-RAM	Spin-Transfer Torque RAM
MRAM	Magnetic RAM
CMOS	Complementary Metal-Oxide-Semiconductor
TMO	Transition Metal Oxides
RS	Resistive Switching
IMB-CNM (CSIC)	Institut de Microelectrònica de Barcelona - Centro Nacional de Microelectrónica (Consejo Superior de Investigaciones Científicas)
QPC	Quantum Point Contact
SILC	Stress Induced Leakage Current
LRS	Low Resistance State
HRS	High Resistance State
MIM	Metal-Insulator-Metal
SSD	Solid-State Drives
CF	Conductive Filaments
SEM	Scanning Electron Microscope
TEM	Transmission Electron Microscopy
DFT	Density Functional Theory
MD	Molecular Dynamics
TAT	Trap-Assisted Tunneling

Abbreviation	Description
MOSFET	Metal – Oxide – Semiconductor – Field - Effect Transistor
FAMOS	Floating Gate Avalanche-injection MOS
CG	Control Gate
FG	Floating Gate
RTN	Random Telegraph Noise
FeFET	Ferroelectric Field-Effect Transistor
FTJ	Ferroelectric Tunnel Junction
FET	Field Effect Transistor
MTJ	Magnetic Tunnel Junction
MIS	Metal-Insulator-Semiconductor
TCM	Thermochemical Mechanism
PVS	Pulsed Voltage Stresses
CVS	Constant Voltage Stress
DC	Direct current
CL	Compliance Current
FeRAM	Ferroelectric RAM
PCRAM	Phase Change Memories
STT-MRAM	Spin-Transfer Torque Magnetic Random-Access Memory
BD	Breakdown
BE	Bottom Electrode
TE	Top electrode
ALD	Atomic Layer Deposition
PLD	Pulsed Laser Deposition
CDF	Cumulative Distribution Function
SCLC	Space Charge Limited Current
P-F	Poole-Frenkel
F-N	Fowler-Nordheim
TDMAH	Tetrakis (Dimethylamido)-Hafnium
WGFMU	Waveform Generator Fast Measurement Unit
1T1R	One Transistor-One Resistor
NMOS	Negative-channel Metal-Oxide Semiconductor
ISPVA	Incremental Step Pulse with Verify Algorithm

Contributions

Journal papers

[1] **Aldana, S.**, García-Fernández, P., Rodríguez-Fernández, A., Romero-Zaliz, R., González, M. B., Jiménez-Molinos, F., ... & Roldán, J. B. (2017). A 3D kinetic Monte Carlo simulation study of resistive switching processes in Ni/HfO2/Si-n+-based RRAMs. Journal of Physics D: Applied Physics, 50(33), 335103.

[2] **Aldana, S.**, Roldán, J. B., García-Fernández, P., Suñe, J., Romero-Zaliz, R., Jiménez-Molinos, F., ... & Liu, M. (2018). An in-depth description of bipolar resistive switching in Cu/HfOx/Pt devices, a 3D kinetic Monte Carlo simulation approach. Journal of Applied Physics, 123(15), 154501.

[3] **Aldana, S.**, García-Fernández, P., Romero-Zaliz, R., Jiménez-Molinos, F., Gómez-Campos, F., & Roldán, J. B. (2018). Analysis of conductive filament density in resistive random access memories: a 3D kinetic Monte Carlo approach. Journal of Vacuum Science & Technology B, Nanotechnology and Microelectronics: Materials, Processing, Measurement, and Phenomena, 36(6), 062201.

[4] **Aldana, S.**, García-Fernández, P., Romero-Zaliz, R., González, M. B., Jiménez-Molinos, F., Gómez-Campos, F., ... & Roldán, J. B. (2020). Resistive switching in HfO2 based valence change memories, a comprehensive 3D kinetic Monte Carlo approach. Journal of Physics D: Applied Physics, 53(22), 225106.

[5] **Aldana, S.**, Pérez, E., Jimenez-Molinos, F., Wenger, C., & Roldan, J. B. (2020). Kinetic Monte Carlo analysis of data retention in Al: HfO2-based resistive random access memories. Semiconductor Science and Technology.

Proceedings of IEEE Xplore Digital Library

[1] **Aldana, S.**, García-Fernández, P., Romero-Zaliz, R., González, M. B., Jiménez-Molinos, F., Campabadal, F., ... & Roldán, J. B. (2018, November). A Kinetic Monte Carlo Simulator to Characterize Resistive Switching and Charge Conduction in Ni/HfO2/Si RRAMs. In 2018 Spanish Conference on Electron Devices (CDE) (pp. 1-4). IEEE Xplore

International conferences

[1] **Aldana, S.**, García-Fernández, P., Romero-Zaliz, R., Jiménez-Molinos, F., Gómez-Campos, F., Roldán, J.B. Analysis of conductive filament density in resistive RAMs, a 3D Kinetic Monte Carlo approach. WODIM 2018 - 20th Workshop on Dielectrics in Microelectronics, 2018.

[2] Cazorla, M., **Aldana, S.**, Maestro, M., González, M.B., Jiménez-Molinos, F., Campabadal, F., Roldán, J.B. A thermal study of multilayer RRAMs based on HfO2 and Al2O3 oxides. WODIM 2018 - 20th Workshop on Dielectrics in Microelectronics, 2018.

[3] **Aldana, S.**, García-Fernández, P., Romero-Zaliz, R., González, M.B., Jiménez-Molinos, F., Campabadal, F., Gómez-Campos, F., Roldán, J.B. A kinetic Monte Carlo simulator to characterize resistive switching and charge conduction in Ni/HfO2/Si RRAMs. CDE 2018- 12th Spanish Conference on Electron Devices, 2018.

[4] **Aldana, S.**, González-Cordero, G., Jiménez-Molinos, F., Roldán, J.B. Simulation and physical compact modeling of resistive switching devices. MemoCIS 7th workshop and MC meeting, Memristors-Devices, Models, Circuits, Systems and Applications, 2018.

Other publications

[1] Rodríguez-Fernandez, A., **Aldana, S.**, Campabadal, F., Suñé, J., Miranda, E., Jiménez-Molinos, F., ... & Gonzalez, M. B. Resistive Switching with Self-Rectifying Tunability and Influence of the Oxide Layer Thickness in Ni/HfO 2/n+-Si RRAM Devices. IEEE Transactions on Electron Devices, 2017, 64(8), 3159-3166.

[2] Cazorla, M., **Aldana, S.**, Maestro, M., González, M. B., Campabadal, F., Moreno, E., ... & Roldán, J. B. (2019). Thermal study of multilayer resistive random access memories based on HfO2 and Al2O3 oxides. Journal of Vacuum Science & Technology B, Nanotechnology and Microelectronics: Materials, Processing, Measurement, and Phenomena, 37(1), 012204.

[3] Complementary material to "**Aldana, S.**, García-Fernández, P., Rodríguez-Fernández, A., Romero-Zaliz, R., González, M. B., Jiménez-Molinos, F., ... & Roldán, J. B. (2017). A 3D kinetic Monte Carlo simulation study of resistive switching processes in Ni/HfO2/Si-n+-based RRAMs. Journal of Physics D: Applied Physics, 50(33), 335103". Video link.

[4] Complementary material to "**Aldana, S.**, Roldán, J. B., García-Fernández, P., Suñe, J., Romero-Zaliz, R., Jiménez-Molinos, F., Long, S., Gómez-Campos, F., Liu, M., "An in-depth description of bipolar resistive switching in Cu/HfOx/Pt devices, a 3D kinetic Monte Carlo simulation approach", Journal of Applied Physics, 123(15), 154501, 2018". Video link.

[5] Complementary material to "**Aldana, S.**, García-Fernández, P., Romero-Zaliz, R., González, M. B., Jiménez-Molinos, F., Gómez-Campos, F., ... & Roldán, J. B. (2020). Resistive switching in HfO2 based valence change memories, a comprehensive 3D kinetic Monte Carlo approach. Journal of Physics D: Applied Physics, 53(22), 225106.". Video link.

[6, Accepted for publication, Springer, book chapter] González, M.B., Maestro-Izquierdo, M., Poblador, S., Zabala, M., Campabadal, F., González-Cordero, G., **Aldana, S.**, Maldonado, D., Jiménez-Molinos, F., Roldán, J.B. Synaptic Devices based on Resistive HfO2 Memristors.

[7] Gonzalez, M. B., Maestro-Izquierdo, M., Campabadal, F., **Aldana, S.**, Jimenez-Molinos, F., Roldan, J. B. Impact of Intrinsic Series Resistance on the Reversible Dielectric Breakdown Kinetics in HfO2 Memristors. IEEE International Reliability Physics Symposium, 2020.

[8] Gonzalez, M. B., Maestro-Izquierdo, M., **Aldana, S.**, Poblador, S., Jiménez-Molinos, F., Roldán, J. B., Campabadal, F. Control of Synaptic Weight Updates in HfO2 based Memristors. International Conference on Memristive Systems, Memrisys, 2019.

[9] **Aldana, S.**, Jiménez-Molinos, F., Roldán, J. B. A kinetic Monte Carlo simulator to characterize resistive switching and charge conduction in Ni/HfO2/Si RRAMs. IV Jornadas de Investigadores en Formación: Fomentando la interdisciplinariedad (JIFFY), 2019.

Abstract

The efforts in this doctoral thesis have been focused on the development of RRAM physical simulators able to reproduce the resistive switching operation that takes place within the devices. The simulators were designed for the two main types of RRAMs, Conductive Bridge RAMs (both for unipolar and bipolar) and for Valence Change Memories. The work includes five publications in scientific journals indexed in the Journal Citation Report of Science Citation Index, one Proceedings published in IEEE Xplore digital library, four contributions to International Conferences. I have also contributed to other publications, where a book chapter is included, three videos detailing the operation of each simulator. The outline of this work is the following:

Chapter 1 exposes the state of the art of RRAM technology, the comparation with flash technology and the flash technology limitations that RRAM devices can overcome. In this sense, the promising future in the field of Non-Volatile Memories and neuromorphic computing is pointed out due to the great electrical and technological features. Different types of RRAM devices as Conductive Bridge RAM and Valence Change Memories have been explained. Furthermore, it has been mentioned the different materials that can be used for fabricate them, in addition to details about the fabrication process, the main physical foundations and the most important characteristics. Furthermore, the main hurdles that must be faced for the complete industrial implementation of this technology have been highlighted and the computational tools that must be used for this task. The different models explained are the microscopic models, in connection to the kinetic Monte Carlo algorithm, Finite Element Methods and compact models. Based on our purpose to study the system physics, the kinetic Monte Carlo algorithm has been selected as a good choice for the kernels of the physical simulators we present.

Chapter 2 describes the kinetic Monte Carlo algorithm, the grid used for the simulation domain and the Finite Element Method used for solving the Poisson and heat equations that are included in the simulators. Besides, some techniques for the conductive filament density and compactness calculation are exposed as well as the effect of the virtual electrode evolution versus the electric field.

Chapter 3 deals with Conductive Bridge RAMs, both for unipolar and bipolar operation. The resistive switching mechanisms are explained for both types of operation and two different simulators are developed and presented, one for the unipolar case and the other for bipolar devices. The resistive switching process is based on redox processes and on the migration of ions coming from the electrochemically active electrode which form percolation paths (conductive filaments). In this context, the main difference between unipolar and bipolar devices relies on how they carry out the CF rupture process (RESET). The unipolar rupture is due to thermally activated dissolution

of the percolation paths, while the reset in the bipolar case is controlled by means of the electric field. Then, once the simulators are fully developed, they are used for analyzing the CF density and compactness and their relation to the device resistance.

The chapter includes the following contributions:

- [Aldana2017] **Aldana, S.**, García-Fernández, P., Rodríguez-Fernández, A., Romero-Zaliz, R., González, M. B., Jiménez-Molinos, F., ... & Roldán, J. B. (2017). A 3D kinetic Monte Carlo simulation study of resistive switching processes in Ni/HfO2/Si-n+-based RRAMs. Journal of Physics D: Applied Physics, 50(33), 335103.
- [Aldana2018] **S. Aldana**, J. B. Roldán, P. García-Fernández, J. Suñe, R. Romero-Zaliz, F. Jiménez-Molinos, S. Long, F. Gómez-Campos, M. Liu, "An in-depth description of bipolar resistive switching in Cu/HfOx/Pt devices, a 3D kinetic Monte Carlo simulation approach", Journal of Applied Physics, 123(15), 154501, 2018.
- [Aldana2018b] **Aldana, S.**, García-Fernández, P., Romero-Zaliz, R., Jiménez-Molinos, F., Gómez-Campos, F., & Roldán, J. B. (2018). Analysis of conductive filament density in resistive random access memories: a 3D kinetic Monte Carlo approach. Journal of Vacuum Science & Technology B, Nanotechnology and Microelectronics: Materials, Processing, Measurement, and Phenomena, 36(6), 062201.
- [Aldana2018c] **Aldana, S.**, García-Fernández, P., Romero-Zaliz, R., González, M. B., Jiménez-Molinos, F., Campabadal, F., ... & Roldán, J. B. (2018, November). A Kinetic Monte Carlo Simulator to Characterize Resistive Switching and Charge Conduction in Ni/HfO2/Si RRAMs. In 2018 Spanish Conference on Electron Devices (CDE) (pp. 1-4). IEEE Xplore.

Chapter 4 deals with Valence Change Memories. The resistive switching mechanism is explained for these types of devices and a simulator to study the physics behind its operation has been developed and presented. The resistive switching is based on the generation of a Frenkel defect-rich region (oxygen vacancies and oxygen ions) which form the percolation paths. Only bipolar operation it is expected for these devices as one bias is needed for extracting the oxygen ions from the dielectric layer to the storage layer and the opposite bias for injecting them back in the dielectric. After developing the simulator, it has been used to carry out data retention tests in order to analyze experimental results.

The chapter includes the following contribution:

[Aldana2020] **Aldana, S.**, García-Fernández, P., Romero-Zaliz, R., González, M. B., Jiménez-Molinos, F., Gómez-Campos, F., ... & Roldán, J. B. (2020). Resistive switching in HfO2 based valence change memories, a comprehensive 3D kinetic Monte Carlo approach. Journal of Physics D: Applied Physics, 53(22), 225106.

[Aldana2020b] **Aldana, S.**, Pérez, E., Jimenez-Molinos, F., Wenger, C., & Roldan, J. B. (2020). Kinetic Monte Carlo analysis of data retention in Al: HfO2-based resistive random access memories. Semiconductor Science and Technology.

Chapter 5 summarizes the main conclusions of this doctoral thesis.

Chapter 6 is an appendix, where the conduction mechanisms through the dielectric (the device in the High Resistance State and during the Low Resistance State are treated). Also, details about the percolation path determination algorithm and explanations of the kinectic Monte Carlo algorithm are given. Besides, it sheds some light about the finite element method used for solving heat and Poisson equation in a 3D domain. Finally, the device fabrication processes used along this work are exposed.

Introduction

Nowadays, there is a demand rise for volatile and non-volatile data storage. This rise comes from the need of these memories for internet of things (IoT) devices, solid-state drives (SSD), 5G circuits, cloud storage, artificial intelligence, data mining or smartphones and laptops [Gupta2019]. The low power consumption is a key factor for these latter applications but also for mimicking biological synapses in neural networks [Prezioso2015, Alibart2013] as they need high density of devices to implement neurons and synapses. It should be noted that a high density of devices with high power consumption is a problem in whatever integrated circuit context in the current nanoelectronics industry [Chen2016, You2014, Munjal2019]. In the non-volatile memory realm, the current dominating technology is the flash due to its high density, reliability and low cost. However, it has some limitations as the low operation speed, the durability and the need of high writing voltages, which means also a high power consumption. In this context, Resistive RAMs (RRAM) technology can face these hurdles and, therefore, it is one of the most promising emerging technologies for substituting flash memories. In this sense, RRAMs offer key features for the former applications as a good scalability, speed and latency, low operation voltage and low power consumption. Furthermore, it has an ease integration in the current CMOS technology in the Back-End-Of-Line (BEOL), in addition to a good data retention, a great endurance and can be vertically stacked in 3D architectures due to its simple structure [Pan2014, Nardi2011, Lim2015, Ielmini2016, Lanza2019, Munjal2019, Gupta2019, Carboni2019, Xie2013, Waser2010, Waser2012, Zahurak2014].

Different kinds of memories as static memories (SRAM), dynamic memories (DRAM) and non-volatile memories (NVM) can be found. The non-volatile ones store information when the power systems are turned off. For these types of memories, different technological alternatives rise such as RRAMs, Phase Change Memories (PCM) or Spin-Transfer Torque RAMs (STT-RAMs), which are attracting high research efforts [Xie2013] due to the key role that plays the information storage in the electronic industry. This key role is based on the need of better devices to handle the high amount of information circulating around the world.

The focus on NVM is based on two main reasons:

1. The main problem with the non-volatility is the lower operation speed in comparison with SRAM and DRAM. If this problem were solved the NVMs would displace the two latter ones for many applications [Xie2013].
2. These types of memories are key components of data storage systems [Xie2013].

NVMs based on flash technology are widely used in smartphones, video games, scientific instrumentation and industrial robotics, but they are finding their technological limit [Gupta2019, Xie2013, Waser2010, Waser2012]. In this situation, RRAMs are one of the best positioned as an emerging technology in comparison to Magnetic RAMs (MRAMs), STT-RAM memories or PCM memories [Lanza2019, Xie2013, Waser2010, Waser2012]. These resistive memories are based on the change of the resistance of the device (process known as resistive switching) with a hysteretic behavior.

If RRAMs finally displace the current technology, the electronic landscape would change dramatically, as new electronic applications and computer architectures could develop intensively. For instance, smart distributed systems (out of the classical Von Neumann architecture paradigm) with computation capacities greater than the current ones could be built [Wang2019].

Typically, RRAMs consist of a Metal-Insulator-Metal (MIM) structure, although also Metal-Insulator-Semiconductor structures can be found. Usually the dielectric material is made of an oxide whose resistance can be changed. However, RS phenomena have been also observed in other different materials [Lanza2019, Munjal2019, Gupta2019, Carboni2019, Waser2012]:

1. Transition metal oxides (TMOs).
2. Perovskite family (TMO) with paraelectric, ferroelectric, multiferroelectric and magnetic functionality.
3. Graphene oxides, hexagonal boron nitride and other two-dimensional materials.

While good result can be obtained at the device level, the real challenge is fabricating NVM chips and artificial neural networks as they can have billions of cells [Lanza2019]. Some good results have been obtained until now, as integrated circuits based on RRAMs have been fabricated [Zahurak2014, Liu2014b, Kawahara2013]. A 16Gb Non-volatile Cu-based RRAM circuit has been fabricated with the 27nm node, an operation speed of 180MB/s for writing and 900MB/s for reading operation [Zahurak2014]. Also, a 32 Gbits memory using a 24nm CMOS process, based in a MeOx RRAM device reported at [Liu2014b]. These advances allow one being optimistic about the future of this technology.

However, before the complete industrial implementation of this technology, some hurdles related with endurance and variability must be faced. Both the variability related to the fabrication process (differences between devices) and the one related to the RS process (differences between cycles in the same device) need to be considered. The latter one is linked to the physics behind the RS process [Lanza2019, Pan2014] and this makes the need of computational tools essential to study it.

In the landscape of simulators there can be found different types of models depending on the issues to deal with. Continuum models can be used for the study of the average behavior of the devices [Villena2013, Villena2014, Menzel2015, Ielmini2017], but ab initio techniques (density functional theory and molecular dynamics) are usually preferred for focusing on the atomic characteristics of the dielectric and its interfaces with the electrodes, as they can get more accurate results because they are based on first principles [Zhao2015, Zhao2017, Duncan2016, Duncan2017]. Nevertheless, this work is focused on the development of simulators based on kinetic Monte Carlo algorithms that can combine atomistic and continuum models. This technique has been selected in order to get a microscopic description of the evolution of the conductive filament. Furthermore, it also allows to reproduce in a natural way the stochastic behavior of the system and hence to correctly describe some phenomena linked to it [Menzel2015, Vandelli2013, Vandelli2015, Voter2007, Wong2012, Guy2015].

Objectives

The objectives of this work consist of the development of computational tools based on a 3D kinetic Monte Carlo description of the devices under study, in particular, the generation and rupture of percolation paths that control resistive switching in filamentary conduction. The Poisson and heat equation must be solved for every time step in the simulation. The goal is to study complete cycles of forming, SET and RESET processes for Conductive Bridge RAMs (both for unipolar and bipolar) and Valence Change Memories. Different charge transport mechanisms can be implemented depending on the operation regime. During the high resistance state, some conduction mechanisms through the dielectric can be considered, such as Fowler-Nordheim, Poole-Frenkel, thermionic emission, etc. On the other hand, during the low resistance state, ohmic conduction and quantum conduction through a constriction are considered (the latter by means of the Quantum Point Contact model).

Different simulation tools were developed:

1. A unipolar CBRAM simulator, which is based on electrochemical processes, the oxidation and reduction of atoms that come from the active electrodes. The conductive filament is formed by these reduced and clustered atoms. In this kind of devices, the rupture of the conductive filament is thermally assisted.
2. A bipolar CBRAM simulator, which is also based on electrochemical processes. Although in this case the conductive filament is also formed by the clustering of reduced atoms, the rupture is carried out by means of the electric field, although thermal effects can also play a non-negligible role.
3. A Valence Change Memory simulator where conductive filaments are formed by means of vacancies (usually oxygen vacancies) and they are ruptured by means of the recombination between vacancies and oxygen ions driven by the electric field. Again, in some technologies, thermal effects have to be also considered.

Methodology

The development of the simulators was based on the following tasks:

1. Unipolar CBRAM simulator:
    a. The first step was the study of the previous models and the different physical mechanisms involved in the device operation. In this case, it was considered the ion oxidation/reduction, the migration and clustering of ions and the temperature and electric field distributions.
    b. Experimental data obtained by the fabricated devices at the Institut de Microelectrònica de Barcelona IMB-CNM (CSIC) was analyzed. This was made in the context of a coordinated research project and funded by the Ministry of Economy and Competitiveness.
    c. A kinetic Monte Carlo with thermal and electric field description was developed. The simulator includes the formation and rupture of the conductive filaments.
    d. The charge transport mechanisms were implemented (such as ohmic conduction, Poole-Frenkel emission, Quantum Point Contact model, etc.).
    e. The simulator was fitted by means of comparisons to experimental data.
2. Bipolar CBRAM simulator:
    a. The former simulator was adapted to include bipolar operation.
    b. The simulator was fitted by means of experimental data of fabricated devices. The devices were made at the Laboratory of Nanofabrication and Novel Device Integration, Institute of Microelectronics, Chinese Academy of Sciences, Beijing.
3. VCM simulator:
    a. Description of the main physical mechanisms involved in the resistive switching such as generation of Frenkel defects (vacancies and ions generation), migration of ions and recombination between vacancies and ions was performed.
    b. Thermal and electric field descriptions were implemented.
    c. The charge transport mechanisms were implemented (ohmic conduction, Poole-Frenkel, etc.).
    d. The simulator was fitted by means of experimental data measured in devices fabricated at the Institut de Microelectrònica de Barcelona IMB-CNM (CSIC)

Chapter 1

1. Introduction to RRAM technology and computational tools

During the last decades, the non-volatile memory market has been dominated by the flash technology, both in its NOR and NAND architecture. The features that made possible the wide extension of the flash memories were their high density and low cost, but there are some disadvantages which point out its limitations, as the low operation speed (write/erase time: 1 ms/0.1 ms), poor endurance (10^6 write/erase cycle) and high write voltage (> 10V) [Pan2014, Ielmini2015]. Furthermore, some physical hurdles have been found in the development of this technology. Mainly in relation to its miniaturization limits. Some mechanisms that can hinder or block its scaling race would be: the Stress Induced Leakage Current (SILC), Random Telegraph Noise, charge trapping and threshold voltage shift [Villena2015b, Pan2014, Ielmini2009, Gupta2019, Xie2013]. Besides the internal operational problems at each cell, there are other issues associated to the cell number per surface unit like the Cross-Talk. This latter effect is linked to the parasitic capacities due to the coupling between two adjacent cells that are too close. [Villena2015b, Lee2002, Atwood2004].

There are some candidates for substituting flash technology that can solve the intrinsic problems reported above [Pan2014, Villena2015b, Chen2016, Xie2013, Waser2010, Waser2012, Lanza2019]. The two best candidates for achieving this are assumed to be the Spin-Transfer Torque-Magnetoresistive RAM (STT-MRAM) and the Resistive Random Access Memory (RRAM). These last ones will be subject of this work. These devices show a miniaturization potential down to < 10 nm and a sub-ns operation speed, besides an <0.1 pJ energy consumption and a high endurance (>

10^{12} switching cycles) [Pan2014, Chen2016, Lanza2019, Lanza2014, Gupta2019, Xie2013, Waser2012, Waser2010, Zahurak2014, Munjal2019, Carboni2019]. Furthermore, RRAMs have simple enough structures to be integrated in passive crossbar arrays with a small size and also to be vertically stacked in 3D architectures, reducing even more the effective size [Pan2014, Nardi2011, Lim2015, Ielmini2016].

RRAM devices, the ones we are interested in, base its operation on the switching between different resistance states, a process known as resistive switching (RS). This property allows their operation as memories since the resistance states can be used to determine different logic states [Lanza2019, Pan2014, Lanza2014, Chen2016, Ielmini2017, Waser2010, Wong2012b, Yang2013b, Ielmini2016]. One can distinguish various types of RRAMs depending on the physical-chemical mechanisms that control the change between the device inner resistance [Waser2009, Ielmini2017, Chen2016, Guy2015, Waser2012, Yang2013, Pan2014, Lee2015, Ielmini2015]; in particular, the low resistance state (LRS) and the high resistance state (HRS). The switching event from the HRS to the LRS is denoted as the SET process (or forming process when it is carried out in the device pristine state) and the opposite switching event, from the LRS to the HRS, is called RESET process. Some devices can achieve more than two stable resistive states, this operation mode is useful for multilevel information processing and also for neuromorphic computing applications (although to distinguish each conductive state could be a challenge because of the variability of the resistance states) [Lanza2019, Rao2016, Poblador2018, Maestro-Izquierdo2019, Jo2010, Banerjee2017, Ielmini2018, Covi2016, Matveyev2016, Alibart2013, Prezioso2015, Yao2020, Berdan2016].

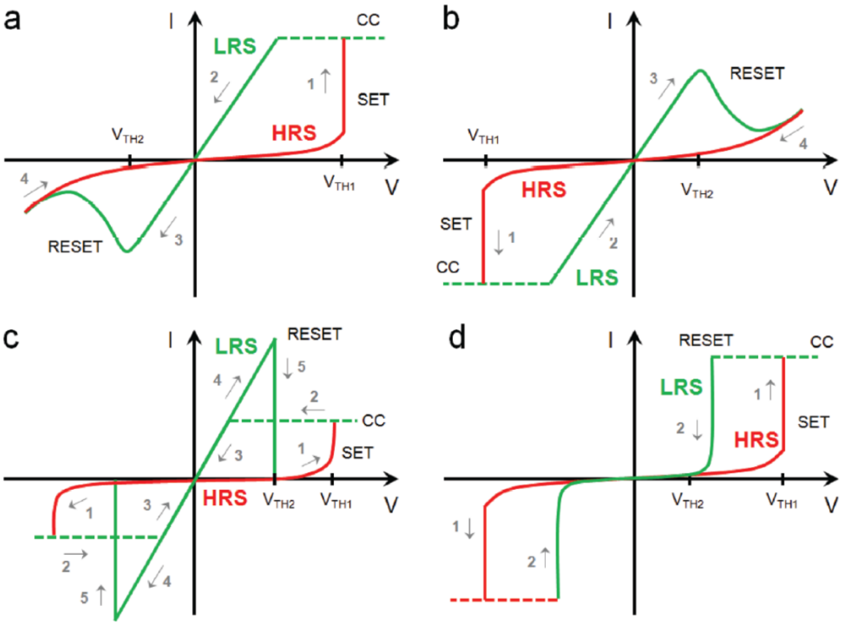

Figure 1-1. Typical I-V curves for RS in RRAM devices. One I-V bipolar cycle curve when the SET is carried out with positive voltage (a) and negative (b). c) Typical unipolar I-V curves for positive and negative stresses. d) shows threshold I-V curves for positive and negative voltages [Lanza2019].

Insulator	**Structure**	**Type**	**Operation speed (set-reset) || Endurance or data retention || ON-OFF ratio**			**Made by**
ZrO_2:Cu	Cu/ZrO_2:Cu/Pt	Nonpolar/unipolar CBRAM	50-100 ns	10^4 s readout	10^6	[Guan2008]
HfO_X	TiN/TiO_X/HfO_X/TiN	VCM	10-10 ns	10^6 cycles	10	[Chen2010]
AlO_X	Al/AlO_X/CdTe:Sb	Nonpolar/unipolar Charge trap	<10-10 ns	10^4 cycles	10^6	[Xie2013b]
Cr_2O_3	Pt/Cr_2O_3/TiN	VCM	-	6 × 10^4 cycles	10^2	[Chen2011]
SiO_2	Pt-dispersed SiO_2	Bipolar charge trap	100-100 ps	10^8 cycles	10^7	[Choi2013]
HfO_X	TiN/Hf/HfO_X/TiN	VCM	<1 ns	5 × 10^7 cycles	50	[Govoreanu2011]
CuO	Metal/CuO/Metal (metal= Ni and Pt)	Unipolar CBRAM	-	-	-	[Fujiwara2008]
HfO_2	Au/HfO_2/TiN	Unipolar CBRAM	120-80 ns	10^2 cycles	10^4	[Walczyk2009]
Al_2O_3	Al/Ti/Al_2O_3/s-CNT	VCM	50-50 ns	10^6 cycles	100	[Ahn2015]
HfO_2	Ni/HfO_2/Si	Unipolar CBRAM	-	-	-	[Aldana2017]
HfO_X	Cu/HfO_X/*Pt*	Bipolar CBRAM	-	-	-	[Aldana2018, Sun2017, Liu2014]
HfO_2	TiN/Ti/HfO_2/W	VCM	-	-	-	[Aldana2020]
HfO_2	TiN/Ti/HfO_2/TiN		-	10 years	-	[Perez2019b]
Al_2O_3/HfO_2/Al_2O_3	Pt/Al_2O_3/HfO_2/Al_2O_3/TiN/Si	VCM	-	10^3 cycles	>10	[Wang2015]
GaO_X	Pt/GaO_X/TiN	VCM	<400-600 ns	> 10^4 cycles	>10^2	[Yang2013c]
Cu-doped SiO_2	Cu/Cu-doped SiO_2/W	Unipolar (u) and bipolar (b) CBRAM	-	5 × 10^4 s 10^7 cycles	(u) 10^3 (b) 10^6	[Schindler2007]
GeS	Ag/GeS/W	Bipolar CBRAM	50-50 ns	> 7.5 × 10^6 cycles	>10^5	[Symanczyk2007]
Gd_2O_3	Pt/Gd_2O_3/Pt	VCM	-	10 years	> 2 × 10^6	[Cao2009]
Graphene oxide	ITO/Graphene oxide/Al	Bipolar. Charging/discharging of graphene oxide	<5-5 ns	>10^3 cycles	>10^4	[Jin2012]
PFN-C	Au/PFN-C/Al	-	<300-500 ns	3.6 × 10^6 s >10^7 cycles	> 4 × 10^3	[Kwan2007]
NiO	NiO/Pt	Threshold. Nickel vacancies and defects	-	Volatile	-	[Seo2004]
PI: PCBM	Al/PI:PCBM/Al	Unipolar, bipolar.	<200-200 ns	10^5 cycles	10^8	[Kim2012]
HfO_X	TiN/TiOx/HfO_X/TiN	VCM	300 ps	10^{10} cycles	>10	[Lee2010]
PCMO	Al/PCMO/Pt	VCM	<8-8 ns	10^{10} cycles	>10^3	[Liao2011]
SiN	Pt/SiN/Ti	Bipolar charge trap	<100-100 ns	>10^9 cycles	>10^7	[Kim2013]
a-Si	Poly-Si/a-Si/Ag	Bipolar CBRAM	<5-10 ns	>10^8 cycles	>10^7	[Kim2010]

Table 1. Compilation of storage media with some important characteristics, such as device structure, the type of devices (operation mode and RS mechanism), operation speed, endurance, data retention and the ratio between the LRS and HRS.

RRAM devices have a simple structure; therefore, their fabrication difficulties are linked to the material growth and stabilization. They consist of two electrodes (usually metallic, although they can also be made of semiconductors) that sandwich a dielectric and, in general, they are CMOS technology compatible. Their scaling capacity, operation simplicity and high-speed commutation make them very attractive to face future industrial challenges.

One must take into account that when different materials are used for fabricating the metal/insulator/metal (MIM) cell, different electrical stresses will be required to achieve RS. In this sense, the devices can be classified as unipolar (**Figure 1-1c**), bipolar (if they need respectively the same or opposed polarity of stress to achieve the RS, as shown in **Figures 1-1a** and **1-1b**), non-polar (when the polarity does not matter) and threshold RS (if the LRS is volatile and the RESET process takes place when the stress is switched off, as shown in **Figure 1-1d**) [Lanza2019, Pan2014]. A compilation of different RRAM technologies, their RS operation and their main features are shown in **Table 1**. A great number of different technologies with reasonably good results have been fabricated until now.

Depending on the space occupied by the atomic rearrangements responsible for the resistance change, the RS can be classified as filamentary and area dependent. The filamentary case is when the atomic rearrangements take place in the form of small spots ($< 100\, nm^2$), as can be see in **Figure 1-2f** and **1-2g**. In this case, the percolation path is formed in a limited volume, much smaller than the total dielectric volume [Lanza2019, Pan2014, Poblador2020, Niu2016, Privitera2015, Wu2013, Yang2009, Brivio2014, Celano2015, Molina2017, Qi2018]. As can be seen in **Figure 1-2**, this kind of CF structures have been characterized by means of SEM [Poblador2020, Celano2015, Pan2014, Lanza2019], TEM [Niu2016, Privitera2015, Wu2013, Molina2017, Pan2014, Lanza2019] and AFM [Bersuker2010, Niu2016, Yang2009, Brivio2014, Celano2015, Qi2018, Pan2014, Lanza2019]. It should be noted that the size and CF conical shape shown in **Figure 1-2a**, **1-2b** and **1-2c** are in line with what will be exposed in section **3**, where unipolar and bipolar models of CBRAM are presented. **1-2d** and **1-2e** show a cylindrical-like CF usually related to the presence of a grain boundary, also in line with the results presented in section **4**. Also, **Figure 1-2f**, **1-2g**, **1-2h** shed some light about the RS filamentary nature in VCM devices and about the CF degradation process (the permanent dielectric breakdown).

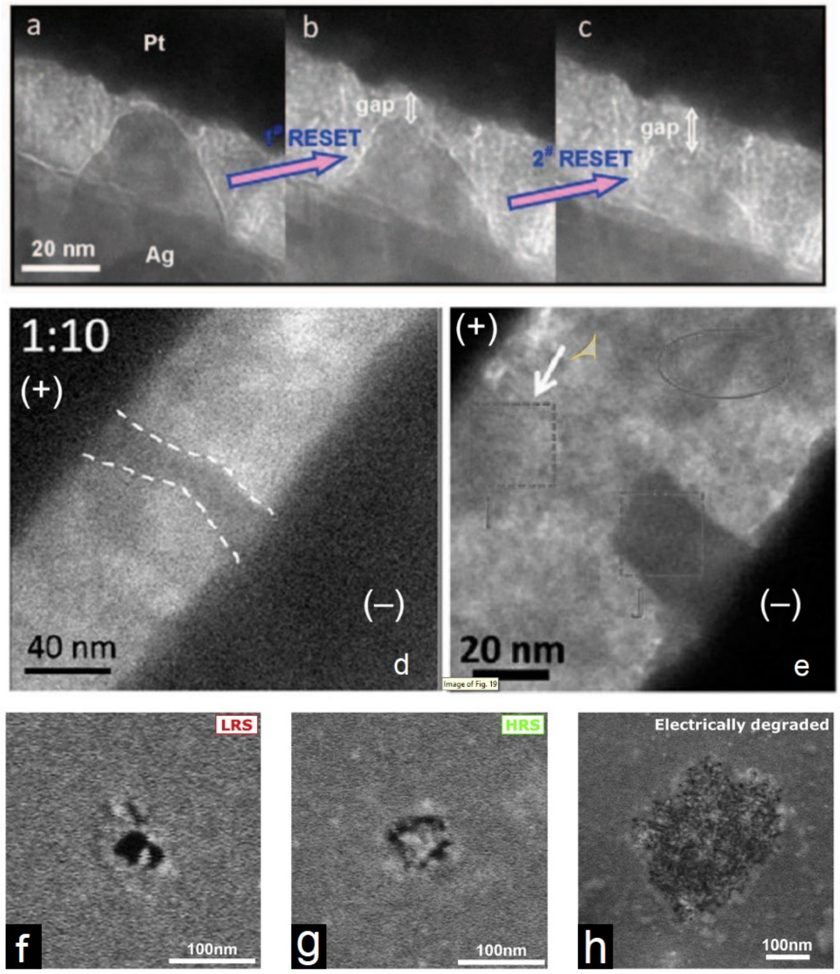

Figure 1-2. Physical characterization using TEM and SEM images to observe the CF shape and size, just like the RS phenomena involved in each kind of device. TEM images of the CF for a bipolar CBRAM device based on $Ag/ZrO_2/Pt$ cell after SET process (a) and after two RESET processes (b and c) [Sun2013]. The cone-like CF has its narrowest part near the Pt electrode. Figures b and c show the CF dissolution when opposite bias is applied. TEM images of unipolar CBRAM device based on Pt/ZnO/Pt cell are shown in figures d and e [Pan2014]. It can be seen that after the SET process (d) the RESET process is carried out with the same polarity. Figures f-h: SEM top view image of the HfO_2 layer of a VCM device based on a $TiN/Ti/HfO_2/W$ stack [Poblador2020]. Figure f corresponds to the LRS, Figure g to the HRS and Figure h to a degradated case of the CF.

RRAM memories form part of a wider group called memristors. Memristors are resistances with memory, which can change their characteristics in a controlled way and then return to the original state [Chua1971]. The name comes from the contraction between the words memory and resistor. This device would be the element which completes the classical electric passive elements: resistor, inductor and capacitor. These elements are related through the basic electrical magnitudes, such as voltage, charge, flux and intensity as shown in **Figure 1-3a**. The current versus voltage plot for memristor devices has a loop shape (**Figure 1-3b**), what means that for the same voltage value it can be found two different values of current, depending on the resistance state. This is the foundation of the operation as a memory device.

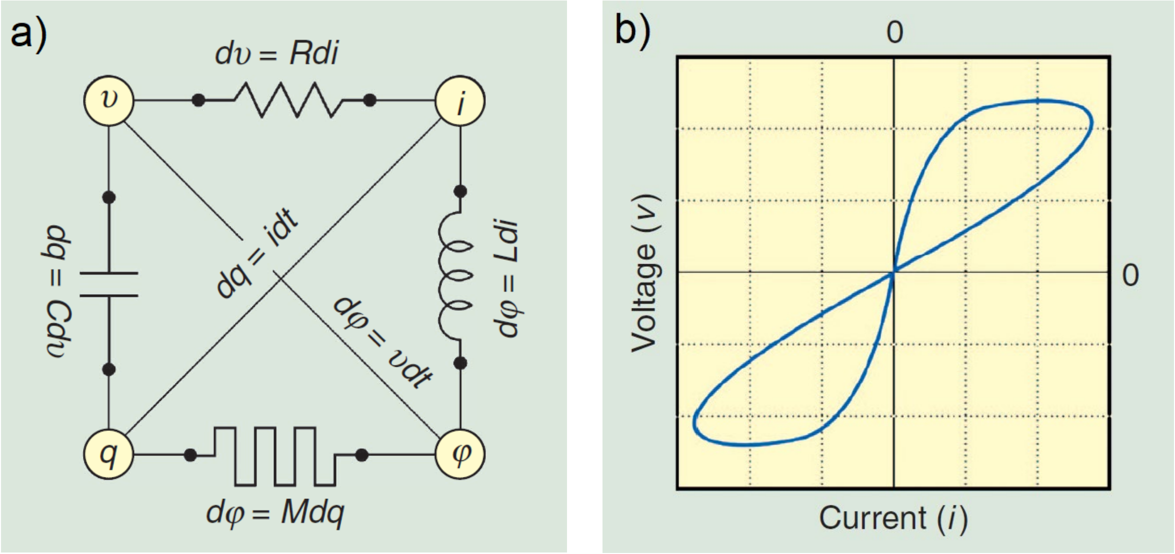

Figure 1-3. a) Scheme of the four basic passive electrical elements (resistor, inductor, capacitor and memristor) and their corresponding six relations between the fundamental magnitudes (voltage, charge, flux and intensity). Two of them are basic relationships (the definition of current and the Faraday's law) and the other four are the definitions of the four circuit elements (resistor, inductor, capacitor and memristor). b) Typical hysteresis I-V loop for a memristor element [Pazienza2011].

RRAMs or RS devices, in general, are revolutionizing applications like neuromorphic circuits because they can easily mimic biological synapses and reduce the size and power consumption of hardware neural networks [Villena2015b, Lanza2019, González-Cordero2019b, Prezioso2015, Alibart2013, Merolla2014, Yao2020, Wang2019, Berdan2016]. Current von-Neumann architecture has many problems in terms of efficiency and scalability. This becomes evident when dealing with memory, communication and computation issues related to highly interconnected neural networks [Merolla2014]. In this sense, Moore's law and von Neumann architecture act as a constraint for the implementation of learning algorithms that use neural networks for solving problems without human supervision [Wang2019]. This constriction is due to the fact that memory and processing tasks are carried out in different unis (or circuits). This leads to high energy consumption and a relevant latency in data transfer between units [Yao2020]. Otherwise, memristors in general, open a computing paradigm in which data are stored at the same place where they are processed, eliminating the cost of data transfer [Yao2020]. This is due to the fact that this kind of devices allows to mimic the synaptic weights, the most abundant element in artificial neural networks. The implementation of this hardware is still a great challenge [Alibart2013]. The neuromorphic systems can assist the fabrication of smart distributed systems with computation capacities greater than current ones. As opposed to the current schemes for which a processor and memory are separated and defined by the architecture of the system [Villena2015b, Berdan2016]. It still has to be developed an artificial neural network capable of being comparable in information processing efficiency to the biological brain. The mammalian brain can recognize complex images faster, with a better fidelity and with a fraction of energy than today computers. Because of the development of robotics, bioinformatics and distributed sensor networks and the problems about energy consumption, the need of efficient artificial neural networks is quite relevant [Alibart2013].

Depending on the application, the circuits can contain different amounts of RS cells. For instance, detectors and logic gates usually have less than ten RS cells, but nonvolatile memories (NVM) and artificial neural networks can have billions [Lanza2019]. Not only RRAM devices have been fabricated, but also integrated circuits based on them [Zahurak2014, Liu2014b, Kawahara2013]. A 16Gb Non-volatile Cu-based RRAM circuit has been fabricated at the 27nm node with an operation speed of 180MB/s for writing and 900MB/s for reading operations [Zahurak2014]. Also, a 32Gb RRAM circuit in a 24nm process has been made in a cross-point architecture array to stack multiple memory layers minimizing the chip area [Liu2014b].

One of the main hurdles that it is necessary to face in the NVMs fabrication is to ensure that all devices show good performance and nearly identical behavior. That is, low cell-to-cell variability (also named extrinsic variability) has to be achieved. Another problem is cycle-to-cycle variability. This variability is other of the main challenges for the industrial mass production of RS-based NMVs. Because of that, a better understanding of the resistive switching physics is neccesary, which is the source of intrinsic variability. These variabilities are manifested in the dispersion of the forming, RESET and SET voltages and in the resistance distributions when the CF is fully formed or ruptured [Lanza2019, Pan2014]. The goal of this work is to focus on the RS process, related to the intrinsic variability.

For the study of the device average behavior continuous models are used. These models are based on the resolution of partial differential equations that describe some processes or physical magnitudes in the computational domain [Menzel2009, Menzel2015, Villena2013, Villena2014, Villena2014b, Villena2015, Villena2017, Villena2017b, Vandelli2013, Vandelli2015, Aldana2017, Aldana2018, Aldana2018b, Aldana2018c, Aldana2020]. In this sense, Poisson, heat or current continuity equations just like charge carriers drift-diffusion equations can be solved. For facing these partial differential equations, some discretization techniques must be used such as finite element method (FEM), finite difference method (FDM) or finite volume method (FVM) [Ielmini2015]. It should be noted that different materials are implemented in these models through their macroscopic physical properties, such as electrical and thermal conductivities. And, although continuous models can be used to understand the behavior of the device, one of the disadvantages is the lack of information about the atomic configuration.

On the other hand, in order to study the device at the atomic scale, *ab initio* techniques are the best ones, as they are based on first principles. Two of these techniques are the density functional theory (DFT) and the molecular dynamics (MD), which are computationally costly [Ielmini2015, Lanza2019]. This is the reason why only small volumes and short times can be dealt with [Voter2007]. For this kind of simulations, a certain structure (like crystal structure) has to be considered. These two techniques can be combined, for instance, using DFT for calculating a field force needed for MD. This force field can also be empirically chosen, which has less computational burden. The selection of these force fields determines the accuracy of the method. Complete RS processes in RRAM devices cannot be achieved with this technique because of the high computational cost previously commented [Voter2007]. Although it can be useful for calculating a specific electronic structure or the migration energy barrier [Zhao2015, Zhao2017, Duncan2016, Duncan2017].

Other simulation approachs are based on the kinetic Monte Carlo (kMC) algorithm [Wong2012, Guy2015, Pan2011, Pan2014, Dirkmann2018, Vandelli2015, Menzel2009, Menzel2015, Aldana2017, Aldana2018, Aldana2018b, Aldana2018c, Aldana2020] . These methods can combine atomistic and continuous models, selecting the occurring event by means of rate equations. Among them, some stand upon percolation theories [Raghavan2012, Long2013, Chae2008]. The simulation domain is an important characteristic of these simulators because it determines the geometric features. One can find 2D domain approaches [Pan2014, Guy2015, Wong2012, Menzel2015] and also 3D [Vandelli2015]. There is even a mixed case with 2D and 3D domain, which can be useful to optimize the computation burden [Dirkmann2018]. The selection of the simulation domain is a trade-off between accuracy and computational cost. 3D simulations have better results, but also have to carry out many more operations which can extend the simulation time if it is not designed carefully, making them useless from the industrial viewpoint. In this sense, according to the simulation approach, there are some simulators that implement the Poisson and heat equations in 2D or 3D [Guy2015, Wong2012, Vandelli2015, Villena2014, Villena2013]. Regarding the reproduced processes, there are some simulators that are prepared to simulate complete RS cycles [Wong2012, Vandelli2015, González-Cordero2016] and others are optimized to cover only one or two processes like the forming and SET [Guy2015, Pan2011]. Concerning the charge transport mechanism through the dielectric, some simulators implement trap-assisted tunneling (TAT) that takes into account the defects (such as vacancies) distribution in the dielectric [Guy2015, Wong2012, Vandelli2015, Dirkmann2018]. A different approach could be implemented from a macroscopic point of view, focusing on the average behavior of the device. This approach is mostly used during the HRS in compact models [Garcia-Redondo2016, González-Cordero2016] and it is usually based on conduction mechanisms like Thermionic emission, Direct Tunneling, Fowler Nordheim or Poole-Frenkel [Ouyang2016]. A combination of this technique with kMC algorithm could be interesting. This strategy could let to achieve a microscopic description of the particles with a macroscopic description of the current with a low computational cost. A more detailed description of these conduction mechanisms in the HRS are presented in appendix **6.1**. When the conductive filament is fully formed (LRS), a different approach from the one used in the HRS has to be assumed. Many studies assume ohmic conduction [Miranda2012, Dirkmann2018, González-Cordero2016], calculating the CF resistance, the set-up resistance and the Maxwell resistance in an equivalent circuit that models the device [Villena2013, Villena2014]. In some cases, also the Quantum Point

Contact model is necessary to be incorporated for the calculation of the current [Villena2014, Roldán2018, Calixto2020]. The description of these conduction mechanisms for LRS and the equivalent circuit model can be found in appendix **6.2**.

In this thesis there have been developed some kMC based computational tools for Conductive Bridge RAMs and Valence Change Memories. This latter kind of RRAM memories will be explained in section **1.3.1**. The kinetic Monte Carlo (kMC) algorithm has been selected in order to get a microscopic description of the evolution and structure of the conductive filament. This kind of algorithm also allows to get in a natural way the stochastic behavior of the system and hence it is able to reproduce some phenomena linked to this stochasticity. Furthermore, the simulators also incorporate the solution of the 3D heat and Poisson equations point by point and in every step time in the whole simulation domain to get an accurate description of the system physics. The differential equation modules are an important part of the simulators because they allow to estimate internal variables which are hard to obtain by means of experiments. Besides, the electric field and temperature affect the majority of the processes involved in the resistive switching, hence it is essential to have an accurate description of them. The thermal run-away is one of the major mechanisms of the real devices failure and resistive switching. In summary, these simulators are able to reproduce complete RS cycles, with a good correspondence between the experimental and simulated data. Moreover, they will give reasonable internal physical variables and can explain some phenomena that are difficult to describe experimentally. These tools could be used to probe different materials and cover a wide range of RRAMs, therefore, they are a good help in the fabrication process and in the device design.

1.1. Non-volatile technologies: Flash memories and its limitations

The flash memory technology is based on the MOSFET transistor with a floating gate, which is also known as Floating Gate Avalanche-injection MOS (FAMOS). This device is a conventional MOSFET transistor with an additional gate added just below the Control Gate (CG) known as Floating Gate (FG), as is shown in **Figure 1.1-1**.

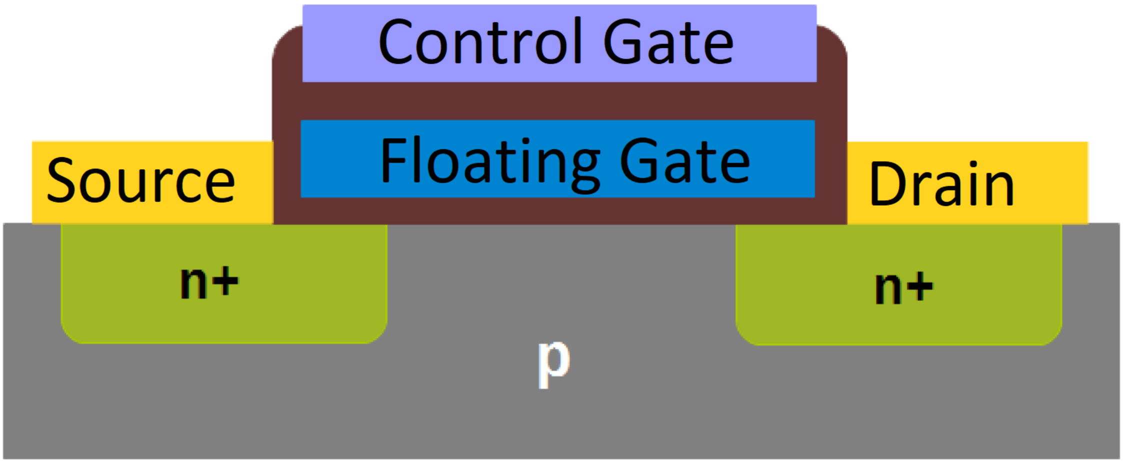

Figure 1.1-1. Scheme of a MOSFET transistor with a Floating Gate (FG) [Villena2015b].

This gate is electrically isolated from the rest of the terminals as it is inside the oxide. It is important to point out that one can change the threshold voltage of the transistor (V_T), that is to say, the minimum voltage to create the MOSFET inversion channel. This can be carried out by injecting hot electrons from the channel to the FG applying a strong electric field between the CG and drain [Frohman-Bentchkowsky1971]. This mechanism is based on charge carriers that are stocked in the FG. These charges screen the electric-field between the CG and the channel of transistor canceling it partially. This leads to a greater threshold voltage (V_{T2}) to create the conduction channel [Bez2003]. Once the electrons are injected in the FG they can stay there permanently (around 10 years).

This phenomenon allows to define two (or more in the case of multilevel devices) memory states which can be used as unit of logic information (0 and 1), charging and discharging the FG. If the FG is charged and a voltage (V) is applied to the CG, being $V_T < V < V_{T2}$, no channel will be created and, therefore, there will not be conduction, defining this state as a logic 0. On the contrary, if the FG is discharged, with the same voltage there will be conduction, defining this state as a logic 1. For the discharge process, that is, for erasing, it is needed to extract the electrons from the FG. This process can be performed applying a strong vertical electric field from the CG to the source.

Although this technology is quite versatile and have dominated the non-volatile market over several decades (it still does), the reduction of the cell size is facing a physical limit. When the cell scale is below 25 nm, some problems related to charge fluctuation and loss of charge appear. Some of these issues are the following [Ielmini2009]:

- Stress Induced Leakage Current (SILC): some defects can show up in the oxide due to the intensive programming, which wear it away. These defects can act as intermediate levels for the electrons to escape from the FG. This charge loss could change V_T in an uncontrolled way, hindering the control over the cell.

- Charge trapping in the oxide: charge accumulation in the FG by means of strong electric field can lead to trapped charges in the oxide. These charges provoke a screening of the charges stocked in the FG modifying V_T.
- Random Telegraph Noise (RTN): the traps in the tunnel oxide can also affect the reading process by capturing a channel electron and releasing it back to the channel. This trap charging/discharging modifies the vertical electric field modulating the channel charge changing the measured current and consequently V_T. This phenomenon produces random fluctuations in the current during the read process.
- Cross-talk (parasitic capacities): the closeness of neighbor cells can influence FG capacities. This is essential when working with a low number of charge carriers where the V_T level is strict.

In summary, in this technology the low number of charge carriers, as a consequence of the small size of the cells, can lead to the control loss of the device operation.

1.2. Emerging technologies in the context of non-volatile memories

The limitations described in the previous section **1.1** have pushed to the use of new technologies. One way is to develop new materials which allow the improvement of CMOS technology with respect to the device speed, the storage density and the power consumption. Other line of development would be the use of CMOS technology with new architectures to improve the information processing. Finally, our focus here would be the study of new devices based on new operation principles with the aim of replacing the current flash technology for non-volatile memory purposes. Some of the new devices with potential to substitute the flash technology would be the following:

- Ferroelectric memories, such as the Ferroelectric Field-Effect transistor (FeFET) and the Ferroelectric Tunnel Junction (FTJ). In the FeFET cell, a ferroelectric capacitor is added to the FET transistor gate that can be polarized modifying the charge distribution in the channel which changes the output current [Ma2000, Horiuchi2008]. The main problem in these devices is the retention time, as they lose the information due to the leakage current and the electric field that depolarize the ferroelectric layer [Ma2002]. The FJT has two electrodes with a thin ferroelectric layer in between in which a current is produced by a quantum tunnel effect [Zhuravlev2005, Kohlstedt2005]. With an applied voltage one can control the polarization of the ferroelectric and so the energy barrier height that determines the tunnel current.
- Mott memories are a type of device based on the transition between metal and insulator in materials with correlated electrons or Mott materials [Mott2004] which present two

different resistance states. Usually, the cell structure consists in a metal-insulator-metal (MIM) where the insulator is a Mott material whose transition can be induced by the electric field, carrier injection [Asamitsu1997] or by thermal activation [Pickett2012].

- Phase Change Memories (PCM) operate by using the change of the crystalline phase with a low associated resistance and an amorphous phase with high resistance [Burr2010, Chen2016]. These kinds of devices are made of chalcogenides and the transition from amorphous to crystalline (SET) determines the operation speed while the opposite process (RESET) is the power-limiting step [Burr2010, Chen2016].
- Spin-transfer-torque random-access-memories (STTRAM) are devices that can improve the writing mechanism based on spin transfer torque processes [Chen2016]. These devices are more scalable and efficient than MRAMs. They are made with a magnetic tunnel junction (MTJ) with two ferromagnetic layers separated by a thin oxide barrier (usually 1-2 nm MgO layer) [Chen2016, Yu2016]. The orientation in a parallel and anti-parallel way of the two ferroelectric layers is the base for the achievement of the LRS and HRS [Chen2016].
- Memories fabricated with materials based on carbon are proposed as non-volatile memories using different types of allotropes as nanotubes, graphene-like conductive or insulating carbon for their application as resistance-change material [Kreupl2008]. Also, amorphous carbon has been used in some devices [Chai2011]. Some of the devices are based on the transition between diamond-like (HRS) and graphite-like (LRS) phases [Qin2012] and other change between the HRS and the LRS with the thermal creation and rupturing of nano-holes [Kreupl2008].
- Macromolecular devices are based on a tunnel diode MIM with a polymer layer incorporated. The switching between the different resistance states is carried out by the polarization of the metal electrodes which change the resistance of the polymer. This behavior can be achieved for different polymers with unipolar and bipolar operation [Liu2012, Bai2013, Siebeneicher2012].
- Molecular memories are based on a few molecules that operate as a percolation path between the electrodes. The operation is facilitated by the application of an external voltage to change the device resistance state [Song2011, Reed2001, Tour2003].
- Resistive Random Access Memories are the devices considered here. This is the most promising technology in the non-volatile landscape. These cells are made of a MIM or MIS (metal-insulator-semiconductor) structure and the RS takes place in the insulator [Villena2015b]. Dielectrics based on transition metal oxides, chalcogenides, semiconductors and organic materials can change its resistance state through different physical mechanisms [Villena2015b, Chen2016]. The compatibility with the CMOS technology and its simple structure allow the great scalability of the RRAM technology (below 5 nm) with the traditional procedures of fabrication [Villena2015b, Chen2016, Yu2016]. Furthermore, for these devices the fabrication process is quite cheap, they need a low voltage to operate (~3 V) [Villena2015b, Pan2014], they show a low power consumption

(~0.1 pJ/bit) [Zahoor2020], have a high-speed of processing (<1 ns) [Munjal2019] and the possibility of 3D stacking [Villena2015b, Pan2014, Munjal2019]. Depending on the main physical mechanisms that govern RS, one can classify the devices in Conductive Bridge RAM (CBRAM), Valence Change Memory (VCM), thermochemical RRAM memory and metal oxide bipolar non-filamentary RRAM memories [Villena2015b, Chen2016, Yu2016]. This latter RRAM classification has been selected here, although other taxonomies are also possible. A more detailed description of the physics of each kind of device will be treated in section **1.5**.

1.3. Physical and technological foundations of RRAMs

1.3.1. Theoretical foundation of the device operation

Resistive switching is the most important physical phenomenon in resistive RAMs because it is the basis of its operation. Usually, the material that changes its resistance is a metallic oxide and the transition occurs between two (or more) different states known as High Resistance State (HRS) and Low Resistance State (LRS). The structure is quite simple and consist of a metal-insulator-metal (MIM) or a metal-insulator-semiconductor (MIS) with a cheap fabrication process and also compatible with the CMOS technology which allow the scalability of the device. In the **Figure 1.3-1** is shown a scheme of the structure and some schematic I-V curves of the RS process for unipolar and bipolar devices.

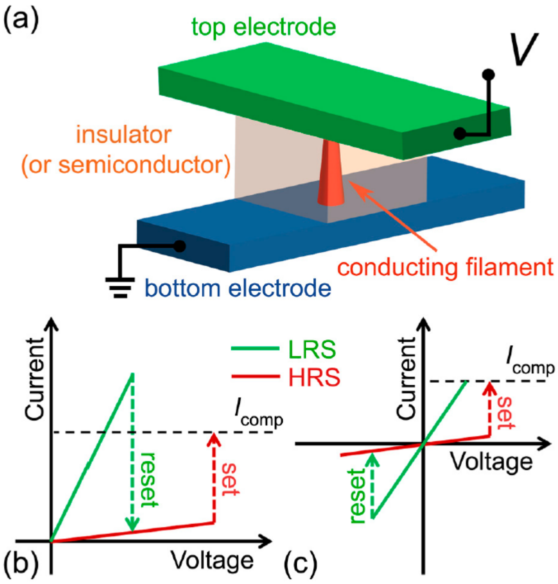

Figure 1.3-1. a) Scheme of the typical MIM (or MIS) structure of a RRAM cell. Schematic I-V curves for RS process for b) unipolar and c) bipolar devices. Also, a compliance current is pointed out with a dashed line and it is usually established to prevent the permanent breakdown during the SET [Pan2014].

One can classify RRAMs according to the nature of resistive switching in two great groups: Electrochemical Metallization Cells (EMC), also named as Conductive Bridge RAM (CBRAM), and Valence Change Memories (VCM). The majority of these devices commute between the HRS and the LRS with the creation and destruction of conductive filaments (CFs), i.e. the conduction in the LRS has filamentary nature [Menzel2009, Menzel2015, Vandelli2013]. In the case of the CBRAM (where thermochemical RRAM memories might be included) the CF is formed by metallic atoms coming from the active electrode [Waser2012, Yang2013, Guy2015, Ielmini2015] and in VCM the CF is usually formed by oxygen vacancies [Menzel2009, Menzel2015, Vandelli2013]. The exception would be the metal oxide bipolar non-filamentary RRAM memories, which have a disperse distribution of oxygen vacancies instead of a CF [Sawa2004]. In the **Figure 1.3-2** there is a schematic representation of the operation of these mechanisms.

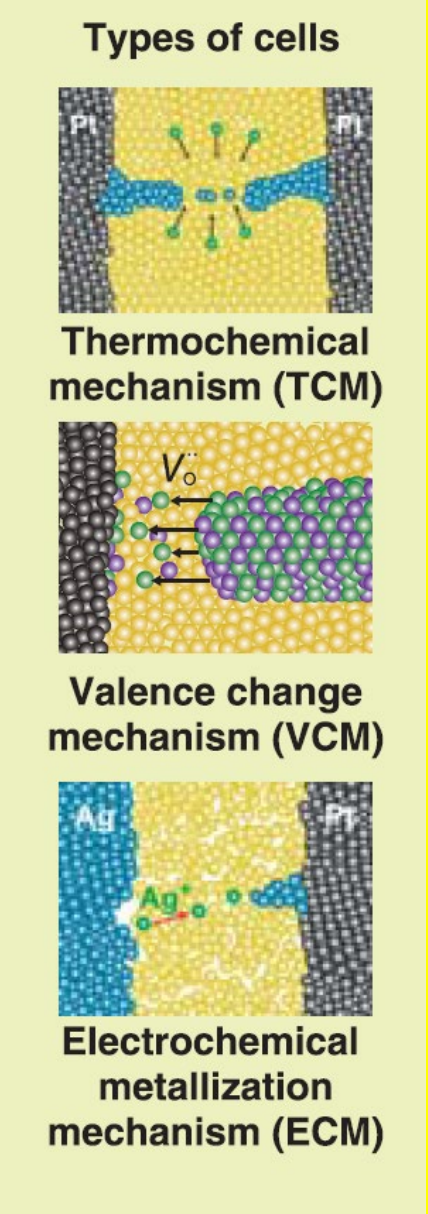

Figure 1.3-2. A rough representation of thermochemical mechanism (TCM), valence change mechanism (VCM) and electrochemical metallization mechanism (ECM). In TCM and ECM the main process is the oxidation and reduction of atoms, while in the VCM is the generation of Frenkel pair defects (vacancy and ion) and its recombination [Ielmini2015].

CBRAM form and rupture the CF responsible of RS by means of electrochemical processes. These electrochemical processes consist mainly of the oxidation and reduction of atoms that come from the active electrodes. Because of that, at least one of the electrodes has to be electrochemically active, i.e., to be the source of ions needed to form the CF. Thus, when a high enough external electrical field is applied, the atoms of the active electrode oxidize and travel along the dielectric medium dragged by the electric field. These processes are the basis of the forming and SET process, that is, the transition from the HRS to the LRS. Thereby, enabling the formation of cluster of reduced atoms that can grow inside the dielectric forming a CF with metallic-like behavior that bridges the electrodes. These ions can be reduced anywhere in the dielectric, but usually they are reduced when they reach the inert electrode [Hasegawa2010, Lu2012, Pan2011]. At this point, it is important to point out that depending on the ion mobility (in relation with the reduction probability) the atoms will reduce near the active electrode (if the mobility is low enough) or the inert electrode (for high mobilities) [Pan2014]. So the cluster will start forming close to one of the electrodes (or even in the middle for some determined proportion between the ion mobility and the reduction probability) [Pan2014], and if it is in contact with one of the electrodes, it will form a layer that would work as an extension of the electrode, what is called virtual electrode [Waser2010, Waser2012]. In the case of the CF rupture, if some of the remnants are in contact with the electrodes, they would also work as virtual electrodes. Regarding the RESET process one can find two kinds of devices depending on the polarity needed to rupture the CF: bipolar and unipolar, as explained in **Figure 1.3-3**. Of course, this is not just a technical operational characteristic but there are different physical phenomena behind this behavior. The unipolar case is the so-called thermochemical RRAM memory where the rupturing of the filament is basically thermally assisted, oxidizing the CF and then diffusing thermally (and by the electric field) the ions, leading the device to the HRS [Pan2014, Villena2014] as represented in the **Figure 1.3-2** in a simplified way. The unipolar devices allow a great scalability and also simplify the external control circuits, which make them very interesting. On the other hand, the bipolar devices are dominated also by the effect of the applied electric field. The thermal effects are secondary or share relevance with the electric field [Pan2014, Lanza2014, Villena2017]. Because of that, the operation of these devices must be bipolar, in order to oxidize and drag the ions away from the CF, leading the device to the HRS.

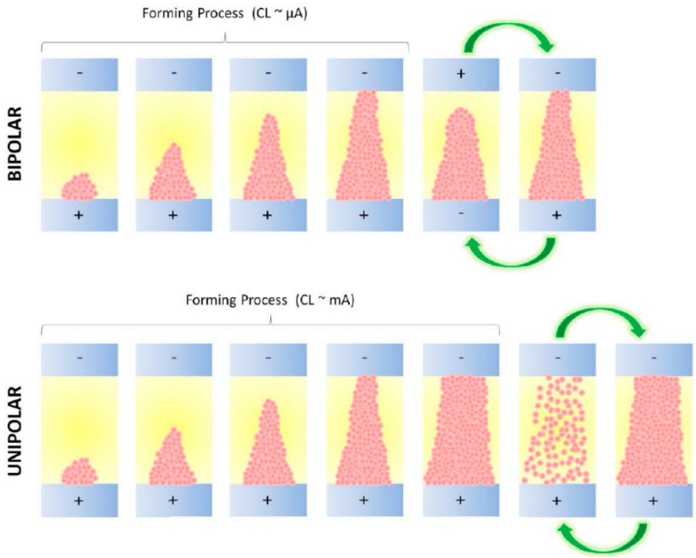

Figure 1.3-3. The main differences we have between the unipolar and bipolar devices is the polarity we need to carry out the RESET process. In the unipolar case one need the same polarity for the forming, SET and RESET processes. For bipolar base one need one bias for forming and SET and the opposite for the RESET [Lanza2014].

VCMs are the other important group of resistive memories, whose conductive filaments are formed by means of vacancies (usually oxygen vacancies). For this kind of devices, it is essential a metal layer that works as an oxygen reservoir (such as Ti) for their good operation [Dirkmann2018]. The dielectric breakdown is produced by the combined effect of the electric field and the temperature.

These would break the bonds of the molecules generating Frenkel pair defects (a vacancy and an ion, usually oxygen) that can form a defect-rich region leading the device to operate in the LRS [Vandelli2015, Vandelli2011, Dirkmann2018]. These devices always have a bipolar operation because an opposite bias is needed to carry out the RESET process. When the opposite voltage is applied, the ions stored in the reservoir layer are injected again in the dielectric and field-driven till they reach the CF and recombine with the vacancies. If enough ions are injected in the dielectric the CF can be ruptured [Vandelli2015]. It is important to note that ions are much smaller than vacancies, so their mobility is higher. This lead to assume that vacancies are immobile in some simulation approaches [Vandelli2011, Vandelli2011b, Huang2013, Vandelli2015]. **Figure 1.3-4** illustrate the main processes involved in the RS of a VCM.

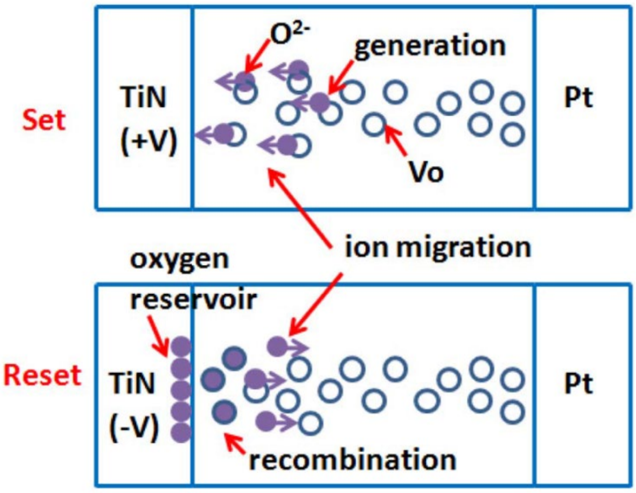

Figure 1.3-4. Schematic operation of the SET/RESET process in a VCM. During the SET process Frenkel pair defects are generated and the ions drift until the reservoir layer where they are stored. This cause a rich-defect region which form the CF that leads to the LRS. When an opposite voltage is applied, the ions are injected into the dielectric, traveling until they reach the CF and they recombine with the vacancies rupturing the CF [Wong2012].

1.3.2. RRAM main characteristics

In order to achieve a good characterization of these devices, the most important characteristics have to be unveiled. This is especially relevant for scrutinizing RS performance to shed light on the applications they are good for. There are two current versus voltage (I-V) sweeps (for the SET and RESET) that form one of the most usual figures when studying RRAMs, as much information about its performance can be extracted. It is important to point out that these I-V sweeps operate for longer times than real memory applications under short (<100ns) pulsed voltage stresses (PVS). A current limitation (CC, a compliance current) is employed in order to prevent a permanent damage in the dielectric [Ielmini2015]. The main characteristics that one should take into account to describe RRAMs would be endurance, data retention, switching time, power consumption, variability, scalability and charge transport mechanisms [Lanza2019, Chen2016, Ielmini2015].

Endurance is important for the industrial implementation. A non-durable device would make difficult the displacement of flash technology from a dominant position in the non-volatile memory market. It can be defined as the number of times that can be switched between two or more resistance states maintaining a reasonable resistance ratio to correctly operate [Ielmini2015, Lanza2019, Munjal2019, Gupta2019, Wong2012b, Villena2017]. So, for a good characterization, one must find the maximum number of RS cycles that a device can achieve with an acceptable ratio between the HRS and LRS. It is a common figure of merit the representation of the R_{HRS} and R_{LRS} versus cycle, where the wear of the device can be observed as a progressive process. Because of that, one must set up a threshold conductance ratio between on and off states below which the device is considered to have failed [Lanza2019]. However, the criterion to define the failure will depend on the application. It should be highlighted that the cell endurance measured is related to the relaxation time, that is, the LRS stability during the current measurement over time. In this sense, it is found the larger the relaxation time, the higher the endurance measured [Lanza2019]. As the measurement stresses used can affect the degradation of the CF, different endurance results can be obtained with different experiments (such as direct current or pulsed I-V curves).

Device retention must also be studied to know how volatile information storage is. As the transition between states is generally linked to the presence of a CF that bridges both electrodes, the state retention will depend on the CF stability if the technology shows filamentary conduction. In summary, the study of the data retention consist in the stability analysis of the LRS and HRS after the corresponding SET or RESET processes [Lanza2019, Munjal2019, Gupta2019, Villena2017, Wong2012b]. One way to analyze retention is by means of constant voltage stress (CVS) experiments with low read voltages (~0.1V) and later on measuring the current versus time (I-t) for each resistive state [Lanza2019]. An inherent difficulty for this is the need to keep the LRS for enough time, as the atomic configuration achieved during the SET process may vanish over time. On the other hand, the HRS should not be a problem because this is the natural state of the device. No variations will be found if high voltages are not applied. It should be noted that the stability of the LRS depends on the current limitation (CL), which prevents the permanent dielectric breakdown, as previously commented. The CL is the way to control the CF growth when the forming or SET process is carried out, getting a more stable CF with higher CL [Lanza2009]. In this sense, the CL has to be indicated. Regarding the duration of a good data retention for NVMs, this would be 10 years at 85°C [Lanza2019]. Of course, the higher the temperature, the lower will be the LRS retention, as the particles which form the CF will rearrange more easily. It is also important to study the retention time in threshold-type RS cells because it is quite useful for neuromorphic computing. This is due to the fact that RS devices operate in a similar way to biological synapses [Shi2017, Villena2015b, Lanza2019, González-Cordero2019b, Prezioso2015, Alibart2013, Merolla2014, Yao2020, Wang2019, Berdan2016]. The way to mimic biological synapses with this kind of RRAM technology is based mainly on two features. One of them is the similarity between the RS cell retention time and the relaxation time of electronic synapses where retention time range from some microseconds to few seconds. The other one is the analog control of the device resistance due to their plasticity. In this manner, the RS can satisfy synaptic biological learning rules operating as the connection strength between neurons by means of relative timing spikes [Song2000, Linares-Barranco2011, Yu2017].

The switching time and energy consumption are two additional important characteristics that must be studied to characterize correctly RS devices and to compare with the current technology. The switching time is related intimately to the write/read time. This speed determines the throughput of a memory system [González-Cordero2019]. Comparing the operation speed between RRAMs and the rest of the emerging technology one finds that RRAMs are the fastest, with write/erase times that can reach values lower than 1 ns, followed by MRAMs with around 10 ns, FeRAMs (65 ns) and PCRAMs with 100 ns [Munjal2019]. Regarding the energy consumption, this variable is crucial for the fabrication of portable devices such as smartphones or laptops and the mimicking of biological synapses in hardware neural networks [Prezioso2015, Alibart2013]. The reason is that these circuits require a high density (in memory, neuromorphic applications, etc.) and this means a very reduced space with low energy consumption [Chen2016, You2014, Munjal2019]. The power consumption will depend on the materials used for fabricating the cells and on the RS mechanism, since filamentary conduction has a higher power consumption than the distributed one [Lanza2019, Munjal2019, Carboni2019, Pan2014, Zangeneh2013, Wong2012]. Among the emerging technologies, the ones with the lowest power consumption are FeRAMs and STT-MRAMs, which have a write energy of ~0.1 pJ/bit. RRAMs operates between 0.1 and 1 pJ/bit and PCMs around 10 pJ/bit [Carboni2019]. For the study of the energy consumption and the switching time is necessary the application of PVS (with square or triangular shape) to the devices. Triangular voltage ramps are used to extract V_{SET} and V_{RESET} [Lanza2019]. As previously commented, it is important the incorporation of the CC element to prevent the breakdown during the SET and forming processes. For calculating the switching energy, one must integrate the current and the voltage over the time, and, therefore, minimum switching energy short pulses with high ramp rates have to be applied.

Variability (both the intrinsic and extrinsic one) manifests in the dispersion of the electrical characteristics of the device (V_{SET}, V_{RESET}, R_{HRS}, R_{LRS} ...), which it is one of the major obstacles for the implementation of this technology in memory and computing applications [Pan2014, Lanza2019, Munjal2019, Ielmini2015]. Some studies that deal with both types of variability (intrinsic and extrinsic) can be found in the literature [Perez2019]. The cycle-to-cycle variability is linked to the system physics and it is the one in which is focused the present work. This last variability, the intrinsic, emerges from the stochasticity of the CF formation and rupture (and how it is affected by the electric field and the temperature). Some statistical approaches have been used to analyze this kind of variability [Acal2019, Roldán2019]. In this sense, as the CF determines the electrical properties of the device, it is important to have a good understanding and control of the

CF shape, which is a big challenge [Lanza2019, Ielmini2015]. In this sense, understanding the physics behind this phenomenon is required. This is the reason why physically realistic computational tools must be developed. They can help to delve into the knowledge of the physics of these devices and so have a better control of their behavior. It is important to highlight that this stochasticity can be useful for random number generation and for implementation of physical unclonable function devices for security applications; although, for the case of information storage applications it has to be avoided. So, it is recommended that every study of RRAMs should include information about variability (cycle-to-cycle) and yield (reproducibility of the device). In Ref. [Lanza2019] a group of figures of merit are exposed in order to have a good methodology to evaluate both types of variability in these devices.

Scalability is one of the characteristics of RRAMs that makes this technology have so much potential. The behavior of RRAMs is usually reported in the literature for very large devices, with areas in the range of $100\ \mu m\ x\ 100\ \mu m$ to $2\ \mu m\ x\ 2\ \mu m$. However, extrapolate this behavior to nanoscale devices must be made very carefully. Mainly because breakdown (BD) of the dielectric and RS are stochastic processes that take place in the weakest part of the material. In this way, the bigger the devices, the higher the probability of finding weaker parts and so lower SET and forming voltages will be found. Larger devices, with area bigger than $25\ \mu m^2$, show a behavior similar to weak parts of the dielectric. Nevertheless, real devices which usually have quite a small dimension ($< 100\ nm^2$) show characteristics closer to the strongest part of the dielectric [Lanza2019]. These differences can be based on the presence or not of grain boundaries [Vandelli2011, Vandelli2015]. It has been found that smaller device areas lead to higher forming voltages [Kim2014, Shi2017]. In this sense, the characteristics of the device must be indicated for different size areas. Therefore, it is recommendable to work in the nanoscale range, although for some universities and research institute is quite difficult because of the technology usually used in these institutions.

1.4. Device fabrication

The study of RS in RRAM devices usually is carried out in a cell (or a few of them) because the most available and extended technology are not able to fabricate an entire circuit. These devices consist of a storage layer sandwiched between two electrodes made of different materials. The most usual structures for studying the electrical characteristics of RRAM devices are: a) a common bottom electrode, b) cross-point and c) cross-bar as shown in the **Figure 1.4-1** marked with the same labels [Lanza2019]. It is important to note that the area of the MIM cell affects the current during HRS and also in LRS when the conduction mechanism is not filamentary (that is, is a distributed mechanism). Furthermore, the devices with a filamentary conduction during LRS present a stochastic behavior in the RS process, due to the fact that the CF will be formed in the weakest parts of the dielectric [Pietronero1988]. Therefore, the larger the devices, the larger the probability of finding weaker points, which modify the SET and RESET voltages [Lanza2019, Kim2014, Shi2017]. In addition, this will produce different BD energies that will create CFs of different sizes and different characteristics, changing the electrical features of the devices. In general, smaller devices show lower I_{HRS} and higher V_{SET}/V_{RESET} [Shi2017]. This is the reason why the former structures are important: they allow to study different device sizes in an easy way. The structure b) shown in the **Figure 1.4-1** allows a greater miniaturization in the fabrication of cells with an easier characterization (in comparison with structure a)), but with a more complex fabrication process. On the other hand, structure c) has some phenomenon found in real circuits (absent in the b) structure) such as sneak path leakage current that is important to characterize. Because of that, it is also interesting to study this kind of structure as a complement of the single device one (for instance, the cross-point structure). It is useful for understanding arrays behaviors and for massive statistical D2D variability studies [Lanza2019].

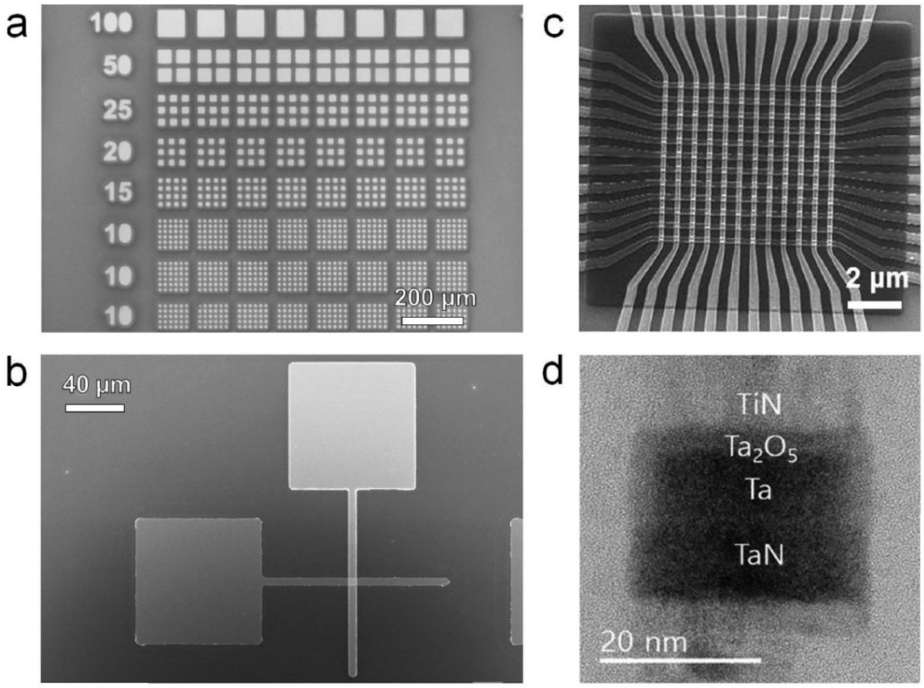

Figure 1.4-1. SEM images for the most usual structures for the study of RS in RRAM devices. a) Top electrode (TE) deposited in blanket samples with a bottom electrode (BE) shared. b) Isolated cross-point RS cell. c) Cross-bar structure formed for many cross-point structures interconnected. d) Cross-sectional TEM image of a 28 nm wide MIM structure [Lanza2019].

Additionally, it is quite important to point out that the fabrication methods (such as the metal and dielectric deposition and lithography) will determine the quality of the results and the cell-to-cell variability. It is especially relevant the dielectric thickness fluctuations and the cleaning of the interfaces between the electrodes and the dielectric [Lanza2019].

1.4.1. Resistive switching medium: Organic and inorganic

Resistive switching mediums (also known as storage mediums) can be classified depending on the material that is used. The two big categories are the inorganic and organic storage media. While organic materials have great potential in terms of low cost, simple fabrication process and high-mechanical flexibility, the inorganic materials have advantages in switching stability. There is another classification method that pays attention to the dimensionality of the storage media. In this way the groups are zero-dimensional (nanoparticles), one-dimensional (nanowires) and two-dimensional (thin films). It is also interesting to classify the storage media depending on the switching polarity, which are unipolar or bipolar [Pan2014, Son2010, Jo2008]. Regarding the fabrication process, it should be noted that the deposition of the storage film will determine the cell-to-cell variability [Lanza2019]. To avoid this variability, the surface must be as smooth as possible. The most common techniques used are the atomic layer deposition (ALD) [Lanza2009, Choi2005] and sputtering [Chen2012b, Chen2013, Liu2009]. Also, the spin coating technique is used for polymers [Lei2009, Baek2007] and 2D materials [Hui2017, He2009]. The problem with this last technique is that it can cause a prohibitive cell-to-cell variability due to the high surface roughness. That is to say, if the surface of the bottom electrode (BE) is quite smooth, but the RS medium is rough, this would provoke thickness fluctuations between different devices [Pan2014].

According to the first classification, one can find in the inorganic category the following groups: binary, ternary and more complex oxides, chalcogenides, nitrides and others (such as a-C, a-Si, etc.). For a more detailed list of materials corresponding to these groups, Ref. [Pan2014] can be consulted. Binary oxides are the most popular because of the great switching characteristics. An extraordinary set of characteristics can be achieved with these materials, but different materials must be used for optimizing different properties. A device technology (that is, a combination of materials for the components, how they are structured, the fabrication process, etc.) that gathers all the characteristic has to be found yet. Some of the features that one can achieve with different binary oxide materials are the ultra-high ON/OFF ratio $> 10^9$, sub-ns operation speed and extreme endurance ($> 10^{12}$ cycles). Besides, they have a good thermal stability and they are easy to fabricate because they are compatible with CMOS technology, where only an additional oxidation step is needed [Pan2014]. In this sense, one of the most promising technologies is based on devices made of HfO_x and TaO_x because of their great endurance ($> 10^{10}$) and their sub-ns operation speed. The most usual fabrication techniques for inorganic RS medium are the magnetron sputtering [Chen2012b, Chen2013], pulsed laser deposition (PLD) [Yan2011], atomic layer deposition (ALD) [Choi2005], thermal oxidation [Chen2005], plasma oxidation [Tang2013b] and the sol-gel method [Baek2013]. A more detailed explanation of each fabrication technique can be seen in Ref. [Pan2014] besides a compilation of technologies and the main characteristics reached.

The organic materials for RS medium fabrication can be mainly sorted into graphene oxide, its derivative (such as reduced graphene oxide or functionalized reduced graphene oxide), small molecules and polymers. Satisfactory switching characteristic can be found with these materials, but each characteristic needs a determined material to be optimized. An ultra-high OFF/ON ratio of $> 5x10^9$, fast operation speed ($< 5\ ns$) and high endurance performance $> 7.2 \times 10^7$ can be achieved. The main problem with the organic materials is that they are not able yet to get comparable characteristic to the inorganic ones [Pan2014]. The advantage of this kind of materials is the ease of fabrication, the low cost and, the major advantage, the high-mechanical flexibility that opens the door to a promising future of flexible electronics. In Ref. [Pan2014] a long compilation of technologies and their RS characteristics can be found.

1.4.2. Electrode materials

Usually the main role of the electrodes in conventional electronics is acting as transport path for carriers. However, in RRAMs they can also significantly affect the RS behavior of the resistive switching medium. For instance, changing the electrode material can provoke the pass from a stable bipolar RS behavior to an operation where no RS is seen [Gao2012]. Many materials have been studied as electrodes. It can be found carbon materials, like graphene [Son2010] and carbon nanotubes [Tsai2013], pure metals such as Cu, Ag, Pt and Au [Feng2010], nitrides such as TiN [Lee2013], p- and n-type Si [Tang2013] and conductive oxides such as indium-tin oxide (ITO) [Gao2012]. According to the composition, the most usual materials can be grouped in oxide-based electrodes, nitride based electrodes, silicon-based electrodes, alloy electrodes and elementary substance electrodes. Among these groups, the elementary substance electrodes are the most usual and widely used choice. In Ref. [Pan2014], it can be found a list of these kinds of electrodes. There are two types of silicon-based electrodes: p-Si and n-Si [Tang2013]. The most common nitride-based electrodes are TiN and TaN [Lee2013, Tang2013b]. The oxide-based electrodes are also relatively abundant [Pan2014]. Other kinds of classification for the electrode materials can be made depending on the contribution to the RS and it can be distinguished four types. The first type would be the ones that act as transport path for carriers with almost no effect in the RS [Yang2012, Schindler2009, Chen2010b]. There is a second type that helps the formation of CFs in RRAMs based on vacancies generation [Lin2013, Chen2013b]. In this kind of devices, the CFs are formed by means of vacancies which can be highly affected by the electrodes. In the third type, the electrodes are the responsible for the CF generation; this is the case of the CBRAMs [Gao2012, Gao2013], based on the migration of cations coming from the oxidation of the active electrode. That is, the CFs are formed via electrochemical dissolution and deposition of the active electrodes, Cu and Ag are among the most characteristic metals. The last type is linked to the electrode materials that are chosen for a concrete purpose, such as ITO for transparent electrodes [Kim2011, Won2009, Tang2013].

It is important to point out that when working with cross-point and cross-bar structures, both electrodes are deposited by photolithography or electron beam lithography. The use of these techniques ensures that all the structures will have the same shape and avoid the deposition of metal outside the selected areas [Lanza2019]. Concerning the substrate, it is important that the surface is as flat as possible. The aim is reducing the number of bonding defects and avoid thickness fluctuations of the layers deposited on top. This is something that should be controlled to prevent the cell-to-cell variability [Lanza2019]. Noble metals (Au, Pt) are used for bottom electrodes instead of oxidable ones like Cu and Ti. Furthermore, when working without air and humidity control, they are also recommended because they collect less oxygen during the BE and RS medium deposition. The introduction of oxygen during the formation of RS media in an uncontrollable way is something to avoid. Something different would be the introduction of oxygen by doping techniques or thermal treatments in a controlled way [Lanza2019]. For fabricating the BE, the most recommended way is electron beam evaporation which allows to get a very smooth surface. Sputtering also gives acceptable results. However, the metallic foils would be the worst option for metallic substrate serving as BE [Lanza2019].

It can be seen in **Table 1** that RRAMs can be made of many different types of materials. Many of them have been investigated to gain a better understanding of the RS mechanisms just like to obtain their electrical features.

1.5. State of the art: Hurdles and the necessity of a better understanding of the RS physics

In the development of the RRAM technologies many challenges have to be faced in order to achieve a complete implementation in applications such as non-volatile memories, sensor arrays, neuromorphic circuits and others that might emerge in the near future. There exist some trade-offs among the main RRAM characteristics such as speed-retention, power-speed, endurance-retention, etc. Some of the most challenging features to face are reliability and variability.

Endurance is a very important characteristic because RRAM devices must be more durable than the current technology to displace it in an effective way. High endurance over 10^6 cycles is usually achieved [Baek2004] and even longer endurance (10^9 cycles, with best performances between 5×10^9 and 10^{12} depending on the technology) have been reported in some cases [Chen2012, Lanza2019]. Regarding this issue, it should be taken into consideration that endurance will depend on the criterion used to define the failure and how it is measured. Besides, this would be only an estimation because it is not measured in real conditions of operation, as more aggressive conditions are usually used [Lanza2019]. In general, technology requirements for NVM applications are around 10^9 cycles [Lanza2019].

The relaxation behavior it is another relevant characteristic and it is quite related to the state of retention. This is because a quick relaxation just after the programming (it should be remembered that the natural state of the device is the HRS) would mean a fast retention loss. This means that it would affect negatively memory stability and retention, leading to a possibly loss of information [Fantini2015, Chen2016]. So, the study and control of the CF stability would be an analysis of how volatile is the information storaged in the cell. The presence or not of the CF defines the state of resistance (LRS or HRS), which in turn defines the memory states [Lanza2019, Munjal2019, Gupta2019, Villena2017, Wong2012b, Hui2017, Fantini2015]. The way to control the CF stability (that is, the LRS stability) would be through the CC established for the SET/forming process because this limitation controls the size of the CF [Lanza2009]. As it has been mentioned previously in the section **1.3.2**, a good data retention for NVMs would be 10 years at 85°C and the current RRAM technology is able to achieve longer times in its best performance [Lanza2019].

Among all the difficulties found in the implementation of this technology in memory and computing applications, the cell-to-cell and cycle-to-cycle variability are the major hurdles [Pan2014, Lanza2019, Munjal2019, Ielmini2015, Fantini2013, Ielmini2017, Chen2016]. This problem manifests itself in the dispersion of its electrical characteristic such as V_{SET}, V_{RESET}, R_{HRS} and R_{LRS}. The cell-to-cell variability, also existent in other electron devices, is related to the fabrication process and can be solved by improving it. On the other hand, the cycle-to-cycle variability is a problem that emerges from the physical nature of these devices. This variability comes from the stochasticity of the formation and rupturing of the CF, which are also quite influenced by the electric field and temperature distributions within the active region of the device. Different techniques have been employed to characterize this variability, for instance, the influence of the magnetic field on the RS has being explored [Maldonado2019]. There are available new statistical tools developed to study this kind of variability [Acal2019, Roldán2019]. As the CF shape will determine the device electrical characteristics, it is something that should be well understood and controlled. This is not an easy task, and because of that it is clear the necessity of accurate physical simulators [Lanza2019, Ielmini2015].

In summary, a physical simulator that is accurate and flexible enough is needed in order to deepen in the foundation of the device endurance, the relaxation behavior (that is, the state retention), the cycle-to-cycle variability and the forming process (which has critical effect on the switching characteristics). Moreover, some failure mechanisms of RRAMs can be studied. Some of them, such as the proportion of thicknesses between the oxygen storage layer (added to the electrode in the VCM, see section **1.3.1**) and the dielectric that facilitates RS in the device, the permanent dielectric breakdown or the thermal CF dissolution, the vanishing of the LRS (see section **1.3.2**), besides the study of forming-free devices, are of most interest.

1.6. RRAMs simulators

The development of computational tools is something unavoidable for enhancing the RRAM technology, as it is the case for every electron device [Silvaco, Synopsys]. These tools are key for design optimization purposes, for resources saving in fabrication processes, for the sake of knowing about the complex physical mechanisms that govern the operation of the devices and for predicting device performance and to screen new materials and device architectures [Lanza2019, Ginestra, Silvaco, Synopsys].

In the landscape of electron device simulators, there can be found a wide spectrum of different tools with several characteristics in terms of accuracy and computational burden. There are some powerful computational techniques that can be employed for groups of atoms like density functional theory (DFT) and molecular dynamics (MD). These techniques, named *ab initio* because they are based on first principles, allow a very accurate physical description with a high computational cost, but for a reduced set of atoms [Ielmini2015, Lanza2019, Voter2007, Zhao2015, Zhao2017, Duncan2016, Duncan2017]. In the opposite case, there can be found continuum models that include the self-consistent solution of partial differential equations (e.g., like continuity, Poisson or heat equations). This has the advantage of a lower computational cost with a macroscopic description of the system, but with no details about the dynamic of the particles [Ielmini2015, Lanza2019, Villena2013, Villena2014, Menzel2015, Ielmini2017]. The kinetic Monte Carlo algorithm would be an alternative technique in between the two previous approaches, which reproduces the stochastic behavior of the system using random numbers and relatively simple rules [Voter2007, Menzel2015, Aldana2017, Aldana2018, Aldana2018b, Aldana2018c, Aldana2020, Vandelli2013, Vandelli2015]. In **Figure 1.6-1** a summary scheme of the different tools that one can find and their main characteristics is shown.

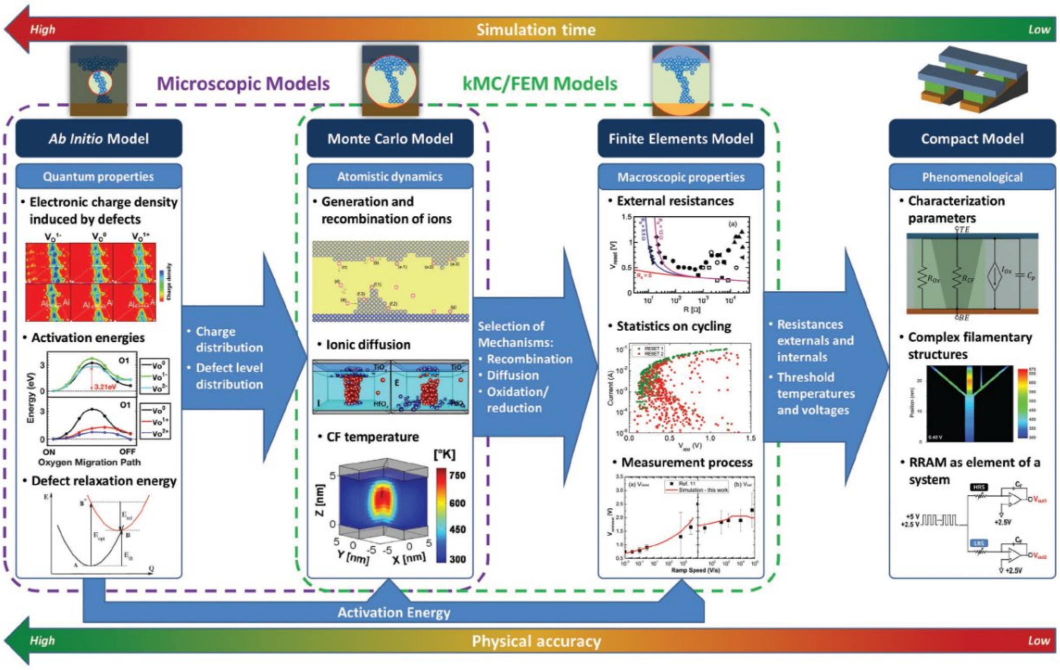

Figure 1.6-1. A compilation of the most used simulation tools for RRAM device characterization, describing the provided information level and detail. The information that can be obtained in the higher level tools can be used in the approximations used by other models. The choice of a model would depend on the level of accuracy that is needed and the simulation time that can be afforded, which works as a limitation [Lanza2019].

It would be quite useful a multiscale tool that connects the material properties to devices and circuits performances. To achieve that, one must take into account three different levels: i) material properties calculation making use of *ab initio* methods to calculate fundamental properties and defect characteristics; ii) device models based on kMC and finite element method (FEM) to link the material properties with the performances of the devices, including variability and reliability; iii) semi-empirical/compact models that are used for circuits simulation to study the behavior of a complete circuit/system making use of an individual device characteristics.

1.6.1. Microscopic models

These kinds of simulation tools are of great importance for the comprehension of the physical processes in RRAM devices, such as recombination, creation and diffusion of defect species (like the oxygen vacancies of HfO_2 in VCMs) or the generation of ions, their reduction and migration (as in the case of CBRAMs). They are also useful for studying the function of the former processes in the resistive switching and charge transport mechanisms. Either in the CF formation and dissolution, the changes in the structure of the material, charge transport through the defects and the heat dissipation which increases the temperature [Deleonibus2014, Kamiya2012].

This kind of models can include the physics of the system without the need to define a concrete material through parameters or the resistive state, just the atomic structure [Duncan2016, Lanza2019, Ielmini2015, Ielmini2017, Duncan2017]. For achieving this, they must include the major phenomena related with the defects, the atoms and the materials, like the generation, recombination, migration of defects/atoms, clustering of particles, structural and phase changes in the materials, electrical/thermal/optic properties, reactions at interfaces, etc., and how they interact between them [Duncan2016, Duncan2017]. Another important component that must be included (to catch the physics regardless the composition of the device and the resistance state) is the electron and ion transport models, including carrier tunneling mechanisms, defects sub-band creation and generalized Landauer approach/ballistic transport. A kinetic Monte Carlo is usually required in order to reproduce the stochasticity of the system in a natural manner and simulate its evolution.

Furthermore, these simulators can be calibrated making use of experimental information (such as thermal conductivity, work function, bandgap, etc.) to reach a more realistic description [Duncan2017]. The most important information that must be included in the model are the activation energies (like the one for creation and recombination of defect species, their mobility, the oxidation and reduction processes, etc.) that can be obtained by *ab initio* models (density functional theory) [Jiang2016, Duncan2016, Duncan2017, Zhao2017], and/or molecular dynamics models or even by comparison of experimental results of electrical characterization (time-dependent dielectric breakdown, variable ramp-rate and temperature switching, random telegraph noise) [Lanza2019, Onofrio2015, Ielmini2017, Zhao2015].

Once a simulator is fully developed following the former indications, after a tuning process, it can be satisfactory used to understand the complex physics of the formation of CFs in different materials [Duncan2016, Zhao2017, Duncan2017, Zhao2015]. In this sense, it can be also used in the design of specific devices for different applications [Jung2017]. The tools allow the search for the most suitable material for a concrete application and get a very useful information for semi-empirical and compact models [Lanza2019]. Besides, no information about the CF shape is needed and it is compatible with multilayer structures. Finally, as these kinds of simulations are quite costly in computational time, it is important to study which are the most dispensable processes. The aim would be excluding them without a high loss of the physics behind the operation of the devices under study.

1.6.2. KMC and Finite Elements Methods

The use of kMC algorithms and 3D finite element methods (FEM) allow the study of the electrical characteristic of RS devices with a lower computational cost and quite good accuracy, which make them a widely used tools.

Continuum models include the solution in a self-consistent approach of partial differential equations, such as the continuity, Poisson, drift diffusion (for ionic motion) and heat equations [Villena2017, Menzel2015, Aldana2017, Aldana2018, Aldana2018b, Aldana2018c, Aldana2020, Vandelli2013, Vandelli2015, Villena2013, Villena2014, Ielmini2017]. In this way, with the definition of a computational domain and the characteristic parameters of the material, a macroscopic description of the system can be obtained. For solving the partial differential equations, a discretization of the simulation domain is needed and some techniques can be employed as the finite element method (FEM), the finite difference method (FDM) and the finite volume method (FVM) [Ielmini2015, Ielmini2017, Lanza2019].

The kinetic Monte Carlo algorithm is a methodology that reproduces the stochastic behavior of the system in a natural manner, as it takes into account the individual contribution of defects/ions/vacancies. This is because it is based on the use of random numbers with relatively simple rules that reproduce the evolution of a system through its evolution along its states [Voter2007, Menzel2015, Aldana2017, Vandelli2013]. This allows to simulate variability and reliability in a coherent and natural manner, which is one of the main differences compared to continuum models. Furthermore, as the processes involved in the RS take place in much longer time than the vibrational period (a time scale that cannot be reached by DFT and MD) it can be considered that the evolution of the system consists in the transition between equilibrium states [Voter2007]. This makes kMC simulation tools a better choice to study complete resistive switching processes (in comparison to the *ab initio* approach), as they can achieve much longer operation times. The main processes involved in the forming and, in general, resistive switching are the generation and recombination of vacancies in VCMs. For the case of CBRAMs, the oxidation and reduction of atoms coming from the active electrode are the main processes. Besides, the migration of the particles would be also important processes in both kind of devices. In general, it could be posed as cations or anions oxidation and reduction processes, including their movement, generation and formation of percolation paths [Wong2012, Guy2015, Pan2011, Pan2014, Dirkmann2018, Vandelli2015, Menzel2009, Menzel2015, Aldana2017, Aldana2018, Aldana2020].

Finally, a combination of kMC algorithms and FEM for partial differential equations can be used to design a model that agree with characteristics observed experimentally (such as the forming, RESET and SET under different operation voltages, pulsed operation, temperature behavior, etc.) [Villena2014, Puglisi2016]. The FEM can be used to obtain the average evolution of electric potential and temperature distributions, something needed to calculate the physical mechanisms probabilities (they are mostly thermally activated). Some studies of how it is used this technique for analyzing the thermal distribution for multilayer devices [Cazorla2019, Maestro-Izquierdo2020] or simple materials [Chawa2016] have been made with interesting results. In addition, kMC simulation tools can reproduce the current fluctuations and variability of electrical features of RRAMs. Current fluctuations such as Random Telegraph Noise (RTN), based on the existence of active defects that alter the current [González-Cordero2019a, González-Cordero2019c, González-Cordero2019d] could also be studied. Other important characteristics of this simulation approach are that no CF shapes and sizes have to be assumed previously, as the models can simulate the complete forming operation from the pristine state. Both FEM and kMC models need to include some parameters that represent the materials which can be obtained using *ab initio* calculations or can be calibrated by comparison with experimental data. The importance of the thermal effects in these devices is high because RS is linked to thermal run away processes that lead to reset and set events. Also, the accurate calculation of the electric field is fundamental for the correct description of the system, as the charged particles are field-driven, the redox processes in the CBRAMs are also affected, just as the vacancies generation processes in the VCMs. There are many kinds of simulators based on different versions of the general model exposed here, which can provide information of internal variables quite difficult to be obtained experimentally. Some of them are also able to reproduce complete cycles of RS under ramped and pulsed voltage operation with good agreement with experimental data [Wong2012, Guy2015, Pan2011, Pan2014, Dirkmann2018, Vandelli2015, Menzel2009, Menzel2015].

1.6.3. Compact Models

When a full set of RRAMs or circuits based on these devices need to be simulated, a compact model running in SPICE-like simulation environment is needed. *Ab initio* and kMC methods have to be avoided because the computational cost would be impossible to deal with. This means that some simplifications have to be made, such as defining the filament shape (e.g. cylindrical or conical) and consider some average behavior for some important phenomena like the electric field, temperature or the average drift of the particles [Patterson2018, Vourkas2015, González-Cordero2016b, González-Cordero2016c, González-Cordero2017c, González-Cordero2017d, Jiménez-Molinos2017, González-Cordero2017e]. Besides, some stochastic techniques can be employed to simplify the compact models [Aguilera-Morillo2019]. Depending on the behavior that is assumed for the CF, different models can be proposed: i) ohmic conduction [Villena2013], ii) an hourglass-shaped quantum-point-contact [Villena2014], iii) space-charge region [Ouyang2014], iv) a semi-conductive region that may create a Schottky junction with the electrodes [Tallarida2009], v) a highly defective region in the dielectric in which either delocalized transport or hopping conduction may occur [Ouyang2013]. The corresponding charge transport mechanisms can be estimated and fitted with the shape and magnitude of the experimental I-V sweeps. This procedure can be used both for LRS and HRS, making use of compact analytical expression models such as Schottky or Poole-Frenkel emission, variable-range or fixed-range hopping, Landauer formula (ballistic transport), Ohm's law and tunneling (direct, Fowler-Nordheim or trap-assisted). Some approaches can be included for the switching mechanism employing information extracted from FEM and/or kMC models.

Some simplifications can be made as the use of differential equations to model the motion of particles, generation and recombination. Empirical expressions can be used accounting for the dependence on the voltage and the temperature [Huang2013, Kang2015, Bocquet2014b]. Also, these compact models can be calibrated making use of the FEM/kMC models [González-Cordero2017d] and experimental I-V curves obtained under different conditions [Chawa2018, Picos2015, Picos2016]. In addition to the analytical development of expressions, some methods to extract important parameters from the experimental data such as the RESET voltage [Barrera2019, Ibáñez2019] are needed. The models will depend on parameters extracted from experimental data or simulated such as the Schottky barrier height, Poole-Frenkel barrier, hopping range, number of open Landauer channels, CF resistivity, thermal resistance and capacitance, etc.

1.6.4. CBRAM models

The computational tools already developed to describe CBRAM operation can be divided in different groups. One of them could be defined by the polarity needed to achieve the RS, finding the unipolar (also called thermochemical RRAMs) [Villena2014] and bipolar [Guy2015, Pan2011, Pan2014, Menzel2009, Menzel2015, Villena2013, González-Cordero2016] devices. In the unipolar case, the same polarity is needed for the forming, SET and RESET processes. For bipolar case, one bias is needed for forming and SET and the opposite for the RESET. This is because the filament rupture is thermally assisted (or dominated) in the unipolar case, oxidizing the CF and then thermally enhanced ion diffusion. On the other hand, the bipolar devices operate differently since they are mainly controlled by the applied electric field and the thermal effects are less significant. In this respect, although the main mechanisms involved in the devices are basically the same, they have different importance. In this sense, the computational tools must be calibrated very carefully according to the experimental data. Concretely, in the unipolar case, the accuracy of the heat equation is strongly recommended and the same is required for Poisson equation in the bipolar case.

For the CBRAM devices, both for unipolar and bipolar, there can be found very different models depending on the problem at hand. For instance, for reproducing the behavior of a device in an average way, FEM could be a good option. Some unipolar models face the heat and Poisson equations in a 1D approach in a continuum model, where also the CF evolution is calculated with same methodology dealing with thermal RESETs with Quantum Point Contact (QPC) conduction mechanism [Villena2013, Villena2014, Villena2014b, Villena2015, Villena2017b]. Some compact models are specifically designed to focus on RESET processes accounting for filamentary transport (sometimes including QPC conduction mechanism) and an accurate thermal description [González-Cordero2016b, Jiménez-Molinos2017, González-Cordero2016e, Jiménez-Molinos2015, Jiménez-Molinos2017]. To deal with the simulation of complete systems or circuits with a great amount of RS cycles, compact modeling is good option due to the low computational burden [González-Cordero2016, González-Cordero2016d]. Other FEM based simulators focus in analyzing the SET process with no temperature description [Menzel2009] or the RESET process including both temperature and electric field equations in 1D [Villena2013]. Concerning the kMC based simulators, they are the best option because they combine an accurate physical description with a reasonable computational cost. Depending on the level of description that it is wanted to be achieved, it can be found different kinds of simulators. For instance, there are some 2D simulators [Pan2011, Pan2014, Guy2015, Menzel2015], but there is a lack of 3D ones. Some are focused on describing the evolution during the SET (or forming) [Pan2011, Guy2015, Pan2014] and others offer complete RS cycles [Menzel2015]. The kMC algorithm is also combined with FEM for solving Poisson and heat equations in some simulators. Some of them include the resolution of the Poisson equation in 1D or 2D [Pan2011, Guy2015, Pan2014, Menzel2015], while the 3D approach should be explored. Poisson and heat equations have to be incorporated in a 3D simulation domain for having a good point by point description, quite valuable for the simulation. Also, an important characteristic like the virtual electrode [Waser2010, Waser2012] (which would modify the effective gap between the electrodes during the CF evolution) can be incorporated. Including this characteristic allows the reproduction of current fluctuations experimentally observed. A tool with all of these features can describe the microscopic characteristics of the system such as the CF density and compactness from a microscopic viewpoint. As the CF resistance is related to the CF density and compactness, the microscopic description of RS is of high value. Regarding the conduction mechanisms, it can be distinguished some approaches depending on the accuracy and the operation regime. It can be found the TAT [Guy2015, Vandelli2013, Vandelli2015, Dirkmann2018, Wong2012], which takes into account the defects distribution in the dielectric material. Low computational burden macroscopic models for LRS like ohmic conduction can be also found [Huang2013, Dirkmann2018] (where Maxwell and set-up resistances can be included [Villena2013] or even QPC if needed [Villena2014, Dirkmann2018]). For the sake of clarity, the QPC model would be included when the CF is narrow and presents a constriction that quantizes the electron energy in the direction perpendicular to the current flow. As a complement, it is worth commenting on the techniques to extract useful parameters for characterizing conduction in the LRS, mainly the ohmic conduction [Villena2016]. Macroscopic models for the HRS that can be considered are the dielectric conduction mechanisms models (like Poole-Frenkel, Direct Tunneling, Fowler Nordheim, etc.), that can reproduce the general behavior of the current [Vandelli2013, Ouyang2014, Ielmini2015, Ouyang2016]. In summary, a tool that combines kMC algorithms and FEM could achieve a good combination between accuracy and computational burden. See appendix **6.1** and **6.2** for a more detailed description of the conduction mechanisms.

1.6.5. VCM models

Concerning VCM devices, bipolar operation is mandatory, as it is needed for the RS. In this sense, only one type of computational tool should be needed in terms of bipolarity [Bocquet2014b, Huang2013, Kang2015, Wong2012, Dirkmann2018, Vandelli2015, González-Cordero2017]. In these devices the CF is formed by a percolation path made of oxygen vacancies and usually they need a metal layer between the dielectric and one of the electrodes that works as an ion reservoir. As the CF formation is based mainly on the generation of oxygen vacancies and oxygen ions, the ions are field-driven until they reach the reservoir layer during SET and forming process. However, for carrying out the RESET, an opposite polarity is needed to inject the ions again in the dielectric layer, field-drive them until they reach the CF and recombine with the vacancies. Some simulation approaches consider that the vacancies are immobile because the ions are much smaller and have a much higher mobility [Vandelli2011, Vandelli2011b, Huang2013, Vandelli2015]. We do also consider this approach here.

As in former cases, depending on the type of problem that is faced, the design of the computational tool can make use of different techniques or a combination of them. Some simulators are based on compact models with some FEM approximations [Bocquet2014b, Huang2013, Kang2015, González-Cordero2017, González-Cordero2017b, González-Cordero2017d] and others on a more physical description based on kMC with FEM approximations [Wong2012, Dirkmann2018, Vandelli2015]. Regarding the dimensionality, there exists a trade-off between accuracy and computational burden, there can be found 3D tools [Vandelli2015] and 2 dimensional ones [Wong2012]; besides, in some cases mixed dimensionality it is implemented [Dirkmann2018]. In several approaches, the solution of the heat equation and the CF evolution is considered in 1D, mostly in compact models [González-Cordero2017b, González-Cordero2016c]. Some simulators are designed to carry out complete RS cycles [Wong2012, Vandelli2015, Dirkmann2018], focused on the physics behind RS, while others (compact models) carry out RS cycles and only reproduce the average device operation [Bocquet2014b, Huang2013, Kang2015]. Many computational tools solve both Poisson and heat equations in a more or less complex and accurate way depending on the purpose of the tool [Bocquet2014b, Huang2013, Kang2015, Wong2012, Vandelli2015, Dirkmann2018]. With respect to the conduction mechanisms through the dielectric, there can be found different perspectives. Some simulators take into account the defect distribution in the dielectric making use of the TAT for the charge conduction [Wong2012, Vandelli2015, Dirkmann2018]. A different approach can be employed for a less costly computational calculation making use of a macroscopic perspective [Bocquet2014b, Huang2013, Kang2015]. For instance, it could be used Poole-Frenkel model emission with effective parameters that account for the possibility of different mechanisms that might happen simultaneously depending on the voltage regime such as Fowler-Nordheim, direct tunneling, thermionic emission, etc. See appendix **6.1** for a more detailed explanation for the HRS conduction mechanisms. During the LRS, other mechanisms are used, mainly the ohmic conduction [Dirkmann2018], but also the QPC model can be implemented if needed [Miranda2012, Dirkmann2018]. Also, the set-up and Maxwell resistances could be taken into account in an equivalent circuit as explained in appendix **6.2**.

Chapter 2

2. Kinectic Monte Carlo simulation

2.1. Introduction

As explained in the section **1.5**, there are some hurdles in the development of RRAM technology for its implementation as non-volatile memories and neuromorphic circuit artificial synapses that prevent them from being mass produced from the industrial viewpoint. Although a small-scale fabrication is possible at laboratory level and for some commercial applications, for a real industrial implementation of non-volatile memories some obstacles must be faced as device reliability, variability, retention, etc. Reliability is a device characteristic related to the endurance, and the intrinsic variability (the extrinsic one is related to fabrication process), also called cycle-to-cycle variability, is related to the dispersion of electrical features of the device. This intrinsic variability comes from the stochasticity of the formation and rupturing of the CF, which are quite influenced by the electric field and the temperature. This is one of the major challenges that has to be dealt with. The reason is that the shape of the CF is something that has much influence in the electrical characteristics, so it must be understood and controlled. The most important electrical variables that are usually dispersed because of the intrinsic variability are V_{SET}, V_{RESET}, R_{HRS} and R_{LRS}. For understanding all of these phenomena, it is necessary to study the processes involved, so a physically based simulator that is accurate enough is needed. As reported in the previous chapter, kMC is a good option for device simulation. In this approach, based on the simulation of transitions between equilibrium states, long time scales can be used with respect to *ab initio* calculations. Besides, this method can reproduce the stochastic nature of the CF rupture and creation in a natural way reproducing the random physical processes behind resistive switching operation. The Poisson and heat equations are self-consistently solved in the context of this simulation procedure.

2.2. Grid

The grid chosen for the computational tool we present here needs to characterize the main operation region of the device. The grid has to fit correctly the device dimensions, taking into account the physical properties of the materials (such as the grain boundaries in the dielectric, material interfaces, etc.). The electric and thermal conductivities are also important since they are involved in the resolution of the heat and Poisson equations. In this respect, dielectric and electrode multilayers have to be considered. The selection of a good grid is basic for a good physical description. Again, as most elements in the simulator, a trade-off between accuracy and computational burden must be achieved. An example of a grid can be seen in Appendix **6.4**.

In general, the conduction in RRAMs has a filamentary nature during LRS both for VCMs and CBRAMs [Menzel2015, Vandelli2013, Waser2012, Yang2013, Ielmini2015, Poblador2020]. This means that the simulation domain could be designed to visualize just the active part of a real device, which usually has a larger area [Dirkmann2018, Vandelli2013, Vandelli2015, Aldana2017, Aldana2018, Aldana2018b, Aldana2020].

The distance between the grid points will depend on the structure of the dielectric and the ions involved in RS. For instance, the HfO_2 (which is a common dielectric material) crystallizes in a monoclinic crystal structure with grid constant close to $a = 5$ Å [Dirkmann2018]. Therefore, a 3D cubic grid could be used with a grid constant of 5 Å. These grid points represent the lattice sites in the dielectric material where the particles can be (in the case of HfO_2, the oxygen vacancies and the oxygen ions) and where the following physical processes take place: migration of particles, the oxidation/reduction of atoms/ions in CBRAMs or the generation/recombination of vacancies and ions in VCMs. The electrodes can be modeled as stopping layers for the particles and the lateral surfaces as boundaries that eliminate particles (assuming that the device is larger than simulation domain). The top electrode can be modeled as a cation generator in CBRAMs or as ions reservoir in VCMs.

2.3. Heat and Poisson equations, finite difference approach

In order to get a accurate enough computational tool the solution of the heat and Poisson equations must be included. The importance of the temperature is clear since the physical processes are thermally activated. It affects particle migration, redox processes in CBRAMs, generation and recombination in VCMs, etc. It is important to understand correctly these phenomena, as temperature is responsible for the positive feedback processes that lead to RS. Regarding the electric field, it has also a very important role in the field-driven migration of charged particles, on the oxidation of atoms in CBRAMs or on the generation of vacancies in VCMs, also on the magnitude of the electric current. In this way, both the electric field and the temperature distributions are quite related to RS phenomena.

The problem with a 3D approach is the computation time in a simulation domain with many grid points, so, a low cost numerical method has to be selected. For instance, the finite difference method. For the use of this method, a good grid has to be defined, as commented in the previous section **2.2**. In this work, 3D grid structures between 5 and 10 nanometers have been used with a grid step size between 0.25 and 0.5 nanometers. A more detailed explanation of how these equations are solved can be seen in the appendix **6.4**.

2.4. Conductive filament density, 2D/3D percolation and field approximation

An advantage of the kMC based tools is the information given about the CF structures and the defect distribution in the dielectric. This information allows to study the density and compactness of the filament, its relation with the resistance or the stochastic evolution of the gap due to the CF formation/rupture.

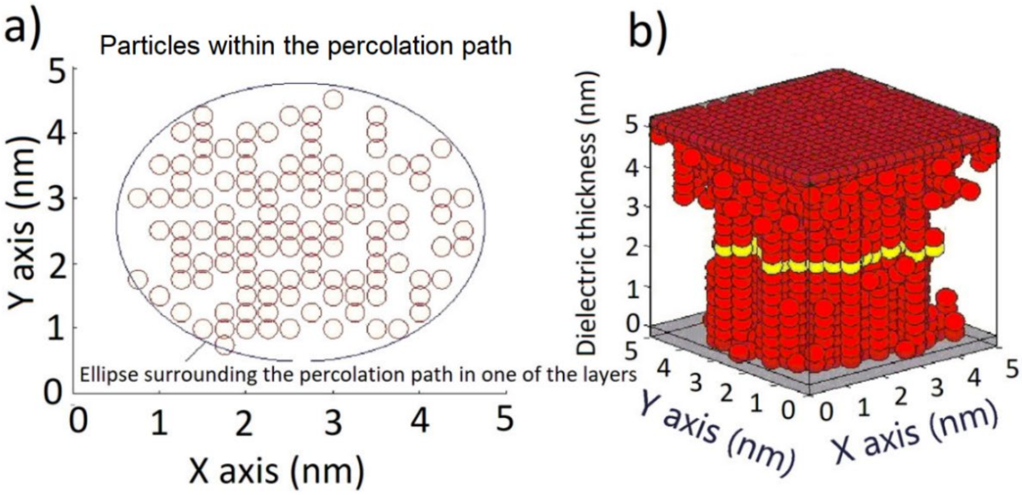

Figure 2.4-1. a) The ellipse needed for calculating the CF density, which is drawn by surrounding the percolation path for a grid layer. b) The CF layer particles shown in a) [Aldana2018b].

A procedure to calculate conductive filament density can be implemented. A good way could be considering the ellipse that better fits the surroundings of the percolation path in every CF layer in the simulation domain, as shown in **Figure 2.4-1**. The ellipse foci can be obtained using a clustering algorithm. In this manner, the volume and density of the CF can be estimated using different ellipses for each layer of the CF.

The compactness of the CF is a magnitude that can be related to the density and the resistance of the device. It can be understood as a measurement of the CF porosity, that is, the amount of holes within the percolation path. One strategy would be the analysis of the 2D percolation paths that constitutes the CF. **Figure 2.4-2** shows different planes in the X and Y axis where the percolation paths are searched. This kind of analysis allows to compare the percolation paths in a 3D and 2D perspective, where it is possible to find paths in 3D while in 2D there is still none. This is because of the lateral interaction between different layers in the 3D description. The situation where many 2D percolation paths are found is clearly more stable than the case where only 3D percolation path exists. In this way, the 3D simulation domain it is recommended for a realistic device description.

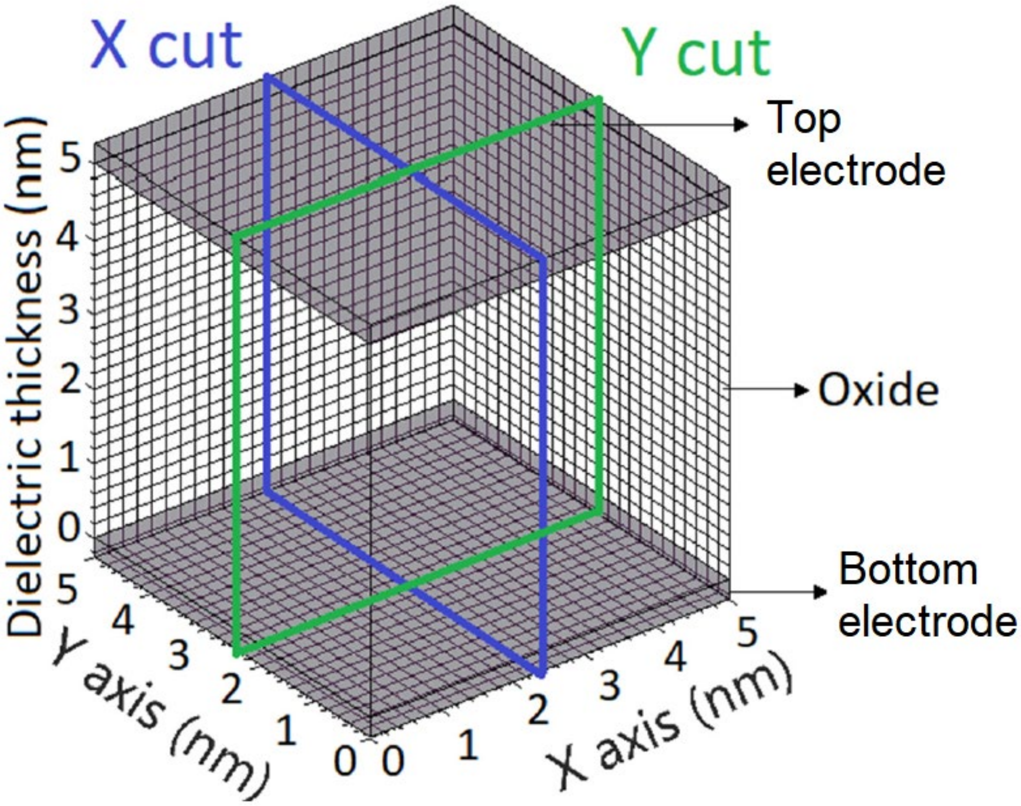

Figure 2.4-2. Representation of slices made in X and Y axis in a whole 3D simulation domain [Aldana2018].

Other strategy for the study of the CF compactness is the analysis of the number of nearest neighbor particles surrounding each particle in the simulation domain. The maximum number of neighbors for each particle (neglecting the diagonals) would be six. The way to study the CF compactness through this perspective is to compare the number of occurrences in which a particle has a determined number of neighbors. That is, the number of particles that have six neighbors, five neighbors, etc. In this way, when the volume is fixed, the higher the number of particles with higher number of neighbors, the higher the CF compactness. It is clear that the CF compactness is quite related with the ohmic resistance, the denser the CF the higher the metallic area for current conduction.

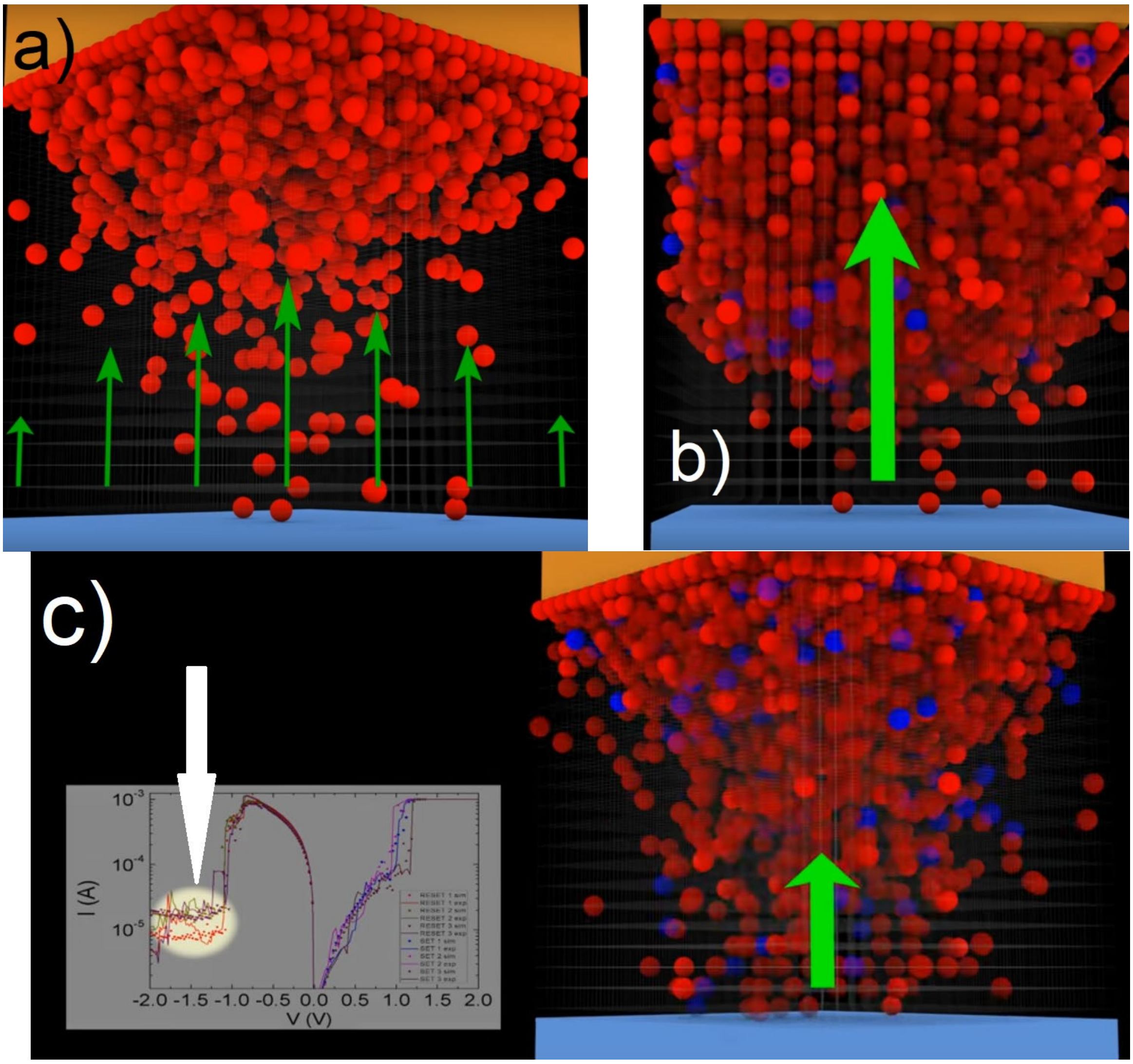

Figure 2.4-3. a) and b) are two different phases of the growing of the virtual electrode during a SET process. In c) the current fluctuations due to the stochastic evolution of the virtual electode (that is, the gap) are pointed out [videoBipolar].

The study of the stochastic evolution of the gap between the electrodes is other of the important analysis that this kind of tools allow to carry out. To understand the evolution of the gap we have to understand that clusters that are formed near the electrodes (both the top and the bottom) act like an extension of the electrodes, named virtual electrodes. It should be noted that the bigger the virtual electrodes (that is, the smaller the gap) the greater would be the electric field, as it depends on the distance between electrodes, as shown in **Figure 2.4-3a** and **2.4-3b**. The stochastic evolution of the virtual electrode, related with the formation (or ruptured) of the CF, is shown in Ref. [videoBipolar]. As the current depends on the magnitude of the electric field, this stochastic changes in the electric field would provoke also current fluctuations as shown in **Figure 2.4-3c**. In this sense, this study lets us understand the stochastic behavior of the current when the CF is ruptured (that is, during the HRS), as it depends on the gap.

Chapter 3

3. Conductive Bridge RAM

3.1. Resistive switching mechanism

As already described above, the Conductive Bridge RAM (CBRAM), also known as Electrochemical Metallization Cell RAM (EMC) [Menzel2009, Menzel2015, Waser2009, Schindler2009, Ielmini2015, Lu2012], has this name because of the conductive percolation paths that govern the device resistance changes. Depending on the bias needed to carry out the RS, it can be distinguished the unipolar (called in some circumstances thermochemical RRAM memory) and bipolar devices.

As has been exposed in the section **1.3.1**, the CF formation and rupture in these devices are based on electrochemical processes, that is, the oxidation and reduction of atoms that come from the active electrodes and take place in the dielectric (the solid electrolyte) [Ielmini2015, Lu2012, Menzel2009, Menzel2015]. To achieve the oxidation of these atoms, a high enough electric field must be applied, which also drags the ionized atoms through the dielectric until they are reduced. The reduced atoms can be grouped and the different clusters overlap until the CF is completely formed (a complete forming or SET process is achieved when the CF shorts the electrodes). This CF usually has a metallic-like behavior and starts growing near the bottom electrode or the top electrode depending on the mobility and reduction probabilities [Pan2014, Hasegawa2010, Lu2012, Pan2011]. In **Figure 3.1-1a-e** it is shown how a CF grows from the active electrode (Ag) to the inert electrode (W) and in **Figure 3.1-1f-i** how the CF grows from the middle region to both electrodes (Ag and Pt). This effect will be treated in the section **3.2**.

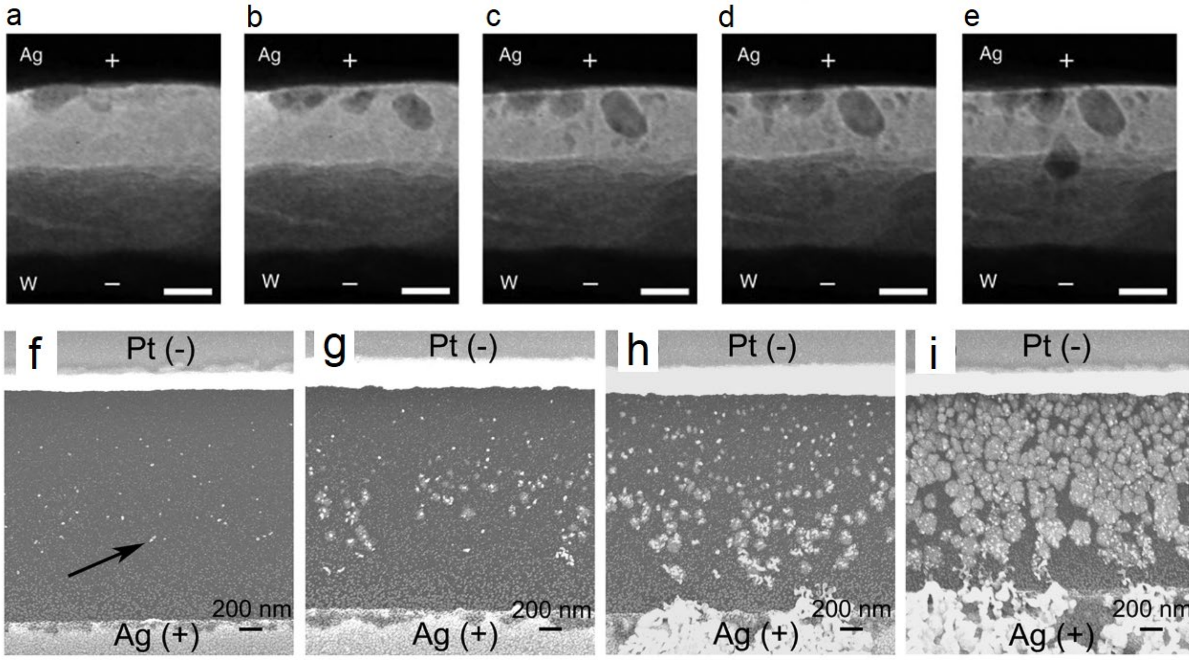

Figure 3.1-1. a-e are TEM observation of an Ag filament in a Ag/a-Si/W ECM cell during a forming process. A conical-like CF shape is shown with the broadest part near the Ag electrode. The scale bar is 20 nm. In f-i the Ag filament formation for a Ag/PEDOT:PSS/Pt ECM cells is shown in SEM images. The clusters are formed from the middle region toward both electrodes [Pan2014].

If the starting clusters are in contact with the electrodes, they would work as an extension of these electrodes. In this case, they are called virtual electrodes [Waser2010, Waser2012]. This is also the case when the CF is ruptured and the remnants are in contact with some of the electrodes. In thermochemical devices, the CF rupture is thermally assisted, as the atoms get oxidized and then diffuse due to the temperature rise. The electric field can also have some importance, but it is not the dominant factor [Pan2014, Villena2014]. However, for the bipolar case, the importance is the opposite one, being the most relevant factor the electric field, with the temperature as a subsidiary factor [Pan2014, Lanza2014, Villena2017]. This is the reason why the operation must be bipolar for this kind of devices.

In general, the electrodes in most devices are selected for their conductive properties for working as transport path for carriers. However, in this case, as it has been explained in section **1.4.2**, the selection of the electrode materials is crucial because they can affect the RS operation. It can be the difference between having a stable bipolar RS operation or no RS at all. As explained above, the electrodes are the responsible of the generation of the CFs [Gao2012]. The materials used for the active electrodes in our case were Ni for unipolar devices (see appendix **6.6.1**) and Cu for bipolar devices (see appendix **6.6.2**). It should be highlighted that Ag electrodes are also widely used in many CBRAMs as it was one of the first electrodes employed for these devices. Ag ions have high mobility due to his small size; this is why it has been also intensively studied and used [Yang2012b, Terabe2005, Valov2013, Lee2015, Pan2014]. Two examples of CFs made of Ag have been shown in

Figure 3.1-1. For the dielectric materials, as presented in section **1.4.1**, the most common are the binary oxides for their RS promising characteristics. Some of the device characteristics are the ultra-high ON/OFF ratio $> 10^9$, sub-ns operation speed and extreme durance ($> 10^{12}$ cycles), just like the thermal stability and the compatibility with CMOS technology. Among the binary oxides, one of the most promising is HfO_x because of its great endurance ($> 10^{10}$) and its sub-ns operation speed [Pan2014, Lanza2019].

For the design of the simulators that can reproduce the behavior of CBRAMs (unipolar and bipolar), taking into consideration their complexity, the kinetic Monte Carlo algorithm has been chosen as a nucleus. The main processes that the kMC algorithm includes are the oxidation, reduction and migration processes, among others. It is important to point out that no assumption about the CF shape is needed as the model can simulate the complete forming process since the pristine state (this is substantially different to what happens in the compact modeling context). In this sense, an algorithm like the one presented in appendix **6.3** has to be used to calculate the percolation paths in order to know when the device is in the LRS, that is, when the CF is fully formed and ruptured. Besides, some FEM approaches for solving the heat and Poisson equations have been used to deal with the temperature and electric field, as explained in section **1.6.2**. For a more detailed description about this approach, i.e., the solution of the heat and Poisson equations, it can be seen appendix **6.4**. These two magnitudes are quite important, in particular the temperature since the device operation is temperature-driven. The RESET is thermally triggered (most of the physical mechanisms behind RS are thermally activated). The electric field is also essential as it is involved in the redox and migration processes. Regarding the conduction mechanisms, different approaches for LRS and HRS have been used. For the current during the LRS, the Maxwell resistance, the set-up resistance and CF ohmic resistance have taken into account in an equivalent circuit, which can even include the QPC conduction model if needed. For a deeper explanation of these mechanisms, see appendix **6.2**. Concerning the conduction mechanisms during the HRS, a Poole-Frenkel model with effective parameters can be used. It is important to note here that many mechanisms can operate at the same time and thus many experiments would be necessary for understanding which are the dominant. A compilation of the main mechanisms that can be found for the charge transport through a dielectric is given in appendix **6.1**.

The simulator consists of 3855 code lines and the estimated time to carry out a complete cycle (including the forming, RESET and SET processes) is around 8 hours.

3.2. Unipolar CBRAM

The unipolar CBRAM is one of the main device types that can be reproduced by means of a computational tool.

The main characteristics of the simulator presented here [Aldana2017] are:

- It is based in a kMC algorithm that implements the main redox processes in CBRAM devices: among others, the reduction and the oxidation of atoms, and the field-driven migration of charged particles (ions).
- The percolation paths are calculated using the Hoshen-Kopelman algorithm [Hoshen1976], as explained in appendix **6.3**. This kind of algorithms allows to take into account the virtual electrodes, that is, the metallic-like clusters in contact with the top or the bottom electrodes.
- No CF shape is necessary to be assumed in these simulations, as complete RS cycles can be reproduced since the pristine state.
- In the simulation domain, Neumann (for lateral faces of the cubic grid) and Dirichlet (for the top and bottom electrode) boundary conditions have been implemented for the resolution of the Poisson and heat equations.
- Regarding the conduction mechanisms, an equivalent circuit has been used for the LRS, where CF ohmic resistance, the QPC conduction, the Maxwell resistance and the set-up resistance have been included. However, the conduction mechanisms used through the dielectric in the HRS was the Poole-Frenkel emission with effective parameters.

The fabricated devices used to calibrate the simulator was a $Ni/HfO_2/Si$ made at the Institut de Microelectrònica de Barcelona IMB-CNM (CSIC) Bellaterra, Spain. A more detailed explanation of how the fabrication has been performed and the measurement process can be found in appendix **6.6.1**. The thickness of the dielectric layer (HfO_2) was 5 nm and the cubic grid used was 5 nm x 5 nm x 5 nm. The size of the Ni atoms, that is, the separation between grid points was assumed to be 0.25 nm. Two sorts of measurements have been made with the aim of fitting the simulator:

- The current-voltage (I-V) curves at 300 K in ramped voltage sweeps experiments. This information can also be used for extracting V_{SET} and V_{RESET} values for a distribution plot.
- Constant voltage stress measurements (CVS) for evaluating the forming time and other RS features.

Once the tool is calibrated, it has been used to reproduce several RS cycles, to study the evolution of the device temperature, the dispersion of some electrical characteristics (V_{SET} and V_{RESET}), the forming times and the relation between the mobility of the atoms and the reduction probability of the ions (which allows to form the CF from the top electrode to the bottom or following the opposite direction).

A detailed video with the main measurement characteristics, fabrication process, simulation characteristics and simulation results exposed above has also been made for illustrating the computational tool capability [videoUnipolar]. In **Figure 3.2-1a,** the real device structure is represented in a Blender design as well the measuring setup, where some explanation of the fabrication process and measurement conditions are given. **Figure 3.2-1b** corresponds to the next section of the video, where details about the simulation techniques are exposed. In the video, the physics behind the resistive switching in unipolar CBRAMs is reproduced in a scientific way, as it was made with simulation data after the fitting process. In this sense, the motion of the particles and the I-V curves shown along the video are not an idealization, but they are simulated data. This part of the video corresponds to the **Figure 3.2-1c-d**. The video was published on 4th of February 2017, and it garnered 3700 views on YouTube until 7rd of September 2020. It also should be noted that the video is highly positioned for Youtube and Google searchs when the keywords "kinetic monte carlo RRAM" are used, being between the first places.

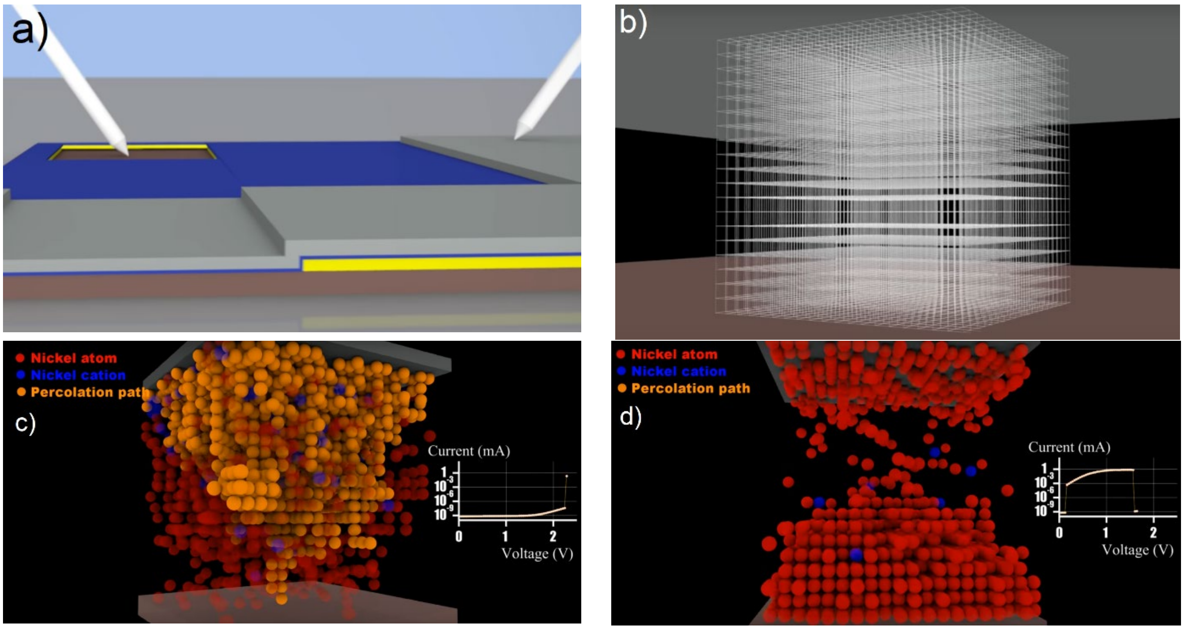

Figure 3.2-1. Figure a) corresponds to the part of the video when a cross section of the RRAM stack (Ni/HfO_2/Si) is shown, the measurement conditions are explained and the fabrication process is detailed. In b) the 3D grid used is presented with the main characteristics of the simulation, as the boundary conditions. This grid is used for solving the Poisson and heat equation. The electrodes are shown for clarity. In c) and d) it is shown the real movement of the particles given by the simulator, just like the I-V curve shown along the video corresponds to the data obtained after the fitting process. In c) the fully formed CF just after the forming process is presented and in d) the CF remnants after the RESET process [videoUnipolar].

The following section is an already published work [Aldana2017].

S. Aldana et al.

Journal of Physics D: Applied Physics (2017)

Aldana, S., García-Fernández, P., Rodríguez-Fernández, A., Romero-Zaliz, R., González, M. B., Jiménez-Molinos, F., Campabadal, F., Gómez-Campos, F., Roldán, J. B. (2017). A 3D kinetic Monte Carlo simulation study of resistive switching processes in Ni/HfO2/Si-n+-based RRAMs. *Journal of Physics D: Applied Physics*, *50*(33), 335103. DOI: https://doi.org/10.1088/1361-6463/aa7939

Quality metrics 2017

Data base	Rating	Quartile
Web of Science	Impact factor: 2.373	Q2
Scimago	Scientific journal ranking: 0.717	Q2

Publication citations (**2020-09-07**)

Google Scholar	Web of Science
30	**22**

A 3D Kinetic Monte Carlo simulation study of Resistive Switching processes in Ni/HfO2/Si-n+-based RRAMs

S. Aldana[1], P. García-Fernández[1], Alberto Rodríguez-Fernández[4], R. Romero-Zaliz[3], M.B. González[2], F. Jiménez-Molinos[1], F. Campabadal[2], F. Gómez-Campos[1], J.B. Roldán[1*]

[1]*Departamento de Electrónica y Tecnología de Computadores. Universidad de Granada. Facultad de Ciencias. Avd. Fuentenueva s/n, 18071 GRANADA, Spain. Email: jroldan@ugr.es*

[2]*Institut de Microelectrònica de Barcelona, IMB-CNM (CSIC), Campus UAB, 08193 Bellaterra, Spain*

[3]*Departamento de Ciencias de la Computación e Inteligencia Artificial. Universidad de Granada. Escuela Técnica Superior de Ingenierías Informática y de Telecomunicación, 18071 GRANADA, Spain*

[4]*Dept. Enginyeria Electrònica. Universitat Autònoma de Barcelona, Edifici Q. 08193 Bellaterra, Spain*

ABSTRACT

A new RRAM simulation tool based on a 3D kinetic Monte Carlo algorithm has been implemented. The redox reactions and migration of cations are developed taking into consideration the temperature and electric potential 3D distributions within the device dielectric at each simulation time step. The filamentary conduction has been described by obtaining the percolation paths formed by metallic atoms. Ni/HfO2/Si-n+ unipolar devices have been fabricated and measured. Different experimental characteristics of the devices under study have been reproduced with accuracy by means of simulations. The main physical variables can be extracted at any simulation time to clarify the physics behind resistive switching; in particular, the final conductive filament shape can be studied in detail.

Keywords: Resistive switching memory, RRAM variability, simulation tools, conductive filaments, Kinetic Monte Carlo

I.-INTRODUCTION

Resistive RAMs (RRAMs) are promising candidates for the next generation of high density non-volatile memories. Because of their outstanding potential, the scientific community follows the great number of research works devoted to unveil the physics behind their operation. RRAMs have a simple structure, excellent scalability, low power, fast speed, the possibility of fabrication in 3D memory stacks and compatibility with the BEOL of CMOS processes [1-14]. The viability of resistive RAMs has been proved at the device level and also in the integrated circuit arena as reported in Refs. [15-17]. The advantages of this technology with respect to Flash devices lie on remarkable improvements in the reading/writing speed, endurance, operation power, etc. Nevertheless, several hurdles have to be overcome to incorporate RRAMs in the industrialization lines, e.g., the poor control of switching uniformity. This lack of uniformity implies variations in the forming, set and reset voltages, and in the resistance distribution [1, 7, 13, 14]. Great research efforts are needed to clarify the mechanisms behind the physics of Resistive Switching (RS) and consequently behind the device variability. In this context, the availability of simulation tools to analyse the main RRAM operation characteristics linked to charge transport, temperature distribution, etc., is essential to deepen on the technological development needed prior to commercialization. To contribute to this issue in this paper we introduce a physically based 3D simulator to describe RRAMs operation at a microscopic level.

RRAMs are formed by a dielectric sandwiched between two electrodes. If RS operation is filamentary, the most common case, the devices switch between two different resistance states that are obtained by means of the formation and destruction of one or more conductive filaments (CFs). There are different mechanisms to explain the CF formation/disruption, among them one is connected with the oxidation and reduction of atoms coming from the active electrode within an electrochemical regime [6, 14, 18]. In this kind of devices, after a forming process on a pristine dielectric, there is a change from a high resistance state (HRS) to a low resistance state (LRS). The device can be switched again to a HRS thanks to the CF partial dissolution (reset) and from the HRS to the LRS through a process that regenerates the CF (set) [1, 4, 6-8, 19, 20]. As a consequence of its simple structure, RRAMs can be easily integrated in a passive crossbar array with a size of $4F^2$, where F is the minimum feature size achievable by lithography. In addition, this size can be reduced to $4F^2/n$ with vertically stacked architectures, where n is the stacking layer number of the crossbar array [1].

For the electrochemical operation mechanism reported above, the set and forming processes are based on the generation of cations by oxidising active electrode atoms. These cations are dragged by the electric field through the dielectric medium where they could be reduced, usually when they reach the inert electrode. This process forms the CF that bridges the electrodes [3, 9, 21]. If the cation mobility in the dielectric is low enough, instead of traveling along the whole structure, the ions could be reduced close to the active electrode, forming a layer of the same atoms found in the electrode. This layer can be treated as an extension of the electrode and it is called virtual electrode [11]; the CF remnants in contact with the electrodes after a reset process can also be considered virtual electrodes. In devices with the latter features the CFs are formed from the active electrode (the CF wider part is close to the active electrode) to the inert electrode. The CFs could be also formed the other way around in high ion mobility dielectrics [1].

There are two types of RRAMs depending on the voltage polarity needed to produce RS processes: bipolar and unipolar. In unipolar devices the same polarity is employed for set and reset, whereas for bipolar devices a different polarity is needed [8, 20, 22]. For unipolar devices based on electrochemical mechanisms, the CF creation is related to ion generation at the active electrode interface and ion reduction in the dielectric till the CF is fully formed. However, the CF destruction is based mainly on thermal phenomena [1, 19]. In this respect, the temperature increase produced in the reset process rises oxidation and ion diffusion velocities and accelerates the processes that lead to the CF disruption. It is clear, then, that the physical description of the device operation requires an accurate device thermal description, and therefore, the 3D solution of the heat equation.

As explained above, we introduced in this work a new microscopic simulator to delve into the RRAM physics. Several microscopic RRAM simulators have been developed so far; some of them rely on a 2D description [1, 6, 7], others are developed in a 3D scheme [8]. Few of them are based on ion generation in the active electrode and the description of their migration and corresponding reduction processes that lead to the CF formation [1, 6, 21]. Others describe the CF formation by means of oxygen vacancies [7, 8] in valence change memories; in most cases, the simulator core is based in Kinetic Monte Carlo algorithms. Some tools based on the physical description of oxide vacancies CFs are employed to describe complete RS processes, including the initial forming process [7, 8]. However, as far as we know, there are not any electrochemical RRAM 3D simulation tools that can describe a forming process followed by several complete RS cycles. Some of them can simulate the forming and set transitions, but not reset [6]; others only describe forming [21] in a partial manner since the number of simulated ions employed is low [1]. In this context, the inclusion of the 3D heat and Poisson equations to account for the RS dynamics is needed [6, 7, 8, 19, 20]. Charge transport is described by trap-assisted tunnelling models in certain tools [6-8] while in others a model based on the ohmic conduction is employed; in the ohmic conduction case, the CF resistance, the set-up and Maxwell series resistance components are included [19, 20].

In the simulator we present here a 3D description for ion generation and migration is employed within a Kinetic Monte Carlo (KMC) algorithm. The 3D Poisson and heat equations are solved at every simulation step. Forming and the subsequent complete cycles of set and reset processes can be simulated continuously for an unipolar device.

The fabricated devices and measurement process are explained in section II, the simulator features are detailed in section III and the main results and discussion are reported in section IV; finally, some conclusions are drawn in section V.

II.-DEVICE DESCRIPTION AND MEASUREMENT

The Ni/HfO_2/Si devices were fabricated on (100) n-type CZ silicon wafers with resistivity (0.007-0.013) Ω cm following a field-isolated process. Atomic layer deposition at 225°C using tetrakis (Dimethylamido)-hafnium (TDMAH) and H_2O as precursors was employed to

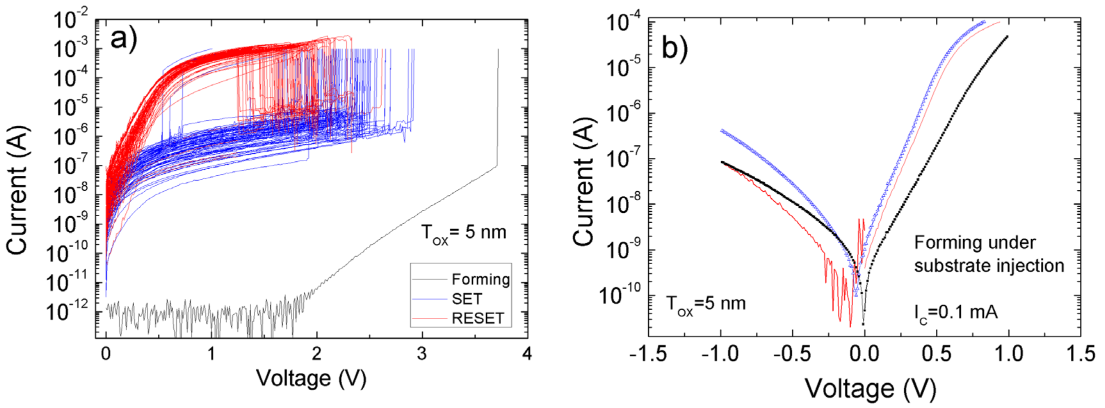

Figure 3.2-2. a) Experimental current versus applied voltage in the RRAMs under study. A forming process and several RS cycles are shown. b) IV curves (in the LRS state) after a forming process under the regime of substrate injection forming. A self-rectifying behavior shows up due to a Schottky barrier built between the Ni based CF and the semiconductor (two decades for the current difference are obtained for an external voltage of ±0.3V). The oxide thickness (Tox) is 5 nm.

deposit 5nm-thick HfO_2 layers. The top Ni electrode with a 200nm thickness was deposited by magnetron sputtering [25].

The current-voltage (I-V) characteristics were measured at 300 K by means of a HP-4155B semiconductor parameter analyser controlled by GPIB with a PC, using MATLAB. In addition, constant voltage stress measurements (CVS) were performed in order to evaluate the forming time of the devices. The CVS curves were measured using the Keysight B1500 semiconductor parameter analyser equipped with the waveform generator fast measurement unit (*WGFMU*) module. The Si substrate was grounded and a positive voltage was applied to the Ni electrode.

The device I-V curves measured for positive voltages correspond to an operation regime that is characterized by electrochemical mechanisms that lead to conductive filaments formation and disruption. See a forming I-V curve and several set/reset cycles that follow in **Figure 3.2-2a**. The use of a positive forming voltage leads to a Substrate Injection Forming (SIF) regime linked to Ni electromigration, as reported in [25]. The impact of cation migration on Ni-based CF formation has also been studied in Refs. [25-27], and can be extended to the case we are presenting here. In our devices a self-rectifying effect was observed due to the presence of a Schottky barrier between the metallic CF and the semiconductor. The curves in the LRS after a forming process are shown in Fig1b. Nevertheless, in this manuscript we will pay attention just to the unipolar operation for positive voltages; i.e., the forward bias operation regime.

In the next section we describe a physically based simulation tool and the experimental comparisons needed to tune the main model parameters. We assume that the unipolar operation of the RRAMs reported above is based on redox processes and Ni cation migration.

III.-SIMULATION DESCRIPTION

As the majority of microscopic solid state systems, the dynamics can be characterized reasonably well by transitions between different states. Due to this, a KMC algorithm is proposed to describe the physics behind the operation of the fabricated RRAMs. A KMC approach takes into account the transition rates between the states found in the conventional device operation [29]. This simulation scheme reproduces device RS variability in a natural manner since the physical processes involved in the simulation of the device operation are generated within a stochastic algorithm. The SET processes depend on previous RESET processes because the new CF formation uses the remnants of the previous RESET as a starting point. The stochasticity of the RS simulation is also linked to the thermal evolution of the device.

The different processes that take place within the system are modelled by the transition state theory (TST), which introduces the rate calculation as in Equation 1,

$$\Gamma = v \exp\left(-\frac{E_A}{k_B T}\right) \tag{1}$$

following Maxwell-Boltzmann statistics [6]. Here Γ stands for the transition rate, v stands for a vibration constant, E_A is the energy barrier height, k_B the Boltzmann constant and T the temperature. The transition rate corresponds to the inverse of the time needed for a determined mechanism to take place. The activation energy will depend on the electric field and other local characteristics described by the simulator such as the presence of CFs or electrodes. The system can be considered memoryless, consequently the probability for a determined action to take place in a time duration t can be expressed as follows [6]:

$$P = 1 - \exp(-\Gamma \cdot t) \tag{2}$$

In the simulations performed, the RRAM physics is described by means of reduction/oxidation reactions, metallic ion movement, ion and atom clustering and the formation and disruption of conductive filaments made of reduced ions.

In the forming and set processes, some important mechanisms are involved like the anodic dissolution of the Ni electrode [1, 5, 9, 18, 21]. This oxidation process is linked to the formation of an ion starting from a neutral atom that can occur at the electrode's interface or in the dielectric (in this latter case considering atoms linked to previous RS cycles). The reduction process consists of electron capture by the ion, and can occur anywhere. In our case, for the generation of ions we assume that the activation energy depends on the electrode current which induces ion drift within the electrode [2]. The migration of Ni ions through the dielectric toward the bottom electrode and the growth of the Ni filaments are electrically controlled [2, 9, 18]. The formation of CFs bridges the electrodes and makes the device resistance state change from HRS to LRS. After that, the Ni-based CF will be destroyed by Joule heating [1, 3, 19, 30] since this process it is carried out with the same polarity as the forming and set process. After the Joule heating process, which increases ion oxidation, there will be ion diffusion and drift till the CF is broken. After the CF rupture and the corresponding current drop the device temperature decreases swiftly [3].

Each ion can migrate to anyone of the adjacent null sites around it (grid sites without ions or reduced atoms). The ion mobility depends on an energy barrier for ion hopping whose value is assumed to be the same in all directions and is modulated by the electric field as follows [6],

$$E_h = E_h(V = 0) - \frac{Qd\epsilon(x, y, z)}{2} \tag{3}$$

where Q is the ion charge, d is the physical distance between the two states, ϵ is the applied electric field and $E_h(V = 0)$ is the energy barrier for the ion hopping in absence of an electric field. For our simulations we have employed a value for $Eh(V = 0) = 0.91\ eV$. Under this simulation approach a determined electric field enhances ion movement in one direction and hinders the opposite movement.

The activation energy for ion reduction (E_R) or oxidation of a Ni atom (E_{ox}) is related to the number of atoms surrounding it (n). If the diagonals are not considered, the maximum of atoms that can surround the ion or atom is n_max (n_max=6). This would mean that the energy will vary in the following way: $E_R(n) = E_R(0) - n * \frac{0.2}{n\_max}$ for the reduction energy and $E_{ox}(n) = E_{ox}(0) + n * \frac{0.2}{n\_max}$ for the oxidation energy (see Ref. [1], a 3D generalization has been included here). In our case the values introduced in our simulation tool are $E_R(0)$=0.8 eV and $E_{ox}(0)$=1.0 eV. These energies are important parameters as their values and the connection with other energies influence the final shape of the CF [1]; nevertheless, as we shall show below, the most important processes to consider in the CF shape determination are the activation energies linked to the ion mobility and generation. In this respect, the relation of the latter parameters can make the CF formation to start close to the top electrode and grow towards the bottom electrode or the other way around. The migration of atoms is ignored since they move much slower than ions under the influence of an external electric field [1].

Once the ions reach the bottom electrode, it is quite difficult for them to reoxidize again, so, the bottom electrode should enhance the reduction of ions and hinder the oxidation of atoms [21, 30]. Taking into consideration these facts, an implementation of this phenomenon is reasonable by decreasing the activation energy for reduction for all the ions that reach the bottom electrode and form the virtual electrode (the atom cluster formed close to the electrode and connected to it by at least one atom).

Another mechanism included in the simulator accounts for the relation between the external voltage and ion generation. It has been highlighted that there exists a voltage threshold for the forming and the set processes [1, 4, 10, 18, 21]. In addition, other studies show that the current through the active electrode produces a potential gradient inside the electrode which drags ions to the sub-surface [2]. We have followed this latter approach by using the following expression for the corresponding activation energy.

$$E_g = E_g(V = 0) - FR_{TE}I_{RRAM} \tag{4}$$

where $E_g(V = 0) = 0.96\ eV$, R_{TE} stands for the top electrode ohmic resistance (assumed to be 20 Ω) and I_{RRAM} the total device current. F is a fitting parameter.

The geometric structure of the RRAMs under study is sketched in **Figure 3.2-3a** [24]. We selected a 3D cubic simulation domain (SD) where the dielectric and the electrodes interfaces are included (**Figure 3.2-2b**). Since the HfO_2 dielectric is 5nm thick, a 20 points grid is needed in every axis since the Ni atomic radius is around 0.125 nm. The z axis in **Figure 3.2-3b** is perpendicular to the device stack.

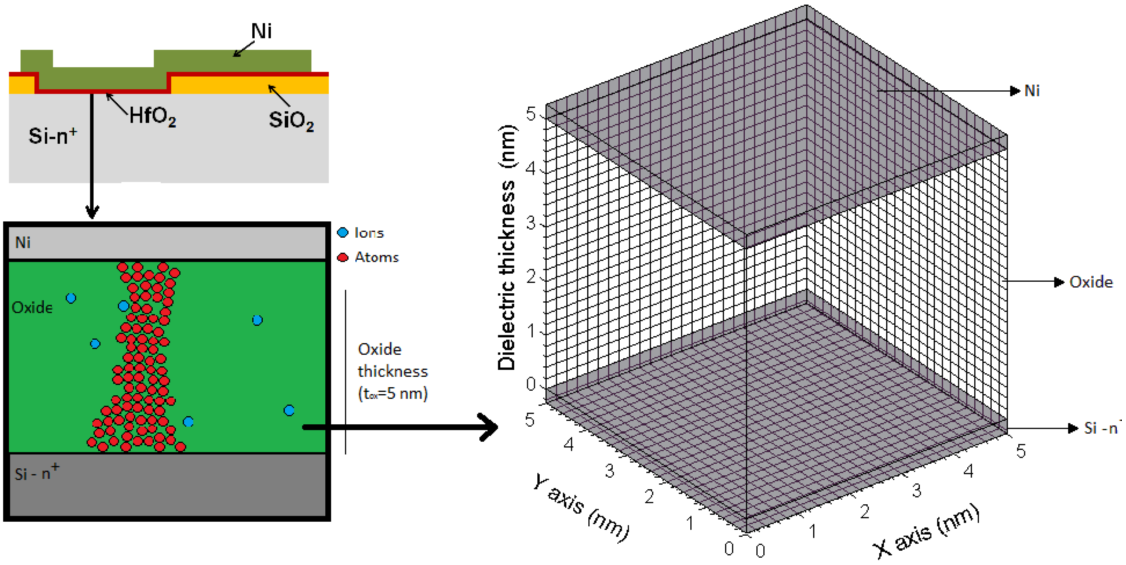

Figure 3.2-3. a) Cross section of RRAM fabricated and scheme employed in the simulations. Below, it is shown the RRAM stack with a Ni active electrode, an inert Si electrode and a dielectric (HfO2) in between, where the conductive filament is formed and ruptured. b) Simulation domain with a 3D grid, the electrodes are shown for clarity. In the simulation domain the 3D Poisson and 3D heat equations are solved making use of mixed boundary conditions.

The temperature determination is performed by solving the 3D heat equation (Expression 5).

$$P(x,y,z) = -K_{th}(x,y,z)\left[\frac{\partial^2 T(x,y,z)}{\partial x^2} + \frac{\partial^2 T(x,y,z)}{\partial y^2} + \frac{\partial^2 T(x,y,z)}{\partial z^2}\right] \tag{5}$$

where $K_{th}(x,y,z) = 0.49\ \frac{W}{m \cdot K}$ is the thermal conductivity of hafnium oxide [31] and *P*(x,y,z) the power density dissipated at each grid point. Mixed boundary conditions are employed to solve equation 5. A constant temperature is assumed at the electrodes and adiabatic boundary conditions are used at the SD lateral faces. Based in previous works related to the thermal behaviour of RRAM devices [32], we have simplified the calculations linked to determine the temperature temporal evolution.

For the 3D Poisson equation, we have also employed mixed boundary conditions: a constant voltage is assumed at the electrode interfaces and Neumann boundary conditions at the SD lateral faces. A simplification scheme based on Ref. [7] can be used to improve computing-time issues.

In order to use the KMC algorithm, the first step is to calculate all the transition rates to weigh each process statistically. Once the transition rates have been calculated, we can determine an optimized iteration duration time *t* as follows [6]:

$$t = -\frac{\ln(1 - randm)}{\sum \Gamma} \tag{6}$$

A random number (*randm*) between 0 and 1 is employed and the value generated corresponds to the probability of at least one event occurring. As can be deduced, the bigger the sum of all mechanism rates the smaller the iteration time *t*.

In order to select the occurring event we compare the calculated number $r \cdot \Gamma_{Total}$ (r is a randomly generated number) with the elements of a vector formed by the partial sums of the transition rates $s(j) = \sum_{q=1}^{j} \Gamma_q$. Then, the first event that fulfil the following condition (Equation 7) is chosen,

$$s(j) > r \cdot \Gamma_{Total} \tag{7}$$

After the movement of the set of ions within the simulation domain, the simulation flow goes on as depicted in **Figure 3.2-3**. We calculated the current and potential at the same time, as in Ref. [6], to save computation time.

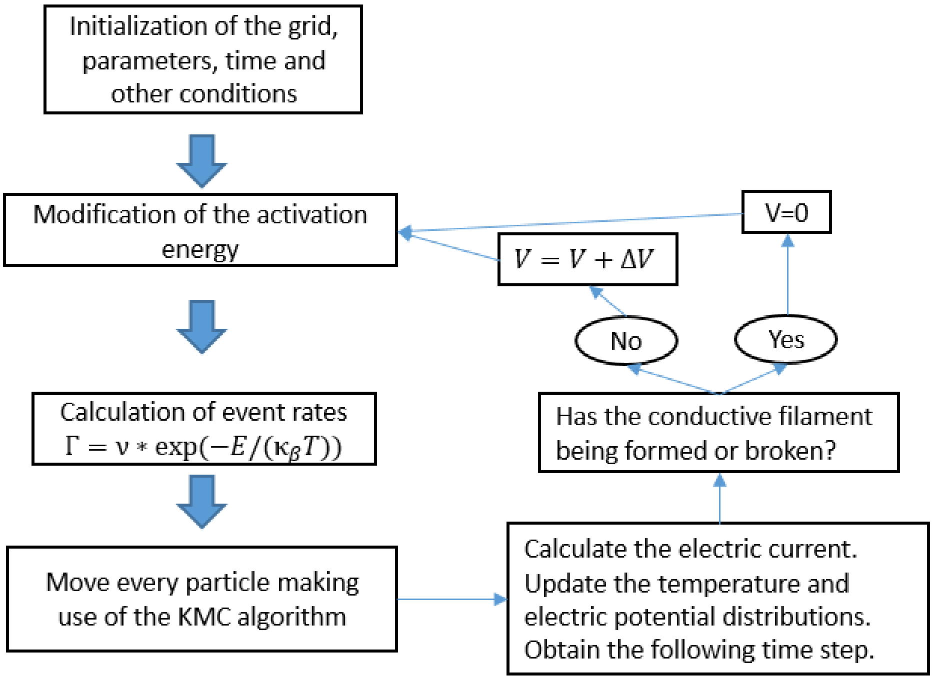

Figure 3.2-4. Simulation flow-graph. A KMC algorithm is the key module in the simulator.

We have included the calculation of virtual electrodes in the simulator; i. e., the Ni atom clusters within the dielectric in contact with both electrodes. In this manner, the effects and phenomena occurring at the electrodes have been transferred to the interface of the virtual electrode. Therefore, the electrode border and the gap between the electrodes changes dynamically along with the simulation.

In the pristine state and the HRS, the main conduction mechanism is described by the Poole-Frenkel model. However, when a fully formed CF shorts the electrodes, the QPC [19, 23] and ohmic conduction mechanisms are included, in addition to Poole-Frenkel which is clearly masked by the conduction mechanisms linked to the conductive filaments.

In the ohmic operation regime, after one or more percolation paths are found, we calculate the device current making use of the equivalent circuit shown in **Figure 3.2-5**. The simulator can deal with an arbitrary number of CFs and can calculate their time evolution simultaneously. The CF resistance (R_{CF}) is obtained by considering the contribution of each Ni atom to the total CF resistance; therefore, we recalculate this resistance at each simulation step.

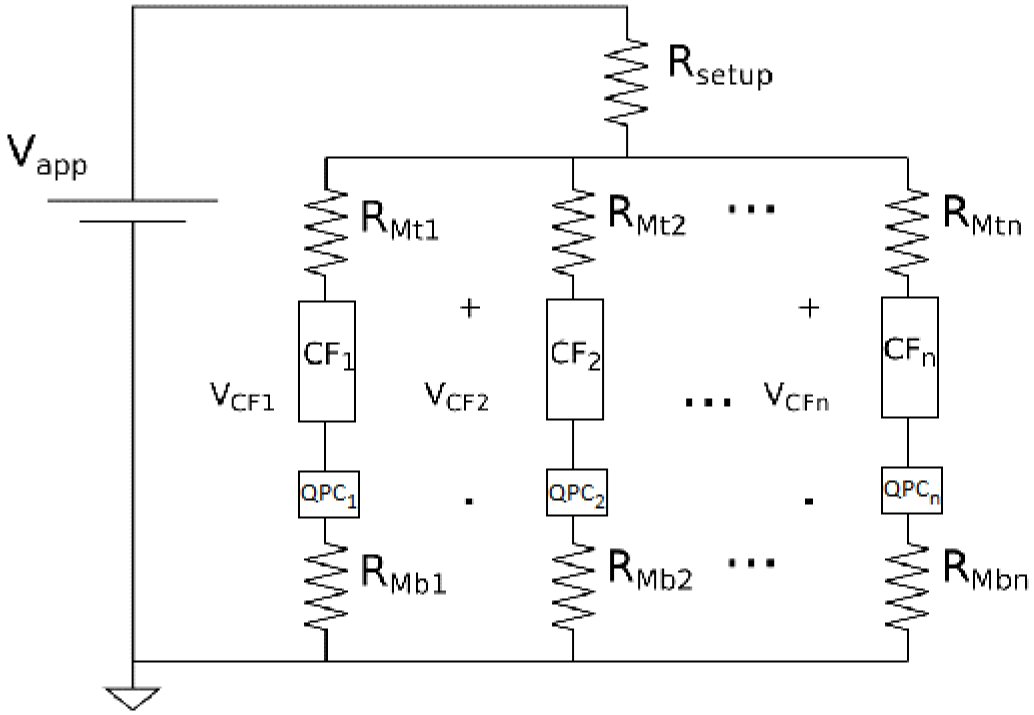

Figure 3.2-5. Electrical equivalent circuit considered in the simulator for the current calculation in the ohmic regime (after one or several percolation paths are found). R_{setup} is the resistance that accounts for the electrodes resistances, and CF_i is the ith conductive filament across the insulator, QPC_i represents a constriction and the current through it is described by means of the Quantum Point Contact model [19, 23]. R_{Mti} and R_{Mbi} are the Maxwell's resistances in the top and bottom electrodes respectively.

A common resistance (R_{setup}=40 Ω) is added to model the effect of both the top and bottom electrode resistances, see **Figure 3.2-5**. Finally, in series with each CF, Maxwell resistances have been added in order to take into account the funnelling of current lines from the large electrodes to the narrow CFs [20, 33]. For the sake of generality, we have split the Maxwell resistance for each CF into two contributions, since the electrodes are different: R_{Mti} and R_{Mbi} (where i stands for the number of the considered filament). The Maxwell resistances are then given by [33] as:

$$R_{Mt,bi} = \frac{1}{4 r_{\min\_i} \sigma_{t,b}} \tag{8}$$

where r_{min_i} is the radius of the narrowest section along the CF and $\sigma_t = 1.43 \cdot 10^7$ S/m is the conductivity of the top (or bottom $\sigma_b = 1.2016 \cdot 10^5$ S/m) electrode. In our case, to calculate r_{min_i}, the narrowest CF section is considered to obtain an equivalent circular area.

The electric conductivity of the cluster of atoms is supposed to have also a dependency on the temperature that it is described as:

$$\sigma\ (x,y,z)=\frac{\sigma_0}{1+\alpha_T\left[T(x,y,z)-T_0\right]} \tag{9}$$

where σ_0 is the electrical conductivity at the reference temperature T_0=300 K and α_T is the temperature coefficient of conductivity (a value of α_T =0.001 K^{-1} is assumed). The electrical conductivity has been considered as a fitting parameter since the conductive nature of the CF in the ohmic regime is not well understood and it is obviously affected by the final CF configuration, in our case a value of σ_0 =0.5x10^{7} Ω^{-1} m^{-1} was employed.

We included a charge transport mechanism according to the Poole-Frenkel model in addition to the ohmic conduction [34]. The current component in the forming process is described with the Poole-Frenkel model [35], making use of the following parameters: $i_0 = 5 \cdot 10^{-12} \frac{A\,m}{V}$ and $\varphi_B = 0.85\ V$. For the set curves, the current can be also described in an effective manner by means of the Poole-Frenkel model. We have employed an average electric field between the virtual electrodes for this model. When a percolation path was found, the circuit shown in **Figure 3.2-5** was used. For the QPC model we used the following parameters N=10, $\alpha = 4\ eV^{-1}$, $\beta = 0.9$ and $\Phi = 1.8\ eV$. For the reset cycles, when the device is in the LRS, in addition to the previous components, as explained above, we employ the circuit shown in **Figure 3.2-5**.

In each iteration the existence of a percolation path is searched in the simulation domain. The algorithms for the search of percolation paths [36] (Hoshen-Kopelman in our case) are based on the consideration of classical clusters, where only horizontal and vertical neighbours are considered. Our algorithm also considers the possibility of having more than one percolative path in the same simulation domain. These alternative paths have no cells in common with each other.

IV.-RESULTS AND DISCUSSION

Once the simulator was developed (see a supplementary explanation in [37] with the visualization of the 3D KMC simulation) the first step in the tuning process of our simulation tool was based on the fitting of different experimental current curves. We were able to reproduce a forming process and an arbitrary number of RS cycles in accordance with measured data, see **Figure 3.2-6**.

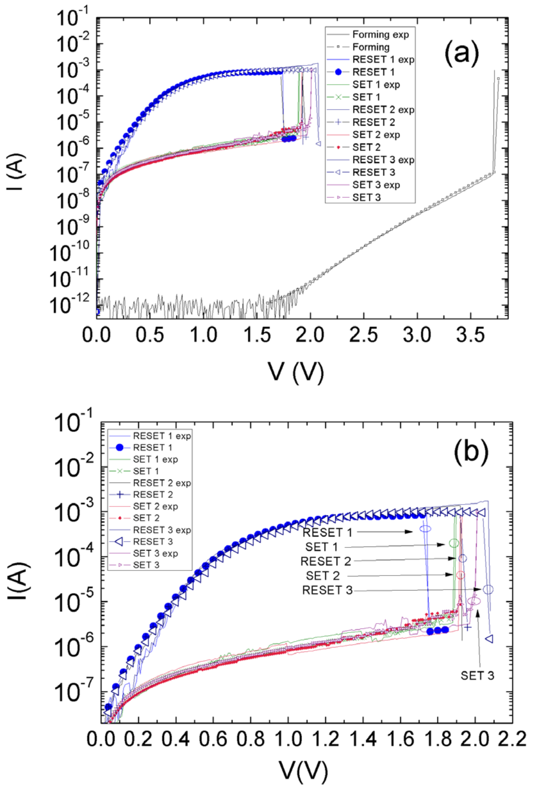

Figure 3.2-6. Current versus applied voltage in the RRAM under study. a) Experimental and simulated data including a forming process and three cycles with their corresponding reset and set processes, b) isolated representation of RS curves corresponding to reset and set processes, the accuracy of the experimental data fit is remarkable.

In **Figure 3.2-7**, the reset current versus reset voltage and set current versus set voltages are plotted both for experimental (non-consecutive cycles) and simulated data (see [38] for the numerical process to extract these parameters from the experimental curves). The spread of experimental data in these plots is higher than the simulation results due to the consideration of bigger dielectric areas in comparison with the simulation domain; consequently, several CFs of different sizes can take place at once and the experimental parameter cloud spreads out further. In addition, for the set curves, it has to be taken into account that the CF formation process is a stochastic process and the remnants of previous broken filaments are different in each cycle affecting the set voltages and currents. We can observe in **Figure 3.2-7** a reasonable agreement between the experimental and simulated data that share a common range of values.

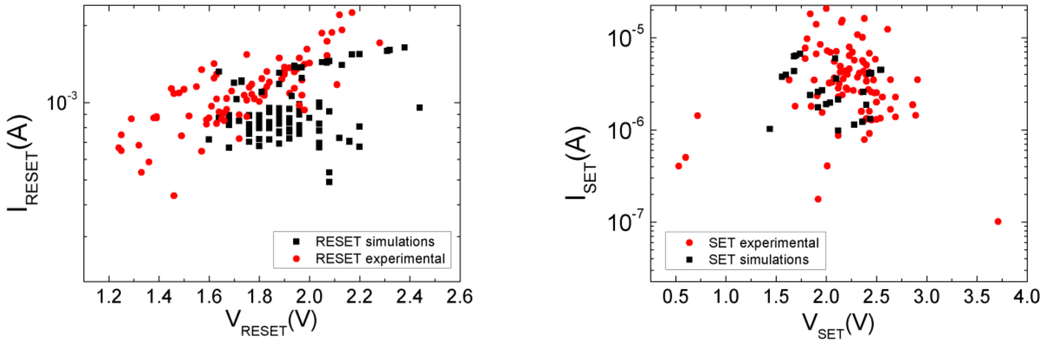

Figure 3.2-7. a) Reset current versus reset voltage for the RRAMs under study, experimental and simulated data are included, b) set current versus set voltage for the RRAMs under study, experimental and simulated data are included.

In **Figure 3.2-8**, we plot the simulated I-V curves of a forming process and the complete RS cycle that follows, consisting of a reset and a set process. The **Figure 3.2-9**, **Figure 3.2-10** and **Figure 3.2-11** show the ion and atom microscopic distribution corresponding to the microscopic states of the I-V curves in **Figure 3.2-8** (marked with letters). In addition, the CF evolution can be seen through **Figure 3.2-9**, **Figure 3.2-10** and **Figure 3.2-11**.

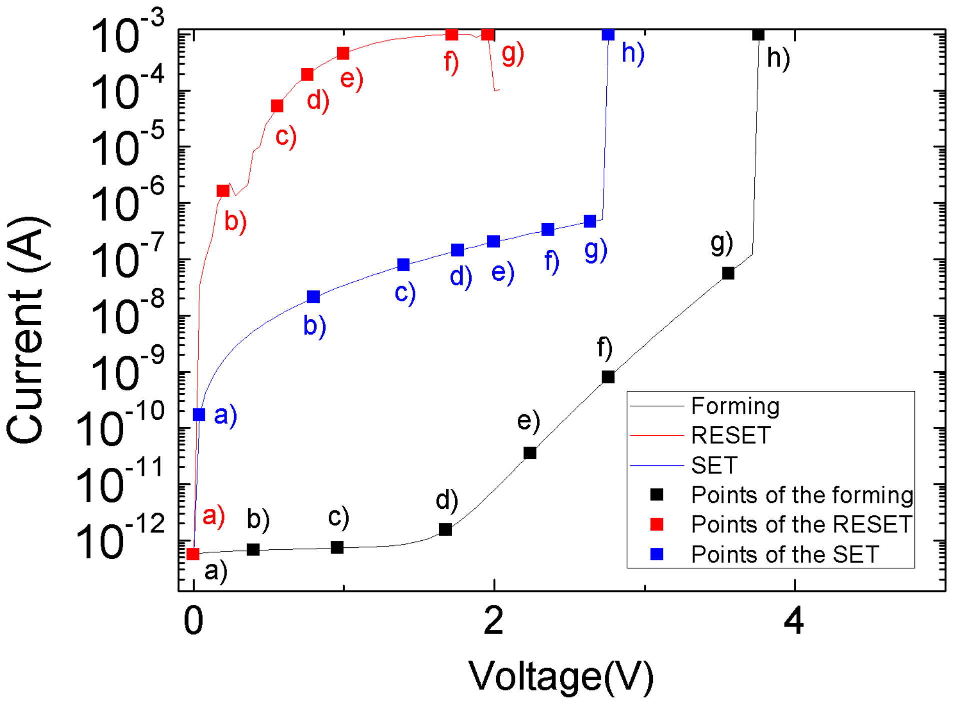

Figure 3.2-8. Simulated current versus applied voltage. The letters along the curves correspond to the stages of the distributions plotted in Figs 8, 9 and 10. A fixed current value has been assumed in the forming curve at low voltages in connection with the minimum resolution of the measurement set-up.

Within the simulation scheme we follow, it is important to understand that the parameter fitting is not a mechanic process (such as the parameter extraction algorithms that are commonly employed for certain compact models), but a progressive process using many I-V

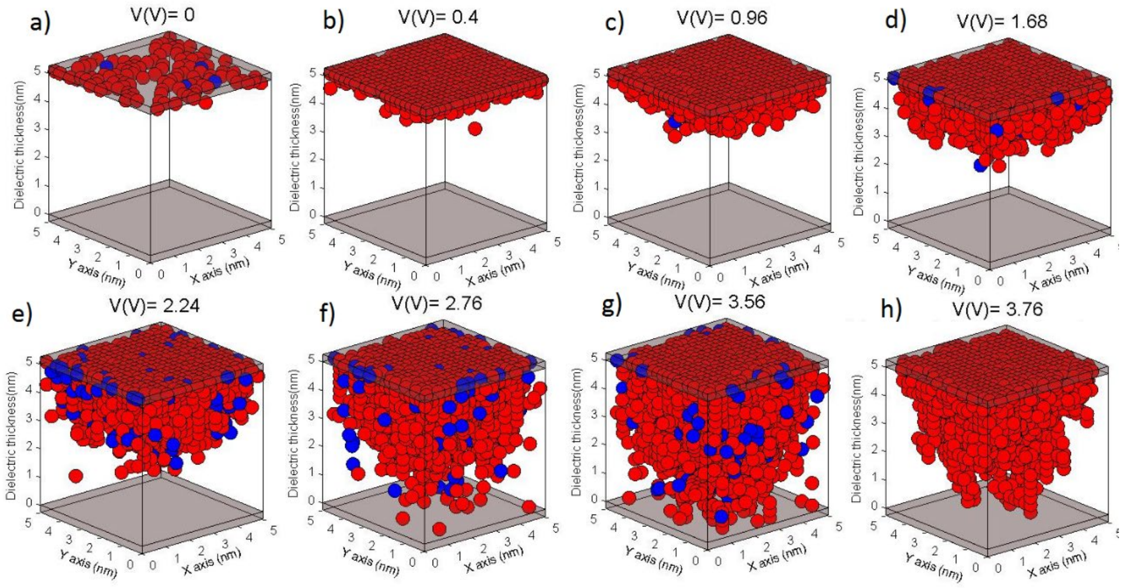

Figure 3.2-9. Forming process in the simulated RRAM. The formation of the conductive filament is shown at different stages. Red balls represent Ni atoms, blue ones represent Ni cations; once the filament is formed (h) the only elements shown are the atoms within the percolation path.

curves (**Figure 3.2-6**), I_{Reset}-V_{Reset} and I_{Set}-V_{Set} distributions (**Figure 3.2-7**), etc. Additionally, the basic functioning of these devices presents a high degree of variability due to the stochastic nature of the CF formation/rupture procedures. These characteristics hinder the calculation of a closed set of parameters in a deterministic manner.

In **Figure 3.2-9**, we show different CF creation stages within a forming process. The formation starts close to the interface of the active electrode because the combination of activation energies controlling the redox reactions and the ion migration processes make the atoms nucleate close to the active electrode. Therefore, the CF grows towards the counter electrode.

Taking into consideration the stochastic nature of a forming process, a CF with irregular surface is expected, as can be seen in **Figure 3.2-9**. Once the forming process is completed (**Figure 3.2-9h**), a reset process is started using a ramped voltage again (**Figure 3.2-10**). The filament is ruptured by means of thermal mechanisms that are triggered by Joule heating. The temperatures (in the order of 972K in the hottest spots) obtained are in line with previous results given by other authors [39].

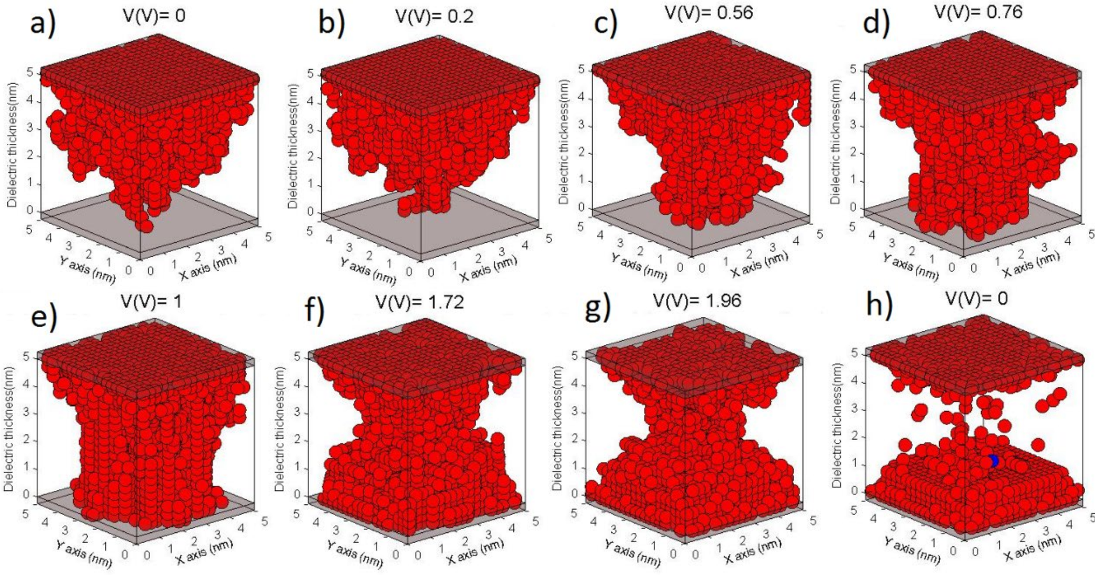

Figure 3.2-10. Different stages in a reset process in the simulated RRAM. Red balls represent Ni atoms and blue ones Ni ions. The reset starts at the stage where the forming process was stopped by limiting the device current, after the CF rupture the set curve starts with a new ramped voltage.

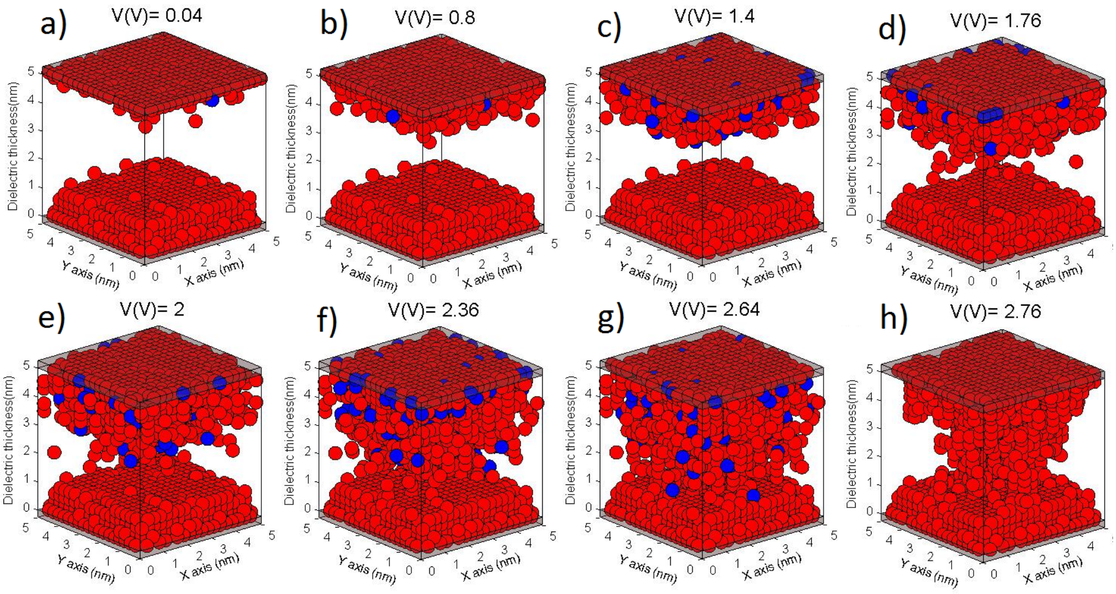

Figure 3.2-11. Set process in the simulated RRAM. Red balls represent Ni atoms and blue ones Ni ions. The formation of conductive filaments is shown at different stages.

During the RESET process, there might be stages where the CF grows in the narrower part (**Figure 3.2-10c**, **3.2-10d**, **3.2-10e**), reducing consequently the device resistance and increasing the current and Joule heating. Later on, the final thermally triggered process takes place till the CF is ruptured (**Figure 3.2-10h**).

Once the reset is over, a set process is launched again with a ramped voltage, making use of the CF remnants shown in **Figure 3.2-10h** as starting point (**Figure 3.2-11**). Because of the presence of the partially formed CF, the set voltage is lower than the forming voltage, as it should be. In addition, the current in the set process, at low voltages, is much higher than in the forming case since the gap in the dielectric between the virtual electrodes is lower than in pristine devices. Notice that we consider the Ni atom clusters in contact with the electrodes as electrode extensions.

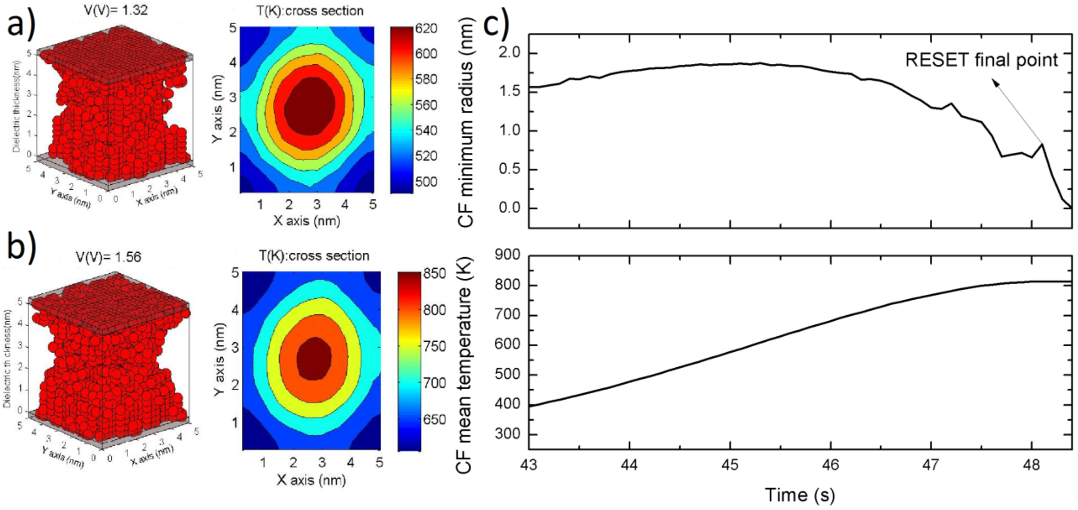

Figure 3.2-12. a) and b) CF shapes and corresponding temperature distributions for different voltages corresponding to the reset curve shown in **Figure 3.2-8** (red curve). c) CF minimum average radius and CF mean temperature versus time for a transient simulation of a CF rupture, using a constant voltage of V_{RRAM}=2 V. The simulation was initiated just after the percolation path is formed and the CF narrow region grows to a 1.5nm radius.

As it can be observed in the **Figure 3.2-11**, the CF reconstruction process is quite similar to what we obtained in the initial forming stage (**Figure 3.2-9**). An irregular CF shape was obtained when the percolation path was found, **Figure 3.2-11h**.

This simulator allows the study of different devices (changing the materials and geometric parameters) and operation regimes since it is a versatile tool. Apart from the analysis of the different physical mechanisms, it allows model development and help in parameter extraction for compact modelling for circuit simulation purposes. As an example of these

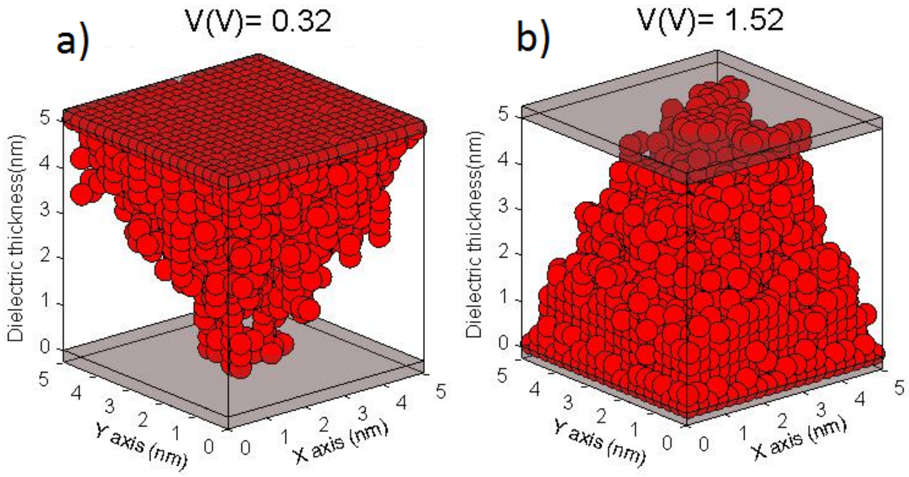

Figure 3.2-13. Different CF formation features dependent on the activation energies linked to the ion generation rate and ion mobility in the dielectric. a) $E_g = 0.451\ eV$ and $E_h = 0.48\ eV$, b) $E_g = 0.465\ eV$ and $E_h = 0.35\ eV$. The voltage employed for comparison is higher in figure b since the time needed (ramped voltages are similar) in case b to form the CF is longer.

applications, the shape of CFs can be studied, as shown in **Figure 3.2-12**. Different CF formation directions are shown depending on the ion generation and hopping features. It is observed that the activation energies determine the final CF shape that grows from the active to the bottom electrode, or the other way around.

The time evolution of the CF minimum average radius (the CFs are not circular; therefore, each CF atomic layer is approximated by a disk of similar area) and the CF mean temperature in a CF rupture simulation are shown in **Figure 3.2-13c**. The temperature distributions for two different voltages in a reset curve are plotted in **Figure 3.2-13a** and **3.2-13b**.

In **Figure 3.2-14**, it is shown the experimental and simulated forming time of the studied devices under CVS conditions. The simulation takes into account the activation energy reduction induced by the electric field, giving rise to an excellent agreement with the experimental data. If look at Eq. 6, we can observe that the simulation step time is calculated through the transition rates of the processes that take place within the KMC algorithm. They depend exponentially on the activation energy as shown in Eq. 1; so, an exponential dependence is inherent in the thermally activated processes behind the physical description of the device (an exponential dependence is seen in **Figure 3.2-14**). Besides, we can find this relationship in previous works [3, 6, 9, 18].

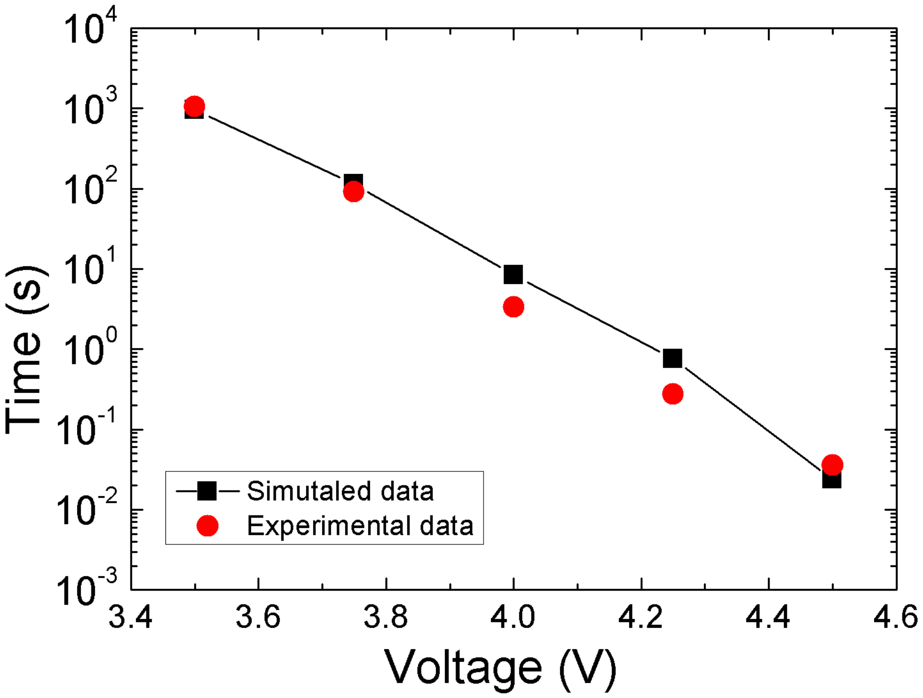

Figure 3.2-14. Forming time versus voltage for constant voltage stress. An exponential dependence of the forming time with the applied voltage is obtained.

V.-CONCLUSIONS

A new 3D kinetic Monte Carlo RRAM simulator has been developed and presented here. The 3D Poisson and heat equations are solved to correctly implement the redox, ion migration and nucleation processes that allow the description of physics behind the operation of resistive memories based on electrochemical processes. Ni/HfO_2/Si unipolar devices have been fabricated and characterized. The measured data were employed to tune the simulator. Different characteristics of the devices under study have been reproduced with accuracy. The evolution of the conductive filaments along the forming, reset and set processes have been analysed in detail. The formation direction of the filament and its shape have also been discussed in terms of the value of the activation energies linked to the ion generation rate and ion mobility in the dielectric.

VI. - ACKNOWLEDGMENTS

UGR authors thank the support of the Spanish Ministry of Economy and Competitiveness under project TEC2014-52152-C3-2-R (also supported by the FEDER program). IMB-CNM authors thank the support of the Spanish Ministry of Economy and Competitiveness under projects TEC2014-52152- C3-1-R and TEC2014-54906-JIN (supported by the FEDER program). This work has made use of the Spanish ICTS Network MICRONANOFABS.

REFERENCES

[1] F. Pan, S. Gao, C. Chen, C. Song, F. Zeng, "Recent progress in resistive random access memories: materials, switching mechanisms and performance", Materials Science and Engineering, 83, pp. 1-59, 2014

[2] T. Hasegawa, K. Terabe, T. Tsuruoka, M. Aono. “Atomic Switch: Atom/Ion Movement Controlled Devices for Beyond Von-Neumann Computers”, Advanced Materials, 24(2), pp. 252-267, 2012.

[3] T. Tsuruoka, K. Terabe, T. Hasegawa and M. Aono, “Forming and switching mechanisms of a cation-migration-based oxide resistive memory”, Nanotechnology, *21*(42), pp. 425205, 2010.

[4] Y. C. Yang, F. Pan, Q. Liu, M. Liu, F. Zeng, “Fully room-temperature-fabricated nonvolatile resistive memory for ultrafast and high-density memory application”, Nano letters, 9, pp. 1636-1643, 2009.

[5] Z. Wei, Y. Kanzawa, K. Arita, Y. Katoh, K. Kawai, S. Muraoka, S. Mitani, S. Fujii, K.Katayama, M. Iijima, T. Mikawa, T. Ninomiya, R. Miyanaga, Y. Kawashima, K. Tsuji, A. Himeno, T. Okada, R. Azuma, K. Shimakawa, H. Sugaya, T. Takagi, R. Yasuhara, K.Horiba, H. Kumigashira, M. Oshima, “Highly reliable TaOx ReRAM and direct evidence of redox reaction mechanism”, IEEE International Electron Devices Meeting, pp. 1-4, 2008.

[6] J. Guy, G. Molas, P. Blaise, M. Bernard, A. Roule, G. Le Carval, V. Delaye, A. Toffoli, G. Ghibaudo, *Fellow, IEEE*, F. Clermidy, B. De Salvo, L. Perniola , “Investigation of Forming, SET, and Data Retention of Conductive-Bridge Random-Access Memory for Stack Optimization”, IEEE Transactions on Electron Devices, *62*(11), pp. 3482-3489, 2015

[7] X. Guan, *Member, IEEE*, S. Yu, H.S. Philip Wong,,"On the switching parameter variation of metal-oxide RRAM—Part I: Physical modeling and simulation methodology", *IEEE Transactions on Electron Devices,* 59, pp. 1172-1182, 2012.

[8] A. Padovani, Member, IEEE, L. Larcher, Member, IEEE, O. Pirrotta, L. Vandelli, G. Bersuker, Member, IEEE, “Microscopic Modeling of HfO x RRAM Operations: From Forming to Switching”, IEEE Transactions on Electron Devices, 62(6), pp. 1998-2006, 2015.

[9] W. Lu, D. S. Jeong , M. Kozicki , R. Waser, “Electrochemical metallization cells-blending nanoionics into nanoelectronics”, MRS bulletin, 37, pp. 124, 2012.

[10] S. Gao, C. Song, C. Chen, F. Zeng, and F. Pan, “Formation process of conducting filament in planar organic resistive memory”, Applied Physics Letters, 102(14), pp. 141606, 2013.

[11] R. Waser and M. Aono, “Nanoionics-based resistive switching memories”, *Nature Materials*, vol. 6, pp. 833-840, 2007.

[12] M. Lanza, G. Bersuker, M. Porti, E. Miranda, M. Nafría, X. Aymerich, “Resistive switching in hafnium dioxide layers: Local phenomenon at grain boundaries”, Applied Physics Letters, vol. 101, 193502, 2012.

[13] M. Lanza, “A Review on Resistive Switching in High-k Dielectrics: A Nanoscale point of View Using Conductive Atomic Force Microscope”, Materials 7, pp. 2155-2182, 2014.

[14] R. Waser (ed.), “Nanoelectronics and Information Technology”, 3rd ed., Wiley-VCH, Berlin, 2012.

[15] J. Zahurak, K. Miyata, M. Fischer, M. Balakrishnan, S. Chhajed,D. Wells, Li Hong, A. Torsi, J. Lim, M. Korber, K. Nakazawa, S. Mayuzumi, M. Honda, S. Sills,S. Yasuda, A. Calderoni, B. Cook, G. Damarla, H. Tran, Bei Wang, C. Cardon, K. Karda, J. Okuno, A. Johnson, T. Kunihiro, J. Sumino, M. Tsukamoto, K. Aratani, N. Ramaswamy, W. Otsuka,K. Prall. "Process integration of a 27nm, 16Gb Cu ReRAM", Electron Devices Meeting (IEDM), 2014 IEEE International, pp.6.2.1-6.2.4, 2014, doi: 10.1109/IEDM.2014.7046994

[16] T.Y. Liu, T. H. Yan, R. Scheuerlein, Y. Chen, J. K. Lee, G. Balakrishnan, G. Yee, H. Zhang, A. Yap et al., “A 130.7-mm^2 2-Layer 32-Gb ReRAM Memory Device in 24-nm Technology” IEEE J. Solid-State Circuits 49, pp. 140-153, 2014.

[17] A. Kawahara, R. Azuma, Y. Ikeda, K. Kawai, Y. Katoh, Y. Hayakawa, K. Tsuji, S. Yoneda, A. Himeno, et al., “An 8 Mb Multi-Layered Cross-Point ReRAM Macro With 443 MB/s Write Throughput”, IEEE J. Solid-State Circuits 48, pp. 178-185, 2013.

[18] Y. Yang, W. Lu, "Nanoscale resistive switching devices: mechanisms and modeling", Nanoscale, 5.21, pp. 10076-10092, 2013.

[19] M.A. Villena, M.B. González, F. Jiménez-Molinos, F. Campabadal, J.B. Roldán, J. Suñé, E. Romera, E. Miranda, “Simulation of thermal reset transitions in RRAMs including quantum effects”, Journal of Applied Physics, vol. 115, pp. 214504, 2014.

[20] M. A. Villena, F. Jiménez-Molinos, J. B. Roldán, J. Suñé, S. Long, X. Lian, F. Gámiz, and M. Liu, “An in-depth simulation study of thermal reset transitions in resistive switching memories”, Journal of Applied Physics, 114(14), pp. 144505, 2013.

[21] F. Pan, S. Yin, V. Subramanian, Member, IEEE, "A detailed study of the forming stage of an electrochemical resistive switching memory by KMC simulation", IEEE Electron Device Letters, 32, pp. 949-951, 2011.

[22] S. Yu, X. Guan, H.S. Philip Wong, "On the switching parameter variation of metal oxide RRAM—Part II: Model corroboration and device design strategy", IEEE Transactions on Electron Devices, 59, pp. 1183-1188, 2012.

[23] E. Miranda, and J. Suñé, “Analytic modeling of leakage current through multiple breakdown paths in SiO_2 films”, *Reliability Physics Symposium, 2001. Proceedings. 39th Annual. 2001 IEEE International,* pp. 367-379, 2001.

[24] M. B. Gonzalez, J. M. Rafí, O. Beldarrain, M. Zabala, and F. Campabadal, “Analysis of the switching variability in Ni/HfO2-based RRAM devices,” *IEEE Trans. Device Mater. Reliab.*, vol. 14, no. 2, pp. 769–771, 2014.

[25] Z. X. Chen, Z. Fang, Y. Wang, Y. Yang, A. Kamath, X. P. Wang, N. Singh, G. Q. Lo, D. L. Kwong, and Y. H. Wu, “Impact of Niconcentration on the performance of Ni silicide/HfO2/TiN resistive RAM (RRAM) cells,” *J. Electron. Mater.*, vol. 43, no. 11, pp. 4193–4198, 2014.

[26] C. B. Lee, B. S. Kang, M. J. Lee, S. E. Ahn, G. Stefanovich, W. X. Xianyu, K. H. Kim, J. H. Hur, H. X. Yin, Y. Park, I. K. Yoo, J. B. Park, and B. H. Park, “Electromigration effect of Ni electrodes on the resistive switching characteristics of NiO thin films”, *Appl. Phys. Lett.*, vol. 91, no. 8, pp. 15–18, 2007.

[27] K. L. Lin, T. H. Hou, J. Shieh, J. H. Lin, C. T. Chou, and Y. J. Lee, “Electrode dependence of filament formation in HfO2 resistive switching memory”, *J. Appl. Phys.*, vol. 109, no. 8, pp. 1–7, 2011.

[28] Y. Y. Chen, G. Pourtois, X. P. Wang, C. Adelmann, L. Goux, B. Govoreanu, L. Pantisano, S. Kubicek, L. Altimime, M. Jurczak, J. A. Kittl, G. Groeseneken, and D. J. Wouters, “Switching by Ni filaments in a HfO2 matrix: A new pathway to improved unipolar switching RRAM”, *2011 3rd IEEE Int. Mem. Work. IMW 2011*, pp. 6–9, 2011.

[29] Voter, Arthur F, "Introduction to the kinetic Monte Carlo method", Radiation Effects in Solids, Springer Netherlands, pp. 1-23, 2007.

[30] S. Menzel, U. Böttger, R. Waser, “Simulation of multilevel switching in electrochemical metallization memory cells”, J. Appl. Phys. 111, 014501/1-5, 2012.

[31] M. A. Panzer, M. Shandalov, J. A. Rowlette, Y. Oshima, Y. Chen, P. C. McIntyre, and K. E. Goodson, "Thermal Properties of Ultrathin Hafnium Oxide Gate Dielectric Films", Transactions on Electron Devices, vol. 30, nº 12, pp. 1269–1271, 2009.

[32] N. D. Lu, Z. W. Zong, P. X. Sun, L. Li, Q. Liu, H. B. Lv, S. B. Long, M. Liu, “Thermal effect and compact model in three-dimensional (3D) RRAM arrays”, IEEE In Simulation of Semiconductor Processes and Devices (SISPAD), International Conference on, pp. 161-164, 2016

[33] R. S. Timsit, “Electrical Contact Resistance: Properties of Stationary Interfaces”, IEEE Transactions on Components and Packaging Technology, vol. 22, n. 1, pp. 85-98, 1999.

[34] D. Ielmini, R. Waser. “Resistive Switching: From Fundamentals of Nanoionic Redox Processes to Memristive Device Applications”, Wiley-VCH, 2015.

[35] P. Rottländer, M. Hehn, A. Schuhl, “Determining the interfacial barrier height and its relation to tunnel magnetoresistance”, Physical Review B, vol. 65, 054422, 2002.

[36] R. M Haralick, and L. G. Shapiro, *Computer and Robot Vision, Volume I,* Addison-Wesley, pp. 28-48, 1992.

[37] https://youtu.be/Rvm88B2AMLY

[38] M.A. Villena, F. Jiménez-Molinos, J.B. Roldán, J. Suñé, S. Long, E. Miranda and M. Liu, *“A comprehensive analysis on progressive reset transitions in RRAMs”*, Journal of Physics D, Appl. Phys., 47, p. 205102, 2014.

[39] Y.D. Zhao, P. Huang, Z.H. Guo, Z.Y. Lun, B. Gao, X.Y. Liu, J.F. Kang, “Atomic Monte-Carlo Simulation for CBRAM with Various Filament Geometries”, Simulation of Semiconductor Processes and Devices, pp. 153-156, 2016

3.3. Bipolar CBRAM

The bipolar CBRAM has a physical foundation very similar to the unipolar case. The main difference is the polarity needed to carry out RS, as it needs one polarity for the forming and SET processes while the opposite polarity is required for the RESET process. The reason of this operation is that the CF does not reach a temperature high enough for the thermal rupture before the oxidation process of atoms induced by the electric field. In this sense, once the CF is ruptured, the ions would be field-driven again toward the active electrode.

The main characteristics of the simulator presented here [Aldana2018] are similar to the unipolar simulator of the section **3.2**:

- It is based on a kMC algorithm that implements the main redox processes in CBRAM devices (that is, the reduction of ions and the oxidation of atoms) and the field-driven migration of charged particles (ions).
- The percolation path is calculated using the Hoshen-Kopelman algorithm [Hoshen1976], as explained in appendix **6.3**. This kind of algorithm allows to take into account the virtual electrodes, that is, the clusters in contact with the top or bottom electrodes.
- No CF shape is assumed in these simulations as complete RS cycles can be achieved starting from the pristine state.
- In the simulation domain, Neumann (for lateral faces of the cubic grid) and Dirichlet (for the top and bottom electrodes) boundary conditions have been implemented for the resolution of the Poisson and heat equations.
- Regarding the conduction mechanisms, an equivalent circuit has been used for the LRS where CF ohmic resistance, Maxwell resistance and the set-up resistances have been included. However, the conduction mechanisms used through the dielectric in the HRS are the Poole-Frenkel and Fowler-Nordheim emission with effective parameters.

The devices used for calibrating (Cu/$\mathrm{HfO_X}$/Pt) were made at the Laboratory of Nanofabrication and Novel Device Integration, Institute of Microelectronics, Chinese Academy of Sciences, Beijing. The details about the fabrication and measurements can be seen in appendix **6.6.2**. The dielectric HfO_X layer has 6 nm thickness and the cubic grid used was 6 nm x 6 nm x 6 nm. The size of Cu atoms, that is, the separation between grid points is 0.29 nm.

In this case, the measurements used for fitting the computational tool were current-voltage (I-V) curves obtained with voltage sweep experiments. Several RS cycles were measured, where the curves for positive voltages correspond to SET processes and the negative voltages to RESET processes. Making use of this information, it can be obtained the distribution of V_{SET} and V_{RESET} values.

After fitting the tool, it has been used to reproduce several RS cycles and the current fluctuations due to the change in the CF structure. Besides, it has also been used to study the CF compactness along the simulation and to study the cycle-to-cycle variability, that is, among other features, the V_{SET} and V_{RESET} distributions.

A video was prepared to explain the potential and the working of the kMC simulation, the device structure and the physics behind the RS process [videoBipolar]. In the part of the video corresponding to the **Figure 3.3-1a**, the fabricated device structure is presented, just like details about the fabrication process and the measuring setup. The simulation details are quite similar to those given in the previous video [videoUnipolar], but some additional explanation for the clustering process is exposed as shown in **Figure 3.3-1b**. This video sheds light on the physics behind the operation of the bipolar CBRAM with simulated data after the fitting process. Complete RS processes are carried out and shown in the video, **Figure 3.3-1c** shows a snapshot that illustrates the CF configuration in a given instant. The representation of the system evolution shown in the video has been made with simulated data; thus, it is not an idealization of the movement of the particles (metal ions). Also, the current and the electric field (**Figure 3.3-1d**) were also obtained with physical realistic calculation as the one used in this work. The video was published on 20th of December 2017, and it garnered 3089 views on YouTube until 7rd of September 2020. It also should be noted that the video is highly positioned for Youtube and Google search for the keywords "kinetic monte carlo RRAM".

This section is an already published work [Aldana2018].

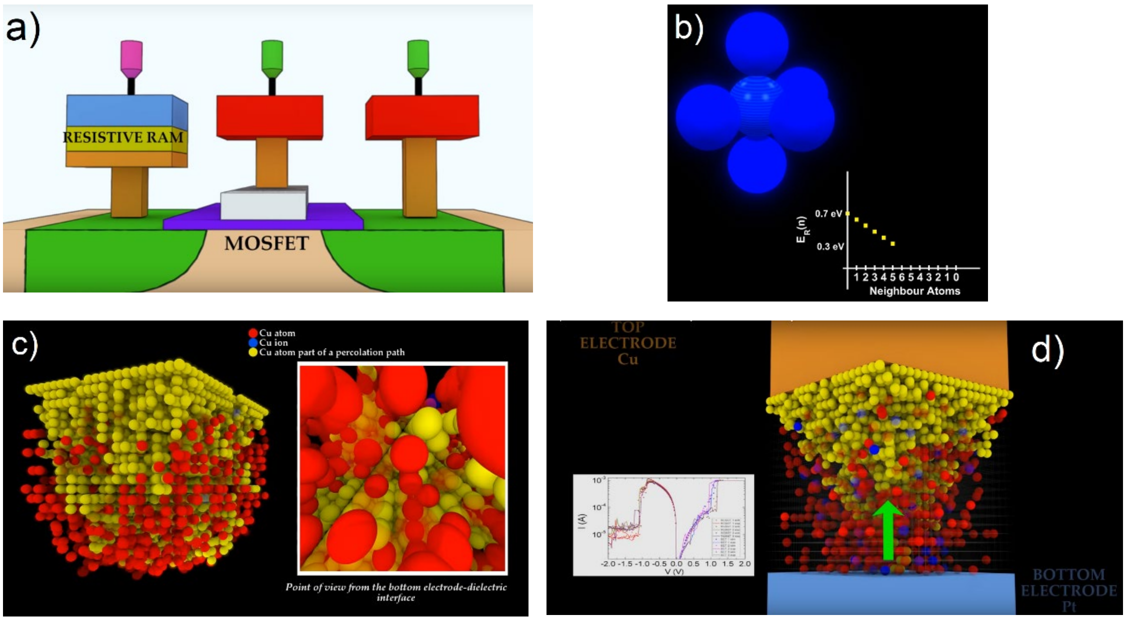

Figure 3.3-1. In a) the bipolar CBRAM device structure (Cu/HfO_X/Pt) is shown. In b) it can be seen a part of the video where the clustering implemented in the simulator is explained. A fully formed CF just after the forming process is presented in c). The effect of the virtual electrode (the gap between the electrodes) in the electric field and so in the current is exposed in d).

S. Aldana et al.

Journal of Applied Physics (2018)

Aldana, S., Roldán, J. B., García-Fernández, P., Suñe, J., Romero-Zaliz, R., Jiménez-Molinos, F., Long, S., Gómez-Campos, F., Liu, M. (2018). An in-depth description of bipolar resistive switching in Cu/HfOx/Pt devices, a 3D kinetic Monte Carlo simulation approach. Journal of Applied Physics, 123(15), 154501. DOI: https://doi.org/10.1063/1.5020148

Quality metrics 2018

Data base	Rating	Quartile
Web of Science	Impact factor: 2.328	Q2
Scimago	Scientific journal ranking: 0.746	Q2

Publication citations (2020-09-07)

Google Scholar	Web of Science
9	**8**

An in-depth description of bipolar resistive switching in Cu/HfOx/Pt devices, a 3D Kinetic Monte Carlo simulation approach

S. Aldana[1], J.B. Roldán[1], P. García-Fernández[1], J. Suñe[2], R. Romero-Zaliz[3], F. Jiménez-Molinos[1], S. Long[4], F. Gómez-Campos[1], M. Liu[4]

[1]*Departamento de Electrónica y Tecnología de Computadores. Universidad de Granada. Facultad de Ciencias. Avd. Fuentenueva s/n, 18071 GRANADA, Spain. Email: jroldan@ugr.es*

[2]*Dept. Enginyeria Electrònica. Universitat Autònoma de Barcelona, Edifici Q. 08193 Bellaterra, Spain*

[3]*Departamento de Ciencias de la Computación e Inteligencia Artificial. Universidad de Granada. Escuela Técnica Superior de Ingenierías Informática y de Telecomunicación, 18071 GRANADA, Spain*

[4]*Key laboratory of microelectronics devices & integrated technology, Institute of Microelectronics, Chinese Academy of Sciences, Beijing 100029, China*

ABSTRACT

A simulation tool based on a 3D kinetic Monte Carlo (KMC) algorithm has been employed to analyse bipolar conductive bridge RAMs (CBRAMs) fabricated with Cu/HfOx/Pt stacks. Resistive switching (RS) mechanisms are described accounting for the electric field and temperature distributions within the dielectric. The formation and destruction of conductive filaments (CFs) is analysed taking into consideration redox reactions and the joint action of metal ion thermal diffusion and electric field induced drift. Filamentary conduction is considered when different percolation paths are formed in addition to other conventional transport mechanisms in dielectrics. The simulator was tuned by using the experimental data of Cu/HfOx/Pt bipolar devices that were fabricated. Our simulation tool allows the study of different experimental results, in particular, the current variations due to the electric field changes between the filament tip and the electrode in the High Resistance State (HRS). In addition, the density of metallic atoms within the CF can also be characterized along with the corresponding CF resistance description.

Keywords: Resistive switching memory, RRAM variability, simulation tools, conductive filaments, Kinetic Monte Carlo, Conductive Bridge RAM.

I.-INTRODUCTION

Resistive Random Access Memories (RRAMs) are currently in the research focus of industry and academia because of their potential to take over in the technological landscape of high density non-volatile memories. Among the outstanding features found in these devices, the following can be counted: low power, fast operation, fabrication in 3D memory stacks and compatibility with the Back End of Line (BEOL) of Complementary Metal-Oxide-Semiconductor (CMOS) processes [1-11]. Results connected with the fabrication of promising integrated circuits based on RRAMs have also been given [12-14]. Nevertheless, some difficulties have to be addressed prior to the industrial use of RRAMs, e.g.: poor variability control of important parameters of the technology such as SET and RESET voltages [7, 8, 9, 10, 15, 16, 17]. The lack of simulation tools and compact models for these devices constitutes another drawback for massive RRAM production. Although some publications devoted to simulation have been reported [1, 4, 5, 6, 17, 18, 19, 20, 21, 22, 23, 24], there is a long way to go in this field.

There are different simulation approaches to describe the physics behind Resistive Switching in RRAMs and related effects such as variability, endurance, retention… [1, 17, 25]. One of the alternatives consists of macroscopic modeling. In this approach, a continuous conductive filament that shorts the electrodes once the set process is over is considered. The CF is often supposed to be a metallic-like cylinder or truncated-cone whose thermal and electrical conductivities are fitted to reproduce experimental measurements [17, 25, 26, 27, 28, 29]. The Poisson and heat equations are solved (usually in 1D) within the device and the RRAM resistance is calculated to obtain the current.

The macroscopic simulation approach allows a reasonable RS description; however, a deeper understanding of the mechanisms controlling RRAM operation can be obtained with a detailed simulation in which metallic ions/atoms [1, 23] and oxygen vacancies [6, 17, 30, 31] are described in a one-by-one manner, calculating the ion dynamics and possible percolation paths that once formed change substantially the device resistance. This simulation technique can be implemented by means of kinetic Monte Carlo algorithms [1, 4, 6, 23, 30]. Recently we presented a 3D kinetic Monte Carlo tool to describe unipolar devices [23]; in this manuscript we introduce a new simulator for describing bipolar Conductive Bridge RAMs (CBRAMs). In this new simulation tool, the role of ion drift is more important; in addition, a new technique is employed to calculate the average electric field in the region between the filament and the electrode and a new method to analyze the compactness of conductive filaments has also been introduced.

The RRAM structure is simple, it consists of two electrodes that sandwich a dielectric layer where RS processes take place. In most of the important cases reported in the literature, the RS operation is filamentary, i.e., the device switches between two different resistance states (a Low Resistance State, LRS, and a High Resistance State, HRS) that are obtained by forming or rejuvenating a CF that shorts the electrodes. We can find in the literature different mechanisms to explain CF creation and rupture; nevertheless, here we will deal with RS processes linked to the oxidation and reduction of atoms coming from the active electrode within an electrochemical regime [4, 10, 23]. Starting from a pristine dielectric, the CF creation process leads to a device in LRS (forming process) [1, 9, 10, 23, 32]. RRAMs can be integrated in passive crossbar arrays with $4F^2$ size, being F the minimum feature size achievable by lithography, with the additional potential for vertically stacked structures [1].

In CBRAMs the cation generation occurs by the active electrode oxidation. These ions get reduced in the dielectric after being dragged by the electric field. The reduced ion clustering, and further percolation path formation, builds CFs that bridge the electrodes [1, 4, 23]. The most probable cation reduction region in the dielectric depends on the relative values of the cation mobility and generation probability at the interface between the dielectric and the active electrode [23]. In particular, for low cation mobility the reduction region would be close to the active electrode. If the formed cluster is in touch with the electrode it works like an electrode extension known as a virtual electrode [7]. If cation mobility is high, the most probable reduction region will be close to the inert electrode. Consequently, the CF shape strongly depends on the cation mobility.

If we attend to the polarity needed to carry out RS processes, we can distinguish two kinds of RRAMs: bipolar and unipolar. The same polarity is employed to create and destroy the CFs (i.e. the set and reset) in unipolar devices, while different polarity is needed for bipolar devices [1, 9, 25]. In general, in unipolar devices, reset processes are linked to some extent to cation diffusion triggered by Joule heating effects; however, for bipolar devices, both diffusion enhanced by thermal effects and electric field induced drift mechanisms have to be taken into consideration. Nevertheless, a profound study is needed to analyze the RS kinetics for each technology.

The CBRAM simulator introduced here portrays a detailed description of the physics behind RS processes in bipolar RRAMs. We will show the CF formation and destruction processes, their shape and conduction properties. In addition, effects such as the stochastic variations of the average electric field between the filament tip and the electrode can be analysed to explain current variations when the CFs are broken. The 3D description employed here is a step forward in comparison with other 2D KMC tools previously presented [1, 4, 5] and a complement to simulators developed in the context of valence change memories [6, 30, 31]. As far as we know, there are no other bipolar CBRAM 3D KMC simulators able to describe a forming process followed by several complete RS cycles. The ion dynamics is implemented with a Monte Carlo (MC) algorithm including the main processes that take place in the RS operation, i.e., ion generation at the active electrode, redox reactions, clustering, and diffusion and drift processes in the dielectric. Moreover, the device current is calculated both in the LRS and HRS.

The fabricated devices and measurement process are explained in section II, the simulator features are detailed in section III and the main results and discussion are reported in section IV; finally, some conclusions are drawn in section V.

II.-DEVICE DESCRIPTION AND MEASUREMENT

The structures consisted of transistors fabricated using a standard 0.13 μm logic process and RRAMs based on a Cu/HfO$_x$/Pt stack integrated with the transistors. A Cu plug serves as electrode. The HfO$_x$ switching dielectric layer and the Pt electrode were grown using electron-beam evaporation with 6 nm and 70 nm thicknesses. They were patterned using a liftoff process. The device size was 300 nm × 400 nm. The measurements of the one transistor-one resistor (1T1R) structure were performed making use of a Keithley 4200 SCS semiconductor parameter analyzer. More details on the fabrication and measurement processes are given in [33, 34].

The I-V curves measured correspond to resistive switching operation characterized by electrochemical mechanisms that lead to the CF formation and destruction. In **Figure 3.3-2** we have plotted several set/reset cycles. The curves for positive (negative) voltages show set (reset) processes, the Cu electrode is positive with respect to the Pt electrode.

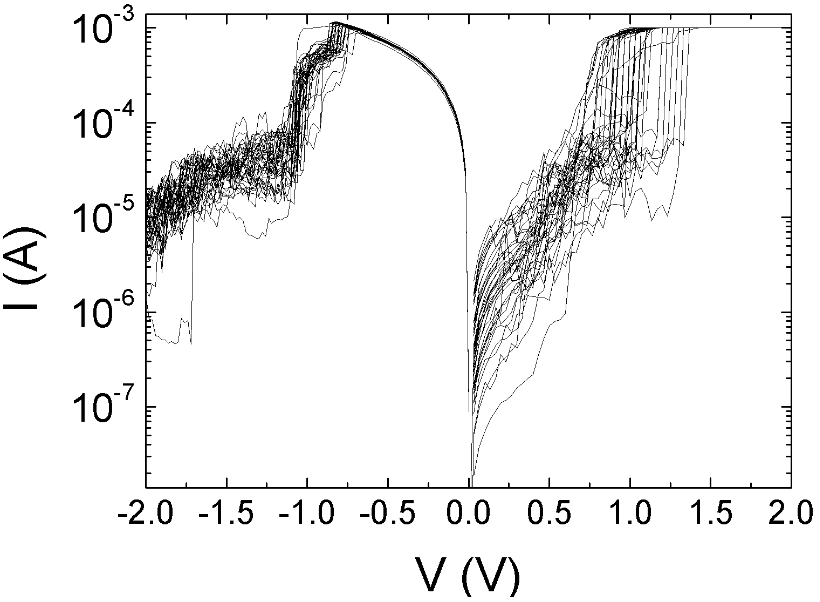

Figure 3.3-2. Experimental current versus applied voltage in the RRAMs under study. We have selected several RS cycles from a total of set of 4072 RS cycles.

III.-KINETIC MONTE CARLO SIMULATOR DESCRIPTION

For simplicity, in our tool we have considered that the top electrode, which is electrochemically active, is made of Cu and the bottom and inert electrode is made of Pt. This consideration has no effects from the numerical viewpoint since the equivalent circuit for the current calculation would give the same results if the device stack is turned upside-down.

This simulator is based on a 3D kinetic Monte Carlo algorithm. The resolution of the 3D Poisson and heat equations is included at every simulation time step and the creation/disruption of metallic conductive filaments (CF) by the combined action of diffusion and electric field drift is taken into account [1, 4, 23, 35, 36, 37]. The numerical solution of heat and Poisson equations by means of the finite-different method allows the calculation of the electric field and the temperature at every node of the simulation domain. In this manner, we can use these distributions to obtain the rates of the different mechanisms considered in the simulator at every grid point.

The simulation flow-graph is similar to that shown in [23]. The electrical conduction equivalent circuit is also close to one presented in **Figure 3.2-5** in [23]; in our case, due to the linearity of the I-V curves at low voltages, there is no need of the inclusion of the Quantum Point Contact (QPC) model [32, 38] and a single ohmic resistance connected to the CF is needed for the device current modeling, in addition to the device series and Maxwell resistances.

The transition state theory is employed for the rate calculation of the different mechanisms considered (Equation 1) [4, 23],

$$\Gamma = v \exp\left(-\frac{E_A}{k_B T}\right) \tag{1}$$

Equation 1 shows that the transition rate is dependent on the activation energy E_A and the temperature T. The transition rates are fundamental to determine the time scale of the different processes that take part in the simulations. The capability to simulate the temporal evolution of different RRAM magnitudes allows studies such as the ones reported in Ref. [39], where RRAM dynamic behaviour is addressed. The selection of the different mechanisms considered in the ion dynamics description is performed by means of the kinetic Monte Carlo algorithm.

The activation energy for ion hopping is modified by the electric field:

$$E_h(x,y,z) = E_h(V=0) - \frac{Qd\epsilon(x,y,z)}{2} \tag{2}$$

Q is the ion charge, d is the physical distance between the two states, ϵ is the applied electric field and $E_h(V=0) = 1.1\ eV$ is the energy barrier for a null electric field. A modification of the activation energy for oxidation and reduction processes accounting for the accumulation of atoms is formulated as follows [1, 23]:

$$E_R(n) = E_R(0) - n * \frac{0.4}{n\_max} \tag{3}$$

$$E_{ox}(n) = E_{ox}(0) + n * \frac{0.4}{n\_max} \tag{4}$$

The activation energies for reduction ($E_R(0) = 0.7$ eV) and oxidation ($E_{ox}(0) = 0.8$ eV) are chosen in line with values employed by other authors [1]. In this counting process, diagonals are not considered (the maximum number of atoms that can surround an ion or atom is n_max (n_max=6) and, therefore, n ≤ n_max). Additionally, ion generation at the active electrode is influenced by the current [23]:

$$E_g = E_g(V = 0) - FR_{TE}I_{RRAM} \tag{5}$$

$E_g(V = 0) = 1.13\ eV$ is the activation energy for ion generation at the electrode surface, R_{TE} is the top electrode ohmic resistance, the device current is I_{RRAM} and F a fitting parameter. We also consider the formation of bottom virtual electrodes (atom clusters in touch with the bottom electrode) since the effects of this formation enhance ion reduction and hinder atom oxidation [23, 36] in these clusters.

For the HRS conduction regime, we have assumed Poole-Frenkel (PF) emission [17, 25, 40] and Fowler-Nordheim (FN) [41] current mechanisms. Their relative influence depends on the electric field value in the dielectric, as it is well known. In this respect, we calculated an average electric field between the reduced ion clusters and the electrodes and use it for the calculation of these current components.

Maxwell resistance was included following Refs. [26, 32, 42] and an algorithm to search for percolation paths [23, 43] was employed at every simulation step. For the grid configuration we have considered the size of Cu atoms (the atom radius equals to 0.145 nm) and the same number of cells or grid points in each axis in a 3D simulation domain. Taking into account the filamentary nature of charge conduction in our devices, it is reasonable to assume a simulation domain smaller than the device area.

Physical parameters	**Value**
$E_h(hopping)$	1.1 eV
$E_R\ (reduction)$	0.7 eV
E_{ox} (oxidation)	0.8 eV
$E_g\ (generation)$	1.13 eV
$d\ (cell\ size)$	0.29 nm
R_{TE} , R_{BE} $(electrode\ series\ resistance)$	20 Ω

Table 2. Main parameters employed in the simulator.

Some improvements in this simulator version are linked to the relation between the oxidation and generation activation energies (the latter works for atoms within the Cu electrode-dielectric interface where five atoms surrounding the ones at the interface are assumed in the context of Equation 4). The calculation of the average electric field in the gap has also been improved.

IV.-RESULTS AND DISCUSSION

Some experimental RS cycles and the corresponding simulation results are plotted in **Figure 3.3-3**, a good fitting accuracy can be observed in all cases [44]. See that for negative voltages, in the reset curves, the current magnitude is much higher due to the complete formation of a percolation path of Cu atoms (the device is in the LRS).

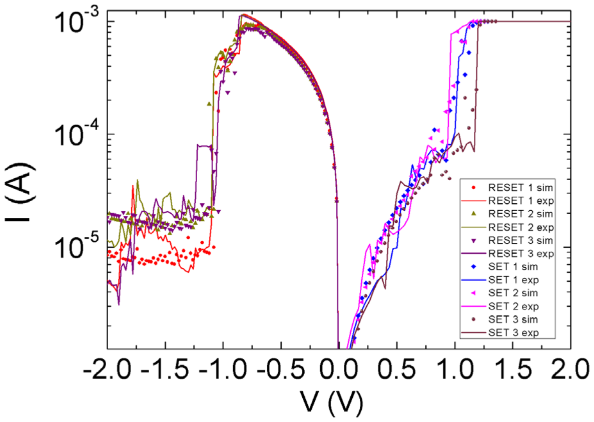

Figure 3.3-3. Current versus applied voltage in the RRAMs under study. Experimental (lines) and simulated (symbols) data including three RS cycles are shown. A reasonably good accuracy is obtained.

In **Figure 3.3-4**, we plot a comparison of the experimental and simulated set and reset currents and voltages. Our simulation tool reproduces well most of the data distribution, this fact implies that the most important physical processes behind RS are captured. Nevertheless, there are minor regions not covered by simulated data; in this respect, the presence of one or several CFs in device area with technological variations (non-homogeneities in the dielectric thickness, presence of grain boundaries, etc.), series resistance effects… could be attributed to be behind these differences.

We made use of a great amount of experimental data to perform the simulator constant fitting procedure. It is important to understand that in our case parameter fitting is not a straightforward process in comparison with parameter extraction algorithms commonly employed in certain classical compact models. In our case, a process using successive iterations employing many I–V curves (**Figure 3.3-2** and **Figure 3.3-3**), I_{Reset}–V_{Reset} and I_{Set}–V_{Set} distributions (**Figure 3.3-4**), etc. has been followed.

The details of a CF rupture along an I-V reset curve are shown in **Figure 3.3-5** and **3.3-6**. As can be seen, points A and B are obtained for negative voltages in a RRAM in the LRS. This state has been reached after a previous successful set process for positive voltages. The alterations in the CF shape are not important in these two first points since both the temperature and the electric field (the sources behind the diffusion and drift processes that modify the CFs) are not high for these operation regimes.

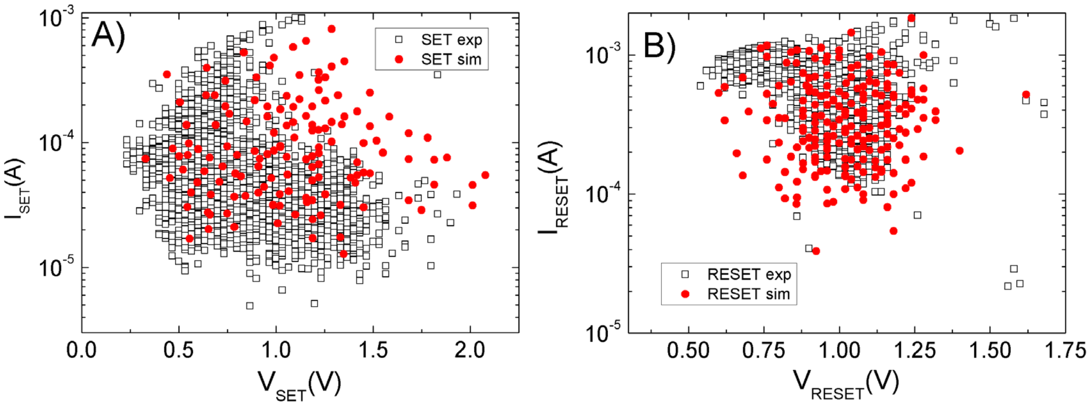

Figure 3.3-4. a) Set current versus set voltage for the RRAMs under study, experimental and simulated data are included. b) Reset current versus reset voltage (absolute value) for the RRAMs under study, experimental and simulated data are included.

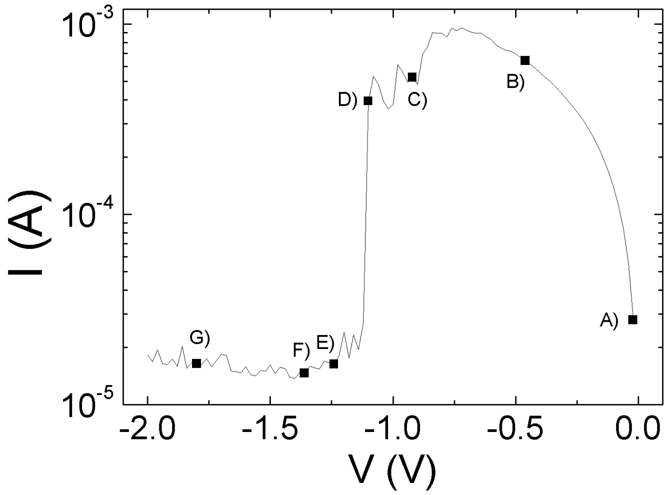

Figure 3.3-5. Reset simulated current versus applied voltage. The letters along the curve correspond to different RS stages (CF destruction stages). The corresponding CFs are plotted in **Figure 3.3-6**.

In stage C, both ion drift and the enhanced diffusion due to higher temperatures and electric fields make the CF slim down; this process goes on in stage D. Finally, the CF is broken in between stages D and E, corresponding to the great current drop characteristic of a reset process. As the negative voltage rises, the CF destruction process keeps on going and the gap between the CF tip and the inert electrode increases. At this stage, it is important to highlight that we have employed a different method to calculate the reset point in comparison with previous works. In this respect, different procedures to obtain the reset voltage are explained in depth in Ref. [19]. Taking into consideration that we can use simulated results, where we can determine when the CF is broken, the reset voltage determination procedure was chosen to ease the comparison with simulation data.

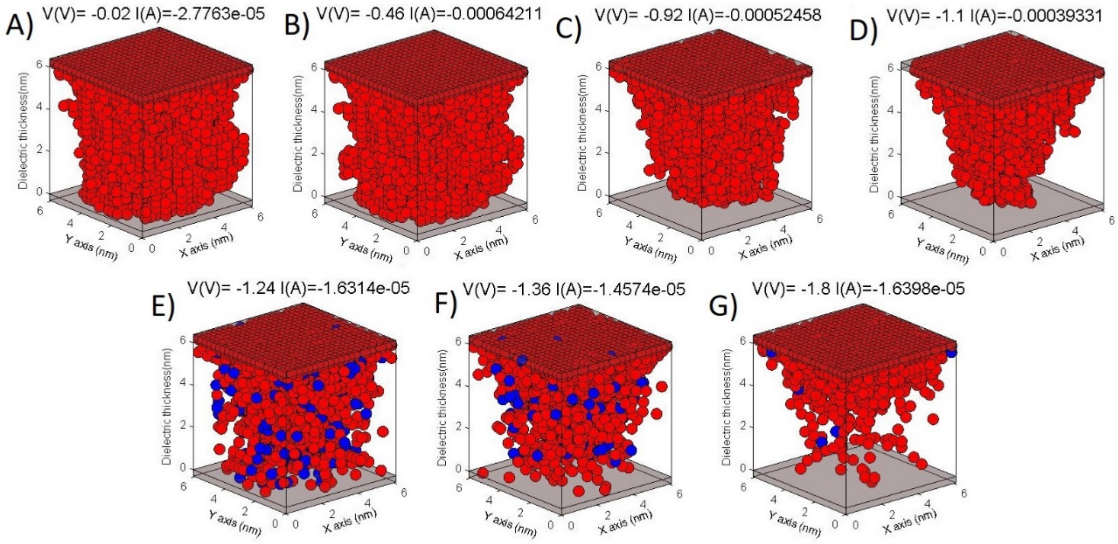

Figure 3.3-6. Different CF destruction stages associated to a reset process (see the corresponding I-V curve in **Figure 3.3-5**). Red balls represent Cu atoms and blue ones Cu ions (Cu ions are erased from the figure once a percolation path is formed).

Once the CF is ruptured, the ohmic component in the current calculation contributes to a lesser extent and the current components linked to FN and PF enhance their contribution. Neither the current nor the average electric field in the gap between the CF tip and the electrode show great variations in the region in between point E and G. On the one hand the applied voltage rises, on the other hand the gap between the CF tip and the electrode also increases, therefore, the average electric field in the gap remains approximately constant and so the current. This fact is reflected both in the experimental and simulation data, as can be seen in **Figure 3.3-3** and **Figure 3.3-4**.

We have also studied the different CF formation stages along a set I-V curve, see **Figure 3.3-7** and **3.3-8**.

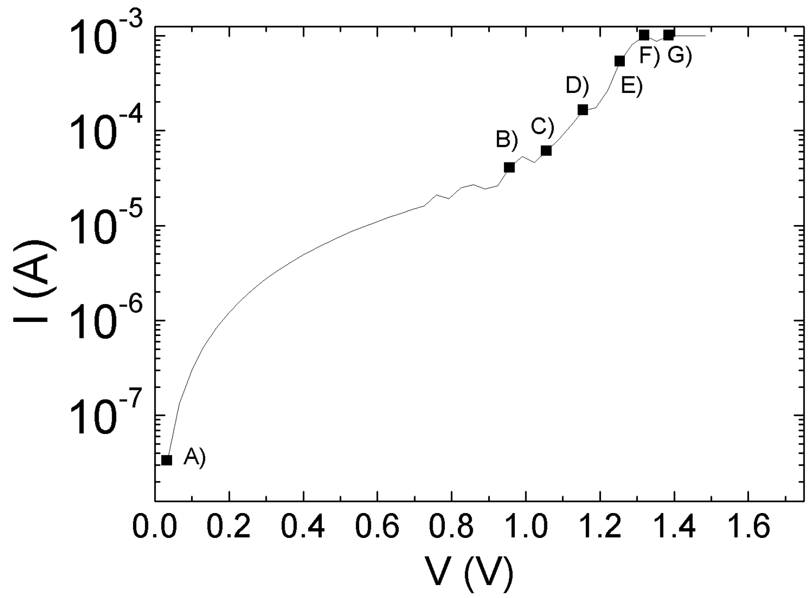

Figure 3.3-7. Simulated set current versus applied voltage. The letters along the curve correspond to different RS stages (CF formation stages) that are plotted in **Figure 3.3-8**.

As can be observed in **Figure 3.3-8**, the effects of diffusion and electric field drift close the gap previously opened in a reset process, and finally (stage E) a fully formed percolation path is achieved. A further CF increase is obtained (stage F). At this point the device current is limited externally (a compliance current is employed); however, for some time (after the compliance current is achieved, and corresponding to higher voltages in a ramped voltage stress measurement scheme) the drift and thermal inertia contribute to the CF growth. Nevertheless, for further voltages the current limitation stops the temperature rise and, therefore, any increase in the thermally activated processes that contribute to RS.

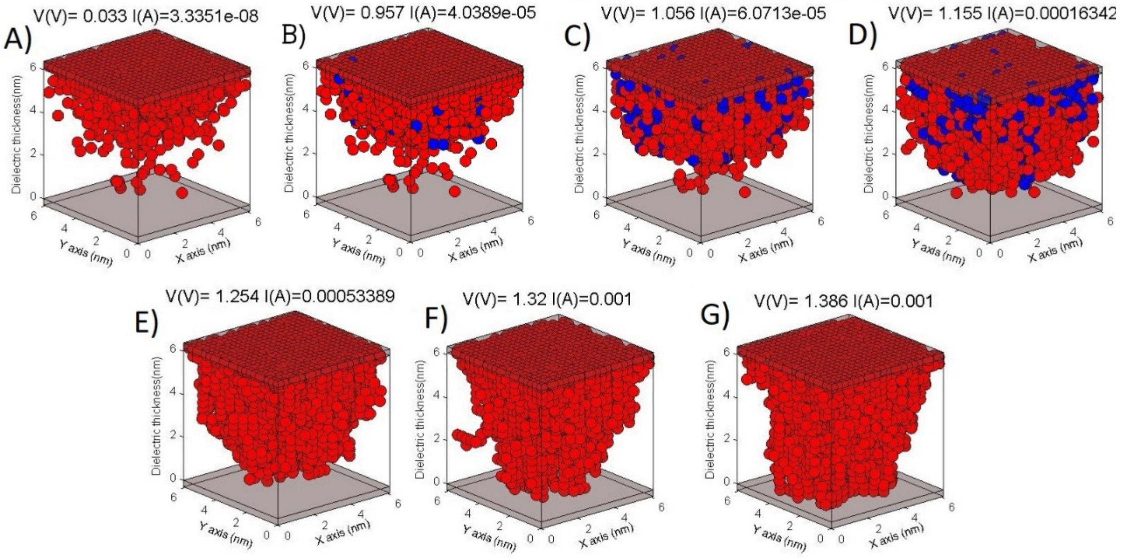

Figure 3.3-8. Different CF formation stages associated to a set process (see the corresponding I-V curve in **Figure 3.3-7**). Red balls represent Cu atoms and blue ones Cu ions (Cu ions are erased from the figure once a percolation path is formed).

It is important to note that in **Figure 3.3-5** an almost constant current is obtained for voltages higher than the reset voltage. In this operation region, the CF is broken and the gap between the CF tip and the bottom electrode rises as the voltage increases (see **Figure 3.3-6**). Nevertheless, the gap growth is a stochastic process that depends on the evolution of the clusters in contact with the electrodes (virtual electrodes [7]). We have calculated this average gap evolution and the corresponding average electric field in this gap for a reset curve. The results helped us to analyse the current behaviour of some reset curves after the CF rupture (**Figure 3.3-3** and **3.3-5**).

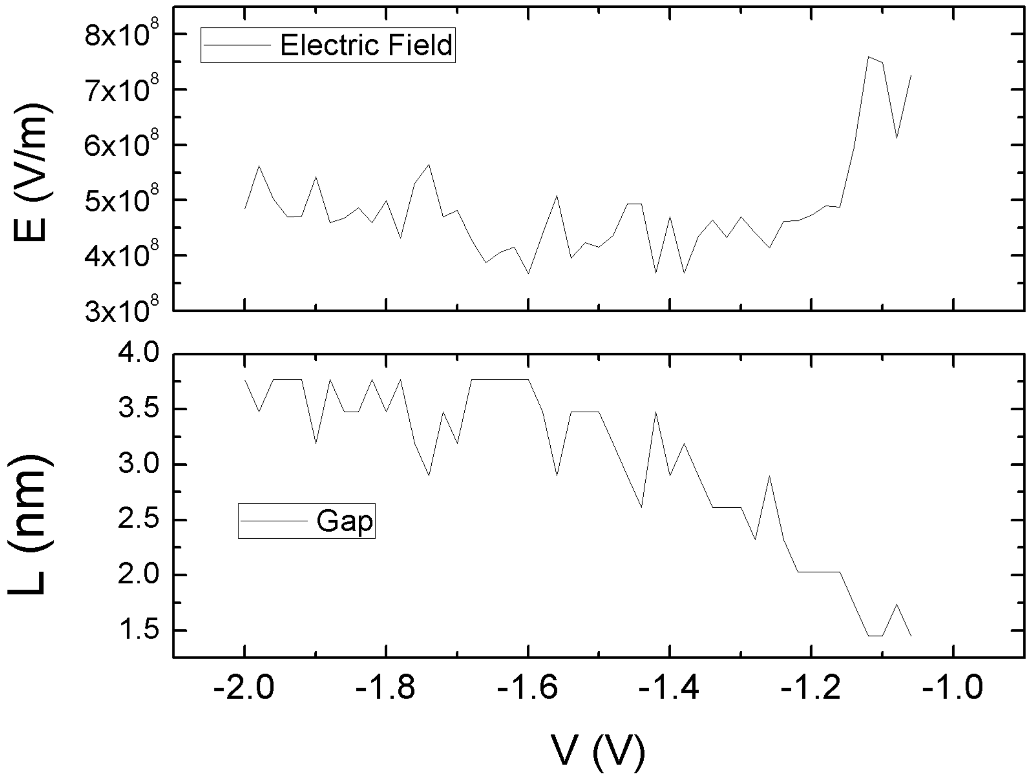

Figure 3.3-9. Average electric field and average gap between the two virtual electrodes left after a reset process versus applied voltage, corresponding to the final region of a reset I-V curve.

As can be seen, the stochasticity of the CF growth and destruction makes the average gap to increase in an irregular manner. A reasonable gap growth can be observed on average as the voltage decreases below the reset voltage, as it is expected [1, 17, 25]. However, there are variations as can be seen in **Figure 3.3-9**. The average electric field in the gap shows a related behavior taking into account its inverse dependence on the average gap length. The HRS current components, which are mainly dependent on the electric field, also show these variations both at the experimental and simulation levels (see **Figure 3.3-3**, **3.3-5**). It is important to note that in certain experimental curves the current variations are even greater than the simulated ones, this behavior could be due to the summation of current components linked to different clusters in greater areas than those employed in our simulator (limited by the computational resources available), the presence of possible grain boundaries, irregularities at the electrode-dielectric interfaces, etc.

In order to deepen on the CF properties, we have analyzed the internal configuration of different CFs simulated at certain voltages in a RS cycle, to do so we have considered different reduction energies. We worked on the reduction energies to study the influence of nearest neighboring atoms surrounding each of the Cu atoms and ions in the simulation domain. In this regard, the CF compactness and the influence of cluster and percolation path formation in the simulation domain can be analyzed. It is clear that, for a certain fixed CF volume, the CF compactness is linked to the ohmic resistance since the denser the CF the higher the metallic area available for current conduction within each CF layer.

The number of nearest neighbors for Cu atoms at different voltages for different reset I-V curves has been shown in **Figure 3.3-10**. The number of occurrences that a Cu atom (the whole simulation domain has been considered) has a determined number of neighbors (the maximum neglecting diagonals is six) has been plotted. At lower voltages the CF is thicker (initial stages of the reset process). As the voltage decreases, it gets reduced or even ruptured as can be seen in **Figure 3.3-10**. Although its apparent volume might seem to increase, its compactness decreases as the voltage decreases. This fact is seen by the reduction of the number of occurrences corresponding to the higher numbers of nearest neighbors.

In the case of a high reduction energy (E_{red}=0.8 eV), the probability for the reduction process is lower and the capacity to regenerate the CF as the voltage decreases and the reset process advances is lower, that is why in this case a CF rupture is achieved. In this regard, we have to note that we have shown here four different reset simulations (for different reduction energies) and we have to keep in mind the randomness of the processes involved. This means that for the same parameters a different curve could be obtained linked to other random number series within the kinetic Monte Carlo algorithm. It can also be noted, that the CFs are modified as the voltage decreases. In general, thinner shapes are seen (stochasticity has to be considered) as well as less compactness as the voltage decreases.

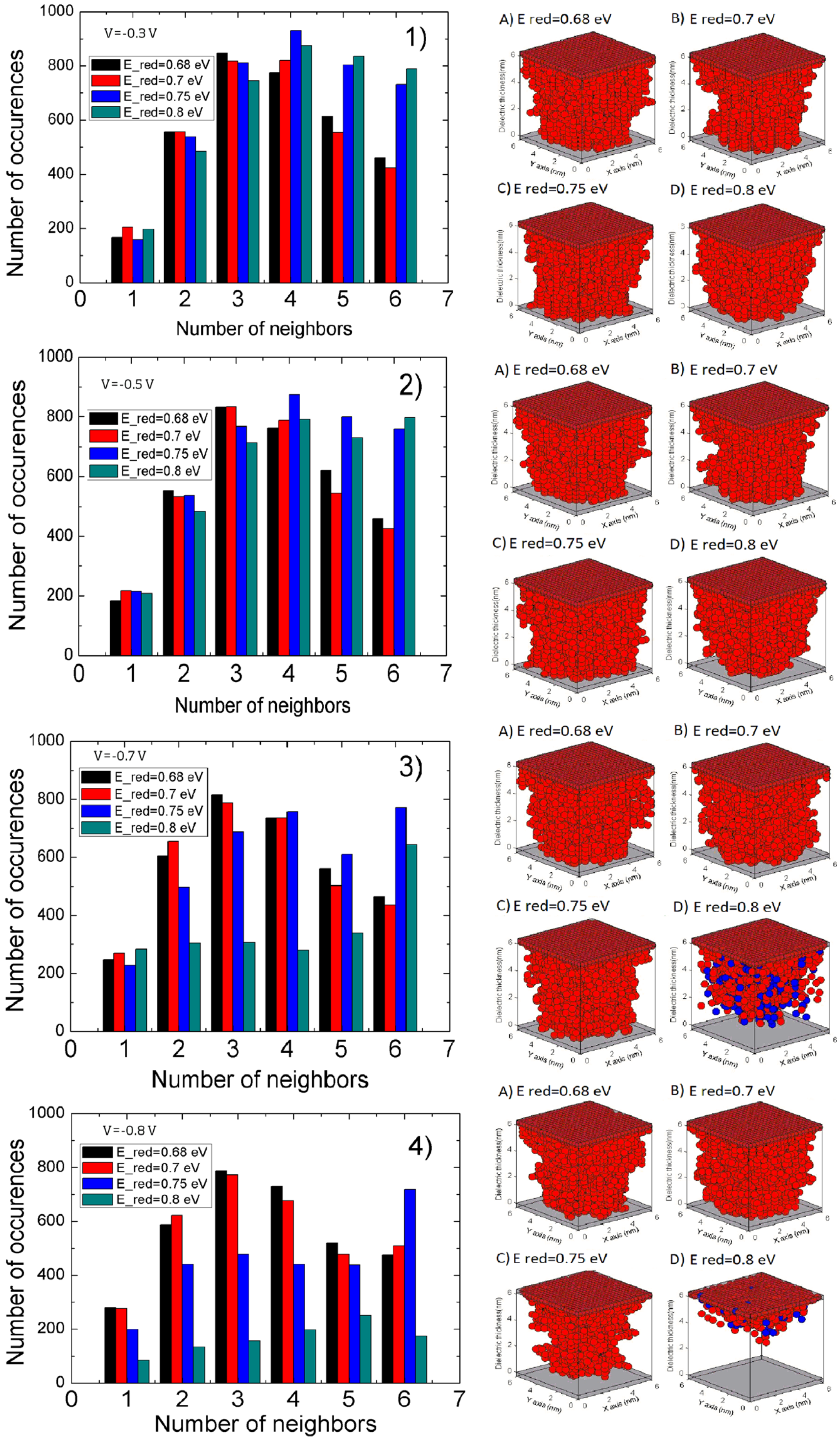

Figure 3.3-10. Number of occurrences for the different possibilities of surrounding neighbors (neglecting diagonals) that can be found in the grid for each Cu atom taken into consideration the whole simulation domain. Four different applied voltages have been considered, and for each voltage four different activation energies are studied ($E_{red} = 0.68\ eV$, $E_{red} = 0.7\ eV$, $E_{red} = 0.75\ eV$ and $E_{red} = 0.8\ eV$). We accompany the figures with the corresponding 3D atom and ion distributions for the voltages and reduction energies under consideration. The CF compactness can be analyzed making use of the data shown.

We have observed that the number of occurrences for 6 nearest neighbors rises prior to a CF rupture (more simulations than the ones shown in **Figure 3.3-10** have been analyzed); however, the occurrences of 4 and 5 nearest neighbors drop off. As the voltage decreases the occurrences of 1 and 2 neighbors increase since many of the greater numbers cases lose atoms and fall into these cases. It can be seen that the CF compactness is reduced as the voltage decreases on average, and therefore, the device resistance increases.

V.-CONCLUSIONS

A new 3D kinetic Monte Carlo simulator for bipolar conductive bridge RAMs fabricated with Cu/HfO_x/Pt stacks has been presented. The physics of resistive switching operation can be studied in depth with this simulation tool. The electric field and temperature distributions within the dielectric are obtained for each simulation step. CF creation/rupture is studied accounting for redox reactions and the joint action of metal ion thermally induced diffusion and ion movement due to electric field drift. A great amount of experimental data was employed to tune the simulator. We were able to replicate I-V reset-set curves and distribution of set and reset voltages and currents. In addition, the evolution of the average electric field between the virtual electrodes was studied to explain current variations in the HRS. We analysed the CF compactness along a reset curve to deepen on the CF destruction process and the density of the clusters that form the percolation paths in the dielectric.

VI. - ACKNOWLEDGMENTS

UGR authors thank the support of the Spanish Ministry of Economy, Industry and Competitiveness under project TEC2014-52152-C3-2-R and ENE2016-80944-R (also supported by the FEDER program).

REFERENCES

[1] F. Pan, S. Gao, C. Chen, C. Song, F. Zeng, "Recent progress in resistive random access memories: materials, switching mechanisms and performance", Materials Science and Engineering, 83, pp. 1-59, 2014

[2] T. Hasegawa, K. Terabe, T. Tsuruoka, M. Aono. “Atomic Switch: Atom/Ion Movement Controlled Devices for Beyond Von-Neumann Computers”, Advanced Materials, 24(2), pp. 252-267, 2012.

[3] Z. Wei, Y. Kanzawa, K. Arita, Y. Katoh, K. Kawai, S. Muraoka, S. Mitani, S. Fujii, K.Katayama, M. Iijima, T. Mikawa, T. Ninomiya, R. Miyanaga, Y. Kawashima, K. Tsuji, A. Himeno, T. Okada, R. Azuma, K. Shimakawa, H. Sugaya, T. Takagi, R. Yasuhara, K.Horiba,

H. Kumigashira, M. Oshima, “Highly reliable TaOx ReRAM and direct evidence of redox reaction mechanism”, IEEE International Electron Devices Meeting, pp. 1-4, 2008.

[4] Jérémy Guy, Gabriel Molas, Philippe Blaise, Mathieu Bernard, Anne Roule, Gilles Le Carval, Vincent Delaye, Alain Toffoli, Gérard Ghibaudo, Fellow, IEEE, Fabien Clermidy, Barbara De Salvo, and Luca Perniola , “Investigation of Forming, SET, and Data Retention of Conductive-Bridge Random-Access Memory for Stack Optimization”, IEEE Transactions on Electron Devices, *62*(11), pp. 3482-3489, 2015.

[5] Ximeng Guan, Member, IEEE, Shimeng Yu, Student Member, IEEE, and H.-S. Philip Wong, Fellow, IEEE ,"On the switching parameter variation of metal-oxide RRAM—Part I: Physical modeling and simulation methodology", *IEEE Transactions on Electron Devices,* 59, pp. 1172-1182, 2012.

[6] Andrea Padovani, Member, IEEE, Luca Larcher, Member, IEEE, Onofrio Pirrotta, Luca Vandelli, and Gennadi Bersuker, Member, IEEE, “Microscopic Modeling of HfO x RRAM Operations: From Forming to Switching”, IEEE Transactions on Electron Devices, 62(6), pp. 1998-2006, 2015.

[7] R. Waser and M. Aono, “Nanoionics-based resistive switching memories”, *Nature Materials*, vol. 6, pp. 833-840, 2007.

[8] M. Lanza, G. Bersuker, M. Porti, E. Miranda, M. Nafría, X. Aymerich, “Resistive switching in hafnium dioxide layers: Local phenomenon at grain boundaries”, Applied Physics Letters, vol. 101, 193502, 2012.

[9] M. Lanza, “A Review on Resistive Switching in High-k Dielectrics: A Nanoscale point of View Using Conductive Atomic Force Microscope”, Materials 7, pp. 2155-2182, 2014.

[10] R. Waser (ed.), “Nanoelectronics and Information Technology”, 3rd ed., Wiley-VCH, Berlin, 2012.

[11] S. Long, C. Cagli, J. Bucley, X. Lian, M. Liu and J. Suñé, “Voltage and power-controlled regimes in the progressive unipolar RESET transition of HfO_2-based RRAM”, Scientific Reports 3, nº 2929, 2013.

[12] J. Zahurak, K. Miyata, M. Fischer, M. Balakrishnan, S. Chhajed,D. Wells, Li Hong, A. Torsi, J. Lim, M. Korber, K. Nakazawa, S. Mayuzumi, M. Honda, S. Sills,S. Yasuda, A. Calderoni, B. Cook, G. Damarla, H. Tran, Bei Wang, C. Cardon, K. Karda, J. Okuno, A. Johnson, T. Kunihiro, J. Sumino, M. Tsukamoto, K. Aratani, N. Ramaswamy, W. Otsuka,K. Prall. "Process integration of a 27nm, 16Gb Cu ReRAM", Electron Devices Meeting (IEDM), 2014 IEEE International, pp.6.2.1-6.2.4, 2014, doi: 10.1109/IEDM.2014.7046994

[13] T.Y. Liu, T. H. Yan, R. Scheuerlein, Y. Chen, J. K. Lee, G. Balakrishnan, G. Yee, H. Zhang, A. Yap et al., “A 130.7-mm^2 2-Layer 32-Gb ReRAM Memory Device in 24-nm Technology” IEEE J. Solid-State Circuits 49, pp. 140-153, 2014.

[14] A. Kawahara, R. Azuma, Y. Ikeda, K. Kawai, Y. Katoh, Y. Hayakawa, K. Tsuji, S. Yoneda, A. Himeno, et al., “An 8 Mb Multi-Layered Cross-Point ReRAM Macro With 443 MB/s Write Throughput”, IEEE J. Solid-State Circuits 48, pp. 178-185, 2013.

[15] S. Long, C. Cagli, D. Ielmini, M. Liu and J. Suñé, “Analysis and modeling of resistive switching statistics”, J. Appl. Phys. 111, 074508 (2012).

[16] S. Long, X. Lian, T. Ye, C. Cagli, L. Perniola, E. Miranda, M. Liu, and J. Suñé, “Cycle-to-cycle intrinsic RESET statistics in HfO_2-based unipolar RRAM devices”, IEEE Electron Device Lett. 34(5), 623–625, 2013.

[17] D. Ielmini, R. Waser. “Resistive Switching: From Fundamentals of Nanoionic Redox Processes to Memristive Device Applications”, Wiley-VCH, 2015.

[18] S. Yu, X. Guan, H.S. Philip Wong, "On the switching parameter variation of metal oxide RRAM—Part II: Model corroboration and device design strategy", IEEE Transactions on Electron Devices, 59, pp. 1183-1188, 2012.

[19] M.A. Villena, F. Jiménez-Molinos, J.B. Roldán, J. Suñé, S. Long, E. Miranda and M. Liu, *“A comprehensive analysis on progressive reset transitions in RRAMs”*, Journal of Physics D, Appl. Phys., 47, p. 205102, 2014.

[20] M.A. Villena, M.B. González, J.B. Roldán, F. Campabadal, F. Jiménez-Molinos, F.M. Gómez-Campos y J. Suñé, "An in-depth study of thermal effects in reset transitions in HfO2 based RRAMs", Solid State Electronics, 111, pp. 47-51, 2015.

[21] S. Menzel, U. Böttger, R. Waser, “Simulation of multilevel switching in electrochemical metallization memory cells”, J. Appl. Phys. 111, 014501/1-5, 2012.

[22] M.A. Villena, J.B. Roldán, M.B. González, P. González-Rodelas, F. Jiménez-Molinos, F. Campabadal, D. Barrera, "A new parameter to characterize the charge transport regime in $Ni/HfO_2/Si\text{-}n^+$-based RRAMs", Solid State Electronics, vol. 118, pp. 56-60, 2016.

[23] S. Aldana, P. García-Fernández, A. Rodríguez-Fernández, R. Romero-Zaliz, M.B. González, F. Jiménez-Molinos, F. Campabadal, F. Gómez-Campos, J.B. Roldán, "A 3D Kinetic Monte Carlo simulation study of Resistive Switching processes in Ni/HfO2/Si-n+-based RRAMs", Journal of Physics D: Applied Physics, 50, 335103, 2017.

[24] A. Rodríguez-Fernández, S. Aldana, F. Campabadal, J. Suñé, E. Miranda, F. Jiménez-Molinos, J. B. Roldán, M. B. Gonzalez, “Resistive Switching with Self-Rectifying Tunability and Influence of the Oxide Layer Thickness in Ni/HfO2/n+Si RRAM Devices”, IEEE Transactions on Electron Devices, 64, n 8, pp. 3159-3166, 2017.

[25] M.A. Villena, J.B. Roldán, F. Jiménez-Molinos, E. Miranda, J. Suñé, M. Lanza, “*SIM^2RRAM*: A physical model for RRAM devices simulation”, Journal of Computational Electronics, 16, pp. 1095-1120, 2017.

[26] M. A. Villena, F. Jiménez-Molinos, J. B. Roldán, J. Suñé, S. Long, X. Lian, F. Gámiz, and M. Liu, “An in-depth simulation study of thermal reset transitions in resistive switching memories”, Journal of Applied Physics, 114(14), pp. 144505, 2013.

[27] Bocquet, M., Deleruyelle, D., Muller, C., Portal, J. M.: Self-consistent physical modeling of set/reset operations in unipolar resistive-switching memories. Applied Physics Letters, 98(26), 263507 (2011).

[28] G. González-Cordero, J.B. Roldán, F. Jiménez-Molinos, J. Suñé, S. Long y M. Liu, "A new model for bipolar RRAMs based on truncated cone conductive filaments, a Verilog-A approach", Semiconductor Science and Technology, 31, p. 115013, 2016.

[29] G. González-Cordero, F. Jiménez-Molinos, J.B. Roldán, M.B. González, F. Campabadal, "An in-depth study of the physics behind resistive switching in TiN/Ti/HfO2/W structures", Journal of Vacuum Science and Technology B, 35, 01A110, 2017.

[30] L. Larcher, A. Padovani, O. Pirrotta, L. Vandelli, and G. Bersuker, “Microscopic understanding and modeling of HfO2 RRAM device physics,” in Proc. IEEE Int. Electron Devices Meeting, pp. 20.1.1–20.1.4, 2012.

[31] L. Vandelli, A. Padovani, L. Larcher, and G. Bersuker, “Microscopic modeling of electrical stress-induced breakdown in poly-crystalline hafnium oxide dielectrics,” IEEE Trans. Electron Devices, vol. 60, no. 5, pp. 1754–1762, May 2013.

[32] M.A. Villena, M.B. González, F. Jiménez-Molinos, F. Campabadal, J.B. Roldán, J. Suñé, E. Romera, E. Miranda, “Simulation of thermal reset transitions in RRAMs including quantum effects”, Journal of Applied Physics, vol. 115, pp. 214504, 2014.

[33] H. Liu, H. Lv, B. Yang, X. Xu, R. Liu, Q. Liu, S. Long, M. Liu, “Uniformity improvement of 1T1R RRAM with gate voltage ramp programming”, IEEE Electron Device Letters, 35(12), pp. 1224-1226, 2014.

[34] H. Sun, M. Zhang, Y. Li, S. Long, Q. Liu, H. Lv, J. Suñé, M. Liu, “A cell-based clustering model for the reset statistics in RRAM”, *Applied Physics Letters*, 110, p. 123503, 2017.

[35] T. Tsuruoka, K. Terabe, T. Hasegawa and M. Aono, “Forming and switching mechanisms of a cation-migration-based oxide resistive memory”, Nanotechnology, *21*(42), pp. 425205, 2010.

[36] Feng Pan, Shong Yin, and Vivek Subramanian, Member, IEEE, "A detailed study of the forming stage of an electrochemical resistive switching memory by KMC simulation", IEEE Electron Device Letters, 32, pp. 949-951, 2011.

[37] Y. Yang, W. Lu, "Nanoscale resistive switching devices: mechanisms and modeling", Nanoscale, 5.21, pp. 10076-10092, 2013.

[38] E. Miranda, and J. Suñé, “Analytic modeling of leakage current through multiple breakdown paths in SiO_2 films”, *Reliability Physics Symposium, 2001. Proceedings. 39th Annual. 2001 IEEE International,* pp. 367-379, 2001.

[39] U. Russo, D. Kamalanathan, D. Ielmini, A.L. Lacaita, M.N. Kozicki, "Study of multilevel programming in Programmable Metallization Cell (PMC) memory", IEEE Transactions on Electron Devices, vol. 56, no. 5, pp. 1040-1047, 2009.

[40] E.W. Lim, R. Ismail, “Conduction mechanism of valence change resistive switching memory: a survey”, Electronics, 4, pp. 586-613, 2015.

[41] Southwick R.G., Reed J., Buu C., Butler R., Bersuker G., Knowlton W.B., "Limitations of Poole-Frenkel conduction in bilayer HfO2/SiO2 MOS devices", *IEEE Transactions on Device and materials reliability,* 10, pp. 201-207, 2010.

[42] R. S. Timsit, “Electrical Contact Resistance: Properties of Stationary Interfaces”, IEEE Transactions on Components and Packaging Technology, vol. 22, n. 1, pp. 85-98, 1999.

[43] R. M Haralick, and L. G. Shapiro, *Computer and Robot Vision, Volume I,* Addison-Wesley, pp. 28-48, 1992.

[44] https://youtu.be/G0YacFensM4

3.4. Density, CF compactness and resistance in CBRAM

Once the simulators are fully developed, they can be used for different studies. In this case, the unipolar CBRAM kMC simulator, presented in section **3.2**, has been used for studies on the CF density and compactness and their relation to the ohmic resistance.

As the kMC algorithm lets a stochastic evolution of every particle in the system, the density of the CF is not something fixed along the simulation. In this sense, a criterion to calculate it has to be selected. In section **2.4**, a methodology for calculating the density has been exposed. For doing this, when the CF is fully formed, as shown in **Figure 3.4-1a**, only the percolation path should be considered (**Figure 3.4-1b**). Then, this CF must be divided in different layers (**Figure 3.4-1c**) and the ellipse that better fits the CF surrounding is chosen for each layer (**Figure 3.4-1d**). The ellipse foci can be obtained using a clustering algorithm. In this way, the volume, and thus the density of the filament, can be defined.

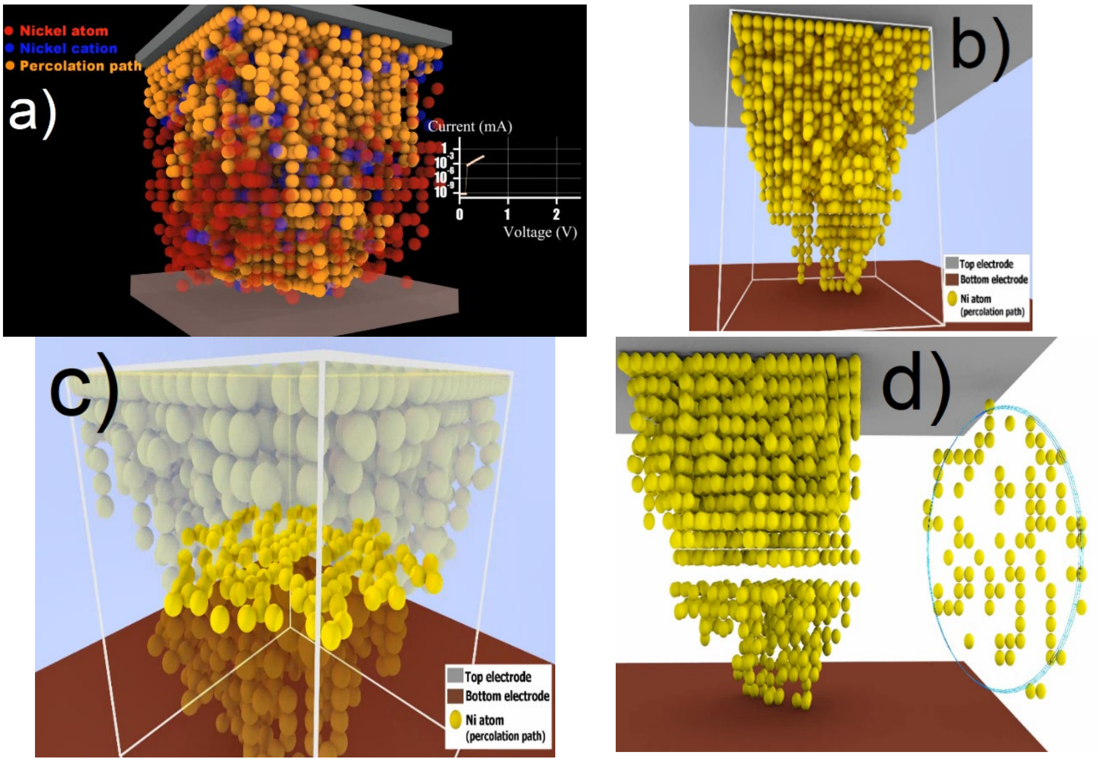

Figure 3.4-1. A complete percolation path is showed in a), where also the nickel atoms and cations appear. In b) only the CF is showed for clarity. An example of a layer is showed in c). In d) the ellipse that better fits the surrounding of a layer is represented.

For the study of the compactness, the strategy followed was the one based on the analysis of 2D percolation paths found within the 3D CF, as presented in section **2.4**.

This section is an already published work [Aldana2018b].

S. Aldana et al.

Journal of Vacuum Science & Technology B, Nanotechnology and Microelectronics: Materials, Processing, Measurement, and Phenomena (2018)

Aldana, S., García-Fernández, P., Romero-Zaliz, R., Jiménez-Molinos, F., Gómez-Campos, F., & Roldán, J. B. (2018). Analysis of conductive filament density in resistive random access memories: a 3D kinetic Monte Carlo approach. Journal of Vacuum Science & Technology B, Nanotechnology and Microelectronics: Materials, Processing, Measurement, and Phenomena, 36(6), 062201. DOI: https://doi.org/10.1116/1.5049213

Quality metrics 2018

Data base	Rating	Quartile
Web of Science	Impact factor: 1.351	Q4
Scimago	Scientific journal ranking: 0.465	Q2

Publication citations (**2020-09-07**)

Google Scholar	Web of Science
3	**2**

Analysis of conductive filament density in resistive RAMs, a 3D Kinetic Monte Carlo approach

Samuel Aldana[1], Pedro García-Fernández[1], Rocío Romero-Zaliz[2], Francisco Jiménez-Molinos[1], Francisco Gómez-Campos[1], Juan Bautista Roldán[1,a)]

[1]*Departamento de Electrónica y Tecnología de Computadores. Universidad de Granada. Facultad de Ciencias. Avd. Fuentenueva s/n, 18071 GRANADA, Spain. Email: jroldan@ugr.es*

[2]*Departamento de Ciencias de la Computación e Inteligencia Artificial. Universidad de Granada. Escuela Técnica Superior de Ingenierías Informática y de Telecomunicación, 18071 GRANADA, Spain*

a) Electronic mail: jroldan@ugr.es

ABSTRACT

An in-depth physical study of conductive filaments (CFs) density in Ni/HfO2/Si-n+ unipolar resistive RAMs (RRAMs) has been performed. To do so, we have employed both experimental measurements and simulations by means of a 3D kinetic Monte Carlo (kMC) tool. The kMC simulator accounts for redox reactions and ion migration considering the three dimensional (3D) temperature and electric potential distributions within the device dielectric at each simulation time step. The formation and destruction of conductive filaments is described; in particular, the CF density is calculated making use of a new methodology proposed here. The CF ohmic resistance can be linked to the CF density. Finally, the 2D and 3D percolation paths within the conductive filaments are analyzed to characterize the low resistance state of the RRAM under study.

I. INTRODUCTION

RRAMs are powerful candidates to substitute flash technology in the non-volatile circuit realm. Among other issues, this is due to their great potential for storage class memory and embedded memory applications. This sort of resistive memories shows low read latency and fast write performance, scalability potential, simple structure, low power consumption, high endurance, feasible structure of 3D memories stacks, etc.[1-5] Another interesting application is the use of RRAM to mimic synaptic interconnections, playing a fundamental role in artificial neural networks, which can get prominence in new neuromorphic developments[1, 3, 4, 5, 6, 7].

RRAMs have a simple structure and this allows easy fabrication techniques and facilitates their incorporation in complex 3D crossbar structures[1, 3, 5]. They consist of two electrodes with a dielectric layer in between; where the CF formation and destruction takes place (this operation is known as resistive switching (RS)). The CF consists of a percolation path made of reduced metal ions that come from the active electrode[8, 9,10] in the case of electrochemical based devices. After the fabrication process, the device is in the High Resistance State (HRS) (the dielectric is in a pristine state). But, as soon as the dielectric layer is full with reduced ions (this is, metal atoms) which migrate inside the dielectric layer, a CF can be formed that bridges the electrodes, changing the device from the HRS to Low Resistance State (LRS). The CF destruction makes the device to return to the HRS (this is known as a reset process)[1-5].

Although RRAM potential is huge, there are hurdles to overcome to make RRAM a key industrial technology. Some intrinsic features pose difficulties, such as variability, which is essential in the dispersion of the reset and set voltages and currents[1, 2, 3, 4, 5, 11] along with the values of the resistances linked to the LRS and HRS. These resistance states correspond to operation after the creation and destruction of CFs for filamentary current conduction, which is the case for the devices analyzed in this manuscript. In this context, the necessity of computational tools that allow a better understanding of the physics behind the resistive switching is clear. Some simulators have already been developed so far focused on different algorithms and complexity levels, such as those based on kinetic Monte Carlo algorithms[8, 9, 10, 12, 13], on a macroscopic description of the device materials with a finite element numerical scheme[4, 14, 15, 16], or on a compact modeling approach[17, 18, 19, 20, 21, 22, 23, 24].

The 3D kMC simulator used here[9] to characterize the CF density sheds light in the CF formation/destruction processes and allows to investigate the CF internal structure thanks to the detailed description of metal ions originated at the active electrode and the metal atoms that are reduced to form a percolation path that shorts the electrodes, after a trajectory due to electric field drift and diffusion. After the CF formation, the tool makes feasible the calculation of the filamentary resistance of Ni/HfO_2/Si-n^+ unipolar resistive RAMs[9, 25]. For the devices under study here (unipolar) the reset process is connected to the thermal CF rupture due to Joule heating effects[9]. Accordingly, the thermal and electrical device description, along with the electrochemical processes involved in the device operation, are essential for an accurate study of RS physics[5, 9, 10].

kMC simulators have stochastic algorithms as their nuclei. Some of them are 2D in nature[8,12] or 3D[9,10,26]. Few of these simulators deal with metal ion migration and reduction originated at the active electrode[8, 9, 10] or otherwise deal with the generation and recombination of oxygen vacancies[12, 26], in the case of Valence Change Memories (VCM). The simulator employed here is based on the description of Conductive Bridge RAMs (CBRAMs), taking into consideration a good description of the thermal and electrical potential distributions obtained autoconsistently with the other simulation routines. It also considers

Maxwell and series resistances[9]. A novelty presented in this manuscript is the implementation of a module for the analysis of percolation paths from the 3D and 2D perspectives. In this manner, it is possible to study the relation between the different percolation paths and the CF density. Results connected to the CF stability can be deduced from this analysis. A new technique to obtain the CF atom density is also presented making use of the percolation paths as starting point. The evolution of the CF ohmic resistance is linked to this density. For the calibration of the simulator we have employed a wide set of experimental measurements from Ni/HfO_2/Si devices[9, 25, 27]. The simulator features are detailed in section II and the main results and discussion are reported in section III; finally, some conclusions are drawn in section IV.

II. SIMULATOR DESCRIPTION

The dynamics of the RRAM operation has been modeled by means of the transition between states through the Transition State Theory[8, 9]. This description has been coded in the context of a kMC algorithm. This sort of methodology implements the stochasticity of the system in a natural way reproducing the variability of resistive switching. To weigh the different processes involved in the simulation with the corresponding transition rates, we have used Maxwell-Boltzmann statistics. These transition rates are related with the time that takes a process to occur, which in turn is related with the activation energy corresponding to this process[8, 9, 10].

The main processes involved in the simulation are the reduction/oxidation processes, metallic ion movement, ion and atom clustering, etc. The formation and disruption of the conductive filaments made of reduced ions is checked along the simulation. During the forming and set processes the Ni atoms at the electrode are oxidized. This process has been implemented as a generation of ions at the interface. However, the oxidation process can also occur in the dielectric, not only in the interface. Furthermore, the reduction process that consists in the capture of an electron by an ion can occur anywhere. An important mechanism is the migration of ions, which is electrically controlled. The electric field lowers the activation energy in one direction and increases it in the opposite direction. This ion drift through the dielectric helps the CF formation[8, 9, 10]. It has been proved that the relation between the ion generation at the electrode surface and ion mobility in terms of the associated activation energies can lead to CFs formed from the top (active) to the bottom electrode or the other way around.

The activation energy for reduction and oxidation is affected by the number of atoms surrounding the ions or atoms[1, 9]. Besides, once an ion reaches the bottom electrode (or the bottom virtual electrode) and gets reduced it is quite difficult to reoxidize it again[1, 9]. The simulation domain is cubic[9, 10]. As the device used has a dielectric 5 nm thick, we employ for the simulation a twenty point grid with a separation of 0.25nm (twice the approximated Ni atom radius).

The temperature is calculated solving the 3D heat equation with boundary conditions of constant temperatures at both electrodes and adiabatic conditions in the lateral faces. We have simplified the temporal evolution of the temperature following a previous work[28]. The 3D Poisson equation has been solved assuming a fixed voltage in both electrodes and Neumann boundary conditions in the lateral faces for each time step.

Different conduction mechanisms are used depending on the operation regime. For the pristine and HRS states, a Poole-Frenkel emission model has been used. When the CF is fully formed and the device is in LRS, a Quantum Point Contact model and ohmic conduction have been implemented, in addition with the Poole-Frenkel model, which is masked by the other mechanisms. In the LRS it has also been taken into account the funneling of the current lines (Maxwell resistance). An additional explanation of the simulator is detailed in Ref. 29.

III. RESULTS AND DISCUSSION

In **Figure 3.4-2**, the I-V curves of the devices under consideration are shown. A good agreement between experimental and simulation data can be observed (the parameter tuning was described in Ref. 9, where long RS series were employed). This Figure shows some characteristic points in the CF evolution along the set process (**Figure 3.4-2a-c**, in blue) and the reset process (**Figure 3.4-2a-d**, in red). The set process starts using the CF remnants remaining from the previous reset process. In the reset process, the CF firstly grows and makes the corresponding current increase; consequently, a rise of temperature due to Joule heating effects takes place. This high temperature will trigger the process of CF rupture that drives the device into the HRS.

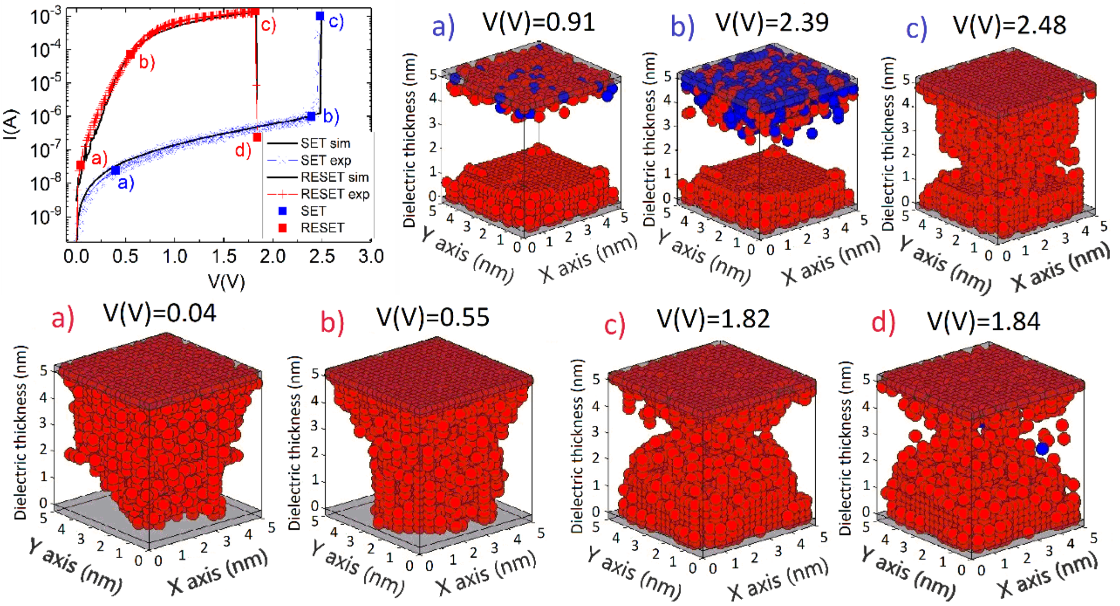

Figure 3.4-2. (**Color online**): Current versus applied voltage in the RRAM under study. The blue points in the set I-V curve (a-c) correspond to the figures with the same label that represent the simulated distribution of the Ni atoms (red balls) and Ni ions (blue balls) during different states of a set process. Red points in the reset curve (a-d) correspond to figures with the same label, that represent the simulated distribution of the Ni atoms (red balls) and Ni ions (blue balls) during the reset process. The accuracy of the experimental data fit is remarkable. Ions are not represented when a fully formed CF is obtained for clarity.

In order to characterize the conductive filaments, we have implemented a procedure to estimate the CF density by considering the ellipse that better fits the surroundings of the percolation path in every CF layer considered in the simulation domain. An example of this estimation is shown in **Figure 3.4-3a**, where the ellipse foci are obtained by means of a clustering algorithm. The CF atom density can be calculated by using different ellipses for each layer. This allows the CF volume and density estimation. A good evidence of the stochasticity of the system is the representation of the density along a reset cycle. Several successive reset cycles CF densities are shown in **Figure 3.4-3c**. The curves show a similar trend, although obvious differences come up due to the stochasticity inherent to resistive switching processes.

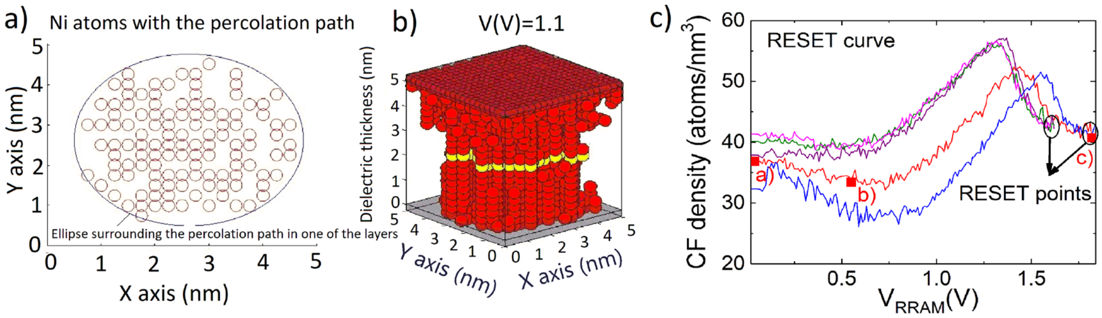

Figure 3.4-3. (**Color online**). a) Ellipse surrounding the percolation path in one of the grid layers. The calculation of the ellipse is needed to obtain the CF density. b) The CF layer atoms shown in a) are plotted in yellow. c) CF atom density versus voltage for reset curves corresponding to consecutive reset cycles. The red curve corresponds to the reset curve shown in **Figure 3.4-2**, the same points (for the CFs shown in **Figure 3.4-2**) are highlighted here.

In **Figure 3.4-4**, the relation between the CF density and the ohmic resistance is shown. This relation was foreseeable; i.e., the more compact is the CF, the lower is the associated ohmic resistance. The final resistance increase is linked to the process of temperature increase and leads to the triggering of ion diffusion that decreases the CF density till the percolation path is broken.

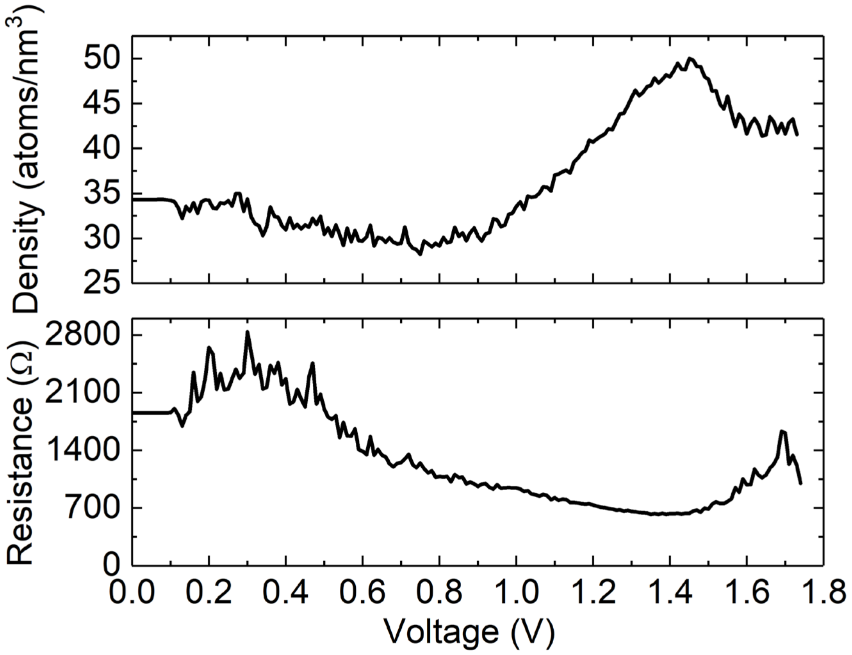

Figure 3.4-4. Representation of the CF density and its corresponding ohmic resistance.

It is important to call the reader's attention to the fact that in the LRS, in addition to the CF ohmic resistance, a resistance linked to quantum effects and modeled by the QPC theory is found in series[30, 31, 32, 33]. It has been shown that the relative contribution of both conduction mechanisms depends on the voltage applied to the RRAM. For the highest voltages in the reset curve, close to the reset voltage, the device resistance is mostly ohmic, as described in Ref. 30. In this case, the calculation of the CF density with new experimental work could be used to shed light on the CF 3D physical constants that are usually employed in compact models[19, 20, 22, 23]. Further uses of the simulator would include the analysis of pulsed signals and their influence on the device RS behaviour[31].

In line with the study of the CF density, other illuminating strategy is linked to the analysis of the percolation paths found in the CF, both from the 3D and 2D perspective. See **Figure 3.4-5**, were the different planes that can be found in the simulation domain in the X axis and Y axis are shown. For the 2D analysis of percolation paths, we will consider a 3D CF such as those plotted in **Figure 3.4-2** and extract all the planes highlighted in **Figure 3.4-5**; then the existence of 2D percolation paths is inquired.

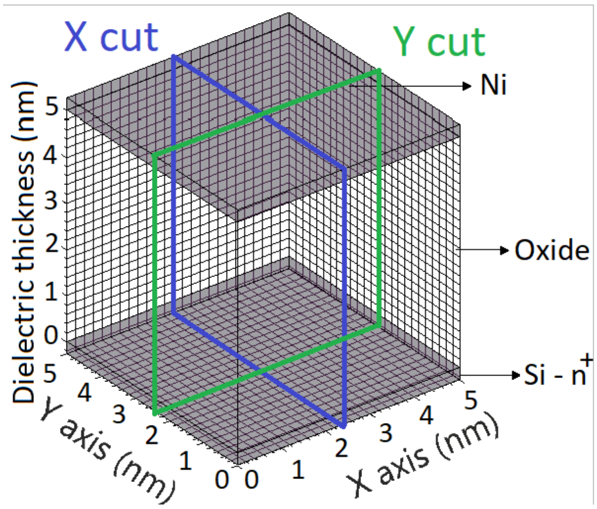

Figure 3.4-5. Representation of the planes (simulation domain slices) in X axis and Y axis for the complete 3D simulation domain. It is clear that in this type of devices, kMC 3D models produce results very different to kMC 2D models due to the inherent features of the percolation paths.

As shown in **Figure 3.4-6**, a notable difference between the percolation path structures is found accounting for a 3D and 2D description. For example, in the simulation time shown in **Figure 3.4-6a** there are time instants where it could be a percolation path in 3D, but none in 2D (see the time marked as d). In these cases, the CF shows high instability since a path with single atom sections bridges the electrodes. Nevertheless, for the time window with a simultaneous high number of 2D percolation paths, the CF is obviously more stable.

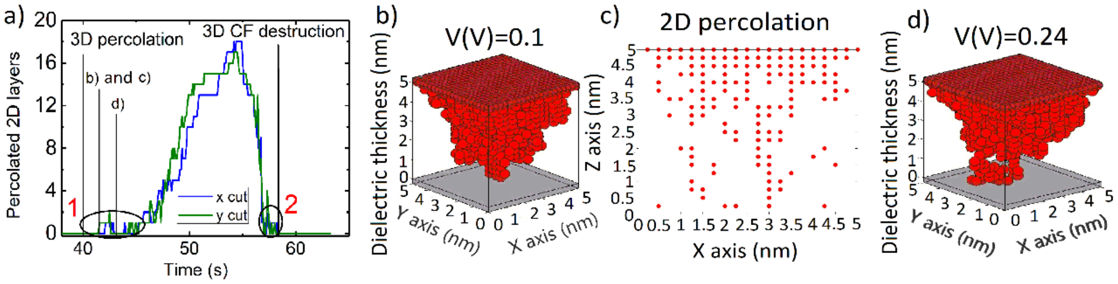

Figure 3.4-6 (**Color online**). a) Representation of the number of layers that percolate in 2D (in the whole 3D simulation domain) for different cuts (slices) in plane X and plane Y in a fully 3D simulation for a reset curve (a ramped voltage is employed). The figure shows important differences between the 2D and 3D analysis. In zones 1 and 2, it is found that while a 3D percolation path exists, this is not the case always for 2D percolation paths. The time window with a higher number of 2D percolation paths correspond to a highly stable 3D CF. b) A 3D CF is shown, in c) 2D slice of the 3D CF shown in b) both figures correspond at the time marked with b) and c) in **Figure 3.4-6a**. It is the first time that a percolation path occurs in 2D. d) Conductive filament that correspond to the point shown in **Figure 3.4-6a** with d) (highlighted with a vertical line) where there is not a percolation path in 2D while it exists in 3D.

The 3D description has the advantage that the lateral interaction between different layers in the simulation domain is taken into consideration. In this manner, real CFs can be reproduced. It is also shown that 2D representations of the simulation domain can be inaccurate in certain operation regimes since no 2D percolation paths could be present while a 3D percolation path could exist. In this respect, the stochastic nature of these devices makes a 3D representation essential to reproduce resistive switching within a kMC simulation approach. Furthermore, a 2D perspective presents shortcomings to analyze and characterize the CF compactness at each stage of a set/reset process.

IV. SUMMARY AND CONCLUSIONS

An in-depth study of the CF density in unipolar $Ni/HfO_2/Si\text{-}n^+$ is presented by means of a kMC simulation tool. The experimental results measured in these devices are reproduced making use of the simulator, and the Ni atoms distributions that form the percolation paths that constitute the conductive filaments are studied for different reset processes. A new procedure to calculate the CF density is presented and the associated CF ohmic resistance is studied accordingly. Moreover, the analysis of 2D and 3D percolation paths found within the conductive filaments is performed. It is shown that 2D representations might lack accuracy due to the stochastic nature of resistive switching that is correctly reproduced by means of kMC simulators.

ACKNOWLEDGMENTS

We thank F. Campabadal and M. B. González from the IMB-CNM for fabricating and providing the experimental measurements. The authors thank the support of the Spanish

Ministry of Economy and Competitiveness and the FEDER program through project TEC2017-84321-C4-3-R, ENE2016-80944-R. This work has made use of the Spanish ICTS Network MICRONANOFABS.

REFERENCES

[1] F. Pan, S. Gao, C. Chen, C. Song, F. Zeng, Mat. Science and Eng. **83**, 1-59 (2014)

[2] M. Lanza, Mater 7, 2155-2182 (2014).

[3] M. Lanza, H.-S. P. Wong, E. Pop, D. Ielmini, D. Strukov, B.C. Regan, L. Larcher, M.A. Villena, J.J. Yang, L. Goux, A. Belmonte, Y. Yang, F. M. Puglisi, J. Kang, B. Magyari-Köpe, E. Yalon, A. Kenyon, M. Buckwell, A. Mehonic, A. Shluger, H. Li, T.-H. Hou, B. Hudec, D. Akinwande, R. Ge, S. Ambrogio, J.B. Roldan, E. Miranda, J. Suñe, K.L. Pey, X. Wu, N. Raghavan, E. Wu, W.D. Lu, G. Navarro, W. Zhang, H. Wu, R. Li, A. Holleitner, U. Wurstbauer, M. Lemme, M. Liu, S. Long, Q. Liu, H. Lv, A. Padovani, P. Pavan, I. Valov, X. Jing, T. Han, K. Zhu, S. Chen, F. Hui, Y. Shi, Adv. Electron. Mater. in press, (2018).

[4] M.A. Villena, J.B. Roldán, F. Jiménez-Molinos, E. Miranda, J. Suñé, M. Lanza, J. Comput. Electron. **16**, 1095-1120 (2017).

[5] D. Ielmini, R. Waser, Resistive Switching: From Fundamentals of Nanoionic Redox Processes to Memristive Device Applications (Wiley-VCH, 2015).

[6] N. Suri, Advances in neuromorphic hardware exploiting emerging nanoscale devices (Springer, 2017).

[7] S. Yu, Y. Wu, R. Jeyasingh, D. Kuzum, H.-S. Wong, IEEE Trans. Electron Devices **58**, 2729–2737 (2011).

[8] J. Guy, G. Molas, P. Blaise, M. Bernard, A. Roule, G. Le Carval, V. Delaye, A. Toffoli, G. Ghibaudo, F. Clermidy, B. De Salvo, L. Perniola, IEEE Trans. Electron Devices **62**, 3482 (2015).

[9] S. Aldana, P. García-Fernández, A. Rodríguez-Fernández, R. Romero-Zaliz, M. B. González, F. Jiménez-Molinos, F. Campabadal, F. Gómez-Campos, J. B. Roldán, J. Phys. D **50**, 335103 (2017).

[10] S. Aldana, J.B. Roldán, P. García-Fernández , J. Suñe , R. Romero-Zaliz , F. Jiménez-Molinos, S. Long , F. Gómez-Campos , M. Liu, J. Appl. Phys. **123**, 154501 (2018).

[11] S. Long, X. Lian, C. Cagli, L. Perniola, E. Miranda, M. Liu, J. Suñé, IEEE Electron Devic. Lett. **34**, 999 (2013).

[12] X. Guan, S. Yu, H.S. Philip Wong, IEEE Trans. Electron Devices, **59**, 1172-1182 (2012).

[13] S. Yu, X. Guan, H.S. Philip Wong, IEEE Trans. Electron Devices **59**, 1183-1188 (2012).

[14] M.A. Villena, M.B. González, F. Jiménez-Molinos, F. Campabadal, J.B. Roldán, J. Suñé, E. Romera, E. Miranda, J. Appl. Phys. **115**, 214504 (2014).

[15] M. Bocquet, D. Deleruyelle, C. Muller, J.M. Portal, Appl. Phys. Lett. **98**, 263507 (2011).

[16] M.A. Villena, M.B. González, J.B. Roldán, F. Campabadal, F. Jiménez-Molinos, F.M. Gómez-Campos y J. Suñé, Solid-State Electron. **111**, 47-51 (2015).

[17] J.B. Roldán, E. Miranda, G. González-Cordero, P. García-Fernández, R. Romero-Zaliz, P. González-Rodelas, A. M. Aguilera, M.B. González, F. Jiménez-Molinos, J. Appl. Phys. **123**, 014501 (2018).

[18] X. Guan, Y. Shimeng, and H-S. Philip Wong. IEEE Electron Devic. Lett. **33**, 1405-1407 (2012).

[19] G. González-Cordero, F. Jiménez-Molinos, J.B. Roldan, M.B. González and F. Campabadal, J. Vac. Sci. Technol. **B 35**, 01A110 (2017).

[20] M. Bocquet, D. Deleruyelle, H. Aziza, C. Muller, J. Portal, T. Cabout, E. Jalaguier, IEEE Trans. Electron Devices **61**, 674-681 (2014).

[21] G. Gonzalez-Cordero, J. B. Roldan, F. Jimenez-Molinos, J. Suñé, S. Long and M. Liu, Semicond. Sci. Technol. **31**, 1–13 (2016).

[22] P. Huang, X. Y. Liu, B. Chen, H.T. Li, Y. J. Wang, Y.X. Deng, K.L. Wei, L. Zeng, B. Gao, G. Du, X. Zhang, J.F. Kang, IEEE Trans. Electron Devices **60**, 4090-4097 (2013).

[23] S. Kvatinsky, M. Ramadan, E. G. Friedman and A. Kolodny, IEEE Trans. Circuits Syst. II, Exp. Briefs, **62**, 786-790 (2015).

[24] F. Jiménez-Molinos, M.A. Villena, J.B. Roldán, A.M. Roldán, IEEE Trans. Electron Devices **62**, 955-962 (2015).

[25] A. Rodríguez-Fernández, S. Aldana, F. Campabadal, J. Suñé, E. Miranda, F. Jiménez-Molinos, J. B. Roldán, M. Bargallo Gonzalez, IEEE Trans. Electron Devices **64**, 3159-3166 (2017).

[26] A. Padovani, L. Larcher, Member, IEEE, O. Pirrotta, L. Vandelli, G. Bersuker, Member, IEEE, IEEE Trans. Electron Devices **62,** 1998-2006 (2015).

[27] M. B. González, J. Martin-Martinez, M. Maestro, M. C. Acero, M. Nafría, Member, IEEE, F. Campabadal, IEEE Trans. Device Mater. Reliab. **14**, 769–771 (2014).

[28] N.D. Lu, Z.W. Zong, P.X. Sun, L. Li. Q. Liu, H.B. Lv, S.B. Long, M. Liu, Thermal effect and compact model in three-dimensional (3D) RRAM arrays Int. Conf. on IEEE in Simulation of Semiconductor Processes and Devices (SISPAD) 161–4, (2016)

[29] https://youtu.be/Rvm88B2AMLY

[30] M.A. Villena, J.B. Roldán, M.B. González, P. González-Rodelas, F. Jiménez-Molinos, F. Campabadal, D. Barrera, Solid-State Electron. **118**, 56-60 (2016).

[31] M. Zhang, S. Long, G. Wang, X. Xu, Y. Li, Q. Liu, H. Lv, X. Lian, E. Miranda, J. Suñé, M. Liu, Appl. Phys. Lett. **105**, 193501 (2014).

[32] X. Lian, X. Cartoixa, E. Miranda, L. Perniola, R. Rurali, S. Long, M. Liu, J. Suñé, J. Appl. Phys. 115, 244507 (2014).

[33] M. Zhang, G. Wang, S. Long, Z. Yu, Y. Li, D. Xu, H. Lv, Q. Liu, E. Miranda, J. Suñé, M. Liu, IEEE Electron Dev. Lett. **36**, 1303 (2015).

3.5. Characterization of Ni/HfO$_2$/Si RRAMs

The unipolar CBRAM kMC simulator exposed in section **3.2** has been used to characterize Ni/HfO$_2$/Si devices. The RS process, the resistance and the density have been studied with this tool.

The density has been studied following the strategies proposed in section **3.4**. In **Figure 3.4-1** has also been exposed the way of achieving a good ellipse that fit the surrounding of the CF, part needed for the density calculation.

Also, the compactness calculated based on the 2D percolation paths analysis has been performed, which is a way of study the stability and porosity of the CF. It is clear that a 3D percolation path with no 2D percolation paths is quite less stable that the situation when many 2D percolation paths exist.

This section is an already published work [Aldana2018c].

S. Aldana et al.

Proceedings of IEEE. 12th Spanish Conference on Electron Devices (CDE 2018). IEEE Xplore digital library

Aldana, S., García-Fernández, P., Romero-Zaliz, R., González, M. B., Jiménez-Molinos, F., Campabadal, F., ... & Roldán, J. B. (2018, November). A Kinetic Monte Carlo Simulator to Characterize Resistive Switching and Charge Conduction in Ni/HfO 2/Si RRAMs. In 2018 Spanish Conference on Electron Devices (CDE) (pp. 1-4). IEEE. DOI: https://doi.org/10.1109/CDE.2018.8597010

Quality metrics

Data base	Rating
Google Scholar Metrics	h5-index: 5 h5-median:6

Publication citations (2020-09-07)

Google Scholar	Web of Science
0	**0**

A kinetic Monte Carlo simulator to characterize resistive switching and charge conduction in Ni/HfO$_2$/Si RRAMs

S. Aldana[1], P. García-Fernández[1], R. Romero-Zaliz[3], M.B. González[2], F. Jiménez-Molinos[1], F. Campabadal[2], F. Gómez-Campos[1], J.B. Roldán[1]

[1]Dpto. de Electrónica y Tecnología de Computadores, Universidad de Granada, Granada, Spain, Email: jroldan@ugr.es

[2]Institut de Microelectrònica de Barcelona, IMB-CNM (CSIC), Campus UAB, Bellaterra, Spain

[3]Dpto. de Ciencias de la Computación e Inteligencia Artificial, Universidad de Granada, ETSII, Granada, Spain

***Abstract*— A 3D kinetic Monte Carlo (kMC) simulation tool has been developed to study the resistive switching (RS) processes that allow Ni/HfO$_2$/Si devices to work as non-volatile memories. The simulator is tuned with numerous experimental data and it can reproduce the device current in forming, set and reset processes, the cycle-to-cycle variability and other characteristics linked to the stochasticity of RS operation. The evolution of conductive filaments (CFs) for different RS cycles is analyzed in depth, as well as the filaments density and resistance.**

Keywords—RRAM, kinetic Monte Carlo, resistive switching, conductive filament, conductive filament density.

I- INTRODUCTION

Among the emerging non-volatile memory technologies, RRAMs are key components that have shown a promising potential for storage class memory and embedded memory applications. RRAMs beat FLASH technology in terms of read latency and faster write performance, lower power operation, scalability and stackability [1-7]. In addition, RRAMs are also gaining momentum as memristive synapses. The latter advances in the analog playground of resistive switching devices could foster new hardware neural networks developments [1, 5-9].

RRAM devices consist of a dielectric sandwiched between two electrodes. This simple structure allows its incorporation in complex 3D crossbar architectures [1, 5, 7]. It is in the dielectric where the conductive filament (CF) is formed or ruptured, leading to the RS phenomenon. In conductive bridge RRAMs (CB-RRAMs, or electrochemical memories, ECM [7]), the CF is formed by means of reduced metal ions that are generated at the active electrode (anodic dissolution of the active electrode). These atoms form a conductive filament that consists of a percolation path between the electrodes [2, 10]. Different evidences of RS operation have been experimentally seen for the devices under study here, based on a Ni/HfO$_2$/Si stack [3, 11]. At the beginning, after fabrication, the device is in a pristine state. However, after the application of a positive voltage (at the active top electrode with the bottom electrode grounded), nickel atoms are oxidized and migrate into the dielectric, where they are reduced, forming nickel atoms clusters. Once a percolation path is formed, the CF bridges the electrodes leading the device from the pristine state to the Low Resistance State (LRS). The first process of formation of a percolation path is known as forming, while subsequent reconstructions of previously broken CFs are named SET processes. The destruction process occurs by Joule heating of the CF, in a process named RESET, leading the device to the High Resistance State (HRS) in which the dielectric is not completely clean, but it has remainders of the previously formed CFs [1, 10-13].

The authors thank the support of the Spanish Ministry of Science and Universities and the FEDER program through projects TEC2017-84321-C4-1-R, TEC2017-84321-C4-3-R, TEC2014-54906-JIN, ENE2016-80944-R. This work has made use of the Spanish ICTS Network MICRONANOFABS.

Nevertheless, for the further development of RS devices, reliability and variability issues have to be addressed. In this way, it is essential to have accurate simulation tools. These simulators can also be extremely useful for compact modeling and circuit design tasks. Previously, we presented a 3D kinetic Monte Carlo (kMC) simulator [10, 11] that correctly reproduces I-V curves and set/reset current and voltage distributions. Now, we use this simulation tool in order to analyse RS, characterize the CFs density and their internal structure, and to calculate the filamentary resistance [10, 11].

We can find different sorts of simulators developed in the past. Some of them follow a 2D approach [1, 2, 13, 14], while others are based on a 3D mesh [10, 12, 15]. We can also classify them according to the physics behind the RS processes: metal ion migration from the active electrode to the dielectric and later reduction of ions (CB-RRAMs) [1, 2, 10, 12, 13]; or generation/recombination of oxygen vacancies [14, 15] and oxygen ions migration in the case of Valence Change Memories (VCMs). The simulator used in this manuscript is used to study Conductive Bridge RAMs. It solves accurately the heat and Poisson equations self-consistently with other routines of the simulator. Furthermore, in order to obtain the resistance of the system once a percolation path is formed, we have used an equivalent circuit which takes into consideration the ohmic resistance, series and Maxwell resistances and tunneling processes described by the Quantum Point Contact model [10].

The fabricated devices and measurement process are described in Sec. II and the simulation tool in Sec. III. The main results and discussion are drawn in Sec. IV. Finally, the conclusions are given in Sec. V.

II- DEVICE FABRICATION AND MEASUREMENT

The studied devices were fabricated at the IMB-CNM and consist on a $Ni/HfO_2/Si$ stack. A wafer of (100) highly doped n-type CZ silicon was employed and a 5nm-thick HfO_2 layer was grown by Atomic Layer Deposition at 225°C [3, 10, 11]. Current-voltage (I-V) measurements were performed at 300 K using a Keysight B1500 semiconductor parameter analyzer. Constant voltage stress (CVS) was used to evaluate the forming time, while voltage ramps were applied to obtain I-V curves. Voltage was applied to the Ni electrode with the Si substrate grounded.

III- SIMULATOR DESCRIPTION

A 3D simulator was built to describe RS physics for $Ni/HfO_2/Si\text{-}n^+$ devices. The 3D heat and Poisson equations are solved at each simulation step and the processes involved in RS are considered under the transition state theory (TST) [2, 10] within a kMC algorithm. A simplified method has been used to accelerate the calculation of the thermal transient response [16]. This methodology implements the stochasticity of the system reproducing the resistive switching cycle-to-cycle variability. In order to weigh the different processes with their transition rates, the Maxwell-Boltzmann statistics have been used. Furthermore, the time that takes an event to occur is determined by its transition rate, which is in turn determined by using the corresponding activation energy [2, 10, 12].

Some of the processes included in the simulator are the reduction/oxidation [2, 10, 12], with some local effects that change the activation energies of these processes: the contact with the bottom electrode or the atom clustering phenomenon [1, 10]. The simulator also deals with the generation of ions at the interface between the electrode and the dielectric and their movement inside the dielectric. The former mechanism plays the role of the anodic dissolution of the electrode [2, 10, 12]. It is important to highlight that both processes depend on by the electric field. The 3D percolation paths are sought and considered to obtain the device current. Once a percolation path is formed, an equivalent circuit including the CF ohmic resistance, series and Maxwell resistances and tunneling processes described by the Quantum Point Contact model, is used [10].

The simulation domain is a cubic structure (5 nm x 5nm) and 20 grid points per dimension. That is, there is a separation of 0.25nm between the points in the mesh, which is equivalent to twice the nickel atom radius.

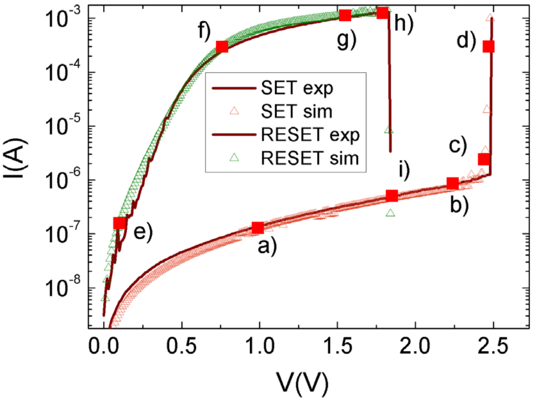

Figure 3.5-1. Experimental (lines) and simulated current (symbols) versus applied voltage for the RRAMs under study. The accuracy of the experimental data fit is reasonable.

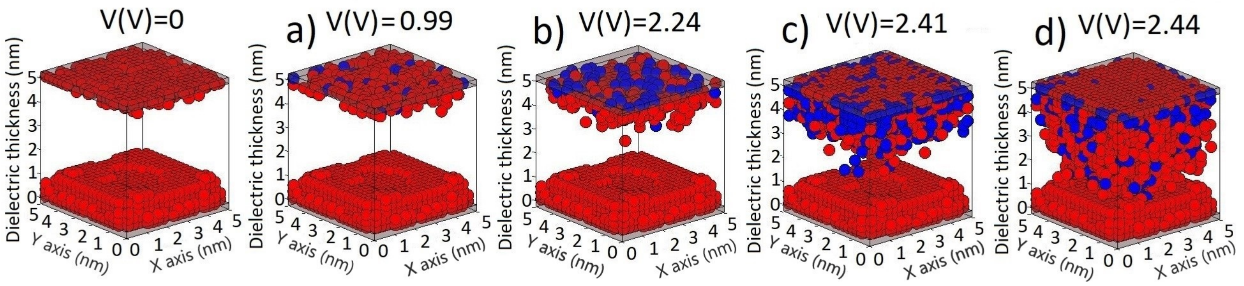

Figure 3.5-2. Different stages for the set simulation shown in Figure 1. The points in the set I-V curve (a-d) of Figure 1 correspond to the simulation figures with the same label here that represent the simulated distribution of Ni atoms (red balls) and Ni ions (blue balls) during different states of a set process.

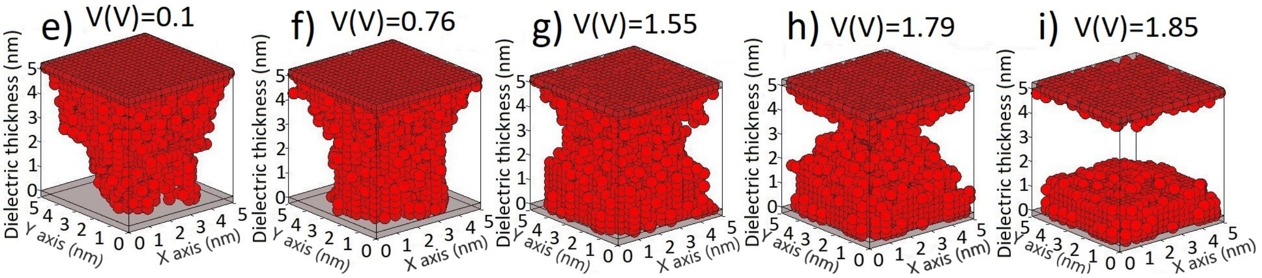

Figure 3.5-3. The points in the reset curve (e-i) in **Figure 3.5-1** correspond to simulation figures with the same label here that represent the simulated distribution of the Ni atoms (red balls) during the reset process. Ni ions are not represented for clarity when a fully formed CF is obtained.

IV- RESULTS AND DISCUSSION

Figure 3.5-1 shows experimental and simulated I-V curves of the studied Ni/HfO_2/Si RRAMs. Notice that a good agreement has been achieved. A considerable amount of experimental data are needed to tune the simulator.

The RRAM filamentary states corresponding to the different labelled points in **Figure 3.5-1** are shown in **Figure 3.5-2** and **3.5-3** for the set and reset processes, respectively. In this way, we obtained an approximated visualization of the CF evolution along set and reset cycles. Each point from a) to i) in **Figure 3.5-1** corresponds to the state labelled with the same letter in **Figure 3.5-2** and **3.5-3**. The forming process has not been shown, although it can be also simulated by our tool. As can be seen, the device in the set initial state shown in **Figure 3.5-2** evolves from some CF remains, which is not the case of a forming process. The origin of these remains is the previous thermal rupture in a reset process that has taken place just before. These remains produce a higher current through the device in comparison with the current measured in the pristine state for the same applied voltage. This is due to the smaller gap between electrodes since the remaining clusters work like virtual electrodes. On the other hand, **Figure 3.5-3** shows the device evolution during a reset process. It is noticeable a widening of the CF at the beginning of the process. This change in the CF morphology and structure provokes a current increase. Consequently, this will trigger a temperature rise by Joule heating which finally leads to the CF thermal rupture.

In order to develop an in-depth analysis of the results and the different simulation approaches regarding the dimensions considered for the simulation domain, we have calculated and represented the number of percolation paths obtained along a reset curve in two and three dimensions (**Figure 3.5-4**). For the calculation of 2D percolation paths, we have considered 40 cross sections in the device (the plane surfaces perpendicular to the electrodes along the axes of the grid and sited on the mesh points). For each slice we determined if a percolation path is found and finally we counted them. The differences between percolation paths obtained in 2D and 3D are highlighted in **Figure 3.5-4**. The figure shows important differences between 2D and 3D analysis. In zones A and B (highlighted by ellipses), it is found that while a 3D percolation path exists, no 2D percolation paths are found. Notice that a 3D percolation path exists between the vertical lines labeled with *3D percolation path* and *3D percolation path rupture*. The time window with a higher number of 2D percolation paths corresponds to a highly stable 3D conductive filament. It is clear that the higher the number of 2D percolated layers, the more stable the filament is (there are many choices to find a path that bridges both electrodes in a dense filament). The more probable existence of a 3D percolation path is reasonable since for each atom there are two more sites that can be covered by other atoms that form the percolation path. In fact, 2D percolation paths can be formed or destroyed depending on a single connection between two atoms.

The CF density can be estimated by using a new procedure that fits an enveloping ellipse for each percolation path layer in the simulation domain, as shown in **Figure 3.5-5**. With this procedure we can estimate the density of the CFs that we simulate and compare their evolution in terms of density. Furthermore, this technique allows the study of the relation between the resistance and the filamentary density of the device. For each parallel-to-electrodes grid layer (**Figure 3.5-5a**), the simulator determines the enveloping ellipse and counts the number of atoms in the CF (**Figure 3.5-5b**). In this way, we can calculate the evolution of the CF density along the time (**Figure 3.5-5c**). Interestingly, as said above, just before the rupture of the CF, the density (and the width) of the filament rises during the reset cycle (**Figure 3.5-3g** and **3.5-5c**).

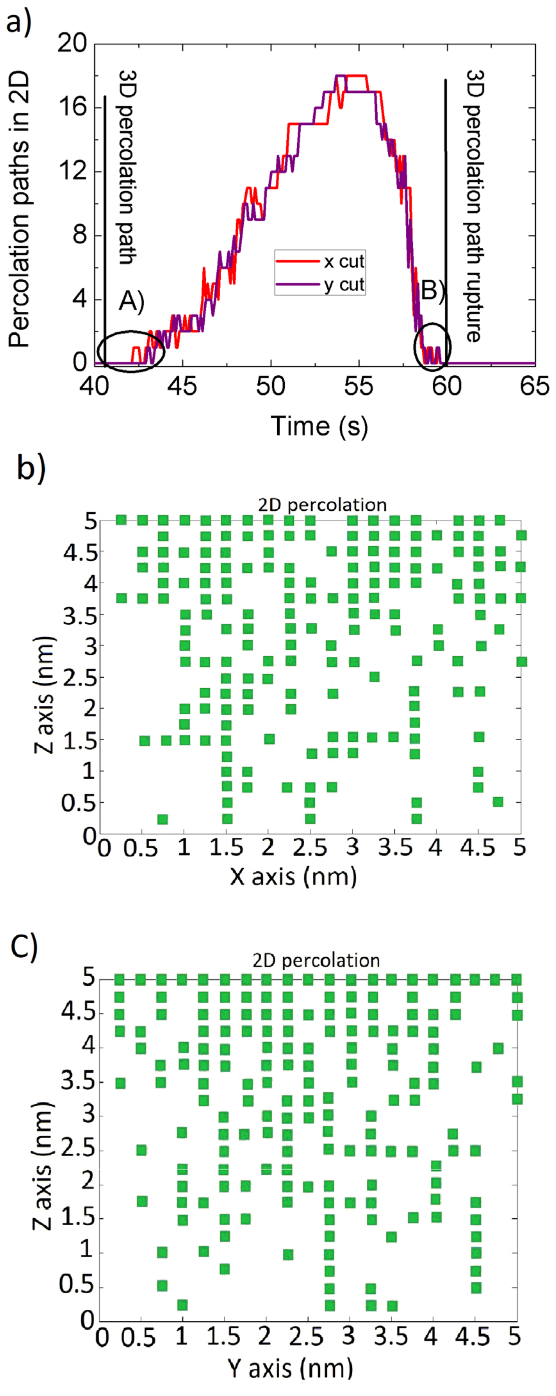

Figure 3.5-5. a) Representation of the number of layers that percolate in 2D (in the whole 3D simulation domain) for different cuts (slices) in plane X and plane Y. The results are obtained from a fully 3D simulation of a reset curve (a ramped voltage is employed). b) Percolation representation of a cut in Y axis. c) Percolation representation of a cut in X axis. It is clear that in this type of devices, kMC 3D models provide very different results from the kMC 2D models because of the nature of the RS underlying physics.

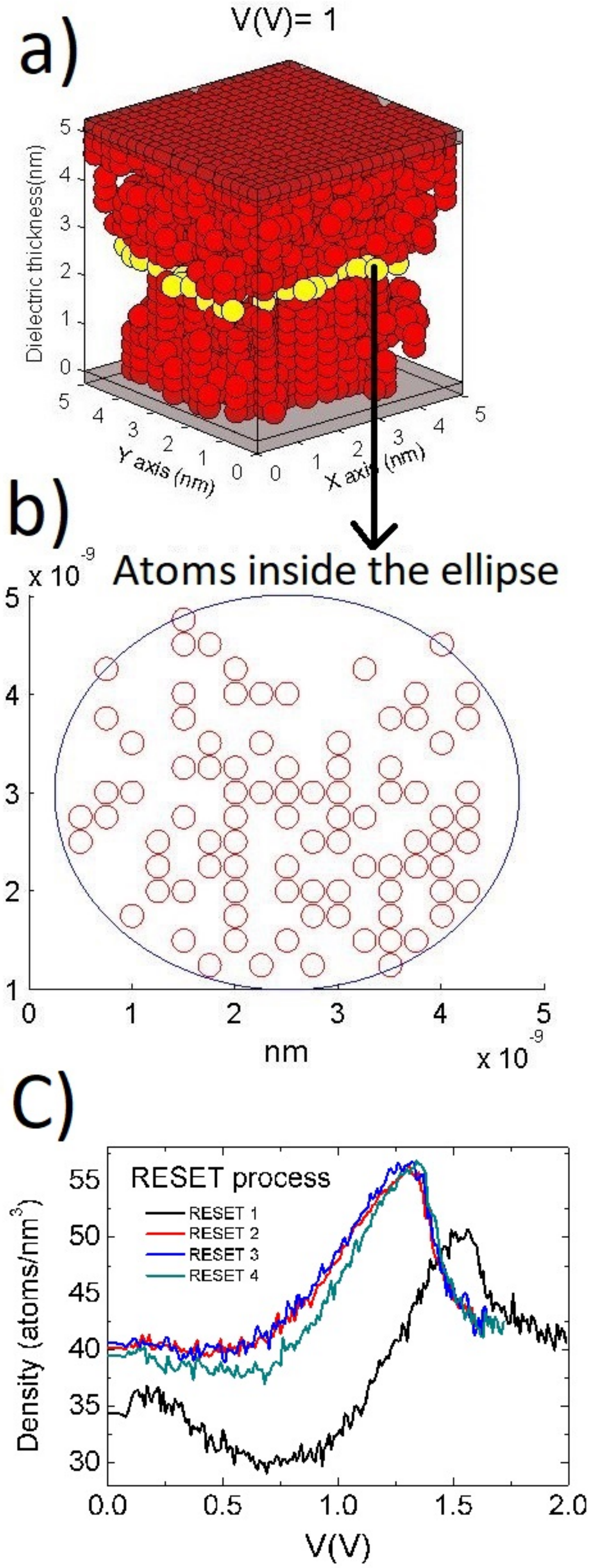

Figure 3.5-4. The atoms of the CF layer shown in b) are plotted in yellow. b) Ellipse surrounding the percolation path in one of the grid layers. The definition of the ellipse is needed to calculate the CF density. c) Conductive filament atom density (for the whole CF, including all the layers) versus voltage for different reset curves.

V- CONCLUSIONS

We have used a simulation tool in order to study forming and reset/set cycles in Ni/5nm-HfO_2/Si RRAMs. The simulator allows us to represent the resistive state and evolution of the filament along the time. Furthermore, an estimation technique has been proposed in order to calculate the density of atoms along the filament and the corresponding resistance. It has been proved that before the rupture during a reset process, the density and width of the filament rise. Finally, a comparison between 2D and 3D simulation approaches has been performed.

REFERENCES

[1] F. Pan, S. Gao, C. Chen, C. Song, F. Zeng, "Recent progress in resistive random access memories: Materials, switching mechanisms, and performance", Mat. Science and Eng., vol. 83, pp. 1-59, 2014.

[2] J. Guy et al., "Investigation of Forming, SET, and Data Retention of Conductive-Bridge Random-Access Memory for Stack Optimization", IEEE Trans. Electron Devices, vol. 62, pp. 3482, 2015.

[3] M. B. Gonzalez, J. M. Rafí, O. Beldarrain, M. Zabala, and F. Campabadal, "Analysis of the Switching Variability in Ni/HfO_2-Based RRAM Devices", IEEE Trans. Device Mater. Reliab., vol. 14, no. 2, pp. 769–771, 2014.

[4] M. M. Al Chawa et al., "Exploring Resistive Switching based Memristors in the Charge-Flux Domain, a modeling Approach", International Journal of Circuit Theory & Applications, 46, pp. 29-38, 2018.

[5] M. Lanza et al., "Recommended methods to study resistive switching devices", Advanced Electronic Matererials, p. 1800143, 2018.

[6] M. A. Villena, J. B. Roldán, F. Jiménez-Molinos, E. Miranda, J. Suñé, M. Lanza, "SIM^{2}RRAM: a physical model for RRAM devices simulation", J. Comput. Electron., vol. 16, pp. 1095-1120, 2017.

[7] D. Ielmini, R. Waser, "Resistive Switching: From Fundamentals of Nanoionic Redox Processes to Memristive Device Applications", Wiley-VCH, 2015.

[8] N. Suri, "Advances in neuromorphic hardware exploiting emerging nanoscale devices", Springer, 2017.

[9] S. Yu, Y. Wu, R. Jeyasingh, D. Kuzum, H.-S. Wong, "An electronic synapse device based on metal oxide resistive switching memory for neuromorphic computation", IEEE Trans. Electron Devices, vol. 58, pp. 2729–2737, 2011.

[10] S. Aldana et al., "A 3D kinetic Monte Carlo simulation study of resistive switching processes in Ni/HfO_2/Si-n$^+$-based RRAMs", J. of Phys. D: App. Phys., vol. 50, pp. 335103, 2017.

[11] A. Rodríguez-Fernández et al., "Resistive Switching with Self-Rectifying Tunability and Influence of the Oxide Layer Thickness in Ni/HfO_2/n$^+$-Si RRAM Devices", IEEE Trans. on Electron Devices, vol. 64, n 8, pp. 3159-3166, 2017.

[12] S. Aldana et al., "An in-depth description of bipolar resistive switching in Cu/HfOx/Pt devices, a 3D kinetic Monte Carlo simulation approach", J. Appl. Phys., vol. 123, pp. 154501, 2018.

[13] F. Pan, S. Yin, V. Subramanian, "A Detailed Study of the Forming Stage of an Electrochemical Resistive Switching Memory by KMC Simulation", IEEE Electron Dev. Lett., vol. 32, pp. 949-951, 2011.

[14] X. Guan, S. Yu, H. S. Philip Wong, “On the switching parameter variation of metal-oxide RRAM - Part I: Physical modeling and simulation methodology”, IEEE Trans. Electron Devices, vol. 59, pp. 1172-1182, 2012.

[15] A. Padovani, L. Larcher, O. Pirrotta, L. Vandelli, G. Bersuker, “Microscopic Modeling of HfOx RRAM Operations: From Forming to Switching”, IEEE Trans. Electron Devices, vol. 62, pp. 1998-2006, 2015.

[16] N. D. Lu et al., “Thermal effect and compact model in three-dimensional (3D) RRAM arrays”, Int. Conf. on IEEE in Simulation of Semiconductor Processes and Devices (SISPAD), pp. 161–164, 2016

Chapter 4

4. Valence change memory

4.1. Resistive Switching mechanism

Valence Change Memories (VCM) are a kind of RRAMs whose mechanism for forming the filament consist in the generation of a defect-rich region, as explained in section **1.3.1**. For the operation of this sort of devices a metal layer that works as ion reservoir (Ti in our case) is needed [Dirkmann2018]. A high temperature and electric field contribute to break the bonds of the molecules generating Frenkel pair defects (a vacancy and an ion, usually oxygen), forming the filament with the vacancies and storing the ions in the metal layer that works as ion reservoir, leading the device to the LRS [Vandelli2015, Vandelli2011, Dirkmann2018]. The bipolar operation is needed in VCM devices as an opposite bias to the one used for set has to be applied to inject the ions stored in the reservoir layer into the dielectric. Then, ions should be field-driven until they reach the CF, where they recombine with the vacancies, destroying the filament. It should be noted that enough ions must be injected in the structure to rupture the filament or RS would not take place [Vandelli2015].

As commented previously, in the section **1.4.2**, the electrodes usually are chosen based on their electrical properties, but in the case of RRAMs they can also affect RS operation. Some of the most common nitride-based electrodes are TiN and TaN [Lee2013, Tang2013b], being TiN the one used in this work, as it has been exposed in appendixes **6.6.3** and **6.6.4**. The sort of electrodes used has to be chosen carefully to help the CF formation in these RRAMs based on vacancies generation since they can affect considerably. For the dielectric materials, HfO2 has been used like in the CBRAM case in the section **3**, mainly because its great potential and its RS promising characteristics.

The kMC algorithm is considered a good technique for reproducing the physics behind the operation of the VCM because its balance between accuracy and computational cost [Wong2012, Dirkmann2018, Vandelli2015]. The design of this tool which takes into account atomic characteristics was developed for studying the variability and reliability of VCM devices. The processes implemented in the kMC algorithm were the generation of vacancies and ions, the migration of particles and the injection of ions in the dielectric from the reservoir layer. It has been taken into account that the ion size is much smaller than that of the vacancy, so its mobility would be quite higher. Following this assumption, only the migration of ions has been implemented in the simulations, as it has been done in previous works [Vandelli2011, Vandelli2011b, Huang2013, Vandelli2015]. It must be remembered that one of the advantages of this tool is that an assumption about the CF shape is not required. The percolation algorithm used in this case is the same as the one previously used in other simulators [Hoshen1976]. Following the FEM approaches exposed in section **1.6.2** and in appendix **6.4**, the Poisson and heat equations have been solved. This is because they are involved in the main failure mechanisms (for instance, thermal vanishing of LRS or permanent dielectric breakdown) and can enhance the generation of vacancies and diffusion of ions or even the injection of ions in the dielectric from the reservoir layer. Regarding the conduction mechanisms during the LRS, an equivalent circuit has been used where ohmic resistance of the CF is implement, in addition to Maxwell and set-up resistances. This equivalent circuit has been exposed in appendix **6.2**. For the case of HRS, a Poole-Frenkel model with effective parameters can be used. The effective parameters can take into consideration many conduction mechanisms that can operate at the same time (Fowler-Nordheim, Direct Tunneling, thermionic emission, etc.), as well as the bigger areas of real devices. A compilation of charge transport mechanism through a dielectric can be found in appendix **6.1**.

4.2. VCM Model

The physics behind the RS in VCM devices is quite different from the one in CBRAMs. While in CBRAMs CFs are made of oxidized atoms that come from the active electrode, in VCMs the CFs are usually made of oxygen vacancies. These vacancies are generated in the dielectric, forming a Frenkel pair defect, that is, a vacancy and an ion. In this way, although the simulator kernel is still based on the kMC algorithm, the processes implemented are quite different.

This simulator has the following characteristics [Aldana2020]:

- The simulator core is a kMC algorithm that implements the generation of Frenkel pairs (a vacancy and an ion), the injection of ions in the dielectric from the reservoir layer and the migration of ions.
- The percolation path is calculated using the Hoshen-Kopelman algorithm [Hoshen1976], explained in appendix **6.3**. For this algorithm it is necessary to take into consideration the virtual electrodes, that is, the clusters in contact with the electrodes.
- The CF can be generated from the pristine state and then several RS can be carried out, therefore no CF shape has to be supposed.
- A 10 nm x 10 nm x 10 nm cubic grid has been used, where mixed boundary conditions were assumed: Neumann (for lateral faces of the cubic grid) and Dirichlet (for the top and bottom electrode) to solve Poisson and heat equations. The approximated oxygen vacancy size is considered as the separation between grid points, 0.5 nm.
- Regarding charge transport mechanisms, an equivalent circuit has been considered for the LRS where the CF resistance, the Maxwell resistance and the set-up resistance have been included. However, a different approach has been used for the HRS, where a Poole-Frenkel emission with effective parameters has been implemented.

The devices used for the calibration of this simulator were memristors based on a TiN/Ti/HfO_2/W stack. These devices were fabricated at the Institut de Microelectrònica de Barcelona IMB-CNM (CSIC) Bellaterra, Spain. The details about fabrication and measurement are given in appendix **6.6.3**. The dielectric layer used was ALD grown HfO_2 10 nm thick. The dielectric thickness coincides with our simulation domain.

The measurements used for the calibration were the following:

- The current-voltage (I-V) curves obtained with ramped voltage sweeps.
- Pulsed input voltage signals.

After calibration, the simulator was used to study the CF evolution under different input voltage signals (ramped and pulsed) to analyze the compactness. The techniques used for studying the compactness were explained in section **2.4**. One of them is based on the study of the number of 2D percolation paths and the other on the number of particles that have a determined number of neighbors.

A video has been developed where a highly detailed exposition of the fabrication process is presented, as well as the measurement characteristics and the main simulation results [videoVCM]. In the first section of the video, a highly detailed explanation for the fabrication and measurement processes is exposed. In **Figure 4.2-1a,** a part of the fabrication process is shown. In this simulator, a grain boundary has been implemented as explained in the video, in the section which corresponds to the **Figure 4.2-1b**. Besides, this tool allows to reproduce the physics behind RS in the VCMs, carrying out a complete RS cycle. In **Figure 4.2-1c** an instant of this process is shown. Also, the CF behavior under pulsed voltage signals has been showed, where some interesting partial SET phenomena can occur within the general RESET process, as it can be seen in **Figure 4.2-1d**. It is important to note that all the data used for this representation were real simulation data, based on physical calculations, thus the representation is not an idealization. That is, the movement of the atoms, the calculation of the electric field or the current have been obtained solving the corresponding equations and using the kMC algorithm. The video was published on 26th of September 2019, and it garnered 1084 views on YouTube until 7rd of September 2020. It should be also noted that the video is highly positioned for Youtube and Google searchs for the keywords "kinetic monte carlo RRAM".

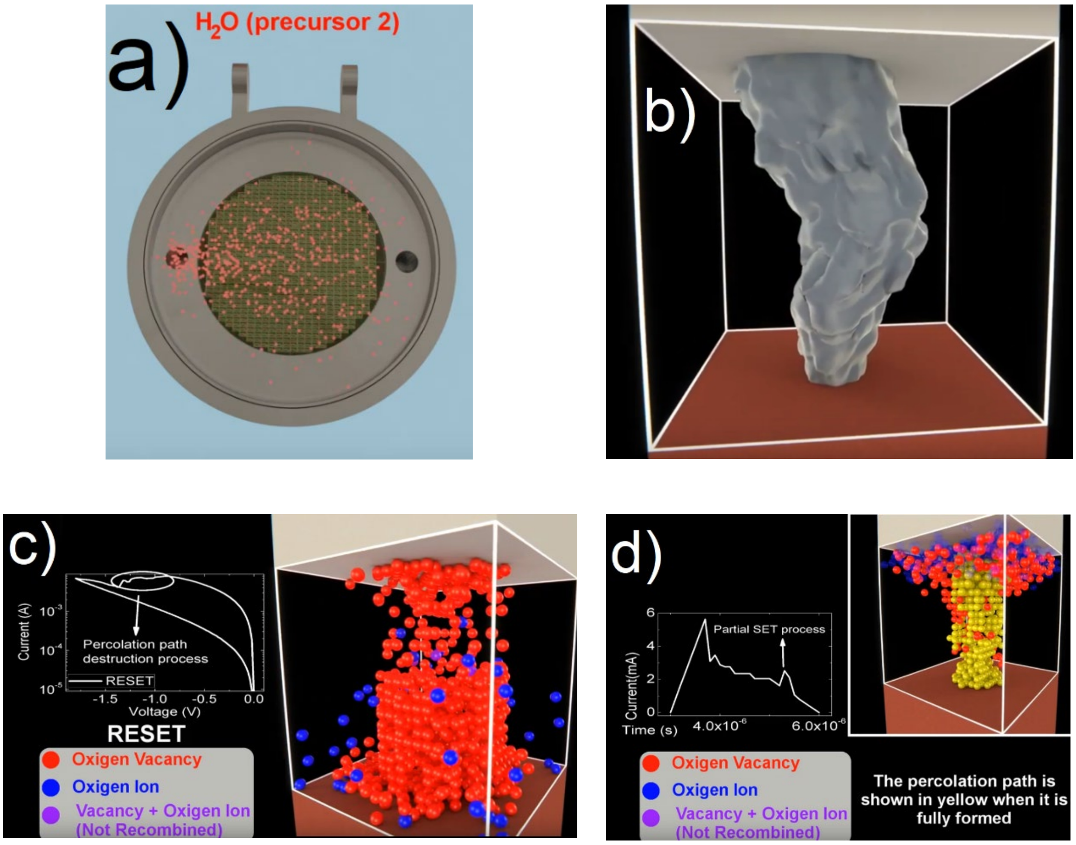

Figure 4.2-1. Figure a shows part of the fabrication process of the VCM (TiN/Ti/HfO_2/W) devices. An example of a grain boundary it can be seen in b). The remnants after a RESET process during a complete RS cycle are shown in c). A partial SET can be found during an overall RESET process when a pulsed voltage signal is applied, as it can be seen in d) [videoVCM].

The contents of this section have been already published [Aldana2020].

S. Aldana et al.

Journal of Physics D: Applied Physics (2020)

Aldana, S., García-Fernández, P., Romero-Zaliz, R., González, M. B., Jiménez-Molinos, F., Gómez-Campos, F., Campabadal, F., Roldán, J. B. (2020). Resistive switching in HfO2 based valence change memories, a comprehensive 3D kinetic Monte Carlo approach. Journal of Physics D: Applied Physics, 53(22), 225106. DOI: https://doi.org/10.1088/1361-6463/ab7bb6

Quality metrics 2019

Data base	Rating	Quartile
Web of Science	Impact factor: 3.169	Q2
Scimago	Scientific journal ranking: 0.899	Q1

Publication citations (2020-09-07)

Google Scholar	Web of Science
1	**0**

Resistive Switching in HfO2 based valence change memories, a comprehensive 3D kinetic Monte Carlo approach

S. Aldana[1], P. García-Fernández[1], R. Romero-Zaliz[3], M.B. González[2], F. Jiménez-Molinos[1], F. Gómez-Campos[1], F. Campabadal[2], J.B. Roldán[1]

[1]*Departamento de Electrónica y Tecnología de Computadores. Universidad de Granada. Facultad de Ciencias. Avd. Fuentenueva s/n, 18071 Granada, Spain. Email: jroldan@ugr.es*

[2]*Institut de Microelectrònica de Barcelona, IMB-CNM (CSIC), Carrer dels Til·lers, s/n. Campus UAB, 08193 Bellaterra, Spain*

[3]*Departamento de Ciencias de la Computación e Inteligencia Artificial. Universidad de Granada. Escuela Técnica Superior de Ingenierías Informática y de Telecomunicación. Calle Periodista Daniel Saucedo Aranda, s/n, 18071 Granada, Spain*

ABSTRACT

A simulation study has been performed to analyze Resistive Switching (RS) phenomena in Valence Change Memories (VCM) based on a HfO2 dielectric. The kernel of the simulation tool consists of a 3D kinetic Monte Carlo (kMC) algorithm implemented self-consistently with the 3D Poisson and heat equations. These VCM devices show filamentary conduction, their RS operation is based on the destruction and regeneration of an ohmic conductive filament (CF) composed of oxygen vacancies. The physics underlying the RS operation is described by means of processes linked to generation of oxygen vacancies, oxygen ion migration and recombination between vacancies and oxygen ions that can be accurately described by using the electric field and temperature distributions in the dielectric. The studied devices consist of TiN/Ti/HfO2/W stacks where the Ti capping layer plays the role of oxygen ion getter material. The simulation tool is useful for obtaining information of internal physical variables, explaining RS dynamics and the CFs evolution from the microscopic viewpoint in terms of their size and shape under different electrical input signals; particularly, the pulsed operation regime has been studied in depth. Furthermore, interesting phenomena, such as partial SETs within overall RESET processes can be accurately reproduced.

Keywords: Resistive switching memory, RRAM variability, valence change memories, simulation tools, conductive filaments, kinetic Monte Carlo.

I.-INTRODUCTION

Resistive Random Access Memories (RRAMs) are electron devices whose resistance changes by means of a proper applied voltage in a non-volatile manner [1-4]. Currently, these devices are drawing the attention of the scientific community because of their promising operation features: non-volatility, scalability, high endurance (>10^{12} R/W cycles) and good retention, their simple structure, low power consumption, short switching times (≈1ns), viability for 3D fabrication and CMOS technology compatibility [1, 2, 4, 5]. This wide set of features makes them good candidates to substitute flash technology for storage class memories.

RRAMs consist of a dielectric layer sandwiched between two electrodes. A classification of these devices in terms of the electrical behavior is possible based on the voltage polarity needed to carry out Resistive Switching (RS): unipolar (SET and RESET produced at the same voltage polarity) [1, 6, 7] and bipolar (SET and RESET produced at different polarities) [5, 8-11]. In the unipolar case the conductive filament (CF) rupture is usually produced by thermal mechanisms; however, for the bipolar case, RS is due to a combination of thermal and electric field driven mechanisms [10, 11].

In the case of the valence change memories (VCM), a metal layer that plays the role of oxygen ion reservoir is generally needed. In VCMs resistive switching has a filamentary nature [10, 12, 13]; we can distinguish three different processes in the CF evolution: i) the forming process, creation of the percolation path starting from a pristine dielectric; ii) the RESET process, i.e., the CF destruction process and iii) the SET process, the CF regeneration over the remnants left by the previous RESET.

RRAM viability has been proved at the device level but also at the integrated circuit level [14, 15, 16]. It is also important to highlight the potential of these devices in the neuromorphic computing landscape, out of the classical Von Neumann architecture paradigm. In particular, since RS physics resembles the internal behavior of biological synapses, they can be used to implement hardware neural networks [1, 17-21].

In order to push forward this technology some hurdles have to be overcome such as variability which is a handicap for massive industrialization. Variability is observed in the forming, RESET and SET voltages and in the resistance distributions when the CF is fully formed (Low Resistance State, LRS) or ruptured (High Resistance State, HRS) [1, 20, 22-25]. There are two sources of variability: extrinsic, which corresponds to the fabrication process and one intrinsic that is linked to the discrete nature of atoms and defects (involved in the CF formation) that lead to the inherent stochasticity of these devices [4, 25]. To deal with this latter issue a deep understanding of the physics behind RS is needed to accurately describe the variability sources. In particular, device resistance variability in the LRS is linked to the CF size and shape that depend on the random oxygen ion motion and vacancies generation within the dielectric. Therefore, the need of simulation tools based on a microscopic model

[2, 7, 10, 11, 13, 26] that describes charge transport, temperature, electric field distributions, etc., is clear.

For many VCMs, dielectric breakdown occurs by the formation of a metal-rich region produced by the application of a voltage that breaks molecule bonds and generate oxygen vacancies, leading the device to the LRS [5, 20]. In this respect, as pointed out in [27], a great concentration of oxygen vacancies lead to a leakage path with metallic properties. In this sort of devices a getter material such as Ti, a layer between the electrode and the dielectric is employed where oxygen ions accumulate [20]. To switch to the HRS, oxygen ions go back to the metal-rich region and recombine with oxygen vacancies partially destroying the CF [5]. It is important to highlight that oxygen ions diffuse much more efficiently than oxygen vacancies [27]. The forming process is important as it determines the shape and the size of the first filament that affect the following SET and RESET processes in a RS series, and therefore the characteristic device features such as stability, retention, endurance, etc. The CF microscopic features determine the device electrical characteristics [5]. In this work, we study this microscopic perspective by means of a new simulator.

In the kinetic Monte Carlo (kMC) landscape, the HRS transition to LRS can be explained at the microscopic level by the CF partial dissolution and regeneration [1, 5, 6, 7, 9, 23, 28, 29, 30, 31, 32]. Sometimes a CF remnant in contact with one of the electrodes is left after a RESET process working like an electrode extension, what is known as a virtual electrode [33]. Taking into consideration that virtual electrodes change throughout the simulation according to the filament evolution, the main gap in the dielectric evolves and consequently the electric field distribution changes [11].

Different flavors of simulation tools can be found in the kMC algorithm realm [1, 5, 7, 10, 11, 12, 20, 23, 30, 32]. Some particular simulation implementations are based on percolation theories [34-36]. The simulation domain determines the geometric features of the simulator, 2D [1, 10, 23, 32] or 3D [5, 7, 11] codes have been developed. In addition, hybrid approaches including 2D and 3D models are performed to optimize the computation burden [20]. The dimensionality and computation time are linked and the trade-off between accuracy and simplicity has to be faced. Some of the kMC simulators are able to reproduce complete RS cycles [5, 7, 11, 23]; nevertheless, others are focused on just reproducing the forming and SET processes [30, 32]. In relation to the solution of the Poisson and heat equations, it has been implemented in 2D and 3D depending on the simulation approach [5, 6, 7, 9, 11, 23, 32]. The charge transport mechanisms considered in the literature can be related to those based on trap-assisted tunneling (TAT) accounting for the defects (vacancies) distribution in the dielectric [5, 20, 23, 32]. Others are linked to Poole-Frenkel emission mechanisms [7, 11] in order to get a macroscopic description of the current and a fast calculation. Some simulation approaches assume ohmic conduction [20, 37] which leads to the calculation of the CF, the set-up and the Maxwell resistances [6, 7, 9, 11] in an equivalent circuit that models the device. Taking into account the issues described above, it is clear that kMC simulators allow the study of RRAM operation facets that cannot be addressed with other kind of tools, such as partial SETs within an overall RESET process, the CF density evolution with the applied voltage, etc.

The issues raised above have to be addressed in a coherent and self-consistent simulation tool to accurately describe RRAM operation. In this manuscript, the fabrication technology and measurement details are explained in section II, the simulation tool is described in section III and the main results and discussion are given in section IV. Finally, the conclusions are presented in section V.

II.-DEVICE DESCRIPTION AND MEASUREMENT

The TiN/Ti/HfO_2/W devices were processed on silicon wafers on a thermally grown 200nm-thick silicon dioxide. Atomic layer deposition (ALD) was employed to grow a 10 nm HfO_2 layer at 225 °C using TDMAH and H_2O as precursors and N_2 as carrier and purge gas. The top and bottom electrodes were deposited by magnetron sputtering. The bottom electrode consists of a 200nm-W layer and the top electrode of a 200nm-TiN and a 10nm-Ti layer acting as oxygen getter material. The resulting structures are square cells of 5 x 5 μm^2 and 15 x 15 μm^2. The device cross section is shown in **Figure 4.2-2**.

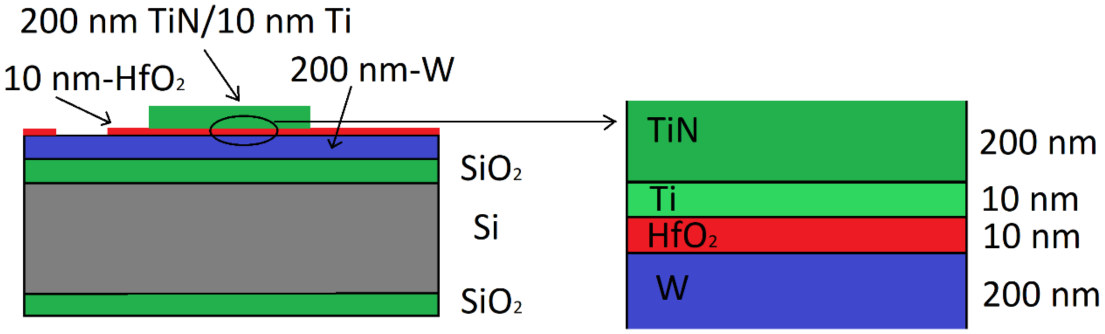

Figure 4.2-2. Cross section of the fabricated and simulated devices. The device stack is enlarged at the right. The Ti capping layer plays the role of an oxygen ion reservoir and the HfO_2 layer is the dielectric where the conductive filament is formed and ruptured.

The measurements (current-voltage (I-V) curves with ramped as well as with pulsed input voltage signals, **Figure 4.2-3**) were performed by means of a HP-4155B semiconductor parameter analyzer (SPA) and a Keysight B1500 SPA equipped with a Waveform Generator and a Fast Measurement unit (WGFMU). The WGFMU can measure IV characteristics synchronized with the applied waveform. The voltage was applied to the TiN/Ti top electrode, while the W bottom electrode was grounded. A software tool implemented in

Matlab was employed to control the instrumentation. A forming process with a current compliance of 100 µA was performed. For the ramped voltage measurements, a RS series with several hundred cycles were obtained for voltages ranging from 0 V to 1 V for the SET process and from 0 V to -1.8 V for the RESET process, see **Figure 4.2-3**. Pulsed voltage signals have also been employed. The device current versus time for four consecutive pulses with alternative positive 1.1 V and negative -1 V (-1.4 V) biases corresponding to SET and RESET processes are shown in **Figure 4.2-3b** (**Figure 4.2-3c**).

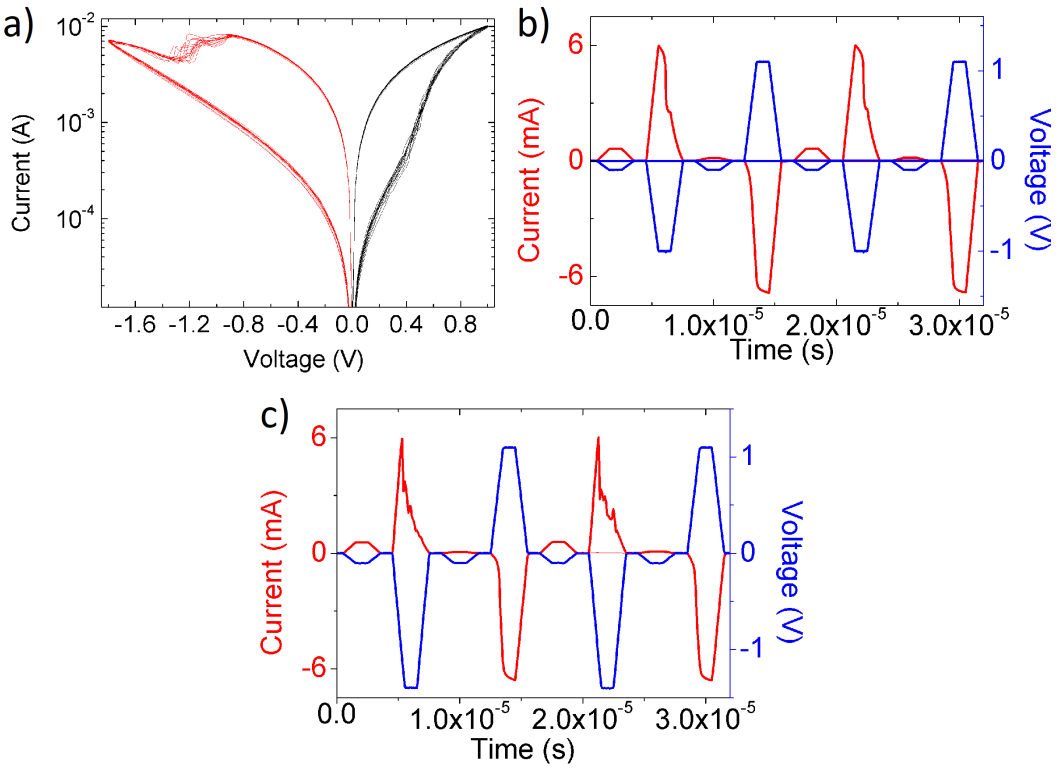

Figure 4.2-3. Typical experimental current for the RRAMs under study. (a) I-V curves for ramped voltage measurements, (b) current versus time for four consecutive pulses with positive (1.1 V) and negative (-1 V) bias corresponding to SET and RESET processes, c) Current versus time for four consecutive pulses with positive (1.1 V) and negative (-1.4 V) bias corresponding to SET and RESET processes.

III.-SIMULATION DESCRIPTION

The simulation tool we present here is based on the Transition State Theory, which serves as a base for the kinetic Monte Carlo (kMC) algorithm [32]. This theory assumes that the system time evolution can be described by the transition between different states. Because of this, a kMC algorithm is chosen to describe the physics behind the operation of the device taking into account the transition rates between the system states [38]. The inclusion of a kMC algorithm allows to reproduce the RRAM operation randomness inherent in RS variability. In this way, it is important to point out that along RS cycles a RESET process determines the following SET as this latter process consist in the CF reconstruction over the CF remnants left in the previous RESET. For a better understanding of the sample fabrication, the simulator fundamentals, its operation and main results, a video supporting material is included [39].

In this work thermal and electrical phenomena are also linked along the RS cycles in a manner similar to previous works [7, 11]. In particular, the simulator includes, besides the 3D kMC algorithm, the solution of the 3D Poisson and heat equations. The electric potential and temperature distributions are obtained for each simulation time step and they are employed in the kMC algorithm (transition rates determination at every grid point within the simulation domain). A finite-difference based methodology is used for solving these equations. The boundary conditions are described in **Figure 4.2-4**.

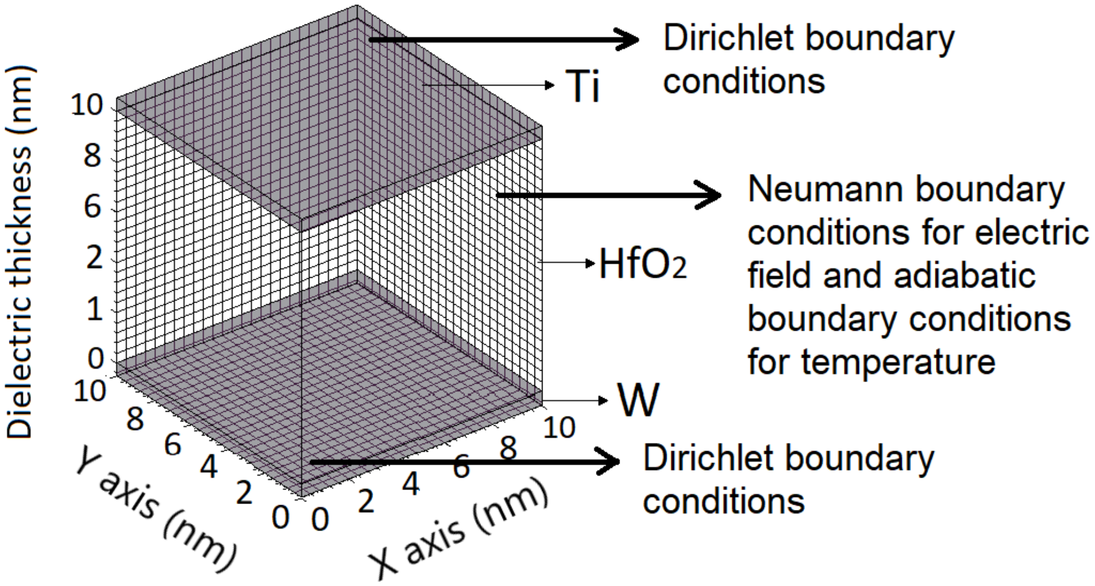

Figure 4.2-4. Representation of the 3D grid used as the simulation domain and specification of the boundary conditions. The electrodes are shown for clarity. Dirichlet boundary conditions were employed for the temperature and electric potential at the interfaces between the electrodes and the dielectric. Neumann boundary conditions were considered for electric potential and temperature distribution at the lateral sides.

For lateral faces Neumann boundary conditions imply adiabatic boundaries for the heat equation since the derivative of the temperature at the boundary is assumed zero. Following previous results from Ref. [20], we use 0.5 nm for the distance between grid points. We have considered a cubic structure for our simulation domain (10 nm x 10 nm x 10nm) that worked reasonable well in most simulations. Other simulation domains could be considered. However, the size of the simulation domain will determine the computational burden linked to the simulation tool, and, therefore, this issue has to be considered carefully.

We do not consider the QPC model in the equivalent circuit employed to describe the device conduction in the LRS since the I-V curves are linear at low voltages. Maxwell and series resistances are also considered.

For the transition rates description, based on the Maxwell-Boltzmann statistics, we use the transition state theory (TST) through Equation 1:

$$\Gamma = \nu \exp\left(-\frac{E_A}{\kappa_B T}\right) \tag{1}$$

Here Γ stands for the transition rate, ν stands for the vibration constant of the particle, E_A is the activation energy (the energy barrier height for the process involved), κ_B the Boltzmann constant and T the temperature [32]. The transition rate corresponds to the inverse of the time needed for a determined process to take place and because of this, it is needed for the estimation of the time step. As the transition rates also depend on the activation energy E_A, and the corresponding barrier height is influenced by the electric potential, it is important to point out its dependence with the electric field.

The iteration time (t) for every simulation step can be obtained with the following calculation:

$$t = -\frac{\ln(1 - randm)}{\sum \Gamma} \tag{2}$$

where randm is a random number between 0 and 1 and the value of the iteration time obtained is the time needed for at least one event to occur [7, 32]. Considering the system memoryless, we can calculate the probability of an action that takes place in t time as follows:

$$P = 1 - \exp(-\Gamma \cdot \mathrm{t}) \tag{3}$$

The RS physics of the devices under study is linked to the generation of oxygen vacancies, recombination between vacancies and oxygen ions and diffusion of the latter.

The generation of oxygen vacancies consist in the breaking of the Hf-O bond leading to the formation of an oxygen vacancy and oxygen ion Frenkel pair (O^{-2} and V^{2+}) [5]. So, the activation energy for the generation process (this is, the Hf-O bond rupture) is:

$$E_G = E_G(F = 0) - b \cdot F(x, y, z) \tag{4}$$

where $F(x, y, z)$ is the electric field in the grid point with x, y and z coordinates, $E_G(F = 0)$ is the activation energy for generation of a Frenkel pair in zero-field conditions (which depends on the material characteristics) and $b = p_0 \cdot [(2 + k)/3]$ is the polarization factor, being p_0 the molecular dipole moment and $k = 21$ the relative dielectric constant [5]. A cylindrical grain boundary (GB) has been implemented where the generation of defects (oxygen vacancies) are more probable, following references [5, 27]. An initial defect random distribution has been generated being more abundant within the GB. The activation energy within the GB is $E_g(F = 0) = 1.4\ eV$ and outside $E_g(F = 0) = 3.6\ eV$. These values are in the line with previous reported energies [40, 41, 42, 43].

With respect to recombination processes, which are intimately linked to CF rupture phenomena, the transition rates do not depend directly on the electric field (the activation energy is E_R=0.3 eV, values in line with this have been published [5]); nevertheless, since oxygen ion diffusion is electric field dependent, the whole CF rupture is affected by the temperature and potential distributions. After the Frenkel pair has been created, oxygen vacancies are assumed to be immobile [5, 26, 27, 42, 44] and oxygen ions are mobile, greatly influenced by the electric field. In our model, once the oxygen ions reach the top electrode, they are captured in the Ti capping layer with a high oxygen affinity [20]. The activation energy for oxygen ion diffusion is obtained as follows:

$$E_D = E_D(F = 0) - k_D \cdot F(x, y, z) \qquad (5)$$

where $E_D(F = 0) = 0.7\ eV$ (as reported by Vandelli et al. [5]) is the activation energy for oxygen ion diffusion in zero-field conditions and k_D is a factor accounting for the field-induced energy barrier reduction [5].

The simulations allow the formation and recombination of oxygen vacancies where, as described above, most of the physical mechanisms involved are included and interconnected. At each time step we employ a 3D percolation path algorithm to detect the formation of conductive filaments. The algorithms for the search of percolation paths (Hoshen-Kopelman in our case) are based on the consideration of classical clusters, where only horizontal and vertical neighbours are considered. Multiple percolative paths are considered in the same simulation domain. These alternative paths have no cells in common with each other. During the forming and SET processes the oxygen ions are stocked up in the Ti layer (top electrode), the electric field reversal produced by the voltage polarity change in the RESET process let the oxygen ions return to the dielectric and increase the recombination processes that lead to the CF rupture.

The current through the device depends on the state of resistance. As mentioned above, one can distinguish between the HRS and the LRS, with different mechanisms of electric conduction. In the LRS state the main conduction mechanism is the ohmic conduction, where Maxwell and in series resistance are considered. In the pristine state, for our case, a functional dependence on the electric field related to a Poole-Frenkel mechanism was observed (dependent on the device area), we made use of effective fitting parameters that allow to reproduce the experimental curves that could also include simultaneously the presence of other dielectric conduction mechanisms depending on the electric field range.

Other dielectric materials could be employed within our simulation tool. In this case, different activation energies for the RS physical processes involved and different physical constants such as the dielectric constant or the electrical and thermal conductivities must be used. In addition, if the physical processes linked to RS in ECM devices are incorporated instead of the ones described here, an ECM simulator should be employed, as reported in [7, 11].

IV.-RESULTS AND DISCUSSION

Once the simulation tool was developed, the first step in its tuning process consisted in the fitting of experimental I-V curves in a RS long series measured under voltage ramps. We were able to reproduce the experimental data of a forming process and complete RS cycles.

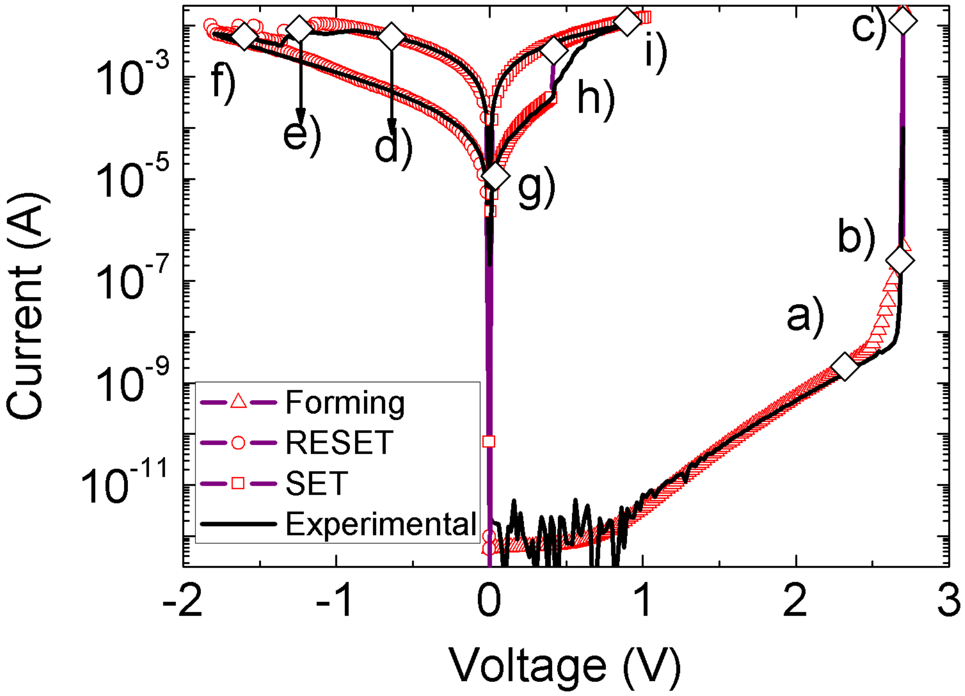

Figure 4.2-5. Typical current versus voltage characteristics of the studied devices. The black line corresponds to the experimental data and the symbols to the simulated ones. The agreement between experimental and simulated data is remarkable. The points marked with rhombus and labelled with letters a) to i) correspond to the snap-shots shown in the **Figure 4.2-6** plotting the state of the conductive filament evolution.

The stages marked in **Figure 4.2-5** are shown in **Figure 4.2-6**, where the CF formation by means of oxygen vacancies can be observed. See the forming process starting from a random distribution of vacancies (pristine device), the CF formation is influenced by the presence of a GB modelled as a vertical cylinder following previous works [27].

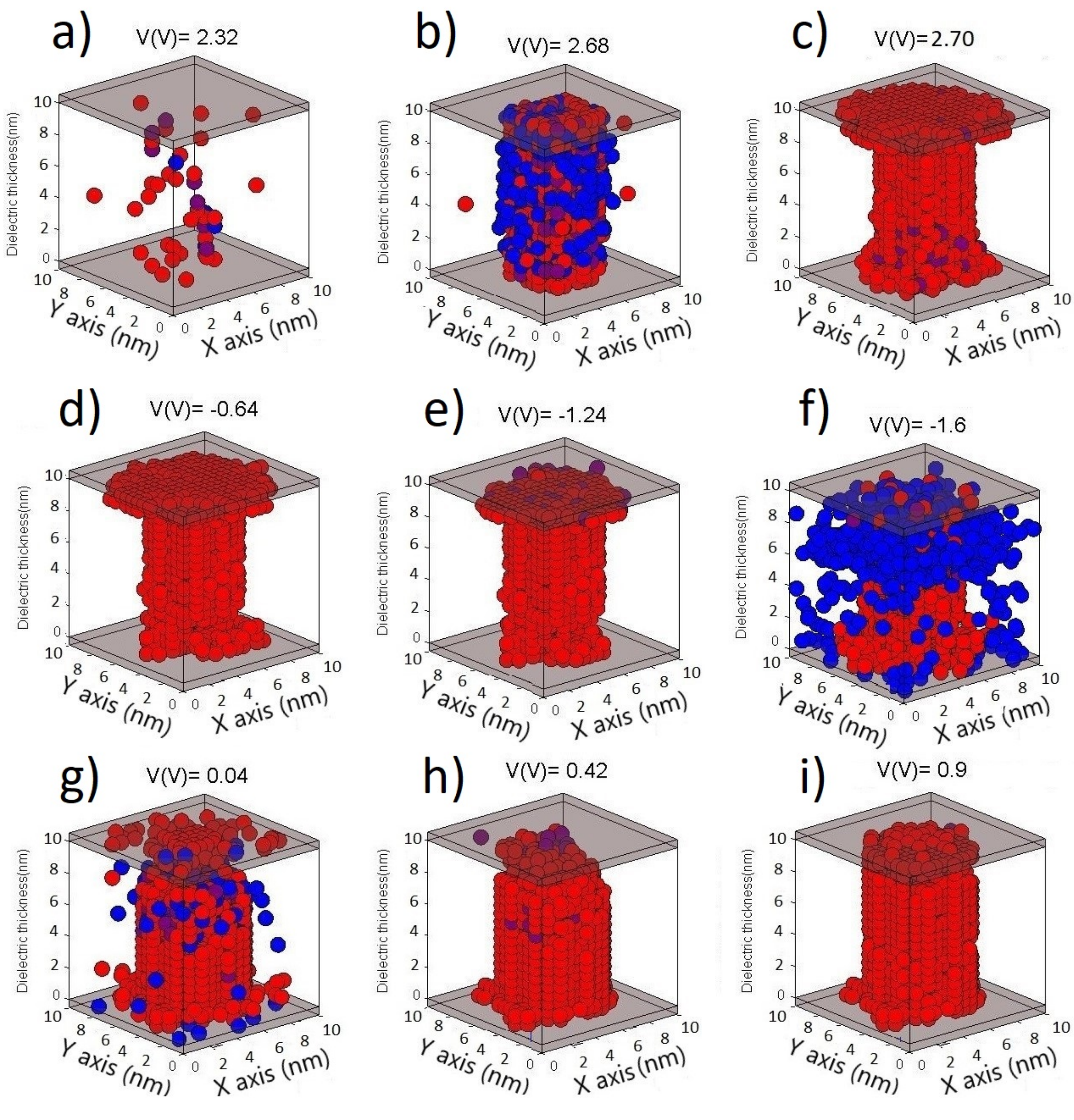

Figure 4.2-6. Simulated device showing the filament configuration corresponding to the labels shown in **Figure 4.2-4**. Different stages of the forming, RESET and SET processes can be seen. The red balls represent oxygen vacancies, the blue ones symbolize oxygen ions and the purple ones represent grid points where both an oxygen vacancy and an oxygen ion (not recombined) are found. Figures a)-c) represent forming process stages, Figures d-f RESET process stages and Figures g)-i) SET process stages that depart from the filament remnants left by the previous RESET process. Once the filament (the percolation path) is fully formed only the red and purple balls are showed.

After the RESET process, the CF remnants left in **Figure 4.2-6f** are the starting point of the following SET process. In addition, pulsed operation is of great interest for these devices since one of their key applications is connected to non-volatile memory circuits. We deal with this issue in **Figure 4.2-7**. The current versus time and the applied voltage signal are shown in **Figure 4.2-7a** for experimental and simulated data showing a good agreement.

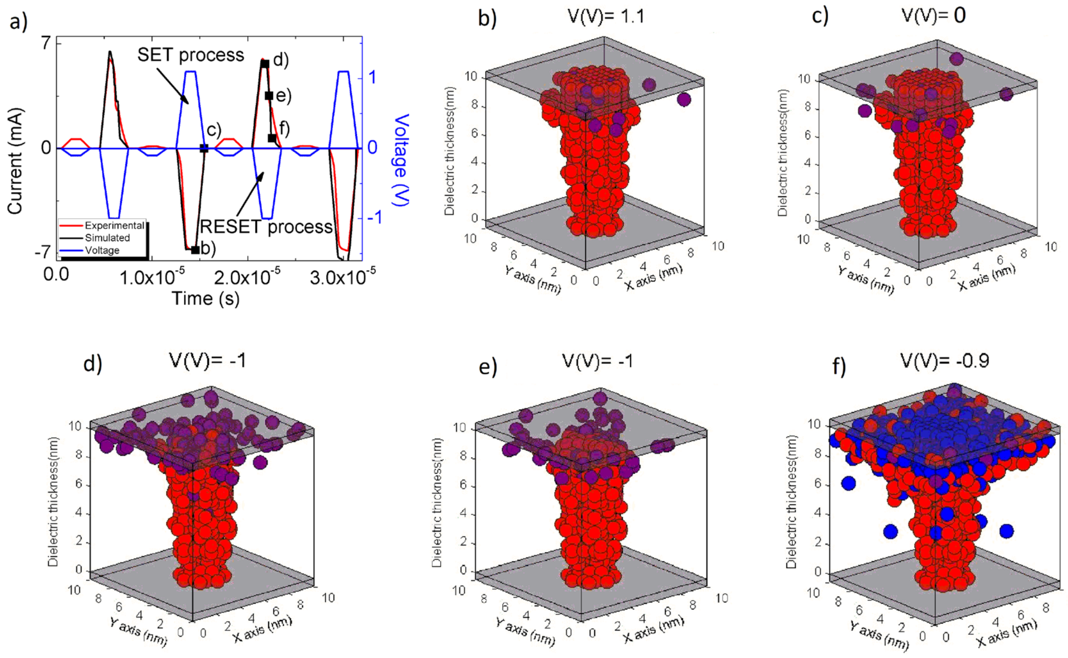

Figure 4.2-7. a) Measured and simulated curves of current versus time for four consecutive pulses with positive (1.1 V) and negative (-1 V) bias corresponding to SET and RESET processes, respectively. Different stages of the simulation performed at different bias voltages are marked with square symbols and the corresponding Figures included from b) to f). The red balls represent oxygen vacancies, the blue ones represent oxygen ions and the purple ones represent grid points where both an oxygen vacancy and ions (not recombined) are found. When the percolation path is fully formed and the electrodes shorted, only red and purple balls are shown; if the filament is ruptured oxygen ions are also plotted.

The simulation of the device in the LRS is shown in **Figure 4.2-7b**, the voltage pulse considered here led to a SET process (1.1 V). Under a decreasing voltage, no great changes occur from **Figure 4.2-7b** to **Figure 4.2-7c** due to the voltage reduction. Then, a RESET process is undergone for negative voltage signals. In this process, the CF rupture is due to a combination of thermal and electric field assisted effects that influence oxygen ion drift and recombination events. **Figure 4.2-7d** shows a filament that it still fully formed; however, the density of oxygen ions has greatly increased in the region close to the Ti-dielectric interface. **Figure 4.2-7e** shows a percolation path with a less dense tip in the region close to the Ti layer. A further step in the RESET process is plotted in **Figure 4.2-7f** where a broken percolation path can be seen, in addition to a great oxygen ion population at the Ti-dielectric interface.

An interesting effect can be seen in some of the RESET processes studied, both at the experimental and simulation levels. It consists of a partial SET process within a long RESET process driven by negative voltages. This effect is shown in **Figure 4.2-8**.

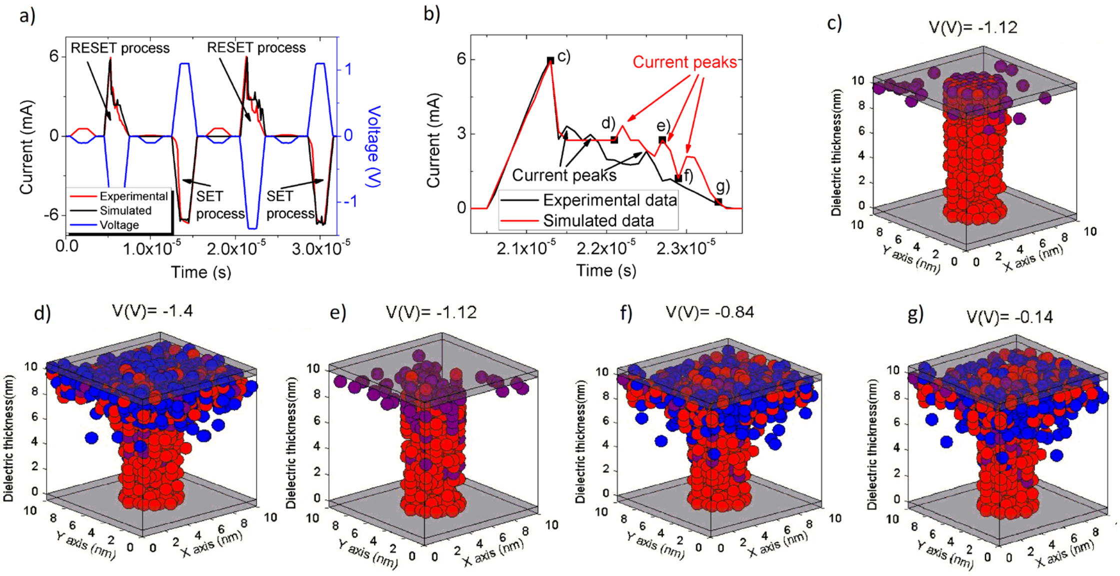

Figure 4.2-8. a) Measured and simulated current versus time curves for four consecutive pulses with positive (1.1 V) and negative (-1.4 V) bias corresponding to SET and RESET processes, respectively. b) Details of the RESET process with a partial SET event. Different stages of the current evolution during the reset pulse are marked with square symbols in **Figure 4.2-8b** that are included in **Figure 4.2-8c** to **Figure 4.2-8g**. The red balls represent oxygen vacancies, the blue ones represent oxygen ions and the purple ones represent grid points where both an oxygen vacancy and ions (not recombined) are found.

Zooming in on **Figure 4.2-8a** we obtain **Figure 4.2-8b**, corresponding to the second RESET process plotted. Different stages of the CF evolution along the RESET process are labelled. The RESET process just starts in a device with a fully formed CF in the previous SET process (**Figure 4.2-8c**). A first RESET event can be seen in **Figure 4.2-8d**, the current drops off in an abrupt manner, as can be seen in **Figure 4.2-8b**. However, the CF is partially reformed again (**Figure 4.2-8e**) due to the stochastic nature of the RS process. In this case, the percolation path is regenerated due to a short generation process embedded within the general RESET process under study. The explanation behind stands upon the fact that once the electric field changes its polarity (the voltage is negative for the RESET process), the oxygen ion flux changes its direction and the number of oxygen ions within the dielectric increases. Therefore, the number of recombination events rises. In addition, depending on the electric field magnitude (whatever the polarity) the oxygen vacancy generation rate could rise. So, there are two competing mechanisms: generation and recombination due to an increased concentration of oxygen ions and oxygen vacancy generation, the former can lead to partial filament growth and eventually to a complete percolation path formation that shorts the electrodes. When the percolation path is at the verge of rupture, different formation and destruction processes can occur till the overall process advances. These effects, seen experimentally, can only be described within a kMC simulation approach. Other numerical procedures based just on the solution of partial differential equations [6, 23, 42, 45] cannot be employed to analyse these phenomena. Due to these partial SET processes there are temporal current increases, in our case, as highlighted above, these current peaks can be seen both in the experiments and in the simulations. See that the RESET process goes on in spite of the partial SET process shown in **Figure 4.2-8e**, as shown in **Figure 4.2-8f** and **4.2-8g**. Since a net oxygen ion flux enters the dielectric from the Ti capping layer, the CF rupture point is close to this electrode.

In addition, different internal magnitudes obtained with the simulation tool presented here can be employed to analyse the operation features of the devices under study. As an example, we have simulated a RESET process (**Figure 4.2-9**) where the compactness of the conductive filaments is analysed.

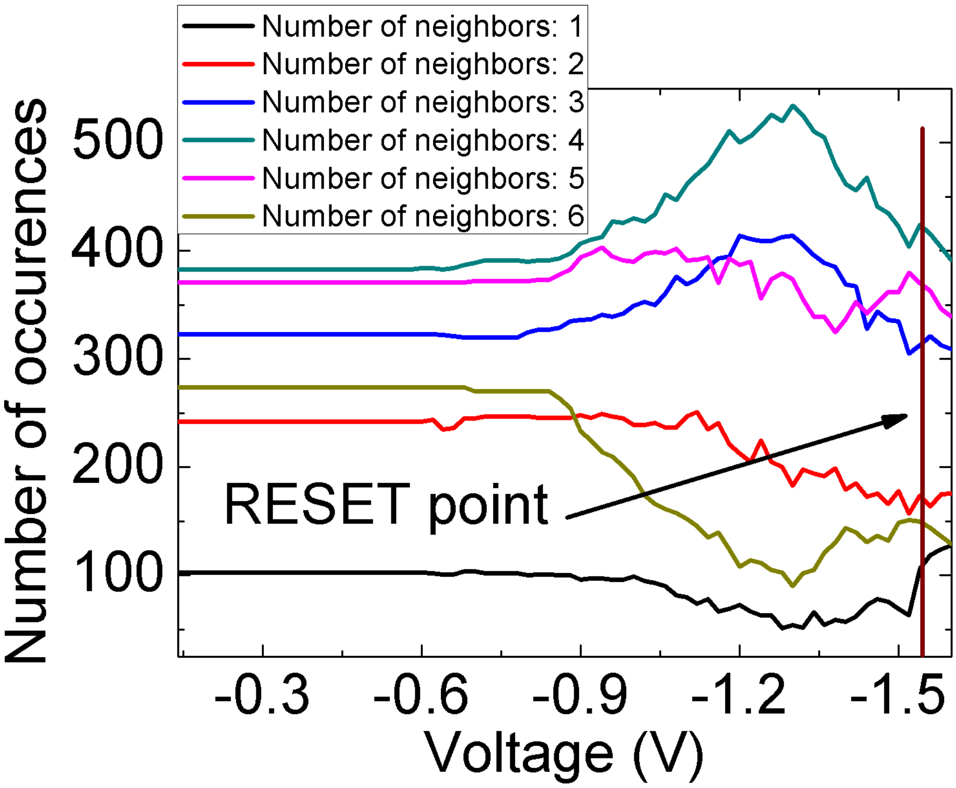

Figure 4.2-9. Number of occurrences of oxygen vacancies with a different number of surrounding neighbours in the dielectric versus voltage along a RESET curve. These magnitudes can be employed to describe the CF compactness and the device resistance [46].

In **Figure 4.2-9** we show the evolution of the number of occurrences (NO) for the neighbor number of each oxygen vacancy within the dielectric along a RESET curve. The NO for the number of neighbors, being 6 the maximum number of neighbors in our cubic grid, describes the filament compactness at each voltage during the simulation. In this respect, the higher the NO for 5 and 6 neighbors the more compact the CF and obviously the lower the CF resistance.

In the simulation linked to **Figure 4.2-9**, the CF rupture takes place at $V = -1.54\,V$ (reset voltage). At low negative voltages, the formed conductive filament has a morphology that remains stable for the first part of the reset curve. The NO for the 4-6 neighbors are higher than for 1-3 neighbors. At $V = -1.32\,V$ there are some transfers from the occurrences of higher values of neighbors to the lower ones. The most likely change is toward the occurrence corresponding to a vacancy count with one neighbor less. This is due to the oxygen ion population rise during RESET and so, the increase in the recombination events. As shown in **Figure 4.2-9**, the number of occurrences for the case with 6 neighbors drops off. For the 5 neighbors case there is a slight reduction, while for the 4 and 3 neighbors case an increase can be seen. Therefore, the transference from the 6 neighbor's case to the 5 one is approximately the same than from the 5 neighbor's case to the 4 and 3. Besides, one would expect a reduction of the NO of one neighbor that is not found. This is due to the rise of NO of one neighbor produced by the loss of one vacancy in the case of 2 neighbors that is indeed reduced.

These effects produce the CF compactness reduction and eventually the CF rupture (the RESET, which is marked in **Figure 4.2-9**). The NO for the higher number of neighbors is linked to the CF density of vacancies and it is also correlated with the device resistance as shown in Ref. [46]. The study of these data can help to understand the device resistance evolution in a complete cycle of resistive switching, and also the inherent RS variability of these devices.

Figure 4.2-10 shows information related to the destruction of percolation paths (conductive filaments) in a RESET process. In our simulation approach, a 3D scheme, the percolation paths are 3D. However, it is important to highlight that a 3D percolation path can exist without including even a single 2D percolation path in the X axis or Y axis cuts of the 3D CF. This fact is highlighted in **Figure 4.2-10** were the number of 2D percolation paths for slices in the X (Y) axis are shown in black (red).

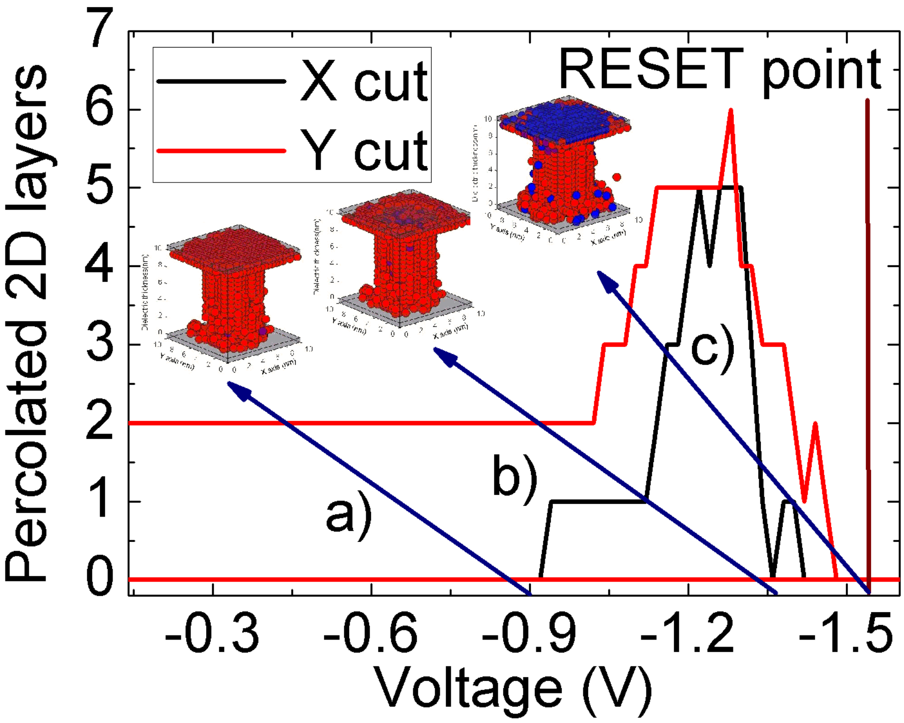

Figure 4.2-10. Number of 2D percolation paths (in the 3D simulation domain) corresponding to CF slices in the X axis and also in the Y axis versus voltage for a reset process. Along the simulation we can find an unstable 3D percolation with few 2D percolation paths a); b) the number of 2D percolation paths is reduced and c) CF is broken.

Along the simulation there are some points labelled with a, b and c which show the evolution of the filament along the RESET process. Around $V = -1.5\ V$ there are no 2D percolated layers but there is still a 3D percolation path. For a slightly more negative voltage the 3D percolation path is broken. It can be seen that after $V = -0.9\ V$ there is an increasing number of 2D percolation paths due to the generation of some vacancies because of the high electric field. The two competing mechanisms reported above are behind the rise and further fall of the number of 2D percolation path prior to the CF destruction.

It is also important to notice, as shown in **Figure 4.2-10** point c), that the 3D percolation path is ruptured after all the 2D percolated layers vanished. Therefore, when using a kMC 2D simulation scheme, special care has to be taken in the study of CF formation, i.e., percolation paths formation, since a 2D simulation approach is substantially different from a more computationally heavy 3D scheme.

V.-CONCLUSIONS

TiN/Ti/HfO_2/W RRAMs have been fabricated, characterized and analysed with the simulation tool presented in this work. The simulator reproduces the operation of Valence Change Memories showing a good agreement between experimental data and simulated results. The 3D heat and Poisson equations are solved in the simulation tool self-consistently. The temperature and potential distributions are needed to correctly describe the physical mechanisms governing the device operation, mainly the generation of oxygen vacancies and ions, the motion of oxygen ions and the recombination processes in the dielectric layer. Experimental data were used to tune the simulator. The conductive filament evolution with applied voltage has been studied along the forming, RESET and SET processes both in voltage ramps and pulsed operation regimes. In the latter case, an interesting phenomenon of a partial SET during a RESET process has been described. An analysis of the conductive filament compactness has been performed by studying the number of neighbors of oxygen vacancies within filaments. Finally, a study of the features of the percolation paths formed both in 2D and 3D during the reset process was presented.

VI. - ACKNOWLEDGMENTS

The authors thank the support of the Spanish Ministry of Science, Innovation and Universities and the FEDER program through projects TEC2017-84321-C4-1-R, TEC2017-84321-C4-3-R and ENE2016-80944-R. This work has made use of the Spanish ICTS Network MICRONANOFABS.

REFERENCES

[1] F. Pan, S. Gao, C. Chen, C. Song, F. Zeng, "Recent progress in resistive random access memories: materials, switching mechanisms and performance", Materials Science and Engineering, 83, pp. 1-59, 2014.

[2] R. Degraeve, A. Fantini, N. Raghavan, L. Goux, S. Clima, Y. Chen, A. Belmonte, S. Cosemans, B. Govoreanu, D. Wouters, P. Roussel, G. Sankar Kar, G. Groeseneken, M. Jurczak, “Hourglass concept for RRAM: a dynamic and statistical device model”, Proceedings of the 21th International Symposium on the Physical and Failure Analysis of Integrated Circuits (IPFA). IEEE, p. 245-249, 2014.

[3] M. A. Villena, J. B. Roldán, F. Jiménez-Molinos, E. Miranda, J. Suñé, M. Lanza, “SIM2RRAM: A physical model for RRAM devices simulation”, Journal of Computational Electronics, 16(4), 1095-1120, 2017.

[4] Lanza, M., Wong, H. S. P., Pop, E., Ielmini, D., Strukov, D., Regan, B. C., ... & Belmonte, A. (2019). Recommended methods to study resistive switching devices. Advanced Electronic Materials, 5(1), 1800143.

[5] A. Padovani, L. Larcher, O. Pirrotta, L. Vandelli, G. Bersuker, “Microscopic Modeling of HfO x RRAM Operations: From Forming to Switching”, IEEE Transactions on Electron Devices, 62(6), pp. 1998-2006, 2015.

[6] M. A. Villena, M. B. González, F. Jiménez-Molinos, F. Campabadal, J. B. Roldán, J. Suñé, E. Romera, E. Miranda, “Simulation of thermal reset transitions in RRAMs including quantum effects”, Journal of Applied Physics, vol. 115, pp. 214504, 2014.

[7] S. Aldana, P. García-Fernández, A. Rodríguez-Fernández, R. Romero-Zaliz, M. B. González, F. Jiménez-Molinos, F. Campabadal, F. Gómez-Campos, J. B. Roldán, “A 3D kinetic Monte Carlo simulation study of resistive switching processes in Ni/HfO2/Si-n+-based RRAMs”, Journal of Physics D: Applied Physics, 50(33), 335103, 2017.

[8] S. Yu, X. Guan, H. S. P. Wong, "On the switching parameter variation of metal oxide RRAM—Part II: Model corroboration and device design strategy", IEEE Transactions on Electron Devices, 59, pp. 1183-1188, 2012.

[9] M. A. Villena, F. Jiménez-Molinos, J. B. Roldán, J. Suñé, S. Long, X. Lian, F. Gámiz, M. Liu, “An in-depth simulation study of thermal reset transitions in resistive switching memories”, Journal of Applied Physics, 114(14), pp. 144505, 2013.

[10] S. Menzel, P. Kaupmann, R. Waser, “Understanding filamentary growth in electrochemical metallization memory cells using kinetic Monte Carlo simulations”, Nanoscale, 7, 12673, 2015.

[11] S. Aldana, J. B. Roldán, P. García-Fernández, J. Suñe, R. Romero-Zaliz, F. Jiménez-Molinos, S. Long, F. Gómez-Campos, M. Liu, “An in-depth description of bipolar resistive switching in Cu/HfOx/Pt devices, a 3D kinetic Monte Carlo simulation approach”, Journal of Applied Physics, 123(15), 154501, 2018.

[12] S. Menzel, B. Klopstra, C. Kügeler, U. Böttger, G. Staikov, R. Waser, “A simulation model of resistive switching in electrochemical metallization memory cells (ECM)”, MRS Online Proceedings Library Archive, 1160, 101–106, 2009.

[13] L. Larcher, A. Padovani, L. Vandelli, “A simulation framework for modeling charge transport and degradation in high-k stacks”, Journal of Computational Electronics, 12(4), 658-665, 2013.

[14] A. Kawahara, R. Azuma, Y. Ikeda, K. Kawai, Y. Katoh, Y. Hayakawa, K. Tsuji, S. Yoneda, A. Himeno, K. Shimakawa, T. Takagi, T. Mikawa, K. Aono, “An 8 Mb Multi-

Layered Cross-Point ReRAM Macro With 443 MB/s Write Throughput”, IEEE Journal of Solid-State Circuits, 48(1), 178-185, 2013.

[15] J. Zahurak, K. Miyata, M. Fischer, M. Balakrishnan, S. Chhajed, D. Wells, Li Hong, A. Torsi, J. Lim, M. Korber, K. Nakazawa, S. Mayuzumi, M. Honda, S. Sills, S. Yasuda, A. Calderoni, B. Cook, G. Damarla, H. Tran, B. Wang, C. Cardon, K. Karda, J. Okuno, A. Johnson, T. Kunihiro, J. Sumino, M. Tsukamoto, K. Aratani, N. Ramaswamy, W. Otsuka, K. Prall, "Process integration of a 27nm, 16Gb Cu ReRAM", 2014 IEEE International Electron Devices Meeting, IEEE, 6.2.1-6.2.4, 2014, doi: 10.1109/IEDM.2014.7046994

[16] T.Y. Liu, T. H. Yan, R. Scheuerlein, Y. Chen, J. K. Lee, G. Balakrishnan, G. Yee, H. Zhang, A. Yap, J. Ouyang, T. Sasaki, S. Addepalli, A. Al-Shamma, C.Y. Chen, M. Gupta, G. Hilton, S. Joshi, A. Kathuria, V. Lai, D. Masiwal, M. Matsumoto, A. Nigam, A. Pai, J. Pakhale, C. H. Siau, X. Wu, R. Yin, L. Peng, J. Y. Kang, S. Huynh, H. Wang, N. Nagel, Y. Tanaka, M. Higashitani, T. Minvielle, C. Gorla, T. Tsukamoto, T. Yamaguchi, M. Okajima, T. Okamura, S. Takase, T. Hara, H. Inoue, L. Fasoli, M. Mofidi, R. Shrivastava, K. Quader, “A 130.7-mm^2 2-Layer 32-Gb ReRAM Memory Device in 24-nm Technology”, IEEE International Solid-State Circuits Conference Digest of Technical Papers, 210-211, 2013.

[17] M. Ignatov, M. Ziegler, M. Hansen, A. Petraru, H. Kohlstedt, “A memristive spiking neuron with firing rate coding”, Frontiers in neuroscience, 9, 376, 2015.

[18] M. Ignatov, M. Hansen, M. Ziegler, H. Kohlstedt, “Synchronization of two memristively coupled van der Pol oscillators”, Applied Physics Letters, 108(8), 084105, 2016.

[19] M. Hansen, F. Zahari, M. Ziegler, H. Kohlstedt, “Double-barrier memristive devices for unsupervised learning and pattern recognition”, Frontiers in neuroscience, 11, 91, 2017.

[20] S. Dirkmann, J. Kaiser, C. Wenger, T. Mussenbrock, “Filament Growth and Resistive Switching in Hafnium Oxide Memristive Devices”, ACS applied materials & interfaces, 10(17), 14857-14868, 2018.

[21] V. Milo, C. Zambelli, P. Olivo, E. Pérez, M.K. Mahadevaiah, O.G. Ossorio, C. Wenger, D. Ielmini, “Multilevel HfO2-based RRAM devices for low-power neuromorphic networks”, APL Materials, 7, p. 081120, 2019

[22] R. Waser, “Nanoelectronics and Information Technology”, 3rd ed., Wiley-VCH, Berlin, 2012.

[23] X. Guan, S. Yu, H. S. P. Wong, "On the switching parameter variation of metal-oxide RRAM—Part I: Physical modeling and simulation methodology", IEEE Transactions on Electron Devices, 59, pp. 1172-1182, 2012.

[24] M. Lanza, “A Review on Resistive Switching in High-k Dielectrics: A Nanoscale point of View Using Conductive Atomic Force Microscope”, Materials 7, pp. 2155-2182, 2014.

[25] R. Degraeve, A. Fantini, N. Raghavan, L. Goux, S. Clima, B. Govoreanu, A. Belmonte, D. Linten, M. Jurczak, “Causes and consequences of the stochastic aspect of filamentary RRAM”, Microelectronic Engineering, 147, pp. 171-175, 2015.

[26] L. Vandelli, A. Padovani, G. Bersuker, D. Gilmer, P. Pavan, L. Larcher, “Modeling of the forming operation in HfO2-based resistive switching memories”, 2011 3rd IEEE International Memory Workshop (IMW), (pp. 1-4), IEEE, 2011.

[27] G. Bersuker, D. C. Gilmer, D. Veksler, P. Kirsch, L. Vandelli, A. Padovani, L. Larcher, K. McKenna, A. Shluger, V. Iglesias, M. Porti and M. Nafría, “Metal oxide resistive memory switching mechanism based on conductive filament properties”, Journal of Applied Physics, 110, 124518, 2011.

[28] Y. C. Yang, F. Pan, Q. Liu, M. Liu, F. Zeng, “Fully room-temperature-fabricated nonvolatile resistive memory for ultrafast and high-density memory application”, Nano letters, 9, pp. 1636-1643, 2009.

[29] T. Tsuruoka, K. Terabe, T. Hasegawa, M. Aono, “Forming and switching mechanisms of a cation-migration-based oxide resistive memory”, Nanotechnology, 21(42), pp. 425205, 2010.

[30] F. Pan, S. Yin, V. Subramanian, "A detailed study of the forming stage of an electrochemical resistive switching memory by KMC simulation", IEEE Electron Device Letters, 32, pp. 949-951, 2011.

[31] W. Lu, D. S. Jeong, M. Kozicki, R. Waser, “Electrochemical metallization cells--blending nanoionics into nanoelectronics”, MRS bulletin, 37, pp. 124, 2012.

[32] J. Guy, G. Molas, P. Blaise, M. Bernard, A. Roule, G. Le Carval, V. Delaye, A. Toffoli, G. Ghibaudo, F. Clermidy, B. De Salvo, L. Perniola, “Investigation of Forming, SET, and Data Retention of Conductive-Bridge Random-Access Memory for Stack Optimization”, IEEE Transactions on Electron Devices, *62*(11), pp. 3482-3489, 2015.

[33] R. Waser, M. Aono, “Nanoionics-based resistive switching memories”, Nature Materials, 6, 833-840, 2007.

[34] S. C. Chae, J. S. Lee, S. Kim, S. B. Lee, S. H. Chang, C. Liu, B. Kahng, H. Shin, D. Kim, C. U. Jung, S. Seo, M. Lee, T. W. Noh, “Random circuit breaker network model for unipolar resistance switching”, Advanced Materials, 20(6), 1154-1159, 2008.

[35] N. Raghavan, K. L. Pey, X. Wu, W. Liu, M. Bosman, “Percolative model and thermodynamic analysis of oxygen-ion-mediated resistive switching”, IEEE Electron Device Letters, 33(5), 712-714, 2012.

[36] S. Long, X. Lian, C. Cagli, L. Perniola, E. Miranda, M. Liu, J. Suñé, “A model for the set statistics of RRAM inspired in the percolation model of oxide breakdown”, IEEE Electron Device Letters, 34(8), 999-1001, 2013.

[37] E. Miranda, D. Jimenez, J. Suñé, “The quantum point-contact memristor”, IEEE Electron Device Letters, 33(10), 1474-1476, 2012.

[38] A. F. Voter, "Introduction to the kinetic Monte Carlo method", Radiation Effects in Solids, Springer Netherlands, pp. 1-23, 2007.

[39] https://www.youtube.com/watch?v=OLk4eJNc_Y8

[40] B. Gao, J. F. Kang, H. W. Zhang, B. Sun, B. Chen, L. F. Liu, ... & H. Y. Yu, “Oxide-based RRAM: Physical based retention projection”, Proceedings of the European Solid State Device Research Conference (pp. 392-395), 2010.

[41] L. Vandelli, A. Padovani, L. Larcher, G. Bersuker, J. Yum, P. Pavan, “A physics-based model of the dielectric breakdown in HfO 2 for statistical reliability prediction”, 2011 International Reliability Physics Symposium, (pp. GD-5), IEEE, 2011.

[42] P. Huang, X. Y. Liu, B. Chen, H.T. Li, Y. J. Wang, Y.X. Deng, K.L. Wei, L. Zeng, B. Gao, G. Du, X. Zhang, J.F. Kang, "A Physics-Based Compact Model of Metal-Oxide-Based RRAM DC and AC Operations", IEEE Transactions on Electron Devices, 60(12), 4090-4097, 2013.

[43] A. Padovani, L. Larcher, G. Bersuker, P. Pavan, “Charge transport and degradation in HfO 2 and HfO x dielectrics”, IEEE Electron Device Letters, 34(5), 680-682, 2013.

[44] F.M. Puglisi, P. Pavan, L. Larcher, A. Padovani, “Statistical analysis of random telegraph noise in HfO2-based RRAM devices in LRS”, Solid-State Electronics, 113, 132-137, 2015.

[45] G. González-Cordero, J. B. Roldan, F. Jiménez-Molinos, J. Suñé, S. Long, M. Liu, “A new compact model for bipolar RRAMs based on truncated-cone conductive filaments—a Verilog-A approach”, Semiconductor Science and Technology, 31(11), 115013, 2016.

[46] S. Aldana, P. García-Fernández, R. Romero-Zaliz, F. Jiménez-Molinos, F. Gómez-Campos, J.B. Roldán, "Analysis of conductive filament density in resistive RAMs, a 3D Kinetic Monte Carlo approach", Journal of Vacuum Science and Technology B, 36, p. 62201, 2018.

4.3. Data retention tests in VCM

When the simulator was fully developed, was used for doing some retention data test in some bunch of VCM memories. The simulator was the same presented in section **4.2**, but adapted to carry out the forming process and then, in almost zero-field conditions, bake the system at high temperatures for long times (several hours). As the time used by the simulator adapts to the time needed for at least occur an event, in this almost zero-field condition, the step time is quite long.

During the simulation, the processes are thermal triggered and this is which makes evolve the CF. In this sense, as higher the temperature the more probable to occur the events and so accelerate the degradation of the CF. The device failure is considered when the current is below the target level established that would be different depending on the applications for what would be destined.

For this study have been compared the experimental data with simulated ones for the cumulative distribution function (CDF) of the current measured for different times and temperatures. Also, the CDF with the failure times of the devices have been compared with good results. Besides, some interesting information about the internal structure of the CFs can be studied with this kind of computational tools. In this way, the evolution of the density and compactness have been studied along the simulations. The way of study the compactness has been exposed in section **3.4**, that is, studying the number of 2D percolation path within the 3D CF and the number of particles that have a determined number of neighbors in the surroundings. In that section, also the way of calculate the density has been presented.

The contents of this section have been already published [Aldana2020b].

S. Aldana et al.

Semiconductor Science and Technology (2020)

Aldana, S., Pérez, E., Jimenez-Molinos, F., Wenger, C., & Roldan, J. B. (2020). Kinetic Monte Carlo analysis of data retention in Al: HfO2-based resistive random access memories. Semiconductor Science and Technology. DOI: https://doi.org/10.1088/1361-6641/abb072

Quality metrics 2019

Data base	Rating	Quartile
Web of Science	Impact factor: 2.361	Q2
Scimago	Scientific journal ranking: 0.79	Q1

Publication citations (**2020-09-07**)

Google Scholar	Web of Science
0	**0**

Kinetic Monte Carlo analysis of data retention in Al:HfO_2-based resistive random access memories

S. Aldana[1], E. Pérez[2], F. Jiménez-Molinos[1], C. Wenger[2,3], J.B. Roldán[1]

[1]Departamento de Electrónica y Tecnología de Computadores. Universidad de Granada. Facultad de Ciencias. Avd. Fuentenueva s/n, 18071 Granada, Spain. Email: jroldan@ugr.es

[2]IHP-Leibniz-Institut für innovative Mikroelektronik. Frankfurt (Oder), Germany

[3]BTU Cottbus-Senftenberg. Cottbus, Germany

ABSTRACT

Kinetic Monte Carlo RRAM simulations are used to understand different retention experiments performed at several temperatures. The physics behind resistive switching allows to explain experimental results, in particular the degradation of the conductive filaments with temperature. It is observed that competing mechanisms control resistive switching in this type of experiments and the thermal dependencies involved are key to explain the measurements. Besides, the simulation approach allows to analyze the existence of percolation paths in the device dielectric and the conductive filament density and compactness. Finally, the key physical mechanisms are detected and some clues related to the retention performance and possible technology improvements are unveiled.

Keywords: Resistive switching memory, valence change memories, simulation tools, conductive filaments, kinetic Monte Carlo, data retention.

I.-INTRODUCTION

One of the emerging devices that shows higher potential in the non-volatile memory realm is the Resistive Random Access Memory (RRAM); these devices are candidates for integrated storage class memory because of their non-volatility and short read/write latencies [1-10]. Some promising and operative non-volatile memory chips based on RRAMs have already been fabricated and tested [11]. In addition, their use as artificial synapses that mimic their biological counterparts is also focusing great research efforts in the neuromorphic computing context [12, 13, 14, 15]. The fabrication of hardware neural networks based on resistive switching (RS) devices shows the way for low power and highly scalable artificial intelligence chips [16-20].

RRAMs present a good degree of scalability and endurance; moreover, they also show low power consumption and viability for 3D fabrication with CMOS technology compatibility [3, 4, 6, 10]. In terms of data retention these devices have shown a great potential [4, 10, 21], although, more studies are needed. Promising devices with great potential for non-volatile memory applications have been reported in the past, such as those based on Ta/TaO_x/TiO_2/Ti stacks that showed endurance data above 1012 cycles [22] and Pt/TaO_x/Pt devices, with retention times above 10 years [23]. Additional interesting comparatives can be found in [4, 10].

Many of the RRAM devices reported in the literature can be included in two great groups: Conductive Bridge RAMs (CBRAMs) and Valence Change Memories (VCMs). CBRAMs are based on redox processes. Metal ions oxidized from the electrochemically active electrode migrate in the dielectric and form percolation paths that short the electrodes producing an important resistance change [1, 5, 4, 10, 24, 25, 26]. Regarding VCMs, they are based on vacancies and ions generation due to the rupture of molecule bonds by the combined effect of the electric field and the temperature [2, 4, 10, 27, 28, 29]. The regions with high density of vacancies show ohmic conduction features.

The RRAM devices fabricated and measured for this study are valence change memories (VCM). In these devices resistive switching (RS) has a filamentary nature [2, 4, 10, 30, 31] where an initial forming process is needed to form a metallic-like percolation path (a conductive filament, CF) through the dielectric. The CF formation is linked to the accumulation of oxygen vacancies, in this process some oxygen ions are moved away from the dielectric layer [6, 9, 31, 32]. Later on, RESET processes where the CF is ruptured (high resistivity state, HRS) and SET processes (CF regeneration over the remnants of the previous RESET to lead to the low resistivity state, LRS) are employed to change the device resistivity [10, 33]. In this sense, for a correct device operation, an oxygen storage layer above the dielectric layer is necessary. Oxygen is stored at the Ti/dielectric interface until it is released again to be recombined with vacancies, carrying out the RESET process [6, 9, 31, 32].

In order to enhance RRAM technology for massive industrialization some difficulties have to be overcome such as variability and data retention [4, 10, 34]. The forming, RESET and SET voltages show variability as well as the device resistance states. Retention is connected to the ability to keep the programmed resistance state intact for a long time in a conventional device operation regime. Retention is in the kernel of the time-voltage dilemma in memory circuits since, as a general rule, long retention times and short write times in combination with write and read voltages in a comparable range (the lower the voltage values, the lower the power consumption, which is crucial in the context of mobile electronic devices) represents a difficult engineering problem [35]. There are several RRAM simulation techniques with different characteristics in terms of accuracy and computational burden. Each one has advantages and disadvantages. Continuum models offer an average description of the device operation with a low computational cost (they are mostly based in the self-consistent solution of several partial differential equations); compact models allow the simulation of complete circuits [7, 10]. Ab initio techniques, as they are based on first principles, allow an accurate physical description at a high computational cost [7, 10, 36]. The need to deepen on the issues reported above leads us to use reasonably accurate simulation tools that can still carry out complete RS cycles. In this sense, some microscopic models can be a good option [2, 4, 5, 31, 37-39], as they describe in detail RRAM charge transport, the temperature and electric field distributions and resistive switching processes with reasonable simulation times. These microscopic models (usually based on kinetic Monte Carlo algorithms), after the corresponding tuning, can deal with the study of complex devices, such as RRAMs with bilayer and trilayer dielectrics [40]. These tools are flexible enough to adapt to these structures by modeling the effects of the different material employed in the device fabrication.

In the kinetic Monte Carlo (kMC) landscape, the HRS to LRS transition can be explained by describing the CF creation from the remnants left by a previous RESET process. The opposite transition, from LRS to HRS, shows the dynamics of the CF rupture [2, 31, 41]. In this context, we simulated VCM devices baked for 10 h at different high temperatures (190 ºC, 210 ºC, 230 ºC, and 260 ºC) to assess their retention properties. We deal with an experimental aggressive thermal acceleration study [21]. Both, room and high temperature measurements were employed to fit the simulator prior to the retention study.

The fabrication technology and measurement technique are explained in section II, the simulation approach is detailed in section III and the main results and discussion are given in section IV. Finally, we wrap up with the conclusions in section V.

II.-DEVICE DESCRIPTION AND MEASUREMENT

The devices employed to assess experimentally the data retention are 1T1R cells integrated in 4 kbit arrays, which are constituted by a select NMOS transistor, manufactured in 0.25 µm CMOS technology, in series with a metal-insulator-metal (MIM) stack [21]. The MIM resistor is composed of 150 nm TiN top and bottom electrode layers deposited by magnetron sputtering, a 7 nm Ti layer, and a 6 nm Al-doped HfO_2 layer deposited by atomic layer deposition (ALD) at 300 ºC with an Al content of about 10%. After patterning the MIM stack with an area of about 0.4 μm^2, an additional thin Si_3N_4 layer was deposited to protect the RRAM cell.

The data retention was tested experimentally on four batches of 128 1T1R cells [21]. All cells were programmed to a common initial LRS by using the incremental step pulse with verify algorithm (ISPVA). Afterwards, each batch was baked for 10 h at one of the following temperatures: 190 ºC, 210 ºC, 230 ºC, and 260 ºC. The evolution of the LRS conductivity was monitored every hour by using the read-out operation at 0.2 V.

III.-SIMULATION DESCRIPTION

The kMC simulation tool methodology employed here has been described in depth in Ref. [16, 20]. The simulation scheme is based in the Transition State Theory (TST), which serves as the basis for the kMC algorithm core. This numerical procedure can reproduce the stochasticity inherent in RS variability. The Poisson and heat equations are also solved in a 3D simulation domain for each simulation step. The temperature and electric field are necessary for the transition rate determination [16]. The simulation domain consists in a cubic structure with a size of 6 nm x 6 nm x 6 nm and with a grid point of 0.5 nm. This simulation domain fits well the real devices that present a 6 nm thick HfO_2 dielectric layer [14, 21]. The filamentary nature of RS makes the simulation domain size reasonable from a kMC perspective. Whatever voltage signal can be introduced in our simulator and the current and RS evolution can be consequently studied. A voltage signal resembling the experimentally defined was taken into account for the forming process. Then, we replicated the external conditions of our experiment; in this respect, the temperature is increased until the baking value and simulations times until the limit of 10 hours. For the read-out current determination, a low voltage was employed (V=0.2V).

The time scale in conventional kMC simulations is typically of a few seconds or lower; however, in this experiment simulations take hours. Taking into consideration the Maxwell-Boltzmann statistics and the TST, the transition rates Γ can be obtained as described in Refs. [16, 22]. They correspond to the inverse of time needed for a determined process to occur. The time for at least one event to occur can be obtained as follows [23],

$$t = -\frac{\ln(1 - randm)}{\sum \Gamma} \tag{1}$$

where *randm* is a random number between 0 and 1. The lower the transition rates, the higher the time needed for an event to occur. In the transition rate calculation, the effect of most of activation energies is reduced considerably by the electric field in ramped voltage experiments. In our simulations, with almost zero-field conditions, only temperature would trigger events making long simulation times less computationally heavy, although for this work intensive computing power was needed. The activation energies used for Frenkel pair generation and for mobility and recombination of oxygen ions are in line with previous works [2, 6, 16, 24-26].

IV.-RESULTS AND DISCUSSION

As reported above, the retention tests were studied by simulation. A tuning process of the simulator was performed previously. In particular, 128 device simulations for each temperature were performed. After the forming process the device external temperature was increased until the baking value; later on, the simulation runs for ten hours.

Figure 4.3-1 shows the experimental and simulated data as cumulative distribution functions (CDFs). The simulated data reproduce reasonably good the measurements [21]. A kMC simulation approach is needed for this study since variability and the experiment stochasticity has to be taken into consideration.

The shift of the curves towards low currents for the longer baking times it is due to thermally induced CF degradation. This effect leads to a current drop and the device failure, which is considered when the current is below the target level established (18 μA as indicated in

Figure 4.3-1. In this Figure, it is seen that the higher the temperature the more device failure counts are produced since the CF degradation is faster (notice that RS mechanisms are thermally induced).

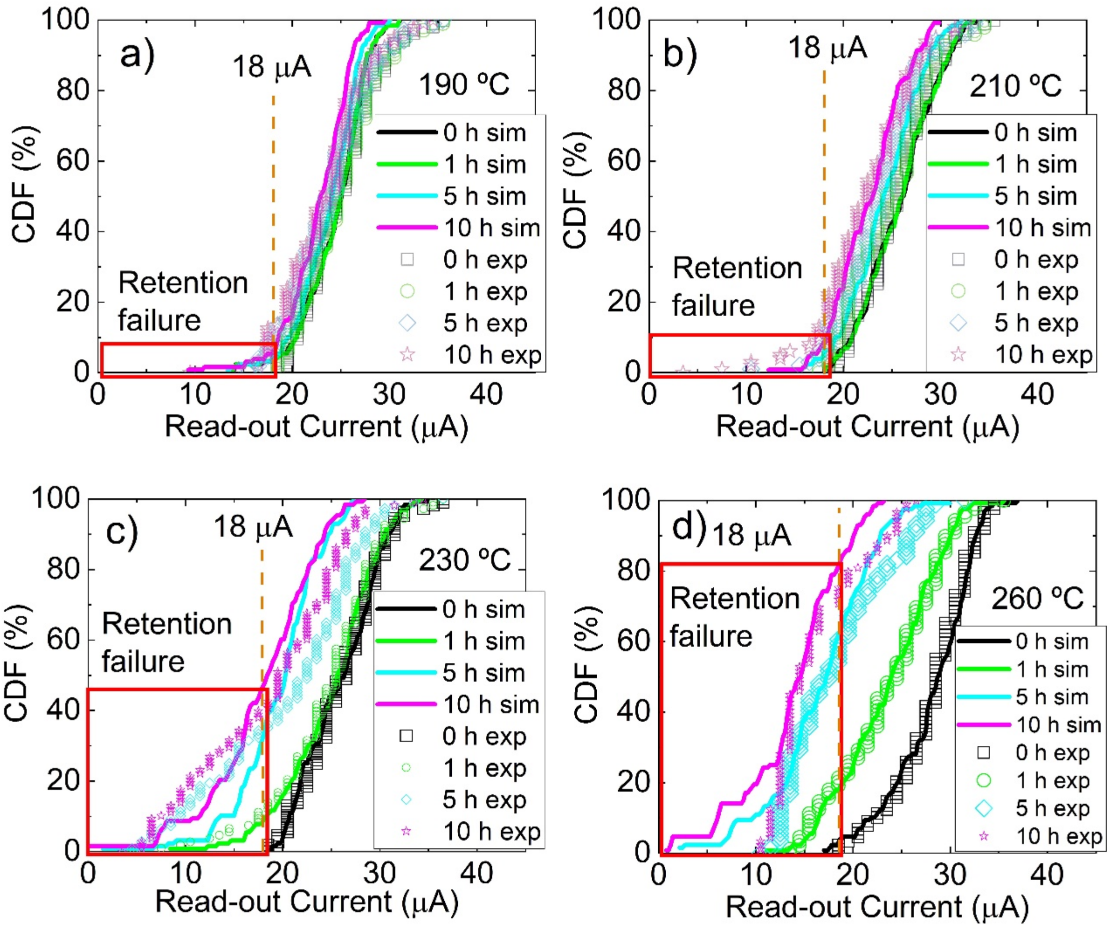

Figure 4.3-1. Read-out experimental and simulated current CDFs for 128 different devices for four different baking times: 0, 1, 5 and 10 h, at the four different temperatures: 190ºC (a), 210ºC (b), 230ºC (c) and 260ºC (d).

It is important to note that the read-out voltage is low enough (0.2 V) not to influence much the CF evolution with time for each of the temperatures considered. Two thermally triggered competing phenomena come into play here: oxygen ion injection to the dielectric from the Ti layer (they diffuse and then they can recombine with existing oxygen vacancies) and the generation of new oxygen vacancy and ion pairs. It should be noted that despite the high oxygen affinity of Ti [9], when a high enough electric field (or temperature) is reached, oxygen ions can be released again to the dielectric layer. If CF degradation is dominant, the CF gets progressively ruptured until the device goes from the LRS to the HRS. **Figure 4.3-2** shows the CDF of the proportion of failure devices along the baking experiments for the temperatures under study.

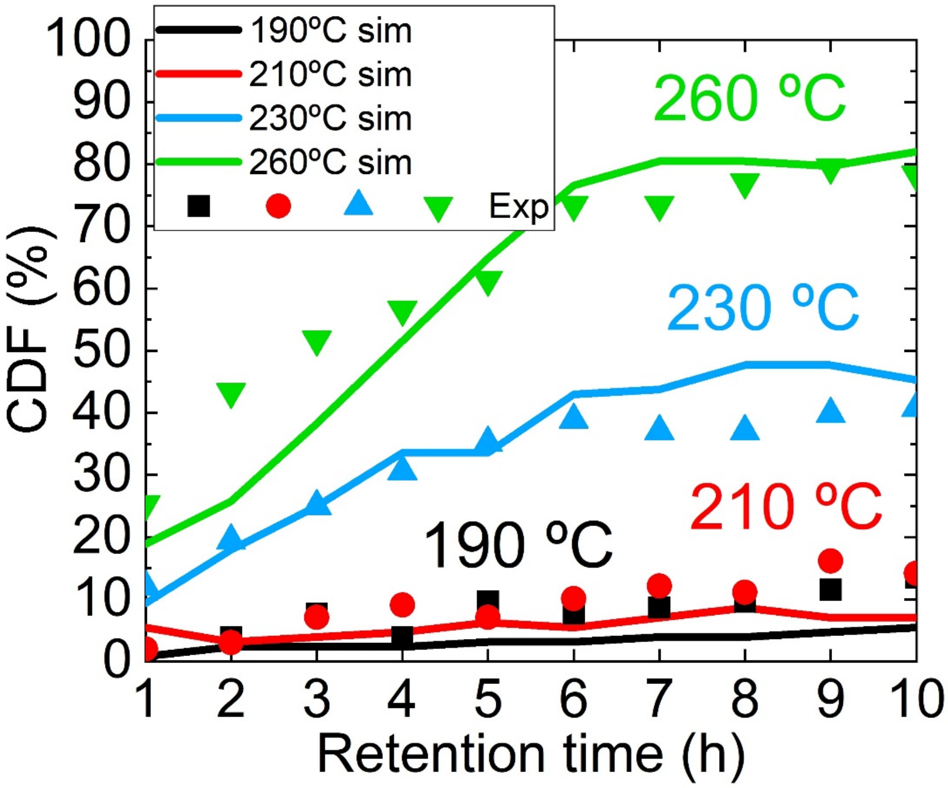

Figure 4.3-2. CDF of failure rate versus retention time for 128 different devices at four temperatures: 190ºC, 210ºC, 230ºC and 260ºC.

These CDFs are assumed to have a positive growth with time; nevertheless, some small drops are seen in the curves that otherwise show an overall increasing trend. These features are linked to the effects of the competition reported above between the CF degradation and regeneration mechanisms.

A typical CF evolution (kMC simulated) is shown in **Figure 4.3-3** where a degradation process with time for a temperature of 260 ºC is shown until the CF ruptured. At the beginning (between t=1.3s and t=361.35s) the CF compactness rises. However, a general destruction process takes place with time, which leads to a current drop. This is coherent with experimental results.

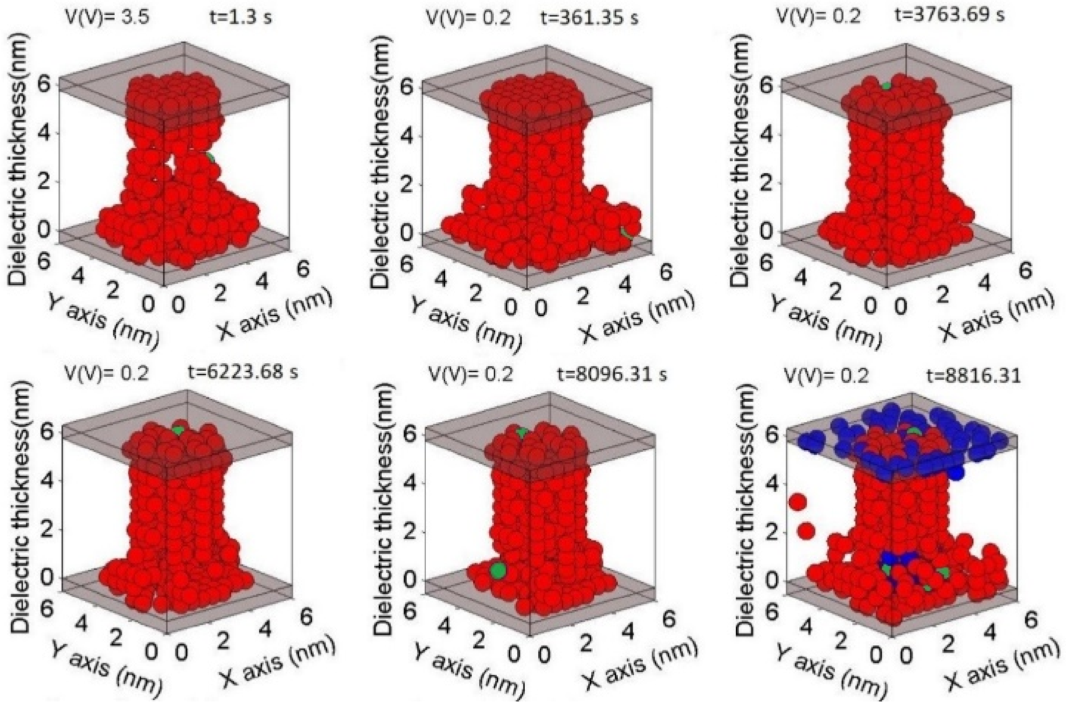

Figure 4.3-3. kMC simulated retention test (CF evolution) at 260ºC. Previously to the test, the CF is formed. After the CF creation, the device temperature is increased until the baking value. A CF degradation is observed with time until the CF rupture. The red balls represent oxygen vacancies, the blue ones symbolize oxygen ions and the green ones represent grid points where both an oxygen vacancy and an oxygen ion (not recombined) are found. The oxygen ions are shown when the percolation path is broken.

For a more detailed description of thermal effects on the CF we have extracted internal data from our kMC simulation (**Figure 4.3-4**). One way to study the CF compactness evolution is to obtain the number of 2D percolation paths within the 3D structure [51], plane by plane (in the X and Y axes) in the simulation domain. The percolation paths are calculated using the Hoshen-Kopelman algorithm adapted to operate in 2D in these planes [52]. These numbers give an idea of the CF compactness and allows the comparison between 3D and 2D simulation approaches [31, 51]. It should be noted that even for no 2D percolation paths, a 3D percolation path can be found due to a lateral connection of different CF regions, which is an unstable situation. In this sense, the lower the number of 2D percolation paths, the lower the CF stability. In **Figure 4.3-4A** and **Figure 4.3-4B**, the number of 2D percolation paths that can be found along the simulation for two devices at different temperatures (210ºC and 230ºC) are shown. For higher temperatures, the number of 2D percolation paths is more unstable and lower. This phenomenon can be described accounting for the CF compactness (**Figure 4.3-4C** and **Figure 4.3-4D**). Here, the oxygen vacancy number having a determined quantity of surrounding neighbors is shown [31, 39]. The maximum number of neighbors would be six neglecting the diagonals. This approximation is related to the way we look for close vacancies by means of the Hoshen-Kopelman algorithm [52] for percolation paths identification and to the cubic grid structure based on finite differences. The approximation is based on the consideration of classical clusters, where only horizontal and vertical neighbors are considered. In this sense, the higher the number occurrences (NO) for 5 and 6 neighbors the higher the CF compactness and obviously the lower the associated CF ohmic resistance. As temperature rises, the NO for 5 and 6 are reduced (the CF compactness drops off). The analysis of the CF density and the Δ parameter is also interesting (**Figure 4.3-4E** and **Figure 4.3-4F**). To estimate the CF density, we consider the surrounding ellipse that better fits the CF in every layer of the simulation domain from the top to the bottom electrodes. The ellipses foci can be obtained by means of a clustering algorithm. In this way, having an ellipse for each layer, one can estimate of the CF volume and its corresponding density [51]. The Δ parameter accounts for the average length of the vertical columns included in the CF free of oxygen vacancies. It can also help to estimate the CF hollowness. This parameter is not the CF gap, although, its use could be interesting in a broken CF to assess the average gap and also the compactness of the CF remnants.

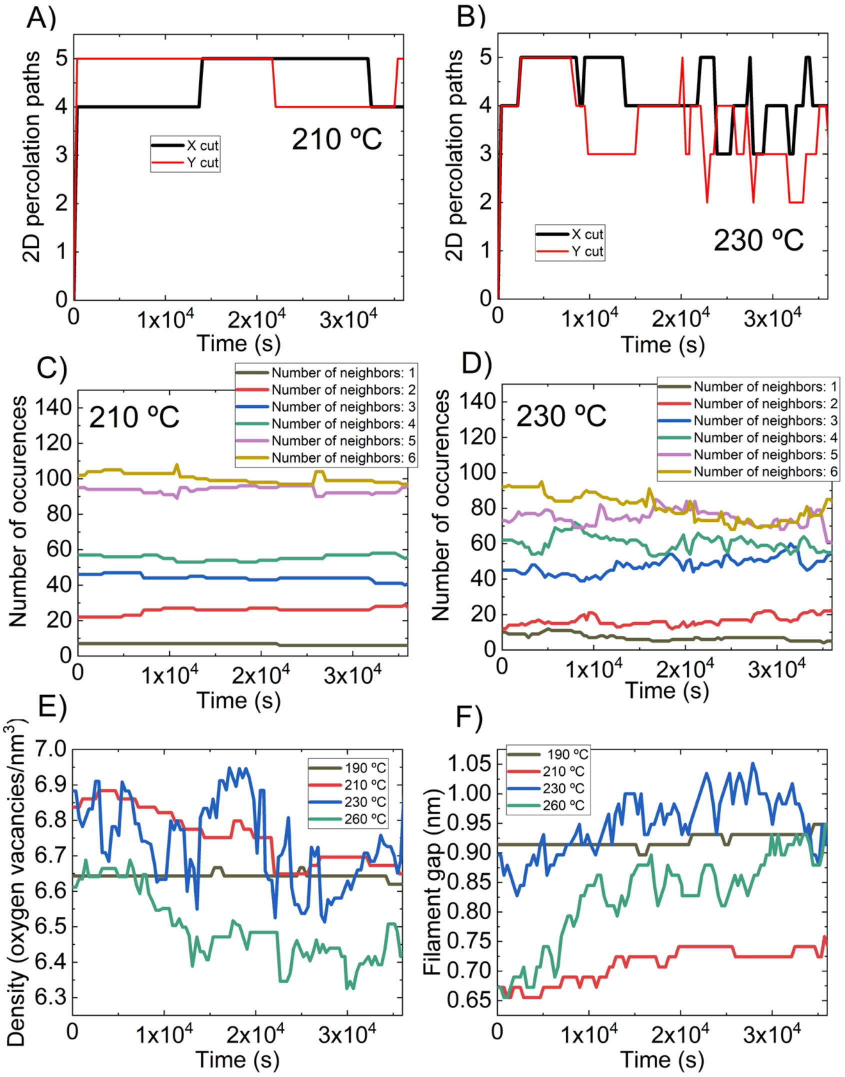

Figure 4.3-4. CF characteristics versus time for different temperatures. A) (B) 2D percolation paths in the CF at 210 ºC (230 ºC). C) (D) Number of occurrences of surrounding neighbors (maximum six when diagonals are neglected) for 210 ºC (for 230 ºC) within the conductive filament. E) Oxygen vacancy density versus time for the conductive filament, F) Δ parameter versus time. The Δ parameter is the mean length

of the part of the vertical columns in the simulation domain included in the CF non occupied by oxygen vacancies. The evolution of the CF compactness and its internal structure can be assessed with these data.

The information shown in **Figure 4.3-4** helps to interpret the experiments in **Figure 4.3-1** and **Figure 4.3-2**. This is, the progressive CF degradation with temperature. This is shown in the reduction of the number of 2D percolated layers plotted in **Figure 4.3-4A** to **Figure 4.3-4B**. A CF compactness drop can be also observed in **Figure 4.3-4D** in comparison to **Figure 4.3-4C**, accounting for the reduction of the NO for 5 and 6 neighbors. In the last two subfigures there is an evident CF density reduction with temperature (**Figure 4.3-4E** and **Figure 4.3-4F**). It is important to highlight the relation between the density and the Δ parameter. If the vacancy density and the Δ parameter were calculated locally (some region within the CF) instead of globally, it would be found that the higher the Δ parameter, the lower the CF vacancy density. These two parameters evolve randomly with time. All these results describe a CF ohmic resistance rise and, hence, a read-out current drop. So, the higher the temperature the higher the probability that a CF failure takes place. The CF degradation is not a continuous process since it is linked to the competition between the CF regeneration and degradation mechanisms. For instance, in **Figure 4.3-4E** it is seen a large regime where regeneration is dominant, before CF degradation takes over. This phenomenon explains some of the subtleties of **Figure 4.3-2**, where a CF degradation is expected and the consequent failure rate increase, but at times a failure rate decrease is also observed.

At the sight of the results shown here, some clues can be suggested for retention improvement in vacancies generation based devices. In this type of studies, a combination of experimental and simulation efforts in the context of low electric fields pays off. For instance, the use of materials with high recombination activation energies would delay the thermally triggered RESET processes. Moreover, materials with lower generation activation energies could help to even the competition against the CF degradation. Finally, the influence of oxygen ion mobility in the thermally triggered RESETs has been observed to influence the device retention. Additionally, with the simulator fully developed and fitted for different materials (that is, with an appropriate activation energy set), it could be used to study more complex technologies, such as bilayer and trilayer RRAMs. It can be useful to study the temperature distribution in these technologies in order to know in which layer the number of vacancies is higher or where is the filament weakest point, and the more probable CF breaking point.

V.-CONCLUSIONS

The main retention failure mechanisms in RRAMs have been analyzed by means of kinetic Monte Carlo simulation at several temperatures. It has been shown experimentally that the higher the temperature the faster the degradation of the low resistance state, this fact has also been shown by simulation. The competing physical processes between the generation of new oxygen vacancies and their recombination with oxygen ions with these vacancies determine the retention behavior for the technology analyzed. The kMC simulator allows to access internal variables, such as the electric field, the temperature; in addition, the formation of percolation paths, the conductive filament density and compactness can be analyzed. This information helps to understand the dynamics of baking experiments performed in the laboratory. The key physical mechanisms have been detected and some clues related to the retention performance and possible technology improvements (e.g. using materials that hinder the recombination process at low electric fields or the injection of oxygen ions to the dielectric) are suggested.

VI. - ACKNOWLEDGMENTS

The authors thank the support of the project A.TIC.117.UGR18 funded by the government of Andalusia (Spain) and the FEDER program. The authors also gratefully acknowledge the financial support by the German Research Foundation (DFG) in the frame of research group FOR2093.

References

[1] S. Menzel, B. Klopstra, C. Kügeler, U. Böttger, G. Staikov, R. Waser, “A simulation model of resistive switching in electrochemical metallization memory cells (ECM)”, MRS Online Proceedings Library Archive, 1160, 101–106, 2009.

[2] L. Larcher, A. Padovani, L. Vandelli, “A simulation framework for modeling charge transport and degradation in high-k stacks”, Journal of Computational Electronics, 12(4), 658-665, 2013.

[3] R. Degraeve, A. Fantini, N. Raghavan, L. Goux, S. Clima, Y. Chen, A. Belmonte, S. Cosemans, B. Govoreanu, D. Wouters, P. Roussel, G. Sankar Kar, G. Groeseneken, M. Jurczak, “Hourglass concept for RRAM: a dynamic and statistical device model”, Proceedings of the 21th International Symposium on the Physical and Failure Analysis of Integrated Circuits (IPFA). IEEE, p. 245-249, 2014.

[4] F. Pan, S. Gao, C. Chen, C. Song, F. Zeng, "Recent progress in resistive random access memories: materials, switching mechanisms and performance", Materials Science and Engineering, 83, pp. 1-59, 2014.

[5] S. Menzel, P. Kaupmann, R. Waser, “Understanding filamentary growth in electrochemical metallization memory cells using kinetic Monte Carlo simulations”, Nanoscale, 7, 12673, 2015.

[6] A. Padovani, L. Larcher, O. Pirrotta, L. Vandelli, G. Bersuker, “Microscopic Modeling of HfO x RRAM Operations: From Forming to Switching”, IEEE Transactions on Electron Devices, 62(6), pp. 1998-2006, 2015.

[7] D. Ielmini, R. Waser. “Resistive Switching: From Fundamentals of Nanoionic Redox Processes to Memristive Device Applications”, Wiley-VCH, 2015.

[8] M. A. Villena, J. B. Roldán, F. Jiménez-Molinos, E. Miranda, J. Suñé, M. Lanza, “SIM2RRAM: A physical model for RRAM devices simulation”, Journal of Computational Electronics, 16(4), 1095-1120, 2017.

[9] S. Dirkmann, J. Kaiser, C. Wenger, T. Mussenbrock, “Filament Growth and Resistive Switching in Hafnium Oxide Memristive Devices”, ACS applied materials & interfaces, 10(17), 14857-14868, 2018.

[10] Lanza, M., Wong, H. S. P., Pop, E., Ielmini, D., Strukov, D., Regan, B. C., ... & Belmonte, A. (2019). Recommended methods to study resistive switching devices. Advanced Electronic Materials, 5(1), 1800143.

[11] J. Zahurak, K. Miyata, M. Fischer, M. Balakrishnan, S. Chhajed, D. Wells, Li Hong, A. Torsi, J. Lim, M. Korber, K. Nakazawa, S. Mayuzumi, M. Honda, S. Sills, S. Yasuda, A. Calderoni, B. Cook, G. Damarla, H. Tran, B. Wang, C. Cardon, K. Karda, J. Okuno, A.

Johnson, T. Kunihiro, J. Sumino, M. Tsukamoto, K. Aratani, N. Ramaswamy, W. Otsuka, K. Prall, "Process integration of a 27nm, 16Gb Cu ReRAM", 2014 IEEE International Electron Devices Meeting, IEEE, 6.2.1-6.2.4, 2014, doi: 10.1109/IEDM.2014.7046994

[12] M. Ignatov, M. Ziegler, M. Hansen, A. Petraru, H. Kohlstedt, “A memristive spiking neuron with firing rate coding”, Frontiers in neuroscience, 9, 376, 2015.

[13] Sokolov, A. S., Ali, M., Riaz, R., Abbas, Y., Ko, M. J., & Choi, C., “Silver-Adapted Diffusive Memristor Based on Organic Nitrogen-Doped Graphene Oxide Quantum Dots (N-GOQDs) for Artificial Biosynapse Applications”, Advanced Functional Materials, 29(18), 1807504, 2019.

[14] Yeon, H., Lin, P., Choi, C., Tan, S. H., Park, Y., Lee, D., ... & Qian, H., “Alloying conducting channels for reliable neuromorphic computing”, Nature Nanotechnology, 1-6, 2020.

[15] Abbas, H., Abbas, Y., Hassan, G., Sokolov, A. S., Jeon, Y. R., Ku, B., ... & Choi, C., “The Coexistence of Threshold and Memory Switching Characteristics of ALD HfO2 Memristor Synaptic Arrays for Energy-Efficient Neuromorphic Computing”, Nanoscale, 2020.

[16] F. Alibart, E. Zamanidoost, D.B. Strukov, “Pattern classification by memristive crossbar circuits using ex situ and in situ training”, Nature Communications, 4, p. 2072, 2013.

[17] Merolla, P. A., Arthur, J. V., Alvarez-Icaza, R., Cassidy, A. S., Sawada, J., Akopyan, F., ... & Brezzo, B., “A million spiking-neuron integrated circuit with a scalable communication network and interface”, Science, 345(6197), 668-673, 2014.

[18] M. Prezioso, F. Merrikh-Bayat, B. D. Hoskins, G. C. Adam, K. K. Likharev, D. B. Strukov “Training and operation of an integrated neuromorphic network based on metal-oxide memristors”, Nature 521, pp. 61-64, 2015.

[19] Z. Wang, C. Li, W. Song, M. Rao, D. Belkin, Y. Li, P. Yan, H. Jiang, P. Lin, M. Hu, J. P. Strachan, N. Ge, M. Barnell, Q. Wu, A. G. Barto, Q. Qiu, R. S. Williams, Q. Xia, J. J. Yang, “Reinforcement learning with analogue memristor arrays”, Nature Electronics, 2, pp. 115-124, 2019.

[20] P. Yao, H. Wu, B. Gao, J. Tang, Q. Zhang, W. Zhang, J. J. Yang, H. Qian, “Fully hardware-implemented memristor convolutional neural network”, Nature, 577, PP. 641-646, 2020.

[21] Perez, E., Mahadevaiah, M. K., Zambelli, C., Olivo, P., & Wenger, C., “Data retention investigation in Al: HfO2-based resistive random access memory arrays by using high-temperature accelerated tests”, Journal of Vacuum Science & Technology B, Nanotechnology and Microelectronics: Materials, Processing, Measurement, and Phenomena, 37(1), 012202, 2019.

[22] Baek, I. G., Lee, M. S., Seo, S., Lee, M. J., Seo, D. H., Suh, D. S., ... & Chung, U. I. (2004, December). "Highly scalable nonvolatile resistive memory using simple binary oxide driven by asymmetric unipolar voltage pulses", In IEDM Technical Digest. IEEE International Electron Devices Meeting, 2004. (pp. 587-590). IEEE, 2004.

[23] Wei, Z., Kanzawa, Y., Arita, K., Katoh, Y., Kawai, K., Muraoka, S., ... & Mikawa, T. (2008, December). Highly reliable TaOx ReRAM and direct evidence of redox reaction mechanism. In 2008 IEEE International Electron Devices Meeting (pp. 1-4). IEEE.

[24] Jeon, Y. R., Abbas, Y., Sokolov, A. S., Kim, S., Ku, B., & Choi, C. (2019), "Study of in situ silver migration in amorphous boron nitride CBRAM device", ACS applied materials & interfaces, 11(26), 23329-23336, 2019

[25] Abbas, Y., Ambade, R. B., Ambade, S. B., Han, T. H., & Choi, C., "Tailored nanoplateau and nanochannel structures using solution-processed rutile TiO2 thin films for complementary and bipolar switching characteristics", Nanoscale, 11(29), 13815-13823, 2019.

[26] Ali, A., Abbas, Y., Abbas, H., Jeon, Y. R., Hussain, S., Naqvi, B. A., ... & Jung, J., "Dependence of InGaZnO and SnO2 Thin Film Stacking Sequence for the Resistive Switching Characteristics of Conductive Bridge Memory Devices", Applied Surface Science, 146390, 2020.

[27] Ku, B., Abbas, Y., Kim, S., Sokolov, A. S., Jeon, Y. R., & Choi, C. "Improved resistive switching and synaptic characteristics using Ar plasma irradiation on the Ti/HfO2 interface", Journal of Alloys and Compounds, 797, 277-283, 2019.

[28] Banerjee, W., Liu, Q., & Hwang, H., "Engineering of defects in resistive random access memory devices", Journal of Applied Physics, 127(5), 051101, 2020.

[29] Abbas, Y., Han, I. S., Sokolov, A. S., Jeon, Y. R., & Choi, C., "Rapid thermal annealing on the atomic layer-deposited zirconia thin film to enhance resistive switching characteristics", Journal of Materials Science: Materials in Electronics, 31(2), 903-909, 2020.

[30] G. González-Cordero, F. Jiménez-Molinos, J. B. Roldán, M. B. González, F. Campabadal, "In-depth study of the physics behind resistive switching in TiN/Ti/HfO2/W structures", Journal of Vacuum Science & Technology B, Nanotechnology and Microelectronics: Materials, Processing, Measurement, and Phenomena, 35(1), 01A110, 2017.

[31] Aldana, S., García-Fernández, P., Romero-Zaliz, R., González, M. B., Jiménez-Molinos, F., Gómez-Campos, F., ... & Roldán, J. B., "Resistive switching in HfO2 based valence change memories, a comprehensive 3D kinetic Monte Carlo approach", Journal of Physics D: Applied Physics, 53(22), 225106, 2020.

[32] X. Guan, S. Yu, H. S. P. Wong, "On the switching parameter variation of metal-oxide RRAM—Part I: Physical modeling and simulation methodology", IEEE Transactions on Electron Devices, 59, pp. 1172-1182, 2012.

[33] Villena, M. A., Roldán, J. B., González, M. B., González-Rodelas, P., Jiménez-Molinos, F., Campabadal, F., & Barrera, D., “A new parameter to characterize the charge transport regime in Ni/HfO2/Si-n+-based RRAMs”, Solid-State Electronics, 118, 56–60, 2016. DOI: 10.1016/j.sse.2016.01.007

[34] Cagli, C., Sandrini, J., Sassine, G., Robayo, D., Hammad, I., Molas, G., & Gaillard, F., “Reliability and Scaling Perspectives of HfO2-Based OxRAM”, ECS Transactions, 97(1), 9, 2020.

[35] R. Waser, “Nanoelectronics and Information Technology”, 3rd ed., Wiley-VCH, Berlin, 2012.

[36] Voter, A. F., “Introduction to the kinetic Monte Carlo method. In Radiation effects in solids”, (pp. 1-23). Springer, Dordrecht, 2007.

[37] L. Vandelli, A. Padovani, G. Bersuker, D. Gilmer, P. Pavan, L. Larcher, “Modeling of the forming operation in HfO2-based resistive switching memories”, 2011 3rd IEEE International Memory Workshop (IMW), (pp. 1-4), IEEE, 2011.

[38] S. Aldana, P. García-Fernández, A. Rodríguez-Fernández, R. Romero-Zaliz, M. B. González, F. Jiménez-Molinos, F. Campabadal, F. Gómez-Campos, J. B. Roldán, “A 3D kinetic Monte Carlo simulation study of resistive switching processes in Ni/HfO2/Si-n+-based RRAMs”, Journal of Physics D: Applied Physics, 50(33), 335103, 2017.

[39] S. Aldana, J. B. Roldán, P. García-Fernández, J. Suñe, R. Romero-Zaliz, F. Jiménez-Molinos, S. Long, F. Gómez-Campos, M. Liu, “An in-depth description of bipolar resistive switching in Cu/HfOx/Pt devices, a 3D kinetic Monte Carlo simulation approach”, Journal of Applied Physics, 123(15), 154501, 2018.

[40] Chen, Y. C., Lin, C. C., Hu, S. T., Lin, C. Y., Fowler, B., & Lee, J., “A Novel Resistive Switching Identification Method through Relaxation Characteristics for Sneak-path-constrained Selectorless RRAM application”, Scientific Reports, 9(1), 1-6, 2019.

[41] https://www.youtube.com/watch?v=OLk4eJNc_Y8

[42] J. Guy, G. Molas, P. Blaise, M. Bernard, A. Roule, G. Le Carval, V. Delaye, A. Toffoli, G. Ghibaudo, F. Clermidy, B. De Salvo, L. Perniola, “Investigation of Forming, SET, and Data Retention of Conductive-Bridge Random-Access Memory for Stack Optimization”, IEEE Transactions on Electron Devices, 62(11), pp. 3482-3489, 2015.

[43] Pérez, E., Grossi, A., Zambelli, C., Olivo, P., Roelofs, R., and Wenger, Ch. (2017) Reduction of the Cell-to-Cell Variability in Hf1-xAlxOy Based RRAM Arrays by Using Program Algorithms, IEEE Electron Device Letters, 38, 175-178.

[44] S. Clima, Y. Chen, A. Fantini, L. Goux, R. Degraeve, B. Govoreanu, G. Pourtois and M. Jurczak, "Intrinsic Tailing of Resistive States Distributions in Amorphous HfOx and TaOx

Based Resistive Random Access Memories," Electron Device Letters, IEEE, vol. 36, pp. 769-771, 2015.

[45] Gao, B., Zhang, H. W., Yu, S., Sun, B., Liu, L. F., Liu, X. Y., ... & Wang, Y. Y., “Oxide-based RRAM: Uniformity improvement using a new material-oriented methodology”, In 2009 Symposium on VLSI Technology (pp. 30-31). IEEE, 2009.

[46] Peng, C. S., Chang, W. Y., Lee, Y. H., Lin, M. H., Chen, F., & Tsai, M. J. “Improvement of resistive switching stability of HfO2 films with Al doping by atomic layer deposition. Electrochemical and Solid State Letters”, 15(4), H88, 2012.

[47] Roy, S., Niu, G., Wang, Q., Wang, Y., Zhang, Y., Wu, H., ... & Ye, Z. G. “Toward a Reliable Synaptic Simulation Using Al-Doped HfO2 RRAM”, ACS Applied Materials & Interfaces, 12(9), 10648-10656, 2020.

[48] Gao, B., Kang, J. F., Zhang, H. W., Sun, B., Chen, B., Liu, L. F., ... & Yu, H. Y., “Oxide-based RRAM: Physical based retention projection”, In 2010 Proceedings of the European Solid State Device Research Conference (pp. 392-395). IEEE, 2010.

[49] P. Huang, X. Y. Liu, B. Chen, H.T. Li, Y. J. Wang, Y.X. Deng, K.L. Wei, L. Zeng, B. Gao, G. Du, X. Zhang, J.F. Kang, "A Physics-Based Compact Model of Metal-Oxide-Based RRAM DC and AC Operations", IEEE Transactions on Electron Devices, 60(12), 4090-4097, 2013.

[50] Bradley, S. R., Shluger, A. L., & Bersuker, G., “Electron-injection-assisted generation of oxygen vacancies in monoclinic HfO2”, Physical Review Applied, 4(6), 064008, 2015.

[51] S. Aldana, P. García-Fernández, R. Romero-Zaliz, F. Jiménez-Molinos, F. Gómez-Campos, J.B. Roldán, "Analysis of conductive filament density in resistive RAMs, a 3D Kinetic Monte Carlo approach", Journal of Vacuum Science and Technology B, 36, p. 62201, 2018.

[52] Hoshen, J., & Kopelman, R.,” Percolation and cluster distribution. I. Cluster multiple labeling technique and critical concentration algorithm”, Physical Review B, 14(8), 3438, 1976.

Chapter 5

5. Conclusions

The need for temporary (volatile) and permanent (non-volatile) data storage is increasing in the field of electronic. This comes from the need of these memories for internet of things (IoT) devices, solid-state drives (SSD), 5G circuits, cloud storage, artificial intelligence, data mining or smartphones and laptops [Gupta2019]. In this sense, RRAMs emerge as one of the main alternatives based on its ease of fabrication and compatibility with CMOS technology in the Back-End-Of-Line (BEOL). Furthermore, it also has a good scalability, endurance, speed and latency, endurance, low energy consumption and the possibility of 3D stacking.

The thesis has been focused in the development of three different RRAM simulators, one for unipolar CBRAMs, other for bipolar CBRAMs and the last one for VCMs. Then, the simulators have been used to study the variability of real devices, study the evolution of the CFs, carry out data retention tests and study some stochastic phenomena. The work includes four publications in scientific journals indexed in the Journal Citation Report of Science Citation Index, one Proceedings published in IEEE Xplore digital library, three contributions to International Conferences. Six other works, where a book chapter is included, are also related this work. Three videos detailing the operation of each simulator and the devices employed to tune the simulation tools were developed for the scientific visualization of this work.

The main results obtained can be summarized as follows:

The three different kMC simulators (unipolar CBRAM, bipolar CBRAM and VCM) take into consideration the different physical mechanisms involved in each resistive switching process. Furthermore, the charge transport mechanisms are implemented.

1. The unipolar CBRAM simulator is based on 3D kMC algorithm. 3D Poisson and heat equations are also solved by means of finite element methods. The electric field and temperature are necessary variables to correctly implement the redox, ion migration and nucleation processes. All of these processes are behind the resistive switching operation in this kind of devices. Ni/HfO$_2$/Si devices were characterized, besides of using the experimental data to fit the simulator.
2. The bipolar CBRAM simulator based on a 3D kinetic Monte Carlo approach was used for characterizing Cu/HfO$_x$/Pt stacks. The physics of the resistive switching operation can be studied with this simulator, which has similar characteristics to the former one, but it has been adapted to bipolar operation. Temperature and electric fields are obtained for every simulation step again. In this case, the CF creation/rupture is also based on the redox reactions and the joint action of metal ion thermally induced diffusion and ion movement due to electric field drift.
3. A VCM 3D kinetic Monte Carlo simulator has been developed and used to characterize TiN/Ti/HfO$_2$/W RRAMs. The simulated results have a good agreement with the experimental data. In this simulator, the 3D heat and Poisson equations have been also solved self-consistently. These two magnitudes, the temperature and the electric field, have an important influence in the physical mechanisms that govern the device operation. These are mainly the generation of oxygen vacancies and ions, the motion of oxygen ions and the recombination process in the oxide layer. The simulator was tuned using experimental data.
4. A new technique to calculate the CF density and its relation with the resistance has been presented, besides two techniques for analyzing the CF compactness. The procedure for the density calculation is based on an algoritm to find the ellipse that better fits the surroundings of the percolation path. Regarding the techniques for the compactness, one of them is based on searching the number of 2D percolation paths within the 3D filament and the other one is based on searching the number of particles that have a certain number of neighbors.
5. For the unipolar CBRAM case, it has been found a good agreement between the simulated and experimental data. Moreover, the evolution of the conductive filament during the forming, SET and RESET processes has been studied intensively. Furthermore, it has been also studied the CF formation direction and its shape depending on the activation energies of migration and generation of ions.
6. The difference between 2D and 3D percolation paths has been presented and it has been concluded that 2D representation might lack accuracy due to the stochastic nature of resistive switching. This study is also useful for analyzing the compactness of the CF. Making use of the technique for calculating the CF density, it has been proved that the density and width of the CF rise before the rupture. This phenomenon has also been observed in the CF compactness when it was studied by means of 2D percolation paths within the 3D conductive filament.
7. Regarding the bipolar CBRAM, it has been found that the electric field is more relevant than the effect of the temperature, unlike the unipolar case. The simulator is tuned

making use of the experimental data, getting a good correspondence with the simulated I-V curves and with the distributions of SET and RESET voltages and currents. Finally, some internal variables have also been studied, like the electric field and the current fluctuations and their relation with the evolution of the virtual electrode. Besides, the CF compactness through the neighbors' technique and the density of the clusters that form the percolation paths have been also analyzed.

8. In VCM case, also a good correspondence between experimental and simulated data has been found. Besides, the percolation path evolution under the applied voltage has been studied along the forming, RESET and SET processes, both for voltage ramp and pulsed operation regimes. During the pulsed operation regime with high enough voltages, an interesting phenomenon of a partial SET during a RESET process has been described. Furthermore, an analysis of the filament compactness has been performed by means of the neighbors technique and through the study of the 2D percolation paths found in the 3D CF during the RESET process.
9. Other interesting study was the analysis of the retention failure mechanisms at different temperatures. It has been concluded that there are two competing processes that determine the retention time, the generation of new vacancies and the recombination. Finally, some clues can be suggested improving device retention, such as using materials with high recombination activation energies, which could hinder the thermally triggered RESET processes. It should be highlighted that the influence of oxygen ion mobility in the RESETs triggered thermally can be studied to understand the relation with the retention time.

6. Appendix

6.1. Conduction mechanism in dielectrics

The conduction mechanisms that dominate the device HRS depend on the state of the device (that is, the effective gap), the device area, the electrode and insulator materials, layer thicknesses and on the applied voltage [Chiu2014]. These mechanisms are shown in **Figure 6.1-1**. For the description of the current some basic conduction models can be used in order to reproduce the behavior of the current/voltage [Ouyang2016, Chiu2014]. Describing or detecting the main physical mechanisms in some experimental currents might be quite complex. The reason is that there can be more than one phenomenon at the same time and multiple experiments would be required to identify which of them are the dominants. In addition, the preeminence of one mechanism over the others is linked to the electric field magnitude [Southwick2009].

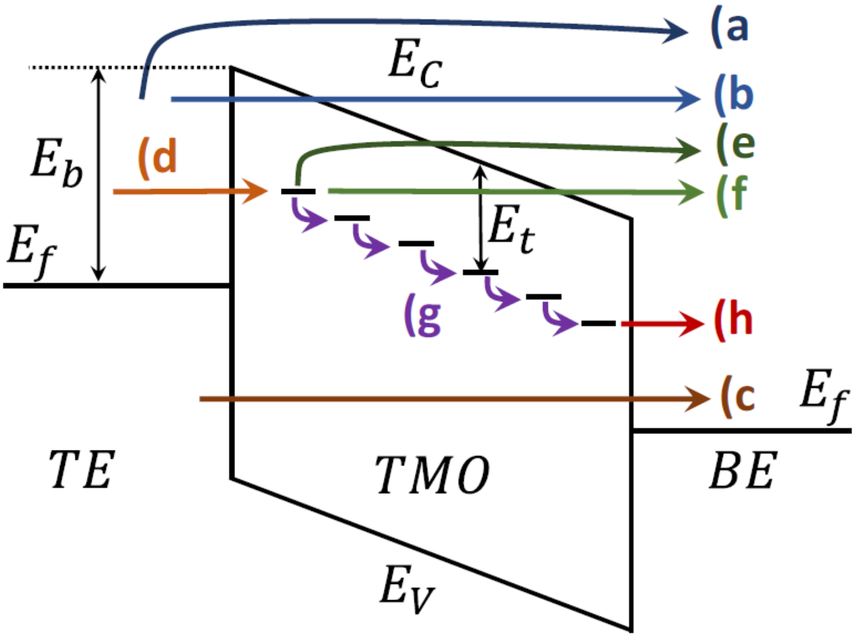

Figure 6.1-1. Energy band diagram of the different conduction mechanisms that can be found in a MIM structure. a) Schottky emission, b) Fowler–Nordheim tunnelling, c) Direct tunnelling, d) Tunnelling from TE to traps, e) Poole–Frenkel emission, f) Trap-assisted tunnelling, g) Electron hopping and h) Tunneling to the BE [González-Cordero2019, Lim2015, Chiu2014, Wong2012, Yu2011].

The main mechanisms in the literature are the following [Garcia-Redondo2016]:

- A power law generalized function can be used to take into account a trap assisted tunneling current (which model the Poole-Frenkel, Schottky emission and the Space Charge Limited Current (SCLC)). This power law between the cell current and the applied voltage depends on two parameters: A_{HRS} and β_{HRS} [Aziza2014, Garcia-Redondo2016, Bocquet2014, González-Cordero2016, González-Cordero2019]:

  $$I_{Oxide} = A_{HRS} \cdot S_{Cell} \left(\frac{V_{Cell}}{t_{ox}}\right)^{\beta_{HRS}} \tag{6.1.1}$$

  being V_{Cell} the voltage applied between the electrodes and t_{ox} the thickness of the dielectric.

- The Fowler-Nordheim (F-N) current is relevant for thin oxides and high electric fields. This tunneling occurs through a triangular barrier (due to the effect of the electric field). It is based on a quantum phenomenon, the penetration of the electron wave function through the potential barrier when it is thin enough (< 100 Å). Thus, the probability that the electron reaches the other side of the potential barrier is not zero. For this to occur, the applied electric field must be large enough to produce that the electron wave function penetrates into the conduction band of the dielectric [Chiu2014]. This is something necessary for the electron to go through the triangular potential barrier mentioned above. The current has the following form [Bocquet2014b, Ranuárez2006, Ouyang2016]:

$$I_{Oxide} = S_{Cell} \cdot A \cdot F^2 \cdot exp\left(-\frac{B}{F}\right) \tag{6.1.2}$$

Being

$$A = \frac{m_e \cdot q^3}{8\pi \cdot h \cdot m_e^{ox} \cdot \emptyset_b} \tag{6.1.3}$$

And

$$\begin{cases} \emptyset_b \geq q \cdot t_{ox} \cdot F \rightarrow B = \dfrac{8\pi\sqrt{2m_e^{ox}}}{3 \cdot h \cdot q}\left[{\emptyset_b}^{3/2} - (\emptyset_b - q \cdot t_{ox} \cdot F)^{3/2}\right] \\ \emptyset_b \leq q \cdot t_{ox} \cdot F \rightarrow B = \dfrac{8\pi\sqrt{2m_e^{ox}}}{3 \cdot h \cdot q}{\emptyset_b}^{3/2} \end{cases} \tag{6.1.4}$$

Besides, $F = V_{Cell}/t_{ox}$ is the electric field, V_{Cell} the voltage applied between the electrodes, t_{ox} the thickness of the dielectric, S_{Cell} the section of the device, m_e and m_e^{ox} the effective electron masses into the cathode and the dielectric, h is the Planck constant, q the electron charge and $\emptyset_b$ the metal-oxide barrier height. To obtain the tunneling current, the current-voltage (I-V) characteristic curves of the device should be measured at very low temperature. The reason is that at low temperature the thermionic emission can be neglected and the tunneling current is dominant [Chiu2014].

- The Schottky Thermionic emission mechanism [Yan2015, Zhong2014, Ouyang2016] is the thermally induced current over an interfacial energy barrier with a dependence on the temperature T. This mechanism is based on the electrons in the metal that can overcome the barrier by thermal energy. This mechanism is quite relevant for relatively high temperatures and can be observed quite often [Chiu2014]. It can be expressed in the following way:

$$I = S_{Cell} \cdot A^{**} \cdot T^2 exp\left[-\frac{q\left(\emptyset_b - \sqrt{\dfrac{qF}{4\pi\varepsilon}}\right)}{K_\beta T}\right] \tag{6.1.5}$$

being $A^{**} = \frac{4\pi m_e K_\beta^2 q}{h^3} = 1.20173 \cdot 10^6\, Am^{-2}K^{-2}$ the Richardson's constant, K_β the Boltzmann constant, ε the dielectric constant of the material, $F = V_{Cell}/t_{ox}$ is the electric field, V_{Cell} the voltage applied between the electrodes, t_{ox} the thickness of the dielectric, S_{Cell} the section of the device, q the electron charge and $\emptyset_b$ the Schottky barrier height, m_e the effective electron masses, h is the Planck constant and T the temperature.

- The Poole-Frenkel (P-F) emission [Garcia-Redondo2016, Ouyang2016] is a charge conduction mechanism that describes the electronic transport through trapping sites. This mechanism is similar to Schottky emission as electrons go from traps into the conduction band of the dielectric by thermal excitation. It must be taken into account that the potential energy barrier of an electron trapped can be screened by the effect of the applied electric field across the dielectric. This reduction would increase the probability of electron transition from the trap to the conduction band of the dielectric [Chiu2014]. The P-F expression is the following:

$$I = S_{Cell} \cdot i_0 \cdot F \cdot exp\left[-\frac{q\left(\emptyset_b - \sqrt{\frac{qF}{\pi\varepsilon}}\right)}{K_\beta T}\right] \tag{6.1.6}$$

being i_0 a fitting parameter, S_{Cell} the section of the device, q the electron charge, $\emptyset_b$ the trap energy level, $F = V_{Cell}/t_{ox}$ is the electric field, V_{Cell} the voltage applied between the electrodes, t_{ox} the thickness of the dielectric, K_β the Boltzmann constant, ε the dielectric constant of the material, q the electron charge and T the temperature. Since this mechanism is based on the thermal activation under an electric field, it is quite relevant in high temperature regimes and high electric field conditions. In this sense, it is easy to find that under high electric fields and temperatures ranging from 300 K to 400 K, the P-F emission is the dominant mechanism [Chiu2014].

- Direct tunneling is the conduction mechanism for charge tunneling through a trapezoidal barrier [Ouyang2016]. It should be noted that if the applied electric field is high enough, the electrons see a triangular barrier. In this case, the current would be due to F-N tunneling. On the opposite hand, if the electric field is low enough, the electrons see the full oxide thickness, this is the direct tunneling mechanism. For instance, for a 4-5 nm and above SiO2 thickness, F-N tunneling would be the dominant mechanism. However, for thickness less than 3.5 nm, direct tunneling is dominant [Chiu2014]. It is important to have into consideration that when the oxides have thicknesses in the order of a few nanometers, this mechanism at lower fields is not negligible [Ranuárez2006]. The mechanism follows this dependence:

$$J \propto V_{Cell} \cdot exp\left(-\frac{2t_{ox}}{\hbar}\sqrt{2m_e^{ox}\emptyset_b}\right) \tag{6.1.7}$$

being V_{Cell} the voltage applied between the electrodes, t_{ox} the thickness of the dielectric, ħ is the Planck constant, m_e^{ox} the effective electron masses into the dielectric and $\emptyset_b$ the metal-oxide barrier height.

- The hopping conduction is based on the electronic transition from one trap to another by means of tunneling effect in the dielectric layer [Chiu2014]. It can be considered the main charge transport mechanism for strongly disordered systems. It has the following form [Ouyang2016]:

$$I = S_{Cell} \cdot qan \cdot V_{Cell} \cdot exp\left(\frac{qaF}{K_\beta T} - \frac{\emptyset_b}{K_\beta T}\right) \tag{6.1.8}$$

being V_{Cell} the voltage applied between the electrodes, S_{Cell} the section of the device, a the mean hopping distance, n the electron concentration, $F = V_{Cell}/t_{ox}$ is the electric field, q is the electronic charge, K_β the Boltzmann constant, T the temperature and $\emptyset_b$ the energy level from the trap states to the bottom of the conduction band. It should be highlighted the difference with the P-F emission, as this latter one corresponds to the thermionic effect, while hopping conduction is based on tunnel effect. In the P-F case, carriers can go over the trap barrier by means of thermionic mechanism. Nevertheless, the carrier energy in hopping conduction mechanism is lower than the energy of the barrier between two trapping sites, but they can still "jump" via tunnel mechanism [Chiu2014].

- The space charge limited current is similar to the carrier transport mechanism in a vacuum diode. It should be remembered that the thermionic cathode of a vacuum diode emits electrons following a Maxwell distribution. This mechanism is observed in materials with low charge carrier mobility [Ouyang2016, Ouyang2014] and has the following form [Garcia-Redondo2016]:

$$J \propto \frac{9\varepsilon\mu {V_{Cell}}^2}{8t_{ox}^3} \tag{6.1.9}$$

being V_{Cell} the voltage applied between the electrodes, t_{ox} the dielectric thickness, ε the dielectric constant of the material and μ is the charge-carrier mobility.

It can be found in **Table 3** some examples of these models reported in the literature:

Structure	**Conduction mechanism**	**Made by**
Cu/SiO/W	P-F	[Zhang2009]
Zr/CeO$_x$/Pt	Space charge limited current	[Ismail2014]
TiN/HfO$_2$/Ti/TiN	P-F	[Walczyk2011]
TiN/Ti/TiO$_x$ /HfO$_x$ /TiN	Schottky emission	[Lee2012]
Ti/Cu$_x$O/Pt	Space charge limited current	[Wang2010]
Ti/TiO$_2$/Pt	Schottky emission	[Huang2010]
Al/AlO/Al	P–F/Schottky emission	[Zhu2012]
Ni/HfO$_2$/Si-n+	P–F	[Villena2014]
Al/TiO$_x$/TiO$_2$/Al	Space charge limited current	[Kim2010b]
Pt/TiO$_2$/Pt	Space charge limited current/ Schottky emission	[Kim2006]

Table 3. Summary of some conduction mechanisms used to model devices in the HRS.

6.2. Circuital model for formed conductive filaments (Low Resistance State)

In this kind of devices, when a fully formed conductive filament shorts the electrodes, charge transport mechanisms different from the previously exposed have to be considered. Moreover, other resistance contributions showed in the equivalent circuit in the **Figure 6.2-1** can be taken into account, where an arbitrary number of CFs are considered. Usually the CFs have ohmic behavior, but in some devices also the CF shows a narrowing and quantum effects show up due to the lateral confinement of the electrons that cross through the dielectric. In this latter case, the Quantum Point Contact conduction model can be included. Furthermore, Maxwell and setup series resistances can also be taken into consideration.

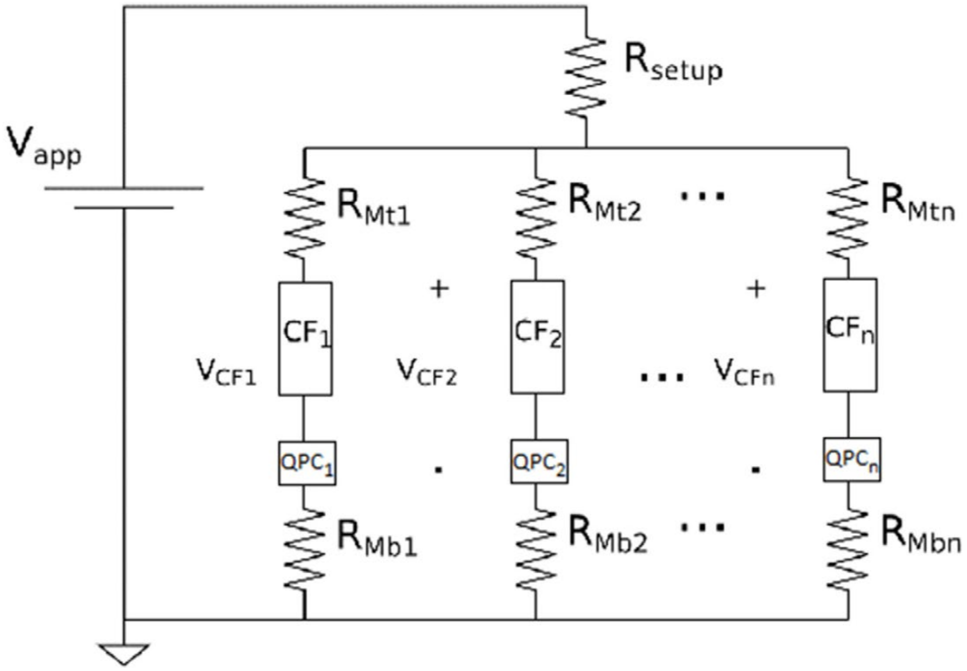

Figure 6.2-1. The electrical equivalent circuit model that can be considered for calculation of the resistance of the system and so the current in the ohmic regime after one or more percolated paths are formed [Aldana2017].

The R_{Setup} accounts for the resistance of electrodes, conductive paths and setup wires, the CF_i is the ith percolation path that shorts the electrodes, R_{Mti} and R_{Mbi} are the Maxwell resistances in the top and bottom electrodes respectively and QPC_i represents the Quantum Point Contact conduction associated to each CF_i based on the following model [Villena2014, Miranda2001]:

$$I = \frac{2eN}{h}\left\{eV_{CTR} + \frac{1}{\alpha}\ln\left[\frac{1 + exp\{\alpha[\emptyset - \beta e(V - V_0)]\}}{1 + exp\{\alpha[\emptyset + (1 - \beta)e(V - V_0)]\}}\right]\right\} \tag{6.2.1}$$

being ∅ the potential barrier height measured with respect to the Fermi level, α a parameter linked to the potential barrier thickness at the Fermi level, V_{CTR} the voltage which is assumed to drop at both ends of the CF constriction, e is the elementary electron charge, I is the CF current and N is the number of active channels in the CF. There are numerical procedures developed to perform the QPC model parameter extraction process [Roldán2018].

Regarding the ohmic resistance of each CF, it can be calculated taking into account the contribution of every layer in the simulation domain of the CF, depending on the number of particles within. The contribution of the ith layer ($R_{layer\ i}$) can be calculated as [Timsit1998]:

$$R_{layer\ i} = \frac{L}{\sigma_i A} = \frac{L}{\sigma_i N_p d^2} \tag{6.2.2}$$

Being L the length of the layer, A the area of the layer, N_p the number of particles in the layer, d the size of each particle (this is, the separation between grid points) and σ_i is the electrical conductivity of the ith layer which has the following dependence on the temperature [Aldana2017]:

$$\sigma_i(x, y, z) = \frac{\sigma_0}{1 + \alpha_T\left(T_{layer} - T_0\right)} \tag{6.2.3}$$

being T_{layer} the mean temperature of the layer, T_0 the room temperature, $\alpha_T(K^{-1})$ the thermal coefficient of the CF electrical conductivity and σ_0 the electrical conductivity at room temperature T_0. It is necessary to notice that to carry out this calculation a kMC simulation step is needed because the 3D heat equation is required as well as a detailed information of every particle in the system.

Maxwell resistances are incorporated to take into account the funneling of the current lines from the large electrode to the narrowing of the CFs. For the sake of generality, the Maxwell resistance can be divided into two contributions for each CF since usually the electrodes are made of different materials: R_{Mti} and R_{Mbi}, where i stands for the number of the considered filament and t and b for the top and bottom electrode respectively. The Maxwell resistance is given by the following expression:

$$R_{Mt,bi} = \frac{1}{4 r_{min} \sigma_{t,b}} \tag{6.2.4}$$

being r_{min} the radius of the narrowest part of the filament and $\sigma_{t,b}$ are the conductivity of the top or bottom electrodes.

In this way, every filament forms a branch with Maxwell resistances and the QPC conduction mechanism, which are in series. And every branch is in parallel with other. This global equivalent resistance would be in series with the R_{Setup} as shown previously in **Figure 6.2-1**.

6.3. Percolation path determination

A basic part in the RRAM simulations is the creation and destruction of percolation paths. The percolation paths define the two main resistance states of the device that allows it to work as a memory device, the HRS and LRS. In the kMC simulations, percolation paths are created or ruptured depending on the formation or disaggregation of a group of clusters of particles of different nature that short-circuit the electrodes. In our case, we employed the Hoshen-Kopelman algorithm to determine possible percolation paths in our simulation domain [Hoshen1976]. This algorithm allows to determine fast and accurately the cluster distribution even in 3D simulation domains. The success of the method and its versatility in solving complex percolation problems is based on the application of alternate labels to sites belonging to the same clusters.

The algorithm will assign to each crystal site i, occupied by a determined type of particle, a cluster label m_t^α. Here α stands for the cluster. This cluster α can also have many clusters labels made up of a set of natural numbers:

$$\{m_1^\alpha, m_2^\alpha, \dots, m_s^\alpha, \dots, m_t^\alpha, \dots\} \tag{6.3.1}$$

From this set of natural numbers, we select the smallest one as a proper cluster label and we will designate it as m_s^α. The following set of integers represents the connections between the different labels (m_t^α) of the α cluster:

$$\{N(m_1^\alpha), N(m_2^\alpha), \dots, N(m_s^\alpha), \dots, N(m_t^\alpha), \dots\} \tag{6.3.2}$$

being $N(m_s^\alpha)$ the only positive which represents the number of particles in the cluster. The rest of the set members of eq. 6.3.2 are negative integers which represent the links between each m_t^α label and the selected m_s^α. That is, $N(m_t^\alpha)$ represents the connection of cluster m_s^α with cluster m_t^α. For instance, if we have two clusters labeled with 7 (with 5 particles) and 2 (with 3 particles), but they are not in contact, $N(7) = 5$ and $N(2) = 3$. However, if these two former clusters are in contact, following eq. 6.3.2, they would have the following relation $N(7) = -2$ and $N(2) = 8$. In this case, as label 2 is the smallest one, it would be the proper cluster $m_s^\alpha = 2$. An illuminating example can be found in Ref. [Hoshen1976]. In this sense, the relation between m_t^α labels and m_s^α follows this sort of expression:

$$m_r^\alpha = -N(m_t^\alpha);\ m_q^\alpha = -N(m_r^\alpha); \dots, m_s^\alpha = -N\left(m_p^\alpha\right) \tag{6.3.3}$$

Equations that must be solved from left to right. The assignation of labels to each site is explained in **Figure 6.3-1**:

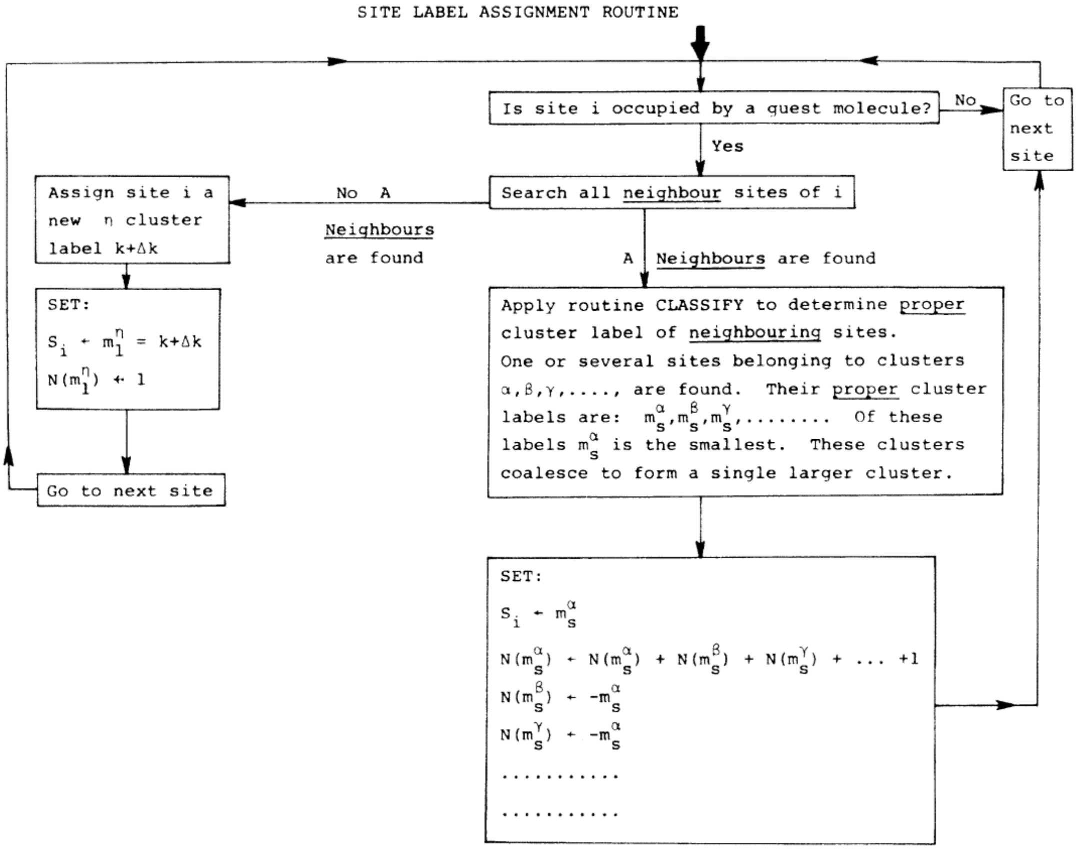

Figure 6.3-1. Routine for assignation of labels. The routine labels the sites occupied by the molecule selected and readjust the N(m_t^α) numbers. The notation D ← E means that E transfer the information to D, without losing the information of E [Hoshen1976].

The first time a molecule appears during the inspection, the label counter k is set to an initial value k_0 (for instance, $k_0 = 0$) and the increment Δk is a small positive integer like $\Delta k = 1$. The routine CLASSIFY, explained in **Figure 6.3-2**, is used for searching previously labeled sites when a newly molecule is created.

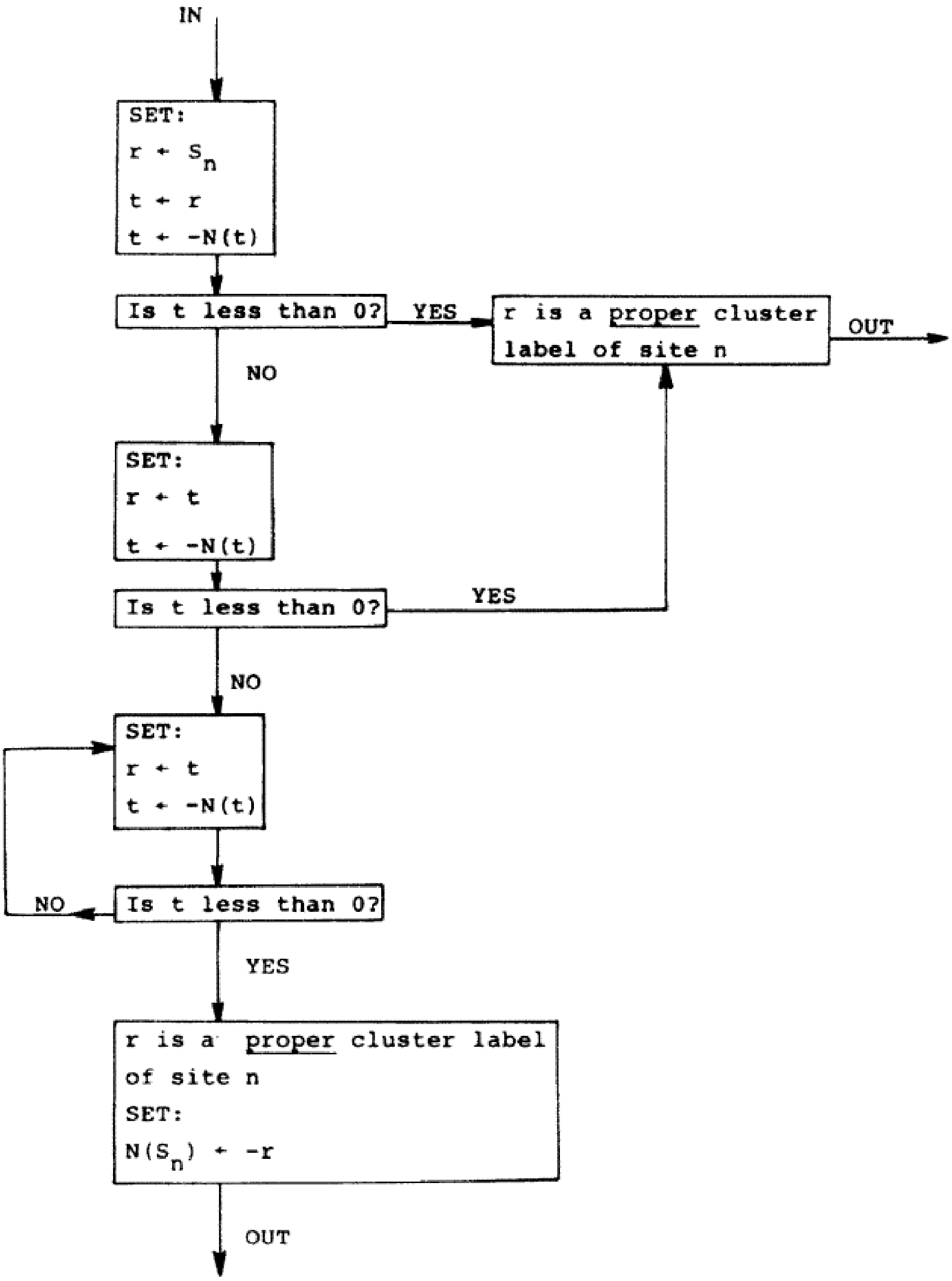

Figure 6.3-2. CLASSIFY routine that determines the proper cluster labels for sites containing molecules. S_n is neighbor site n [Hoshen1976].

The neighbors of site i are the adjacent sites to i, taking into consideration or not the diagonal. The set of all the neighbors in contact can be called the neighborhood. If there are no neighbors in the vicinity of site i, a new label will be assigned after incrementing k. If there is only one neighbor (at site n), site i gets the same label as site n. The cluster multiple labeling technique becomes more evident when there is a site i with a molecule linking two o more previously labeled cluster fragments into a single cluster. The sites belonging to these cluster fragments are not relabeled and once a subcrystal site is labeled, it retains its original labels during the whole simulation process. The readjustments occur within the $N(m_t^\alpha)$ sets, as clusters are newly created, grown, or coalesced in the simulation process. The number of readjusted $N(m_t^\alpha)$ numbers for site i is equal to the number of coalescing cluster fragments at the site i as it is explained in **Figure 6.3-1**.

6.4. Poisson and heat equations

For a good physical description of the device one has to deal with the problem of getting a reliable representation of the temperature and the electric field distributions. The problem to face here is getting an accurate simulation in reasonable computation time. To do this, it is necessary to solve numerically heat and Poisson equations without a high cost. In our case we employ the finite difference method [Nagel2011, Dawson1991, Recktenwald2004]. The simplicity of RRAM structures helps on this issue. If more complicated shapes for the different device regions were used, finite elements methodologies would be needed [Benodekar1978, Winslow1966].

To find a numerical solution to the problem a grid that represent the simulation domain must be defined as shown in **Figure 6.4-1** [Nagel2011, Benodekar1978, Winslow1966, Dawson1991, Recktenwald2004]. The mesh that has been used in this work is a 3D structure between 5 and 10 nanometers (although other sizes can be programmed) with a step size of d, which is the size of the particle considered (usually between 0.25 and 0.5 nanometers).

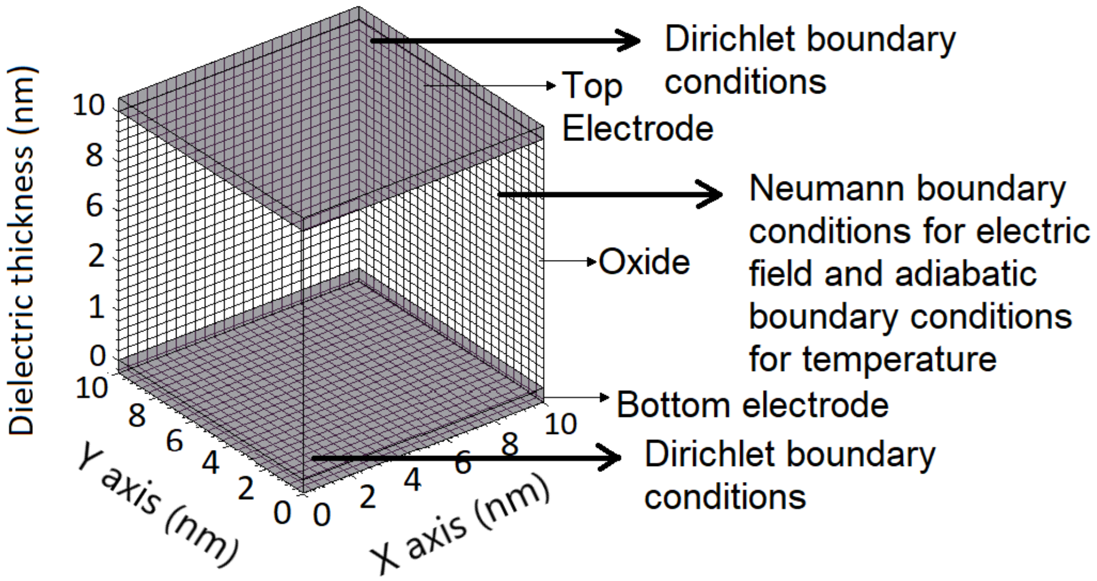

Figure 6.4-1. Simulation domain with 3D grid for a 10 x 10 x 10 nanometers structure where the top and bottom electrode are shown for clarity. The boundary conditions are also pointed out [Aldana2017].

Once the grid is defined, the next step would be solving the Poisson and heat equations. The 3D Poisson equation has the following form [Nagel2011]:

$$\nabla^2\varphi(x,y,z) = \left(\frac{\partial^2\varphi(x,y,z)}{\partial x^2}+\frac{\partial^2\varphi(x,y,z)}{\partial y^2}+\frac{\partial^2\varphi(x,y,z)}{\partial z^2}\right) = -\frac{\rho_c(x,y,z)}{\varepsilon} \tag{6.4.1}$$

being $\varphi(x,y,z)$ the electric potential for a given charge distribution $\rho_c(x,y,z)$ and ε the dielectric permittivity of the medium.

The steady-state heat equation has the following form [Fatullayev2002]:

$$\gamma\nabla^2 T(x,y,z) = \gamma\left(\frac{\partial^2 T(x,y,z)}{\partial x^2} + \frac{\partial^2 T(x,y,z)}{\partial y^2} + \frac{\partial^2 T(x,y,z)}{\partial z^2}\right) = f(x,y,z) \qquad (6.4.2)$$

being $T(x,y,z)$ the temperature, $\gamma = \frac{K}{c_p \rho}$ the thermal diffusivity, K the thermal conductivity, ρ the mass density and c_p the specific heat capacity. The thermal conductivity K for HfO_2, one of the most used dielectric materials, has different values depending on the thickness of the layer, as it depends strongly on the film-thickness-dependent microstructure. For thicknesses between 5.6-20 nm it can be found values between 0.49 and 0.95 $W/(m \cdot K)$ [Panzer2009]. The $f(x,y,z)$ is the source of heat, that is, the power density dissipated at each grid point by means of Joule heating following this expression:

$$f(x,y,z) = |\nabla\varphi(x,y,z)|^2 \frac{\sigma_0}{1 + \alpha_T(T(x,y,z) - T_0)} \qquad (6.4.3)$$

being σ_0 the electrical conductivity at the reference temperature, T_0 the room temperature and α_T is the temperature coefficient of conductivity.

As can be seen, both expressions are second order partial differential equations with comparable form, and so the finite difference method to solve them can have similitudes. The finite difference method consists in approximating the differential operator by replacing the derivatives in the equation using differential quotients [Dawson1991, Recktenwald2004]. As explained above, the space domain is divided in multiple points and approximations of the solution are calculated for every grid point. The error of this method will be determined by the substitution of the differential operator for a difference operator, i.e., the discretization error or truncation error [Benodekar1978, Recktenwald2004]. It is called truncation error because the approximation of a finite part of Taylor series is used.

For the sake of simplicity, the problem can be formulated in one dimension, but the conclusions are easily generalized to a 3D domain. The starting point is the definition of the derivative:

$$u'(x) = \lim_{d\to 0} \frac{u(x+d) - u(x)}{d} \qquad (6.4.4)$$

When d tends to zero (without vanishing) the quotient of the right-side provides a “good” approximation of the derivative. It is possible to quantify this error using a Taylor series expansion:

$$u(x+d) = u(x) + du'(x) + \frac{d^2}{2}u''(x) + \cdots \tag{6.4.5}$$

Retaining only the first two terms of the previous expression, we get the following expression,

$$u(x+d) = u(x) + du'(x) + O(d^2) \tag{6.4.6}$$

where term $O(d^2)$ indicates that the approximation error is proportional to d^2 [Benodekar1978, Recktenwald2004]. In this sense, making use of eq. 6.4.5, we can define the following approximation:

$$\frac{u(x+d) - u(x)}{d} = u'(x) + \frac{d}{2}u''(x) + \cdots = u'(x) + O(d) \tag{6.4.7}$$

Thus, we have the error for the first derivative approximation proportional to d.

On the other hand, the first backward difference approximation of u' at point x can be defined as:

$$u(x-d) = u(x) - du'(x) + \frac{d^2}{2}u''(x) + \cdots \tag{6.4.8}$$

Only with the two first terms:

$$u(x-d) = u(x) - du'(x) + O(d^2) \tag{6.4.9}$$

Now, defining the central difference approximation and assuming that function u is three times derivable:

$$\begin{cases} u(x+d) = u(x) + du'(x) + \dfrac{d^2}{2}u''(x) + \dfrac{d^3}{6}u^{(3)}(x) \\ u(x-d) = u(x) - du'(x) + \dfrac{d^2}{2}u''(x) - \dfrac{d^3}{6}u^{(3)}(x) \end{cases} \tag{6.4.10}$$

Subtracting these two expressions we obtain

$$\frac{u(x+d) - u(x-d)}{2d} = u'(x) + \frac{d^2}{6}u^{(3)}(x) \tag{6.4.11}$$

Having in this way an approximation of the first derivative with an error proportional to d^2:

$$u'(x) \approx \frac{u(x+d) - u(x-d)}{2d} \tag{6.4.12}$$

For the second derivative, which is needed to solve the former expressions, it is necessary to expand the Taylor series until the fourth term

$$\begin{cases} u(x+d) = u(x) + du'(x) + \frac{d^2}{2}u''(x) + \frac{d^3}{6}u^{(3)}(x) + \frac{d^4}{24}u^{(4)}(x) \\ u(x-d) = u(x) - du'(x) + \frac{d^2}{2}u''(x) - \frac{d^3}{6}u^{(3)}(x) + \frac{d^4}{24}u^{(4)}(x) \end{cases} \tag{6.4.13}$$

Adding these two expressions we can get

$$\frac{u(x+d) - 2u(x) + u(x-d)}{d^2} = u''(x) + \frac{d^2}{12}u^{(4)}(x) \tag{6.4.14}$$

Having in this way an approximation of the second derivative with an error proportional to d^2:

$$u''(x) \approx \frac{u(x+d) - 2u(x) + u(x-d)}{d^2} \tag{6.4.15}$$

Making use of this approximation in the Poisson equation, taking into consideration a 3D simulation domain, the same distance between every grid point in every axis ($d_x = d_y = d_z = d$) and changing the notation including the coordinates of the grid point as i, j, k, we get

$$\begin{aligned} \nabla^2\varphi(x,y,z) &= \frac{\varphi_{i+1,j,k} + \varphi_{i-1,j,k} + \varphi_{i,j+1,k} + \varphi_{i,j-1,k} + \varphi_{i,j,k+1} + \varphi_{i,j,k-1} - 6\varphi_{i,j,k}}{d^2} \\ &= -\frac{\rho_{c\,i,j,k}}{\varepsilon} \end{aligned} \tag{6.4.16}$$

As we need the $\varphi_{i,j,k}$ term [Nagel2011]:

$$\varphi_{i,j,k} = \frac{1}{6}\left(\frac{\rho_c(x,y,z)d^2}{\varepsilon} + \varphi_{i+1,j,k} + \varphi_{i-1,j,k} + \varphi_{i,j+1,k} + \varphi_{i,j-1,k} + \varphi_{i,j,k+1} + \varphi_{i,j,k-1}\right) \tag{6.4.17}$$

Making the same assumptions about the stationary heat equation:

$$\begin{aligned} \gamma\nabla^2 T(x,y,z) &= \gamma\left(\frac{T_{i+1,j,k} + T_{i-1,j,k} + T_{i,j+1,k} + T_{i,j-1,k} + T_{i,j,k+1} + T_{i,j,k-1} - 6T_{i,j,k}}{d^2}\right) \\ &= f_{i,j,k} \end{aligned} \tag{6.4.18}$$

As we need the $T_{i,j,k}$ term [Recktenwald2004]:

$$T_{i,j,k} = \frac{1}{6}\left(T_{i+1,j,k} + T_{i-1,j,k} + T_{i,j+1,k} + T_{i,j-1,k} + T_{i,j,k+1} + T_{i,j,k-1} - \frac{f_{i,j,k}d^2}{\gamma}\right) \tag{6.4.19}$$

In order to solve Poisson and heat equations with realistic and physical values, a solution compatible with boundary conditions with the characteristics of the system has to be found. For the Poisson equation, Neumann and Dirichlet boundary conditions will be used, as shown in the **Figure 6.4-1** [Nagel2011, Benodekar1978].

Regarding the Poisson equations, Dirichlet conditions consist in fixing the voltage in both electrodes of the device, one of them to the applied voltage and the other one grounded. This is

$$\varphi(x, y, z = t_{ox}) = V_{applied} \quad ; \quad \varphi(x, y, z = 0) = 0 \tag{6.4.20}$$

Neumann conditions are used for lateral faces, that is, the value of the derivative in these faces is given

$$\frac{\partial \varphi}{\partial n} = g \tag{6.4.21}$$

Being $g = 0$ in our case. Making use of the definition of the derivative and $g = 0$ we can get for each lateral face the following relations:

$$\begin{gathered}
\left.\frac{\partial \varphi}{\partial n}\right|_{(x_1=0,y,z)} = \frac{\varphi(x_2, y, z) - \varphi(x_1, y, z)}{d} = 0 \rightarrow \varphi(x_1, y, z) = \varphi(x_2, y, z) \\
\left.\frac{\partial \varphi}{\partial n}\right|_{(x_{max}=Lx,y,z)} = \frac{\varphi(x_{max}, y, z) - \varphi(x_{max-1}, y, z)}{d} = 0 \rightarrow \varphi(x_{max}, y, z) = \varphi(x_{max-1}, y, z) \\
\left.\frac{\partial \varphi}{\partial n}\right|_{(x,y_1=0,z)} = \frac{\varphi(x, y_2, z) - \varphi(x, y_1, z)}{d} = 0 \rightarrow \varphi(x, y_1, z) = \varphi(x, y_2, z) \\
\left.\frac{\partial \varphi}{\partial n}\right|_{(x,y_{max}=Ly,z)} = \frac{\varphi(x, y_{max}, z) - \varphi(x, y_{max-1}, z)}{d} = 0 \rightarrow \varphi(x, y_{max}, z) - \varphi(x, y_{max-1}, z)
\end{gathered} \tag{6.4.22}$$

Where Lx and Ly are the maximum size of the mesh in the coordinates x and y.

In the **Figure 6.4-2** some results obtained with this methodology for solving the Poisson equation are shown. For illustrating, a two particles simulation, as shown in **Figure 6.4-2a**, has been carried out. After solving the Poisson equation, the electric potential has been plotted in **Figure 6.4-2b** and the electric field in **Figure 6.4-2c**. It should be noted that as the electric field is a vector, it can be easily represented by arrows. **Figure 6.4-2d** shows an electric potential distribution for a random particle distribution in the dielectric where a 2V external voltage is applied.

Concerning the heat equation, Dirichlet conditions consist in fixing the temperature of the electrodes at room temperature (300K), acting like an infinite heat sink. This is

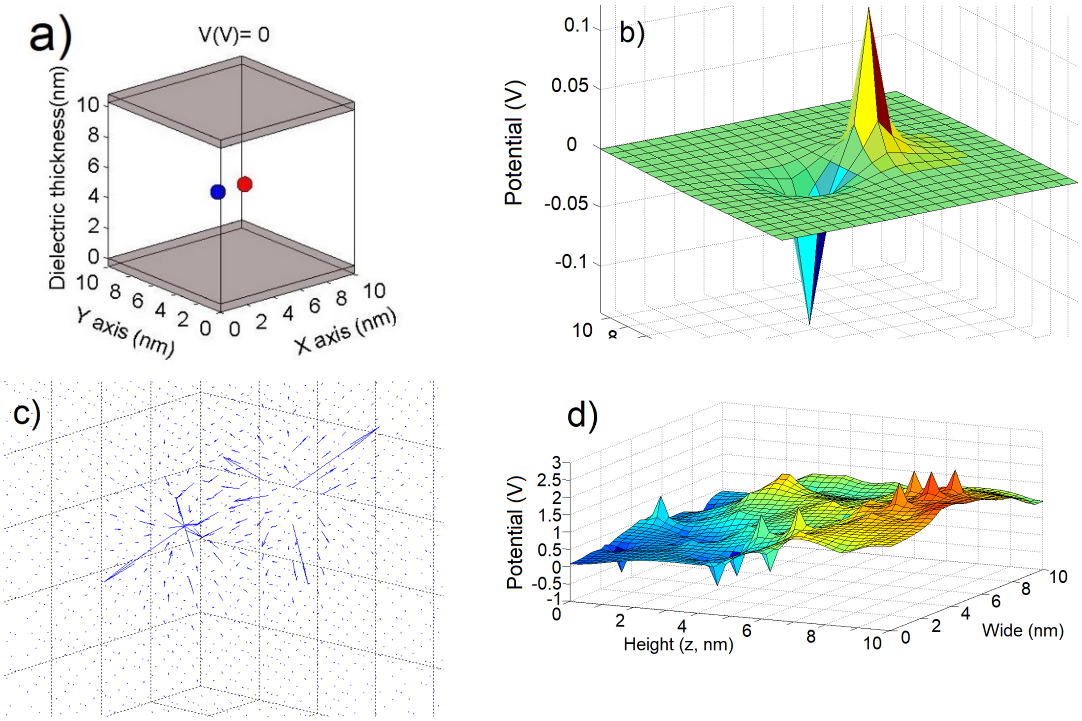

Figure 6.4-2. a), b) and c) correspond to the same simulation. In a) it can be seen the structure simulated and the particles distribution. The blue ball is the oxygen and the red ball is the oxygen vacancy. In b) is plotted the electric potential distribution generated for both particles. In c) the arrows are representing the electric field magnitude and direction. In d) an electric potential distribution in XZ plane with $y = 5\,nm$ is presented for an external applied voltage of 2V. The electric potential is due to randomly distributed charged particles in the dielectric besides the applied voltage.

$$T(x,y,z=t_{ox}) = T_{room} \quad ; \quad T(x,y,z=0) = T_{room} \tag{6.4.23}$$

Adiabatic conditions are used for lateral faces, that is, conditions under which overall heat transfer across the boundary between the thermodynamic system and the surroundings is absent. This is:

$$Q = -K\frac{\partial T}{\partial n} = 0 \tag{6.4.24}$$

being Q proportional to the local heat flux density at surface. Operating like in the case of Neumann boundary condition for Poisson equation we get

$$\begin{aligned}
\left.\frac{\partial T}{\partial n}\right|_{(x_1=0,y,z)} &= \frac{T(x_1,y,z)-T(x_2,y,z)}{d} = 0 \rightarrow T(x_1,y,z) = T(x_2,y,z) \\
\left.\frac{\partial T}{\partial n}\right|_{(x_{max}=Lx,y,z)} &= \frac{T(x_{max},y,z)-T(x_{max-1},y,z)}{d} = 0 \rightarrow T(x_{max},y,z) = T(x_{max-1},y,z) \\
\left.\frac{\partial T}{\partial n}\right|_{(x,y_1=0,z)} &= \frac{T(x,y_1,z)-T(x,y_2,z)}{d} = 0 \rightarrow T(x,y_1,z) = T(x,y_2,z) \\
\left.\frac{\partial T}{\partial n}\right|_{(x,y_{max}=Ly,z)} &= \frac{T(x,y_{max},z)-T(x,y_{max-1},z)}{d} = 0 \rightarrow T(x,y_{max},z) - T(x,y_{max-1},z)
\end{aligned} \tag{6.4.25}$$

After solving the heat equation, some consideration should be made about the system time evolution. As mentioned before, this technique gives stationary solution of the temperature, but this approximation may be not correct. In this sense, based on previous work about the thermal behavior of RRAM devices, a better approximation can be proposed. It can be assumed that a thermal system can be simulated making use of a discrete element of electrical circuit to account for the thermal "inertia" of the system considering a simplifying approach to avoid the computing burden linked to the time dependant solution of the heat equation. An RC equivalent electrical circuit can be chosen for retaining the temperature and thermal power [Lu2016]. These two variables would work in a conventional electrical equivalent of a circuit that accounts for a compact thermal model.

In the **Figure 6.4-3** the heat equation solutions is shown in the LRS of one of the devices we have studied. **Figures 6.4-3a** and **6.4-3d** correspond to different voltages. The corresponding temperature distributions are presented in ZX plane, **Figures 6.4-3b** and **6.4-3e**, and in XY plane, in **Figures 6.4-3c** and **6.4-3f**.

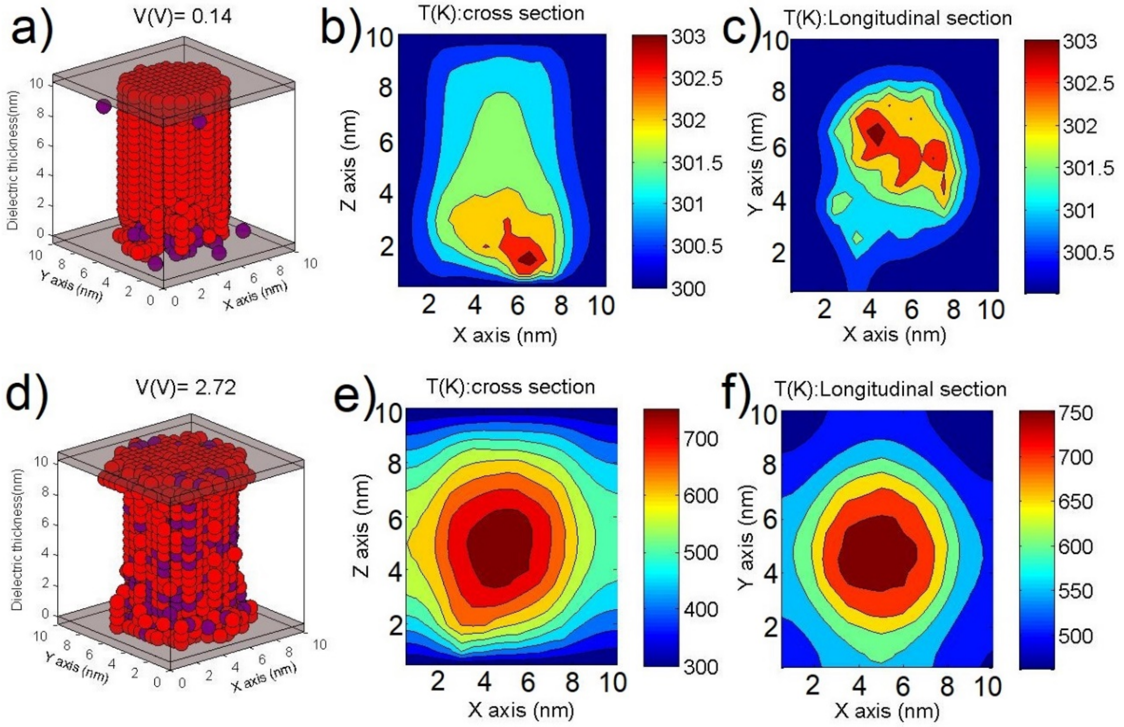

Figure 6.4-3. In a) and d) the percolation paths in the LRS of a RRAM are shown for two different voltages. The corresponding temperature distributions in ZX plane are shown in b) and e) and in XY plane in c) and f). The cross-sections for both representations are chosen where the maximum temperature is reached in the simulation domain.

6.5. Kinetic Monte Carlo (kMC) algorithm

As the devices employed here have stochastic nature (linked to the creation and rupture of the conduction filament), the kMC algorithm has been selected to be the core of the computational tool in order to reproduce in a coherent way the random behavior of the system. This algorithm solves problems using random numbers and relatively simple rules involving the random change of states of one atom at a time.

For the evolution of a system of atoms, the main simulation tool is based on molecular dynamics (MD). This approach shows a dynamical evolution that is a very accurate representation of the real physical system, which explains the popularity of the MD method. However, it presents a hurdle that is inherent to the nature of the physical description: an accurate integration requires time steps short enough ($\sim 10^{-15}\,s$) to resolve the atomic vibrations. Because of that, the total simulation time is usually less than one microsecond, while the processes we want to study take place on much longer time scales. kMC can overcome this limitation because the long-time dynamics of the systems under study consist of transitions between equilibrium states rather than the reproduction of a trajectory through every vibrational period. In this way, the kMC algorithm can reach longer time scales, typically seconds and often much well beyond [Voter2007].

These sorts of infrequent-event systems are characterized by the occasional transition between states with long periods of relative inactivity between these transitions. The case discussed here, expressed in an abstract manner, is the one in which each state corresponds to a single energy valley. In this sense, the long time between transitions arises because the system must surmount an energy barrier to get from one valley to another.

Adjacent to each state i there are other potential valleys separated from this state by an energy barrier. It is important to note that even if only one or a few atoms change their states, the entire system will change to a new state. In this way, the atoms do not move to other states, the entire system move from state to state. The property on which this kind of systems are based is that it remains in each state for a relatively long time (in comparison with the vibrational period) and so it "forgets" how it got there. Then, for each pathway to an adjacent valley there is a rate constant k_{ij} that characterizes the probability, per time unit, to move from the state i to the state j, being these rate constants independent of the beginning state i. That is the typical behavior of Markov's walk systems, i.e., the transition probabilities have nothing to do with the evolution "memory" of the system. Knowing all the transition rates for every state, the state-to-state trajectory would be indistinguishable from a trajectory generated by a molecular dynamics simulation (with a much higher computational cost) and, with this information, one can design a simple stochastic procedure that it is able to propagate the system from one state to another state and so on.

Taking into consideration a first-order process with exponential decay statistics, we can express the probability that the system has not yet changed its state from i in the following way:

$$p_{survival}(t) = exp(-k_{tot}t) \tag{6.5.1}$$

being k_{tot} the total rate for state changing. Thus, the distribution function $p(t)$ for the time of the first change of state at time t' (which must equate to $1 - p_{survival}(t')$) can be obtained by the negative of the time derivative of $p_{survival}(t)$:

$$p(t) = k_{tot}exp(-k_{tot}t) \tag{6.5.2}$$

Now we can obtain the average time for changing the state, τ, by means of the first moment of this distribution

$$\tau = \int_0^\infty tp(t)dt = \frac{1}{k_{tot}} \tag{6.5.3}$$

Each process in the system has its own rate k_{ij} and the total rate for changing the state would be the sum of these rates:

$$k_{tot} = \sum_j k_{ij} \tag{6.5.4}$$

Moreover, for each process there is again an exponential time distribution for changing the state

$$p_{ij}(t) = k_{ij}exp\left(-k_{ij}t\right) \tag{6.5.5}$$

Although only one event can be the first to happen.

In order to generate an exponentially distributed random number one can draw a random number r between $(0, 1)$ and then make use of (6.5.1):

$$t_{draw} = -(1/k)\ln r \tag{6.5.6}$$

Which is an appropriate realization for the time of the first change of state with transition rates k.

The previous elements are enough to design a stochastic algorithm that will propagate the system from state to state. It has to be assumed that all the rate constants are known for every state. The procedure for selecting which event occurs is indicated schematically in **Figure 6.5-1a**. It is supposed that for each of the M events there is an object with a length equals to the rate constant k_{ij}. Putting these objects end to end gives a total length of k_{tot} and then it can be chosen a random position along this stack of objects which would select the event to occur. In this manner, the probability of an occurring event will be proportional to the rate constant. Then, for the advance of the simulation time, it can be used equation 6.5.6 to get a random time of the magnitude needed that at least occurs one event. It is important to note that the time advance has nothing to do with which event is chosen as it only depends on the total rate constant k_{tot}. In every state change, the list of processes that can occur and each of the corresponding rate constants are updated to, afterwards, repeat the procedure.

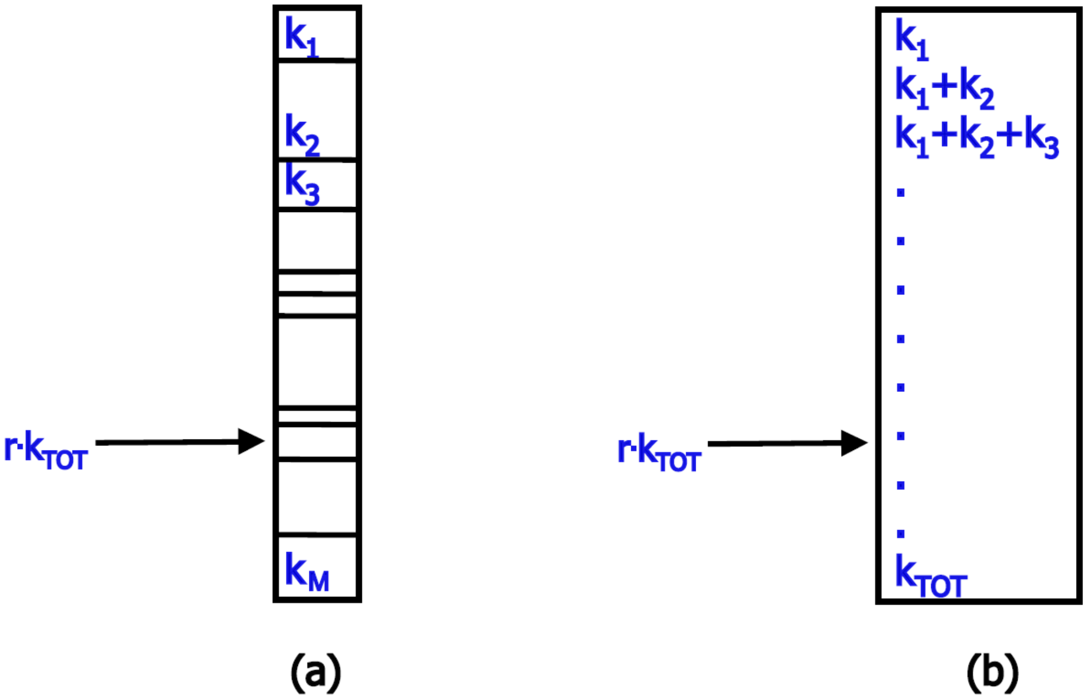

Figure 6.5-1. Schematic illustration of the way of selecting the occurring event to advance the system to the new state in the standard KMC algorithm. (a) The boxes represent the length of the objects in function of the rate constants k_{ij}. A random number r (0, 1), multiplied by k_{tot}, points to one box with the chosen event. (b) It can be implemented computationally comparing the rk_{tot} to the elements in an array of partial sums [Voter2007].

For the computational implementation of the algorithm we are considering, it can be made an array of partial sums, being the arrays element $s(j)$ the length of all the objects up to and including object j as shown in the **Figure 6.5-1b**. This would be the following expression:

$$s(j) = \sum_{q}^{j} k_{iq} \tag{6.5.7}$$

Then, generating a random number r between $(0, 1)$ and multiplying it by k_{tot} allow us to step through the array s until the first element for which $s(j) > rk_{tot}$, which would be the selected event. Finally, for the estimation of k_{ij} it can be assumed that there is a thermal ensemble and so the rate constants would be proportional to the Boltzmann probability of being at the dividing surface relative to the probability of being anywhere in state i. This can be approximated by:

$$k_{ij} = \nu \exp\left(-E_{static}/K_B T\right) \tag{6.5.8}$$

Being E_{static} the static barrier height (energy difference between the saddle point and the minimum), K_B the Boltzmann constant and ν a prefactor that is often in the range of $10^{12}\ s^{-1}$ and $10^{13}\ s^{-1}$.

6.6. Device fabrication and measurement description

Along this work, four different kinds of devices have been used in order to study the behavior of unipolar CBRAM (also known as thermochemical), bipolar CBRAM and VCM devices. In the four cases, the dielectric was hafnium oxide, but the electrodes were made of different materials. The unipolar CBRAM has a Ni top electrode and a Si bottom electrode. For the case of the bipolar CBRAM, it has a Cu top electrode and Pt bottom electrode. Concerning the VCM devices, the top electrodes are made TiN with an oxygen Ti storage layer. However, for the bottom electrode, one of them is made of W and the other one of TiN. The unipolar CBRAMs and one type of the VCM (the one which has the W bottom electrode) devices were fabricated at the Institut de Microelectrònica de Barcelona IMB-CNM (CSIC) Bellaterra, Spain. The bipolar CBRAM devices were made in the Laboratory of Nanofabrication and Novel Device Integration, Institute of Microelectronics, Chinese Academy of Sciences, Beijing. And finally, the VCM devices with the TiN bottom electrode were fabricated at the IHP-Leibniz-Institut für innovative Mikroelektronik, Frankfurt (Oder), Germany.

In the following sections the fabrication processes and the measurement descriptions are exposed.

6.6.1. $\mathbf{Ni/HfO_2/Si}$ devices (unipolar CBRAM)

These devices ($Ni/HfO_2/Si$) were fabricated at the Institut de Microelectrònica de Barcelona IMB-CNM (CSIC) Bellaterra, Spain. They were made on (1 0 0) n-type CZ silicon wafers with a resistivity of (0.007–0.013) Ω cm following a field-isolated process. The deposition of 5 nm thick HfO_2 layers were made by atomic layer deposition at 225 °C with tetrakis (dimethylamido)-hafnium (TDMAH) and H_2O as precursors. The 200 nm thickness top Ni electrode was deposited by magnetron sputtering [Chen2014].

A HP-4155B semiconductor parameter analyzer was controlled by GPIB with a PC, by means of MATLAB. The current-voltage (I-V) characteristics were measured at 300 K. These data are shown in **Figure 6.6-1a**, where a forming curve in black and several RS cycles in red and blue can be seen. Keysight B1500 semiconductor parameter analyzer, which is equipped with the waveform generator fast measurement unit (WGFMU) module, can be used for constant voltage stress measurements (CVS) for evaluating the forming time of the devices for instance. The Si substrate was grounded and a positive voltage was applied to the Ni electrode. A self-rectifying behavior can be observed in these devices as a consequence of a Schottky barrier between the metallic CF and the semiconductor. It can be seen in section **3.2** for a more physical explanation of the operation of these devices.

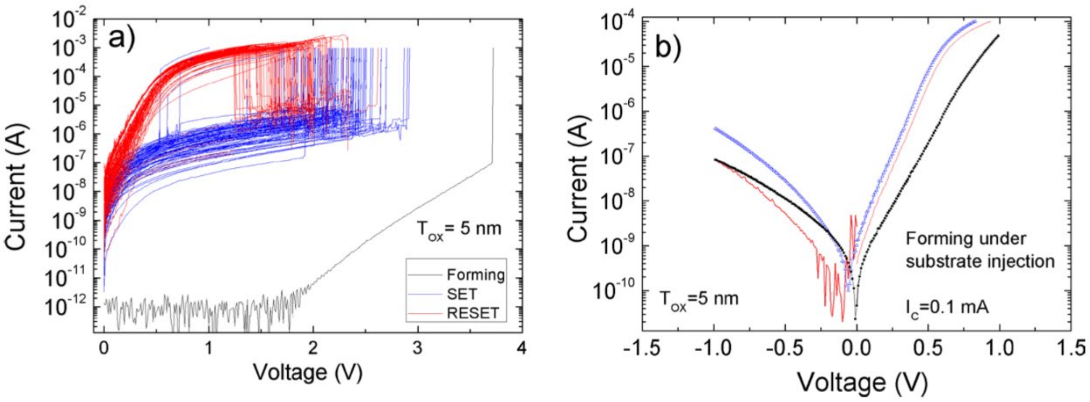

Figure 6.6-1. (a) Some typical characteristic curves of the Ni/HfO_2/Si devices fabricated. The data of the forming process and several RS cycles are plotted. b) I–V curves during the LRS. Due to the Schottky barrier (between the CF and the semiconductor) a self-rectifying behavior can be observed. Two decades of difference in the current is obtained for an external voltage of ±0.3 V [Aldana2017].

6.6.2. Cu/HfO_X/Pt devices (bipolar CBRAM)

These devices ($Cu/HfO_X/Pt$) were made at the Laboratory of Nanofabrication and Novel Device Integration, Institute of Microelectronics, Chinese Academy of Sciences, Beijing. The RRAMs are based on a Cu/HfO_X/Pt stack that is integrated with the transistor. The structures consist of transistors that were fabricated using standard 0.13 μm logic process. A Cu layer works as an electrode. Electron-beam evaporation is used for growing the HfO_X dielectric layer and the Pt electrode with 6 nm and 70 nm thicknesses. The pattern was made by lift-off process. The device size was 300 $nm \times 400\ nm$. Details about the fabrication and measurement process can be found in the literature [Liu2014, Sun2017].

A Keithley 4200 SCS semiconductor parameter analyzer can be used to measure the one transistor-one resistor (1T1R) structure. Several set/reset cycles are plotted in **Figure 6.6-2**. The curves for positive voltages correspond to SET processes and the negative voltages to RESET processes. Section **3.3** can be seen for a deeper explanation of the operation of these devices.

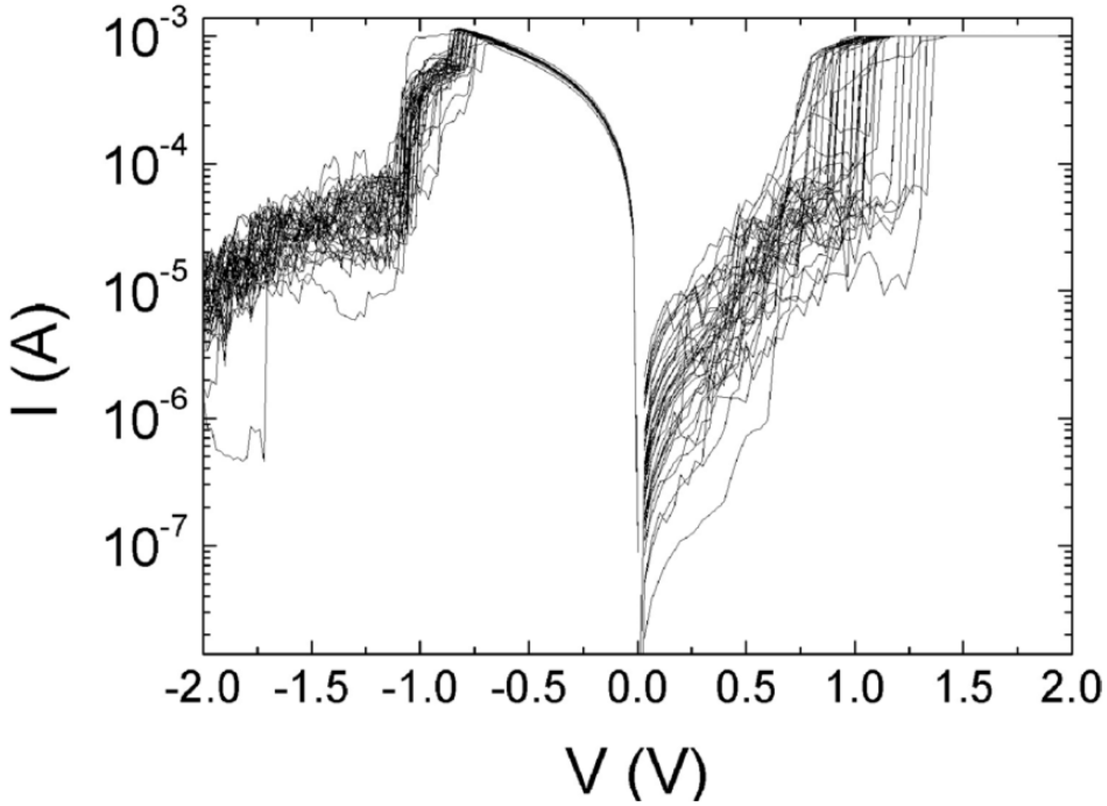

Figure 6.6-2. Some experimental curves of current versus applied voltage of Cu/HfO$_X$/Pt devices. [Aldana2018].

6.6.3. TiN/Ti/HfO$_2$/W devices (VMC)

These devices ($TiN/Ti/HfO_2/W$) were fabricated at the Institut de Microelectrònica de Barcelona IMB-CNM (CSIC) Bellaterra, Spain. The TiN/Ti/HfO2/W devices were processed on silicon wafers on a thermally grown 200 nm-thick silicon dioxide [Aldana2020]. A 10 nm HfO_2 layer at 225 ºC is grown with the atomic layer deposition (ALD) technique by means of TDMAH and H_2O as precursors and N2 as carrier and purge gas. Magnetron sputtering was used for depositing the top and bottom electrodes. The thickness of the bottom (W) and top electrodes (TiN) were 200 nm and the one of the oxygen storage layer (Ti) were 10 nm. The resulting structures are square cells of $5 \times 5\,\mu m^2$ and $15 \times 15\,\mu m^2$.

A HP-4155B semiconductor parameter analyzer (SPA) and a Keysight B1500 SPA equipped with a Waveform Generator and a Fast Measurement unit (WGFMU) can be used for the measurements. In the **Figure 6.6-3**, some current-voltage (I-V) curves with ramped voltage as well as with pulsed input voltage signals are plotted. The WGFMU can be used for measuring I–V characteristic curves synchronized with the applied waveform. The voltage was applied to the TiN/Ti top electrode, while the W bottom electrode was grounded. The instrumentation can be controlled by a software tool implemented in Matlab. Usually, a compliance current should be implemented (100 µA in this case) during the forming process to prevent the permanent breakdown of the dielectric. **Figure 6.6-3a** shows several RS cycles of ramped voltage measurements where voltages ranging from 0 V to 1 V for the SET process and from 0 V to -1.8 V for the RESET process were set. In **Figure 6.6-3b** and **Figure 6.6-3c** pulsed voltage signals have been employed, plotting four consecutive current versus time pulses with alternative positive 1.1 V and negative -1 V (-1.4 V) biases corresponding to SET and RESET processes. A detailed explanation for the operation of these devices can be found in the section **4.2**.

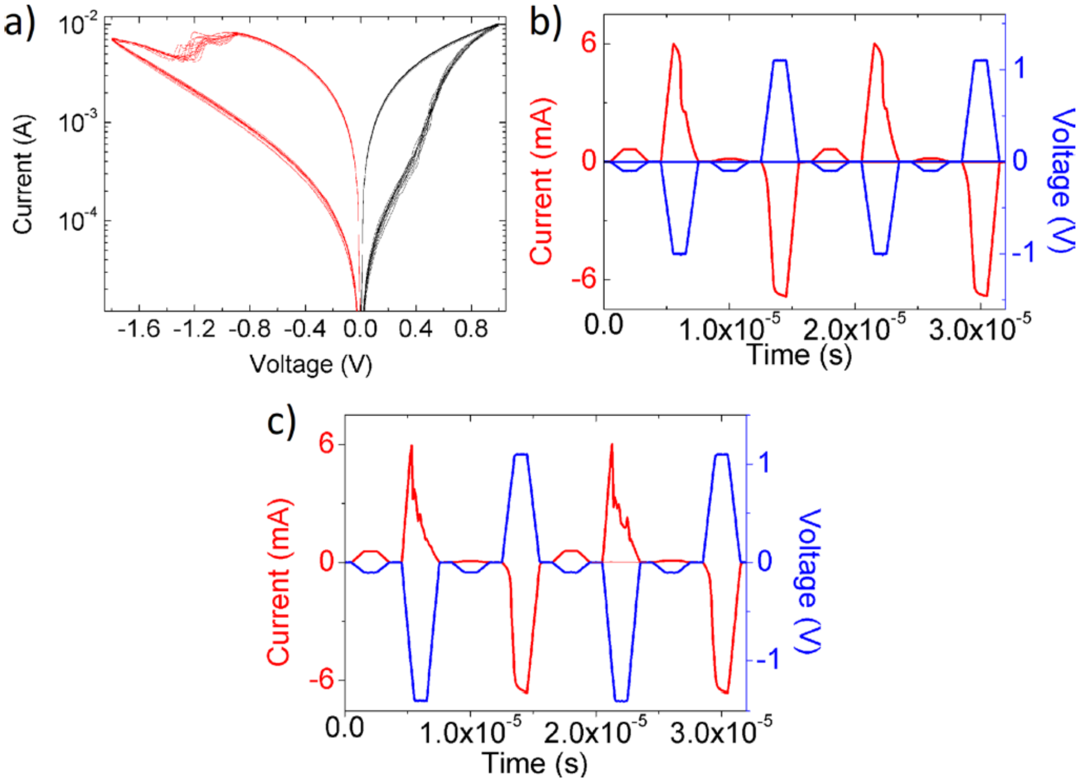

Figure 6.6-3. Typical experimental current for the TiN/Ti/HfO_2/W RRAMs. (a) I–V curves for ramped voltage measurements, (b) current versus time for four consecutive pulses with positive (1.1 V) and negative (–1 V) bias corresponding to SET and RESET processes, (c) Current versus time for four consecutive pulses with positive (1.1 V) and negative (–1.4 V) bias corresponding to SET and RESET processes [Aldana2020].

6.6.4. TiN/Ti/Al: HfO_2/TiN devices (VCM)

These devices $(TiN/Ti/Al\!:\!HfO_2/TiN)$ were fabricated at the IHP-Leibniz-Institut für innovative Mikroelektronik. Frankfurt (Oder), Germany. They are 1T1R cells integrated in 4 kbit arrays, which are formed by a select NMOS transistor, made in 0.25 µm CMOS technology, in series with a metal-insulator-metal (MIM) stack [Perez2019b]. The MIM structure is made of TiN top and bottom electrode with a thickness of 150 nm. These two layers were deposited by magnetron sputtering. The oxygen storage Ti layer is 7 nm thick and the Al-doped HfO_2 dielectric is 6 nm. These former two layers were deposited by atomic layer deposition (ALD) at 300 ºC with an Al content of about 10%. The MIM stack was patterned with an area of about 0.4 μm^2 and an additional thin Si_3N_4 layer was deposited to protect the RRAM cell.

Four batches of 128 1T1R cells were fabricated [Perez2019b]. Incremental step pulse with verify algorithm (ISPVA) can be used to program the cells to a common initial LRS. For the measuring of the experimental data, each batch was baked for 10 h at one of the following temperatures: 190, 210, 230, and 260 °C. Then, the evolution of the LRS conductance was measured every hour by using a read-out operation at 0.2 V. Making use of these data, **Figure 6.6-4** was plotted. The retention data experiments and their simulations can be found in section **4.3**.

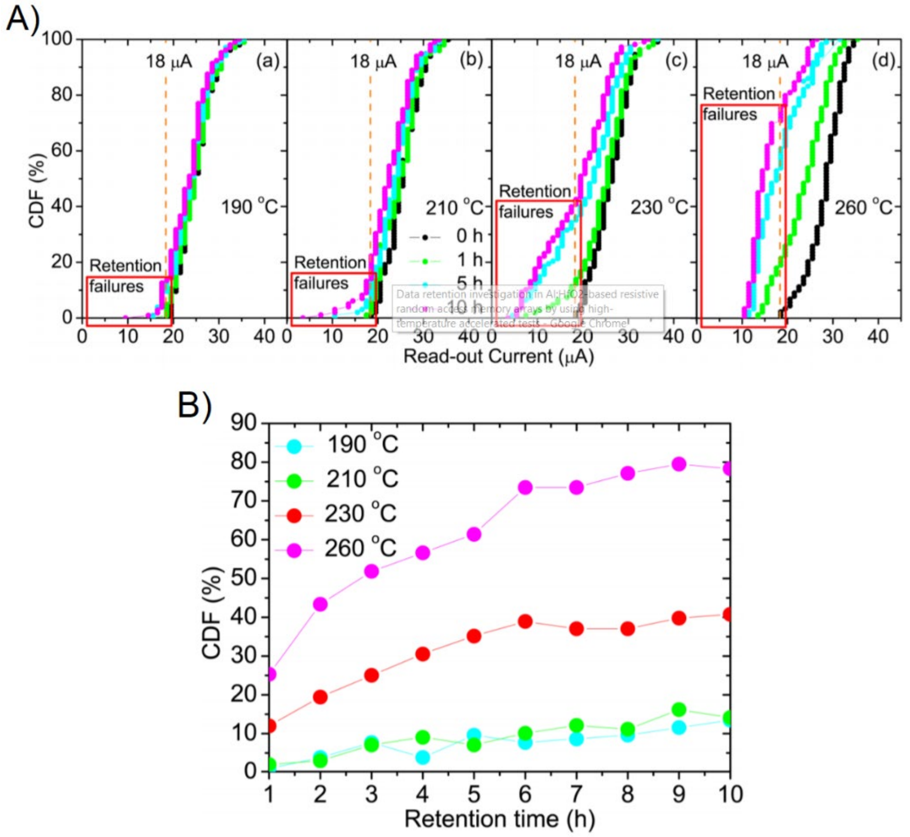

Figure 6.6-4. A) CDFs of the readout currents measured at four different times (0, 1, 5 and 10 hours) and four different temperatures (190°C ($A.a$), 210°C ($A.b$), 230°C ($A.c$) and 260°C ($A.d$)) [Perez2019b]. B) CDFs of retention failure time at four different temperatures: 190°C, 210°C, 230°C and 260°C [Perez2019b].

References

[Acal2019] Acal, C., Ruiz-Castro, J. E., Aguilera, A. M., Jiménez-Molinos, F., & Roldán, J. B. (2019). Phase-type distributions for studying variability in resistive memories. Journal of Computational and Applied Mathematics, 345, 23–32. DOI: 10.1016/j.cam.2018.06.010

[Aguilera-Morillo2019] Aguilera-Morillo, M. C., Aguilera, A. M., Jiménez-Molinos, F., & Roldán, J. B. (2019). Stochastic modeling of Random Access Memories reset transitions. Mathematics and Computers in Simulation, 159, 197–209. DOI: 10.1016/j.matcom.2018.11.016

[Ahn2015] Ahn, C., Jiang, Z., Lee, C. S., Chen, H. Y., Liang, J., Liyanage, L. S., & Wong, H. S. P. (2015). 1D selection device using carbon nanotube FETs for high-density cross-point memory arrays. IEEE Transactions on Electron Devices, 62(7), 2197-2204.

[Aldana2017] Aldana, S., García-Fernández, P., Rodríguez-Fernández, A., Romero-Zaliz, R., González, M. B., Jiménez-Molinos, F., ... & Roldán, J. B. (2017). A 3D kinetic Monte Carlo simulation study of resistive switching processes in Ni/HfO2/Si-n+-based RRAMs. Journal of Physics D: Applied Physics, 50(33), 335103.

[Aldana2018] S. Aldana, J. B. Roldán, P. García-Fernández, J. Suñe, R. Romero-Zaliz, F. Jiménez-Molinos, S. Long, F. Gómez-Campos, M. Liu, “An in-depth description of bipolar resistive switching in Cu/HfOx/Pt devices, a 3D kinetic Monte Carlo simulation approach”, Journal of Applied Physics, 123(15), 154501, 2018.

[Aldana2018b] Aldana, S., García-Fernández, P., Romero-Zaliz, R., Jiménez-Molinos, F., Gómez-Campos, F., & Roldán, J. B. (2018). Analysis of conductive filament density in resistive random access memories: a 3D kinetic Monte Carlo approach. Journal of Vacuum Science & Technology B, Nanotechnology and Microelectronics: Materials, Processing, Measurement, and Phenomena, 36(6), 062201.

[Aldana2018c] Aldana, S., García-Fernández, P., Romero-Zaliz, R., González, M. B., Jiménez-Molinos, F., Campabadal, F., ... & Roldán, J. B. (2018, November). A Kinetic Monte Carlo Simulator to Characterize Resistive Switching and Charge Conduction in Ni/HfO 2/Si RRAMs. In 2018 Spanish Conference on Electron Devices (CDE) (pp. 1-4). IEEE.

[Aldana2020] Aldana, S., García-Fernández, P., Romero-Zaliz, R., González, M. B., Jiménez-Molinos, F., Gómez-Campos, F., ... & Roldán, J. B. (2020). Resistive switching in HfO2 based valence change memories, a comprehensive 3D kinetic Monte Carlo approach. Journal of Physics D: Applied Physics, 53(22), 225106.

[Aldana2020b] Aldana, S., Pérez, E., Jimenez-Molinos, F., Wenger, C., & Roldan, J. B. (2020). Kinetic Monte Carlo analysis of data retention in Al: HfO2-based resistive random access memories. Semiconductor Science and Technology.

[Alibart2013] Alibart, F., Zamanidoost, E., & Strukov, D. B. (2013). Pattern classification by memristive crossbar circuits using ex situ and in situ training. Nature communications, 4(1), 1-7.

[Asamitsu1997] Asamitsu, A., Tomioka, Y., Kuwahara, H., & Tokura, Y. (1997). Current switching of resistive states in magnetoresistive manganites. Nature, 388(6637), 50-52.

[Atwood2004] Atwood, G. (2004). Future directions and challenges for ETox flash memory scaling. IEEE transactions on Device and Materials Reliability, 4(3), 301-305.

[Aziza2014] Aziza, H., Ayari, H., Onkaraiah, S., Portal, J. M., Moreau, M., & Bocquet, M. (2014, October). Oxide based resistive RAM: ON/OFF resistance analysis versus circuit variability. In 2014 IEEE International Symposium on Defect and Fault Tolerance in VLSI and Nanotechnology Systems (DFT) (pp. 81-85). IEEE.

[Baek2004] Baek, I. G., Lee, M. S., Seo, S., Lee, M. J., Seo, D. H., Suh, D. S., ... & Chung, U. I. (2004, December). Highly scalable nonvolatile resistive memory using simple binary oxide driven by asymmetric unipolar voltage pulses. In IEDM Technical Digest. IEEE International Electron Devices Meeting, 2004. (pp. 587-590). IEEE.

[Baek2007] Baek, S., Lee, D., Kim, J., Hong, S. H., Kim, O., & Ree, M. (2007). Novel digital nonvolatile memory devices based on semiconducting polymer thin films. Advanced Functional Materials, 17(15), 2637-2644.

[Baek2013] Baek, H., Lee, C., Choi, J., & Cho, J. (2013). Nonvolatile memory devices prepared from sol–gel derived niobium pentoxide films. Langmuir, 29(1), 380-386.

[Bai2013] Bai, W., Huang, R., Cai, Y., Tang, Y., Zhang, X., & Wang, Y. (2013). Record low-power organic RRAM with sub-20-nA reset current. IEEE electron device letters, 34(2), 223-225.

[Banerjee2017] Banerjee, W., Liu, Q., Lv, H., Long, S., & Liu, M. (2017). Electronic imitation of behavioral and psychological synaptic activities using TiO x/Al 2 O 3-based memristor devices. Nanoscale, 9(38), 14442-14450.

[Barrera2019] Barrera, D., Ibáñez, M. J., Jiménez-Molinos, F., Roldán, A. M., & Roldán, J. B. (2019). A spline quasi-interpolation based method to obtain the reset voltage in Resistive RAMs in the charge-flux domain. Journal of Computational and Applied Mathematics, 354, 326–333. DOI: 10.1016/j.cam.2017.12.020

[Benodekar1978] Benodekar, R. W., & Date, A. W. (1978). Finite difference procedure for solution of Poisson equation over complex domains with Neumann boundary conditions. Computers & Fluids, 6(2), 71-81.

[Berdan2016] Berdan, R., Vasilaki, E., Khiat, A., Indiveri, G., Serb, A., & Prodromakis, T. (2016). Emulating short-term synaptic dynamics with memristive devices. Scientific reports, 6(1), 1-9.

[Bersuker2010] Bersuker, G., Gilmer, D. C., Veksler, D., Yum, J., Park, H., Lian, S., ... & Shluger, A. (2010, December). Metal oxide RRAM switching mechanism based on conductive filament microscopic properties. In 2010 International Electron Devices Meeting (pp. 19-6). IEEE.

[Bez2003] Bez, R., Camerlenghi, E., Modelli, A., & Visconti, A. (2003). Introduction to flash memory. Proceedings of the IEEE, 91(4), 489-502.

[Bocquet2014] Bocquet, M., Aziza, H., Zhao, W., Zhang, Y., Onkaraiah, S., Muller, C., ... & Portal, J. M. (2014). Compact modeling solutions for oxide-based resistive switching memories (OxRAM). *Journal of Low Power Electronics and Applications*, *4*(1), 1-14.

[Bocquet2014b] Bocquet, M., Deleruyelle, D., Aziza, H., Muller, C., Portal, J. M., Cabout, T., & Jalaguier, E. (2014). Robust compact model for bipolar oxide-based resistive switching memories. IEEE Transactions on Electron Devices, 61(3), 674-681.

[Bradley2015] Bradley, S. R., Shluger, A. L., & Bersuker, G. (2015). Electron-injection-assisted generation of oxygen vacancies in monoclinic HfO 2. Physical Review Applied, 4(6), 064008.

[Brivio2014] Brivio, S., Tallarida, G., Cianci, E., & Spiga, S. (2014). Formation and disruption of conductive filaments in a HfO2/TiN structure. Nanotechnology, 25(38), 385705.

[Burr2010] Burr, G. W., Breitwisch, M. J., Franceschini, M., Garetto, D., Gopalakrishnan, K., Jackson, B., ... & Rajendran, B. (2010). Phase change memory technology. Journal of Vacuum Science & Technology B, Nanotechnology and Microelectronics: Materials, Processing, Measurement, and Phenomena, 28(2), 223-262.

[Calixto2020] Calixto, M., Maldonado, D., Miranda, E., & Roldan, J. B. (2020). Modeling of the temperature effects in filamentary-type resistive switching memories using quantum point-contact theory. Journal of Physics D: Applied Physics.

[Cao2009] Cao, X., Li, X., Gao, X., Yu, W., Liu, X., Zhang, Y., ... & Cheng, X. (2009). Forming-free colossal resistive switching effect in rare-earth-oxide Gd 2 O 3 films for memristor applications. Journal of Applied Physics, 106(7), 073723.

[Carboni2019] Carboni, R., & Ielmini, D. (2019). Stochastic memory devices for security and computing. Advanced Electronic Materials, 5(9), 1900198.

[Cazorla2019] Cazorla, M., Aldana, S., Maestro, M., González, M. B., Campabadal, F., Moreno, E., … Roldán, J. B. (2019). Thermal study of multilayer resistive random access memories based on HfO2 and Al2O3 oxides. Journal of Vacuum Science & Technology B, 37(1), 012204. DOI: 10.1116/1.5058294

[Celano2015] Celano, U., Goux, L., Degraeve, R., Fantini, A., Richard, O., Bender, H., ... & Vandervorst, W. (2015). Imaging the three-dimensional conductive channel in filamentary-based oxide resistive switching memory. Nano letters, 15(12), 7970-7975.

[Chae2008] Chae, S. C., Lee, J. S., Kim, S., Lee, S. B., Chang, S. H., Liu, C., ... & Seo, S. (2008). Random circuit breaker network model for unipolar resistance switching. Advanced Materials, 20(6), 1154-1159.

[Chai2011] Chai, Y., Wu, Y., Takei, K., Chen, H. Y., Yu, S., Chan, P. C., ... & Wong, H. S. P. (2011). Nanoscale bipolar and complementary resistive switching memory based on amorphous carbon. IEEE transactions on electron devices, 58(11), 3933-3939.

[Chawa2016] Chawa, M. M. A., Picos, R., Garcia-Moreno, E., Stavrinides, S. G., Roldan, J. B., & Jimenez-Molinos, F. (2016). An analytical energy model for the reset transition in unipolar resistive-switching RAMs. Proceedings of the 18th Mediterranean Electrotechnical Conference: Intelligent and Efficient Technologies and Services for the Citizen, MELECON 2016, (April), 1–4. DOI: 10.1109/MELCON.2016.7495318

[Chawa2018] Al Chawa, M. M., Picos, R., Roldan, J. B., Jimenez-Molinos, F., Villena, M. A., & de Benito, C. (2018). Exploring resistive switching-based memristors in the charge–flux domain: A modeling approach. International Journal of Circuit Theory and Applications, 46(1), 29–38. DOI: https://doi.org/10.1002/cta.2397

[Chen2005] Chen, A., Haddad, S., Wu, Y. C., Fang, T. N., Lan, Z., Avanzino, S., ... & Tripsas, N. (2005, December). Non-volatile resistive switching for advanced memory applications. In IEEE InternationalElectron Devices Meeting, 2005. IEDM Technical Digest. (pp. 746-749). IEEE.

[Chen2010] Chen, Y. S., Lee, H. Y., Chen, P. S., Wu, T. Y., Wang, C. C., Tzeng, P. J., ... & Lien, C. (2010). An Ultrathin Forming-Free $\hbox {HfO} _ {x} $ Resistance Memory With Excellent Electrical Performance. IEEE electron device letters, 31(12), 1473-1475.

[Chen2010b] Chen, C., Yang, Y. C., Zeng, F., & Pan, F. (2010). Bipolar resistive switching in Cu/AlN/Pt nonvolatile memory device. Applied Physics Letters, 97(8), 083502.

[Chen2011] Chen, S. C., Chang, T. C., Chen, S. Y., Chen, C. W., Chen, S. C., Sze, S. M., ... & Yeh, F. S. (2011). Bipolar resistive switching of chromium oxide for resistive random access memory. Solid-state electronics, 62(1), 40-43.

[Chen2012] Chen, Y. Y., Degraeve, R., Clima, S., Govoreanu, B., Goux, L., Fantini, A., ... & Jurczak, M. (2012, December). Understanding of the endurance failure in scaled HfO 2-based

1T1R RRAM through vacancy mobility degradation. In 2012 International Electron Devices Meeting (pp. 20-3). IEEE.

[Chen2012b] Chen, C., Song, C., Yang, J., Zeng, F., & Pan, F. (2012). Oxygen migration induced resistive switching effect and its thermal stability in W/TaO x/Pt structure. Applied Physics Letters, 100(25), 253509.

[Chen2013] Chen, G., Song, C., & Pan, F. (2013). Improved resistive switching stability of Pt/ZnO/CoO x/ZnO/Pt structure for nonvolatile memory devices. Rare Metals, 32(6), 544-549.

[Chen2013b] Chen, C., Gao, S., Zeng, F., Tang, G. S., Li, S. Z., Song, C., ... & Pan, F. (2013). Migration of interfacial oxygen ions modulated resistive switching in oxide-based memory devices. Journal of Applied Physics, 114(1), 014502.

[Chen2014] Chen, Z. X., Fang, Z., Wang, Y., Yang, Y., Kamath, A., Wang, X. P., ... & Wu, Y. H. (2014). Impact of Ni concentration on the performance of Ni silicide/HfO 2/TiN resistive RAM (RRAM) cells. Journal of electronic materials, 43(11), 4193-4198.

[Chen2016] Chen, A. (2016). A review of emerging non-volatile memory (NVM) technologies and applications. Solid-State Electronics, 125, 25-38.

[Chiu2014] Chiu, F. C. (2014). A review on conduction mechanisms in dielectric films. Advances in Materials Science and Engineering, 2014.

[Choi2005] Choi, B. J., Jeong, D. S., Kim, S. K., Rohde, C., Choi, S., Oh, J. H., ... & Reichenberg, B. (2005). Resistive switching mechanism of TiO 2 thin films grown by atomic-layer deposition. Journal of applied physics, 98(3), 033715.

[Choi2013] Choi, B. J., Torrezan, A. C., Norris, K. J., Miao, F., Strachan, J. P., Zhang, M. X., ... & Williams, R. S. (2013). Electrical performance and scalability of Pt dispersed SiO2 nanometallic resistance switch. Nano letters, 13(7), 3213-3217.

[Chua1971] Chua, L. (1971). Memristor-the missing circuit element. IEEE Transactions on circuit theory, 18(5), 507-519.

[Clima2015] Clima, S., Chen, Y. Y., Fantini, A., Goux, L., Degraeve, R., Govoreanu, B., ... & Jurczak, M. (2015). Intrinsic tailing of resistive states distributions in amorphous HfO x and TaO x based resistive random access memories. IEEE Electron Device Letters, 36(8), 769-771.

[Covi2016] Covi, E., Brivio, S., Serb, A., Prodromakis, T., Fanciulli, M., & Spiga, S. (2016, May). HfO2-based memristors for neuromorphic applications. In 2016 IEEE International Symposium on Circuits and Systems (ISCAS) (pp. 393-396). IEEE.

[Dawson1991] Dawson, C. N., Du, Q., & Dupont, T. F. (1991). A finite difference domain decomposition algorithm for numerical solution of the heat equation. Mathematics of Computation, 57(195), 63-71.

[Degraeve2014] Degraeve, R., Fantini, A., Raghavan, N., Goux, L., Clima, S., Chen, Y. Y., ... & Roussel, P. (2014, June). Hourglass concept for RRAM: a dynamic and statistical device model. In Proceedings of the 21th International Symposium on the Physical and Failure Analysis of Integrated Circuits (IPFA) (pp. 245-249). IEEE.

[Deleonibus2014] Deleonibus, S. (Ed.). (2014). Intelligent Integrated Systems: Devices, Technologies, and Architectures (Vol. 1). CRC Press.

[Dirkmann2018] Dirkmann, S., Kaiser, J., Wenger, C., & Mussenbrock, T. (2018). Filament growth and resistive switching in hafnium oxide memristive devices. ACS applied materials & interfaces, 10(17), 14857-14868.

[Duncan2016] Duncan, D., Magyari-Köpe, B., & Nishi, Y. (2016). Filament-induced anisotropic oxygen vacancy diffusion and charge trapping effects in hafnium oxide RRAM. IEEE Electron Device Letters, 37(4), 400-403.

[Duncan2017] Duncan, D., Magyari-Köpe, B., & Nishi, Y. (2017). Properties of Dopants in HfO x for Improving the Performance of Nonvolatile Memory. Physical Review Applied, 7(3), 034020.

[Fantini2013] Fantini, A., Goux, L., Degraeve, R., Wouters, D. J., Raghavan, N., Kar, G., ... & Jurczak, M. (2013, May). Intrinsic switching variability in HfO 2 RRAM. In 2013 5th IEEE International Memory Workshop (pp. 30-33). IEEE.

[Fantini2015] Fantini, A., Gorine, G., Degraeve, R., Goux, L., Chen, C. Y., Redolfi, A., ... & Jurczak, M. (2015, December). Intrinsic program instability in HfO2 RRAM and consequences on program algorithms. In 2015 IEEE International Electron Devices Meeting (IEDM) (pp. 7-5). IEEE.

[Fatullayev2002] Fatullayev, A. G. (2002). Numerical solution of the inverse problem of determining an unknown source term in a heat equation. Mathematics and Computers in Simulation, 58(3), 247-253.

[Feng2010] Feng, P. A. N., Chao, C. H. E. N., Wang, Z. S., Yang, Y. C., Jing, Y. A. N. G., & Fei, Z. E. N. G. (2010). Nonvolatile resistive switching memories-characteristics, mechanisms and challenges. Progress in Natural Science: Materials International, 20, 1-15.

[Frohman-Bentchkowsky1971] Frohman-Bentchkowsky, D. (1971). Memory behavior in a floating-gate avalanche-injection MOS (FAMOS) structure. Applied Physics Letters, 18(8), 332-334.

[Fujiwara2008] Fujiwara, K., Nemoto, T., Rozenberg, M. J., Nakamura, Y., & Takagi, H. (2008). Resistance switching and formation of a conductive bridge in metal/binary oxide/metal structure for memory devices. Japanese Journal of Applied Physics, 47(8R), 6266.

[Gao2009] Gao, B., Zhang, H. W., Yu, S., Sun, B., Liu, L. F., Liu, X. Y., ... & Wang, Y. Y. (2009, June). Oxide-based RRAM: Uniformity improvement using a new material-oriented methodology. In 2009 Symposium on VLSI Technology (pp. 30-31). IEEE.

[Gao2010] Gao, B., Kang, J. F., Zhang, H. W., Sun, B., Chen, B., Liu, L. F., ... & Yu, H. Y. (2010, September). Oxide-based RRAM: Physical based retention projection. In 2010 Proceedings of the European Solid State Device Research Conference (pp. 392-395). IEEE.

[Gao2012] Gao, S., Song, C., Chen, C., Zeng, F., & Pan, F. (2012). Dynamic processes of resistive switching in metallic filament-based organic memory devices. The Journal of Physical Chemistry C, 116(33), 17955-17959.

[Gao2013] Gao, S., Song, C., Chen, C., Zeng, F., & Pan, F. (2013). Formation process of conducting filament in planar organic resistive memory. Applied Physics Letters, 102(14), 141606.

[Garcia-Redondo2016] Garcia-Redondo, F., Gowers, R. P., Crespo-Yepes, A., López-Vallejo, M., & Jiang, L. (2016). SPICE compact modeling of bipolar/unipolar memristor switching governed by electrical thresholds. *IEEE Transactions on Circuits and Systems I: Regular Papers*, *63*(8), 1255-1264.

[Ginestra] Ginestra simulator. Applied Materils. Link.

[González-Cordero2016] G. Gonzalez-Cordero, J. B. Roldan, F. Jimenez-Molinos, J. Suñé, S. Long and M. Liu, "A new compact model for bipolar RRAMs based on truncated cone conductive filaments, a Verilog-A approach," Semiconductor Science and Technology, vol. 31, no. 11, pp. 1–13, 2016. DOI: 10.1088/0268-1242/31/11/115013

[González-Cordero2016b] G. González-Cordero, F. Jiménez-Molinos, J. B. Roldan, M. B. González and F. Campabadal, "Transient SPICE simulation of Ni/HfO2/Si-n+ resistive memories," in XXXI edition of the Design of Circuits and Integrated Systems Conference (DCIS), 2016 in Granada, Spain.

[González-Cordero2016c] G. González-Cordero, J. B. Roldan, and F. Jiménez-Molinos, "Simulation of RRAM memory circuits, a Verilog-A compact modeling approach," in XXXI edition of the Design of Circuits and Integrated Systems Conference (DCIS), 2016 in Granada, Spain. DOI: 10.1109/DCIS.2016.7845386

[González-Cordero2016d] G. González-Cordero, J. B. Roldan and F. Jiménez-Molinos (2016). A model for circuit simulation of bipolar RRAMs based on conductive filaments with truncated cone shapes. In Jornadas de Investigadores en Formación Fomentando la interdisciplinariedad (JIFFI). Granada, Spain.

[González-Cordero2016e] G. González-Cordero, F. Jiménez-Molinos, M. A. Villena and J. B. Roldan. (2016) SPICE simulation of thermal reset transitions in Ni/HfO2/Si-n+ RRAMs including quantum effects. In 19th Workshop on Dielectrics in Microelectronics (Wodim). Catania, Italy.

[González-Cordero2017] G. González-Cordero, F. Jiménez-Molinos, J. B. Roldan, M. B. González and F. Campabadal "In-depth study of the physics behind resistive switching in TiN/Ti/HfO2/W structures,". Journal of Vacuum Science and Technology B. 35, 01A110 (2017). DOI: 10.1116/1.4973372

[González-Cordero2017b] G. González-Cordero, M. B. González, H. García, F. Campabadal, S. Dueñas, H. Castán, F. Jiménez-Molinos and J. B. Roldán, "A physically based model for resistive memories including a detailed temperature and variability description", Microelectronic Engineering, Volume 178, 25 June 2017, Pages 26-29. DOI: 10.1016/j.mee.2017.04.019

[González-Cordero2017c] G. González-Cordero, J. B. Roldán, F. Jiménez-Molinos, "SPICE simulation of RRAM circuits. A compact modeling perspective", in 11th edition of the Spanish Conference on Electron Devices (CDE), 2017 in Barcelona, Spain. DOI: 10.1109/CDE.2017.7905250

[González-Cordero2017d] G. González-Cordero, M. B. González, H. García, F. Jiménez-Molinos, F. Campabadal, S. Dueñas, H. Castán and J. B. Roldán, "A Physically Based Model to describe Resistive Switching in different RRAM technologies", in 11th edition of the Spanish Conference on Electron Devices (CDE), 2017 in Barcelona, Spain. DOI: 10.1109/CDE.2017.7905223

[González-Cordero2017e] G. González-Cordero, J. B. Roldán, F. Jiménez-Molinos. (2017). A time dependent thermal model for RRAM circuit simulation. In 20th Conference on "Insulating Films on Semiconductors (INFOS), Potsdam, Germany

[González-Cordero2019] Gonzalez-Cordero, G. (2019). Compact Modeling of Memristors Based on Resistive Switching Devices.

[González-Cordero2019a] Gerardo González-Cordero, Mireia B. González, Francisco Jiménez-Molinos, Francesca Campabadal, and Juan Bautista Roldán. "New method to analyze random telegraph signals in resistive random access memories" Journal of Vacuum Science and Technology B. 37, 012203 (2019). DOI: 10.1116/1.50593840

[González-Cordero2019b] G. González-Cordero, M. Pedro, J. Martin-Martinez, M.B. González, F. Jiménez-Molinos, F. Campabadal, N. Nafría, J.B. Roldán. "Analysis of resistive switching processes in TiN/Ti/HfO2/W devices to mimic electronic synapses in neuromorphic circuits" Solid State Electronics, Volume 157, July 2019, Pages 25-33. DOI: 10.1016/j.sse.2019.04.001

[González-Cordero2019c] G. González-Cordero, M.B. González, F. Campabadal, F. Jiménez-Molinos, J.B. Roldán. "A new technique to analyze RTN signals in resistive memories"

Microelectronic Engineering, Volume 215, 15 July 2019, 110994 DOI: 10.1016/j.mee.2019.110994

[González-Cordero2019d] G. Gonzalez-Cordero, M.B. González, A. Morell, F. Jiménez-Molinos, F. Campabadal, J.B. Roldán, "Neural network based analysis of Random Telegraph Noise in Resistive Random Access Memories," Semiconductor Science and Technology, (Accepted for publication on December 4, 2019). DOI: 10.1088/1361-6641/ab6103

[Govoreanu2011] Govoreanu, B., Kar, G. S., Chen, Y. Y., Paraschiv, V., Kubicek, S., Fantini, A., ... & Jossart, N. (2011, December). 10× 10nm 2 Hf/HfO x crossbar resistive RAM with excellent performance, reliability and low-energy operation. In 2011 International Electron Devices Meeting (pp. 31-6). IEEE.

[Guan2008] Guan, W., Liu, M., Long, S., Liu, Q., & Wang, W. (2008). On the resistive switching mechanisms of Cu/ZrO 2: Cu/Pt. Applied Physics Letters, 93(22), 223506.

[Gupta2019] Gupta, V., Kapur, S., Saurabh, S., & Grover, A. (2019). Resistive Random Access Memory: A Review of Device Challenges. IETE Technical Review, 1-14.

[Guy2015] Guy, J., Molas, G., Blaise, P., Bernard, M., Roule, A., Le Carval, G., ... & De Salvo, B. (2015). Investigation of forming, SET, and data retention of conductive-bridge random-access memory for stack optimization. IEEE Transactions on Electron Devices, 62(11), 3482-3489.

[Hasegawa2010] Tsuruoka, T., Terabe, K., Hasegawa, T., & Aono, M. (2010). Forming and switching mechanisms of a cation-migration-based oxide resistive memory. Nanotechnology, 21(42), 425205.

[He2009] He, C. L., Zhuge, F., Zhou, X. F., Li, M., Zhou, G. C., Liu, Y. W., ... & Wu, Y. H. (2009). Nonvolatile resistive switching in graphene oxide thin films. Applied Physics Letters, 95(23), 232101.

[Horiuchi2008] Horiuchi, S., & Tokura, Y. (2008). Organic ferroelectrics. Nature materials, 7(5), 357-366.

[Hoshen1976] Hoshen, J., & Kopelman, R. (1976). Percolation and cluster distribution. I. Cluster multiple labeling technique and critical concentration algorithm. Physical Review B, 14(8), 3438.

[Huang2010] Huang, J. J., Kuo, C. W., Chang, W. C., & Hou, T. H. (2010). Transition of stable rectification to resistive-switching in Ti/TiO 2/Pt oxide diode. Applied Physics Letters, 96(26), 262901.

[Huang2013] Huang, P., Liu, X. Y., Chen, B., Li, H. T., Wang, Y. J., Deng, Y. X., ... & Zhang, X. (2013). A physics-based compact model of metal-oxide-based RRAM DC and AC operations. IEEE transactions on electron devices, 60(12), 4090-4097.

[Hui2017] Hui, F., Grustan-Gutierrez, E., Long, S., Liu, Q., Ott, A. K., Ferrari, A. C., & Lanza, M. (2017). Graphene and related materials for resistive random access memories. Advanced Electronic Materials, 3(8), 1600195.

[Ibáñez2019] Ibáñez, M. J., Jiménez-Molinos, F., Roldán, J. B., & Yáñez, R. (2019). Estimation of the reset voltage in resistive RAMs using the charge–flux domain and a numerical method based on quasi-interpolation and discrete orthogonal polynomials. Mathematics and Computers in Simulation, 164, 120–130. DOI: 10.1016/j.matcom.2018.09.028

[Ielmini2009] Ielmini, D. (2009). Reliability issues and modeling of flash and post-flash memory. Microelectronic Engineering, 86(7-9), 1870-1875.

[Ielmini2015] Ielmini, D., & Waser, R. (Eds.). (2015). Resistive switching: from fundamentals of nanoionic redox processes to memristive device applications. John Wiley & Sons.

[Ielmini2016] Ielmini, D. (2016). Resistive switching memories based on metal oxides: mechanisms, reliability and scaling. Semiconductor Science and Technology, 31(6), 063002.

[Ielmini2017] Ielmini, D., & Milo, V. (2017). Physics-based modeling approaches of resistive switching devices for memory and in-memory computing applications. Journal of Computational Electronics, 16(4), 1121-1143.

[Ielmini2018] Ielmini, D. (2018). Brain-inspired computing with resistive switching memory (RRAM): Devices, synapses and neural networks. Microelectronic Engineering, 190, 44-53.

[Ismail2014] Ismail, M., Huang, C. Y., Panda, D., Hung, C. J., Tsai, T. L., Jieng, J. H., ... & Talib, I. (2014). Forming-free bipolar resistive switching in nonstoichiometric ceria films. Nanoscale research letters, 9(1), 1-8.

[Jiang2016] Jiang, H., & Stewart, D. A. (2016). Enhanced oxygen vacancy diffusion in Ta2O5 resistive memory devices due to infinitely adaptive crystal structure. Journal of Applied Physics, 119(13), 134502.

[Jiménez-Molinos2015] Jiménez-Molinos, F., Villena, M. A., Roldan, J. B., & Roldan, A. M. (2015). A SPICE Compact Model for Unipolar RRAM Reset Process Analysis. IEEE Transactions on Electron Devices, 62(3), 955–962. DOI: 10.1109/TED.2014.2387429

[Jiménez-Molinos2017] Jiménez-Molinos, F., G. Gonzalez-Cordero, G., Cartujo-Cassinello, P., & Roldan, J. B. (2017). SPICE modelling of RRAM thermal reset transitions for circuit simulation purposes. In 2017 Spanish Conference on Electron Devices (CDE) (pp. 1–4). DOI: 10.1109/CDE.2017.7905227

[Jin2012] Jin, C., Lee, J., Lee, E., Hwang, E., & Lee, H. (2012). Nonvolatile resistive memory of ferrocene covalently bonded to reduced graphene oxide. Chemical Communications, 48(35), 4235-4237.

[Jo2008] Jo, S. H., & Lu, W. (2008). CMOS compatible nanoscale nonvolatile resistance switching memory. Nano letters, 8(2), 392-397.

[Jo2010] Jo, S. H., Chang, T., Ebong, I., Bhadviya, B. B., Mazumder, P., & Lu, W. (2010). Nanoscale memristor device as synapse in neuromorphic systems. Nano letters, 10(4), 1297-1301.

[Jung2017] Jung, K., Magyari-Köpe, B., & Nishi, Y. (2017). Hydrogen-induced oxygen vacancy bistability and its impact on RRAM device operation. IEEE Electron Device Letters, 38(6), 728-731.

[Kamiya2012] Kamiya, K. (2012). MY yang, SG Park, BM Kope, Y. Nishi, M. Niwa, K. Shiraishi, ON-OFF switching mechanism of resistive-random-access-memories based on the formation and disruption of oxygen conducting channels. Appl. Phys. Lett, 100, 073502.

[Kang2015] Kang, J. F., Gao, B., Huang, P., Li, H. T., Zhao, Y. D., Chen, Z., ... & Liu, X. Y. (2015, December). Oxide-based RRAM: Requirements and challenges of modeling and simulation. In 2015 IEEE International Electron Devices Meeting (IEDM) (pp. 5-4). IEEE.

[Kawahara2013] A. Kawahara, R. Azuma, Y. Ikeda, K. Kawai, Y. Katoh, Y. Hayakawa, K. Tsuji, S. Yoneda, A. Himeno, et al., “An 8 Mb Multi-Layered Cross-Point ReRAM Macro With 443 MB/s Write Throughput”, IEEE J. Solid-State Circuits 48, pp. 178-185, 2013.

[Kim2006] Kim, K. M., Choi, B. J., Jeong, D. S., Hwang, C. S., & Han, S. (2006). Influence of carrier injection on resistive switching of Ti O 2 thin films with Pt electrodes. Applied physics letters, 89(16), 162912.

[Kim2010] Kim, K. H., Hyun Jo, S., Gaba, S., & Lu, W. (2010). Nanoscale resistive memory with intrinsic diode characteristics and long endurance. Applied Physics Letters, 96(5), 053106.

[Kim2010b] Kim, S., Jeong, H. Y., Choi, S. Y., & Choi, Y. K. (2010). Comprehensive modeling of resistive switching in the Al/TiO x/TiO 2/Al heterostructure based on space-charge-limited conduction. Applied Physics Letters, 97(3), 033508.

[Kim2011] Kim, H. D., An, H. M., Seo, Y., & Kim, T. G. (2011). Transparent resistive switching memory using ITO/AlN/ITO capacitors. IEEE electron device letters, 32(8), 1125-1127.

[Kim2012] Kim, T. W., Zeigler, D. F., Acton, O., Yip, H. L., Ma, H., & Jen, A. K. Y. (2012). All-Organic Photopatterned One Diode-One Resistor Cell Array for Advanced Organic Nonvolatile Memory Applications. Advanced Materials, 24(6), 828-833.

[Kim2013] Kim, H. D., An, H. M., Hong, S. M., & Kim, T. G. (2013). Forming-free Si N-based resistive switching memory prepared by RF sputtering. physica status solidi (a), 210(9), 1822-1827.

[Kim2014] Kim, S., Choi, S., & Lu, W. (2014). Comprehensive physical model of dynamic resistive switching in an oxide memristor. ACS nano, 8(3), 2369-2376.

[Kohlstedt2005] Kohlstedt, H., Pertsev, N. A., Contreras, J. R., & Waser, R. (2005). Theoretical current-voltage characteristics of ferroelectric tunnel junctions. Physical Review B, 72(12), 125341.

[Kreupl2008] Kreupl, F., Bruchhaus, R., Majewski, P., Philipp, J. B., Symanczyk, R., Happ, T., ... & Graham, A. P. (2008, December). Carbon-based resistive memory. In 2008 IEEE International Electron Devices Meeting (pp. 1-4). IEEE.

[Kwan2007] Kwan, W. L., Tseng, R. J., Wu, W., Pei, Q., & Yang, Y. (2007, December). Stackable resistive memory device using photo cross-linkable copolymer. In 2007 IEEE International Electron Devices Meeting (pp. 237-240). IEEE.

[Lanza2009] Lanza, M., Porti, M., Nafria, M., Aymerich, X., Sebastiani, A., Ghidini, G., ... & Fasoli, M. (2009). Combined Nanoscale and Device-Level Degradation Analysis of SiO_2 Layers of MOS Nonvolatile Memory Devices. IEEE Transactions on Device and Materials Reliability, 9(4), 529-536.

[Lanza2014] Lanza, M. (2014). A review on resistive switching in high-k dielectrics: A nanoscale point of view using conductive atomic force microscope. Materials, 7(3), 2155-2182.

[Lanza2019] Lanza, M., Wong, H. S. P., Pop, E., Ielmini, D., Strukov, D., Regan, B. C., ... & Belmonte, A. (2019). Recommended methods to study resistive switching devices. Advanced Electronic Materials, 5(1), 1800143.

[Lee2002] Lee, J. D., Hur, S. H., & Choi, J. D. (2002). Effects of floating-gate interference on NAND flash memory cell operation. IEEE Electron Device Letters, 23(5), 264-266.

[Lee2010] Lee, H. Y., Chen, Y. S., Chen, P. S., Gu, P. Y., Hsu, Y. Y., Wang, S. M., ... & Lin, W. P. (2010, December). Evidence and solution of over-RESET problem for HfO x based resistive memory with sub-ns switching speed and high endurance. In 2010 International Electron Devices Meeting (pp. 19-7). IEEE.

[Lee2012] Lee, J. K., Jung, S., Park, J., Chung, S. W., Sung Roh, J., Hong, S. J., ... & Lee, J. H. (2012). Accurate analysis of conduction and resistive-switching mechanisms in double-layered resistive-switching memory devices. Applied Physics Letters, 101(10), 103506.

[Lee2013] Lee, M. J., Lee, D., Cho, S. H., Hur, J. H., Lee, S. M., Seo, D. H., ... & Uddin, M. R. (2013). A plasma-treated chalcogenide switch device for stackable scalable 3D nanoscale memory. Nature communications, 4(1), 1-8.

[Lee2015] Lee, J. S., Lee, S., & Noh, T. W. (2015). Resistive switching phenomena: A review of statistical physics approaches. Applied Physics Reviews, 2(3), 031303.

[Lei2009] Lei, B., Kwan, W. L., Shao, Y., & Yang, Y. (2009). Statistical characterization of the memory effect in polyfluorene based non-volatile resistive memory devices. Organic Electronics, 10(6), 1048-1053.

[Liao2011] Liao, Z., Gao, P., Meng, Y., Zhao, H., Bai, X., Zhang, J., & Chen, D. (2011). Electroforming and endurance behavior of Al/Pr0. 7Ca0. 3MnO3/Pt devices. Applied Physics Letters, 99(11), 113506.

[Lim2015] Lim, E. W., & Ismail, R. (2015). Conduction mechanism of valence change resistive switching memory: a survey. Electronics, 4(3), 586-613.

[Linares-Barranco2011] Linares-Barranco, B., Serrano-Gotarredona, T., Camuñas-Mesa, L. A., Perez-Carrasco, J. A., Zamarreño-Ramos, C., & Masquelier, T. (2011). On spike-timing-dependent-plasticity, memristive devices, and building a self-learning visual cortex. Frontiers in neuroscience, 5, 26.

[Lin2013] Lin, Y. S., Zeng, F., Tang, S. G., Liu, H. Y., Chen, C., Gao, S., ... & Pan, F. (2013). Resistive switching mechanisms relating to oxygen vacancies migration in both interfaces in Ti/HfOx/Pt memory devices. Journal of Applied Physics, 113(6), 064510.

[Liu2009] Liu, Q., Long, S., Wang, W., Zuo, Q., Zhang, S., Chen, J., & Liu, M. (2009). Improvement of Resistive Switching Properties in $\hbox {ZrO} _ {2} $-Based ReRAM With Implanted Ti Ions. IEEE Electron Device Letters, 30(12), 1335-1337.

[Liu2012] Liu, S. H., Yang, W. L., Wu, C. C., Chao, T. S., Ye, M. R., Su, Y. Y., ... & Tsai, M. J. (2012). High-performance polyimide-based ReRAM for nonvolatile memory application. IEEE Electron Device Letters, 34(1), 123-125.

[Liu2014] Liu, H., Lv, H., Yang, B., Xu, X., Liu, R., Liu, Q., ... & Liu, M. (2014). Uniformity improvement in 1T1R RRAM with gate voltage ramp programming. IEEE Electron Device Letters, 35(12), 1224-1226.

[Liu2014b] T.Y. Liu, T. H. Yan, R. Scheuerlein, Y. Chen, J. K. Lee, G. Balakrishnan, G. Yee, H. Zhang, A. Yap et al., "A 130.7-mm2 2-Layer 32-Gb ReRAM Memory Device in 24-nm Technology" IEEE J. Solid-State Circuits 49, pp. 140-153, 2014

[Long2013] Long, S., Perniola, L., Cagli, C., Buckley, J., Lian, X., Miranda, E., ... & Suné, J. (2013). Voltage and power-controlled regimes in the progressive unipolar RESET transition of HfO 2-based RRAM. Scientific reports, 3(1), 1-8.

[Lu2012] Lu, W., Jeong, D. S., Kozicki, M., & Waser, R. (2012). Electrochemical metallization cells—blending nanoionics into nanoelectronics?. MRS bulletin, 37(2), 124-130.

[Lu2016] Lu, N. D., Zong, Z. W., Sun, P. X., Li, L., Liu, Q., Lv, H. B., ... & Liu, M. (2016, September). Thermal effect and compact model in three-dimensional (3D) RRAM arrays. In 2016 International Conference on Simulation of Semiconductor Processes and Devices (SISPAD) (pp. 161-164). IEEE.

[Ma2000] Ma, T. P., & Han, J. P. (2000). U.S. Patent No. 6,067,244. Washington, DC: U.S. Patent and Trademark Office.

[Ma2002] Ma, T. P., & Han, J. P. (2002). Why is nonvolatile ferroelectric memory field-effect transistor still elusive?. IEEE Electron Device Letters, 23(7), 386-388.

[Maldonado2019] Maldonado, D., Roldán, A. M., González, M. B., Jiménez-Molinos, F., Campabadal, F., & Roldán, J. B. (2019). Influence of magnetic field on the operation of TiN/Ti/HfO2/W resistive memories. Microelectronic Engineering, 215(April). DOI: 10.1016/j.mee.2019.110983

[Maestro-Izquierdo2019] Maestro-Izquierdo, M., Gonzalez, M. B., & Campabadal, F. (2019). Mimicking the spike-timing dependent plasticity in HfO2-based memristors at multiple time scales. Microelectronic Engineering, 215, 111014.

[Maestro-Izquierdo2020] Maestro-Izquierdo, M., Gonzalez, M. B., Jimenez-Molinos, F., Moreno, E., Roldan, J. B., & Campabadal, F. (2020). Unipolar resistive switching behavior in Al2O3/HfO2 multilayer dielectric stacks: fabrication, characterization and simulation. Nanotechnology, 31(13), 135202.

[Matveyev2016] Matveyev, Y., Kirtaev, R., Fetisova, A., Zakharchenko, S., Negrov, D., & Zenkevich, A. (2016). Crossbar Nanoscale HfO 2-Based Electronic Synapses. Nanoscale research letters, 11(1), 1-6.

[Menzel2009] S. Menzel, B. Klopstra, C. Kügeler, U. Böttger, G. Staikov, R. Waser, "A simulation model of resistive switching in electrochemical metallization memory cells (ECM)", MRS Online Proceedings Library Archive, 1160, 101–106, 2009.

[Menzel2015] S. Menzel, P. Kaupmann, R. Waser, "Understanding filamentary growth in electrochemical metallization memory cells using kinetic Monte Carlo simulations", Nanoscale, 7, 12673, 2015.

[Merolla2014] Merolla, P. A., Arthur, J. V., Alvarez-Icaza, R., Cassidy, A. S., Sawada, J., Akopyan, F., ... & Brezzo, B. (2014). A million spiking-neuron integrated circuit with a scalable communication network and interface. Science, 345(6197), 668-673.

[Miranda2001] Miranda, E., & Sune, J. (2001, April). Analytic modeling of leakage current through multiple breakdown paths in SiO/sub 2/films. In 2001 IEEE International Reliability Physics Symposium Proceedings. 39th Annual (Cat. No. 00CH37167) (pp. 367-379). IEEE.

[Miranda2012] Miranda, E., Kano, S., Dou, C., Kakushima, K., Suñé, J., & Iwai, H. (2012). Nonlinear conductance quantization effects in CeOx/SiO2-based resistive switching devices. Applied Physics Letters, 101(1), 012910.

[Molina2017] Molina, J., Torres, R., Ranjan, A., & Pey, K. L. (2017). Resistive switching characteristics of MIM structures based on oxygen-variable ultra-thin HfO2 and fabricated at low temperature. Materials Science in Semiconductor Processing, 66, 191-199.

[Mott2004] Mott, N. (2004). Metal-insulator transitions. CRC Press.

[Munjal2019] Munjal, S., & Khare, N. (2019). Advances in resistive switching based memory devices. Journal of Physics D: Applied Physics, 52(43), 433002.

[Nagel2011] Nagel, J. R. (2011). Solving the generalized poisson equation using the finite-difference method (FDM). Lecture Notes, Dept. of Electrical and Computer Engineering, University of Utah.

[Nardi2011] Nardi, F., Balatti, S., Larentis, S., & Ielmini, D. (2011, December). Complementary switching in metal oxides: Toward diode-less crossbar RRAMs. In 2011 International Electron Devices Meeting (pp. 31-1). IEEE.

[Niu2016] Niu, G., Calka, P., der Maur, M. A., Santoni, F., Guha, S., Fraschke, M., ... & Wenger, C. (2016). Geometric conductive filament confinement by nanotips for resistive switching of HfO 2-RRAM devices with high performance. Scientific reports, 6(1), 1-9.

[O'Hara2014] O'Hara, A., Bersuker, G., & Demkov, A. A. (2014). Assessing hafnium on hafnia as an oxygen getter. Journal of Applied Physics, 115(18), 183703.

[Onofrio2015] Onofrio, N., Guzman, D., & Strachan, A. (2015). Atomic origin of ultrafast resistance switching in nanoscale electrometallization cells. Nature materials, 14(4), 440-446.

[Ouyang2013] Ouyang, J. (2013). Solution-processed PEDOT: PSS films with conductivities as indium tin oxide through a treatment with mild and weak organic acids. ACS applied materials & interfaces, 5(24), 13082-13088.

[Ouyang2014] Ouyang, J. (2014). Temperature-sensitive asymmetrical bipolar resistive switches of polymer: nanoparticle memory devices. Organic Electronics, 15(9), 1913-1922.

[Ouyang2016] Ouyang, J. (2016). Emerging Resistive Switching Memories. Springer International Publishing.

[Pan2011] F. Pan, S. Yin, V. Subramanian, "A detailed study of the forming stage of an electrochemical resistive switching memory by KMC simulation", IEEE Electron Device Letters, 32, pp. 949-951, 2011.

[Pan2014] Pan, F., Gao, S., Chen, C., Song, C., & Zeng, F. (2014). Recent progress in resistive random access memories: materials, switching mechanisms, and performance. Materials Science and Engineering: R: Reports, 83, 1-59.

[Panzer2009] Panzer, M. A., Shandalov, M., Rowlette, J. A., Oshima, Y., Chen, Y. W., McIntyre, P. C., & Goodson, K. E. (2009). Thermal properties of ultrathin hafnium oxide gate dielectric films. IEEE Electron Device Letters, 30(12), 1269-1271.

[Patterson2018] Patterson, G. A., Suñé, J., & Miranda, E. (2018). SPICE simulation of memristive circuits based on memdiodes with sigmoidal threshold functions. International Journal of Circuit Theory and Applications, 46(1), 39-49.

[Pazienza2011] Pazienza, G. E., & Albo-Canals, J. (2011). Teaching memristors to EE undergraduate students [class notes]. IEEE Circuits and Systems magazine, 11(4), 36-44.

[Peng2012] Peng, C. S., Chang, W. Y., Lee, Y. H., Lin, M. H., Chen, F., & Tsai, M. J. (2012). Improvement of resistive switching stability of HfO2 films with Al doping by atomic layer deposition. Electrochemical and Solid State Letters, 15(4), H88.

[Perez2019] Pérez, E., Maldonado, D., Acal, C., Ruiz-Castro, J. E., Alonso, F. J., Aguilera, A. M., … Roldán, J. B. (2019). Analysis of the statistics of device-to-device and cycle-to-cycle variability in TiN/Ti/Al:HfO2/TiN RRAMs. Microelectronic Engineering, 214(April), 104–109. DOI: 10.1016/j.mee.2019.05.004

[Perez2019b] Perez, E., Mahadevaiah, M. K., Zambelli, C., Olivo, P., & Wenger, C. (2019). Data retention investigation in Al: HfO2-based resistive random access memory arrays by using high-temperature accelerated tests. Journal of Vacuum Science & Technology B, Nanotechnology and Microelectronics: Materials, Processing, Measurement, and Phenomena, 37(1), 012202.

[Perez2019c] Pérez, E., Mahadevaiah, M. K., Zambelli, C., Olivo, P., & Wenger, C. (2019). Characterization of the interface-driven 1st Reset operation in HfO2-based 1T1R RRAM devices. Solid-State Electronics, 159, 51-56.

[Pickett2012] Pickett, M. D., & Williams, R. S. (2012). Sub-100 fJ and sub-nanosecond thermally driven threshold switching in niobium oxide crosspoint nanodevices. Nanotechnology, 23(21), 215202.

[Picos2015] Picos, R., Roldan, J. B., Al Chawa, M. M., Garcia-Fernandez, P., Jimenez-Molinos, F., & Garcia-Moreno, E. (2015). Semiempirical Modeling of Reset Transitions in Unipolar Resistive-Switching based Memristors. Radioengineering, 24(2), 420–424. DOI: 10.13164/re.2015.0420

[Picos2016] Picos, R., Roldan, J. B., Chawa, M. M. Al, Jimenez-Molinos, F., & Garcia-Moreno, E. (2016). A physically based circuit model to account for variability in memristors with resistive switching operation. In 2016 Conference on Design of Circuits and Integrated Systems (DCIS) (pp. 1–6). IEEE. DOI: 10.1109/DCIS.2016.7845383

[Pietronero1988] Pietronero, L., & Wiesmann, H. J. (1988). From physical dielectric breakdown to the stochastic fractal model. Zeitschrift für Physik B Condensed Matter, 70(1), 87-93.

[Poblador2018] Poblador, S., Gonzalez, M. B., & Campabadal, F. (2018). Investigation of the multilevel capability of TiN/Ti/HfO2/W resistive switching devices by sweep and pulse programming. Microelectronic Engineering, 187, 148-153.

[Poblador2020] Poblador, S., Maestro-Izquierdo, M., Zabala, M., González, M. B., & Campabadal, F. (2020). Methodology for the characterization and observation of filamentary spots in HfOx-based memristor devices. Microelectronic Engineering, 223, 111232.

[Prezioso2015] Prezioso, M., Merrikh-Bayat, F., Hoskins, B. D., Adam, G. C., Likharev, K. K., & Strukov, D. B. (2015). Training and operation of an integrated neuromorphic network based on metal-oxide memristors. Nature, 521(7550), 61-64.

[Privitera2015] Privitera, S., Bersuker, G., Lombardo, S., Bongiorno, C., & Gilmer, D. C. (2015). Conductive filament structure in HfO2 resistive switching memory devices. Solid-State Electronics, 111, 161-165.

[Puglisi2016] Puglisi, F. M., Larcher, L., Pan, C., Xiao, N., Shi, Y., Hui, F., & Lanza, M. (2016, December). 2D h-BN based RRAM devices. In 2016 IEEE International Electron Devices Meeting (IEDM) (pp. 34-8). IEEE.

[Qi2018] Qi, M., Tao, Y., Wang, Z., Xu, H., Zhao, X., Liu, W., ... & Liu, Y. (2018). Highly uniform switching of HfO2− x based RRAM achieved through Ar plasma treatment for low power and multilevel storage. Applied Surface Science, 458, 216-221.

[Qin2012] Qin, S., Zhang, J., Fu, D., Xie, D., Wang, Y., Qian, H., ... & Yu, Z. (2012). A physics/circuit-based switching model for carbon-based resistive memory with sp 2/sp 3 cluster conversion. Nanoscale, 4(20), 6658-6663.

[Raghavan2012] Raghavan, N., Pey, K. L., Wu, X., Liu, W., & Bosman, M. (2012). Percolative model and thermodynamic analysis of oxygen-ion-mediated resistive switching. IEEE electron device letters, 33(5), 712-714.

[Ranuárez2006] Ranuárez, J. C., Deen, M. J., & Chen, C. H. (2006). A review of gate tunneling current in MOS devices. Microelectronics reliability, 46(12), 1939-1956.

[Rao2016] Rao, K. D. M., Sagade, A. A., John, R., Pradeep, T., & Kulkarni, G. U. (2016). Defining Switching Efficiency of Multilevel Resistive Memory with PdO as an Example. Advanced Electronic Materials, 2(2), 1500286.

[Recktenwald2004] Recktenwald, G. W. (2004). Finite-difference approximations to the heat equation. Mechanical Engineering, 10, 1-27.

[Reed2001] Reed, M. A., Chen, J., Rawlett, A. M., Price, D. W., & Tour, J. M. (2001). Molecular random access memory cell. Applied physics letters, 78(23), 3735-3737.

[Roldán2018] J.B. Roldán, E. Miranda, G. González-Cordero, P. García- Fernández, R. Romero-Zaliz, P. González-Rodelas, A. M. Aguilera, M.B. González, F. Jiménez-Molinos. “Multivariate analysis and extraction of parameters in resistive RAMs using the Quantum Point Contact model” Journal of Applied Physics, 2018, 123, 014501. DOI: 10.1063/1.5006995

[Roldán2019] Roldán, J. B., Alonso, F. J., Aguilera, A. M., Maldonado, D., & Lanza, M. (2019). Time series statistical analysis: A powerful tool to evaluate the variability of resistive switching memories. Journal of Applied Physics, 125(17), 174504. DOI: 10.1063/1.5079409

[Sawa2004] Sawa, A., Fujii, T., Kawasaki, M., & Tokura, Y. (2004). Hysteretic current–voltage characteristics and resistance switching at a rectifying Ti∕ Pr 0.7 Ca 0.3 Mn O 3 interface. Applied Physics Letters, 85(18), 4073-4075.

[Schindler2007] Schindler, C., Thermadam, S. C. P., Waser, R., & Kozicki, M. N. (2007). Bipolar and Unipolar Resistive Switching in Cu-Doped SiO_2. IEEE Transactions on Electron Devices, 54(10), 2762-2768.

[Schindler2009] Schindler, C., Staikov, G., & Waser, R. (2009). Electrode kinetics of Cu–Si O 2-based resistive switching cells: Overcoming the voltage-time dilemma of electrochemical metallization memories. Applied physics letters, 94(7), 072109.

[Seo2004] Seo, S., Lee, M. J., Seo, D. H., Jeoung, E. J., Suh, D. S., Joung, Y. S., ... & Kim, J. S. (2004). Reproducible resistance switching in polycrystalline NiO films. Applied Physics Letters, 85(23), 5655-5657.

[Shi2017] Shi, Y., Pan, C., Chen, V., Raghavan, N., Pey, K. L., Puglisi, F. M., ... & Lanza, M. (2017, December). Coexistence of volatile and non-volatile resistive switching in 2D h-BN based electronic synapses. In 2017 IEEE International Electron Devices Meeting (IEDM) (pp. 5-4). IEEE.

[Siebeneicher2012] Siebeneicher, P., Kleemann, H., Leo, K., & Lüssem, B. (2012). Non-volatile organic memory devices comprising SiO2 and C60 showing 104 switching cycles. Applied Physics Letters, 100(19), 105.

[Silvaco] Silvaco, Inc. Link.

[Son2010] Son, J. Y., Shin, Y. H., Kim, H., & Jang, H. M. (2010). NiO resistive random access memory nanocapacitor array on graphene. ACS nano, 4(5), 2655-2658.

[Song2000] Song, S., Miller, K. D., & Abbott, L. F. (2000). Competitive Hebbian learning through spike-timing-dependent synaptic plasticity. Nature neuroscience, 3(9), 919-926.

[Song2011] Song, H., Reed, M. A., & Lee, T. (2011). Single molecule electronic devices. Advanced Materials, 23(14), 1583-1608.

[Southwick2009] Southwick, R. G., Reed, J., Buu, C., Butler, R., Bersuker, G., & Knowlton, W. B. (2009). Limitations of Poole–Frenkel Conduction in Bilayer HfO_2/SiO_2 MOS Devices. *IEEE Transactions on device and materials reliability*, *10*(2), 201-207.

[Sun2013] Sun, J., Wu, X., Liu, Q., Liu, M., & Sun, L. T. (2013, July). Real time observation of nanoscale multiple conductive filaments in RRAM by using advanced in-situ TEM. In

Proceedings of the 20th IEEE International Symposium on the Physical and Failure Analysis of Integrated Circuits (IPFA) (pp. 560-562). IEEE.

[Sun2017] Sun, H., Zhang, M., Li, Y., Long, S., Liu, Q., Lv, H., ... & Liu, M. (2017). A cell-based clustering model for the reset statistics in RRAM. Applied Physics Letters, 110(12), 123503.

[Symanczyk2007] Symanczyk, R., Keller, J., Kund, M., Muller, G., Ruf, B., Albarede, P. H., ... & Duch, A. (2007, November). Conductive bridging memory development from single cells to 2Mbit memory arrays. In 2007 Non-Volatile Memory Technology Symposium (pp. 71-75). IEEE.

[Synopsys] Synopsys Inc. Link.

[Tallarida2009] Tallarida, G., Huby, N., Kutrzeba-Kotowska, B., Spiga, S., Arcari, M., Csaba, G., ... & Bez, R. (2009, May). Low temperature rectifying junctions for crossbar non-volatile memory devices. In 2009 IEEE International Memory Workshop (pp. 1-3). IEEE.

[Tang2013] Tang, G. S., Zeng, F., Chen, C., Liu, H. Y., Gao, S., Li, S. Z., ... & Pan, F. (2013). Resistive switching with self-rectifying behavior in Cu/SiO x/Si structure fabricated by plasma-oxidation. Journal of Applied Physics, 113(24), 244502.

[Tang2013b] Tang, G. S., Zeng, F., Chen, C., Gao, S., Fu, H. D., Song, C., ... & Pan, F. (2013). Resistive switching behaviour of a tantalum oxide nanolayer fabricated by plasma oxidation. physica status solidi (RRL)–Rapid Research Letters, 7(4), 282-284.

[Terabe2005] Terabe, K., Hasegawa, T., Nakayama, T., & Aono, M. (2005). Quantized conductance atomic switch. Nature, 433(7021), 47-50.

[Timsit1998] Timsit, S. (1998, October). Electrical contact resistance: properties of stationary interfaces. In Electrical Contacts-1998. Proceedings of the Forty-Fourth IEEE Holm Conference on Electrical Contacts (Cat. No. 98CB36238) (pp. 1-19). IEEE.

[Tour2003] Tour, J. M., Cheng, L., Nackashi, D. P., Yao, Y., Flatt, A. K., St. Angelo, S. K., ... & Franzon, P. D. (2003). Nanocell electronic memories. Journal of the American Chemical Society, 125(43), 13279-13283.

[Tsai2013] Tsai, C. L., Xiong, F., Pop, E., & Shim, M. (2013). Resistive random access memory enabled by carbon nanotube crossbar electrodes. Acs Nano, 7(6), 5360-5366.

[Valov2013] Valov, I., Linn, E., Tappertzhofen, S., Schmelzer, S., van den Hurk, J., Lentz, F., & Waser, R. (2013). Nanobatteries in redox-based resistive switches require extension of memristor theory. Nature communications, 4(1), 1-9.

[Vandelli2011] G. Bersuker, D. C. Gilmer, D. Veksler, P. Kirsch, L. Vandelli, A. Padovani, L. Larcher, K. McKenna, A. Shluger, V. Iglesias, M. Porti and M. Nafría, “Metal oxide resistive memory switching mechanism based on conductive filament properties”, Journal of Applied Physics, 110, 124518, 2011.

[Vandelli2011b] Vandelli, L., Padovani, A., Bersuker, G., Gilmer, D., Pavan, P., & Larcher, L. (2011, May). Modeling of the forming operation in HfO2-based resistive switching memories. In 2011 3rd IEEE International Memory Workshop (IMW) (pp. 1-4). IEEE.

[Vandelli2013] L. Larcher, A. Padovani, L. Vandelli, "A simulation framework for modeling charge transport and degradation in high-k stacks", Journal of Computational Electronics, 12(4), 658-665, 2013.

[Vandelli2015] A. Padovani, L. Larcher, O. Pirrotta, L. Vandelli, G. Bersuker, "Microscopic Modeling of HfO x RRAM Operations: From Forming to Switching", IEEE Transactions on Electron Devices, 62(6), pp. 1998-2006, 2015.

[videoBipolar] Complementary material to "S. Aldana, J. B. Roldán, P. García-Fernández, J. Suñe, R. Romero-Zaliz, F. Jiménez-Molinos, S. Long, F. Gómez-Campos, M. Liu, "An in-depth description of bipolar resistive switching in Cu/HfOx/Pt devices, a 3D kinetic Monte Carlo simulation approach", Journal of Applied Physics, 123(15), 154501, 2018". Video link. URL: https://youtu.be/G0YacFensM4

[videoUnipolar] Complementary material to "Aldana, S., García-Fernández, P., Rodríguez-Fernández, A., Romero-Zaliz, R., González, M. B., Jiménez-Molinos, F., ... & Roldán, J. B. (2017). A 3D kinetic Monte Carlo simulation study of resistive switching processes in Ni/HfO2/Si-n+-based RRAMs. Journal of Physics D: Applied Physics, 50(33), 335103". Video link. URL: https://youtu.be/Rvm88B2AMLY

[videoVCM] Complementary material to "Aldana, S., García-Fernández, P., Romero-Zaliz, R., González, M. B., Jiménez-Molinos, F., Gómez-Campos, F., ... & Roldán, J. B. (2020). Resistive switching in HfO2 based valence change memories, a comprehensive 3D kinetic Monte Carlo approach. Journal of Physics D: Applied Physics, 53(22), 225106.". Video link. URL: https://www.youtube.com/watch?v=OLk4eJNc_Y8

[Villena2013] Villena, M. A., Jiménez-Molinos, F., Roldán, J. B., Suñé, J., Long, S., Lian, X., ... & Liu, M. (2013). An in-depth simulation study of thermal reset transitions in resistive switching memories. Journal of Applied Physics, 114(14), 144505. DOI: 10.1063/1.4824292

[Villena2014] Villena, M. A., González, M. B., Jiménez-Molinos, F., Campabadal, F., Roldán, J. B., Suñé, J., ... & Miranda, E. (2014). Simulation of thermal reset transitions in resistive switching memories including quantum effects. Journal of Applied Physics, 115(21), 214504. DOI: 10.1063/1.4881500

[Villena2014b] Villena, M. A., Roldán, J. B., Jimenez-Molinos, F., Suñé, J., Long, S., Miranda, E., & Liu, M. (2014). A comprehensive analysis on progressive reset transitions in RRAMs. Journal of Physics D: Applied Physics, 47(20). DOI: 10.1088/0022-3727/47/20/205102

[Villena2015] Villena, M. A., González, M. B., Roldán, J. B., Campabadal, F., Jiménez-Molinos, F., Gómez-Campos, F. M., & Suñé, J. (2015). An in-depth study of thermal effects in reset transitions in HfO2 based RRAMs. Solid-State Electronics, 111, 47–51. DOI: 10.1016/j.sse.2015.04.008

[Villena2015b] Villena Sánchez, M. A. (2018). Estudio, modelado y simulación de memorias RRAM. Villena2018

[Villena2016] Villena, M. A., Roldán, J. B., González, M. B., González-Rodelas, P., Jiménez-Molinos, F., Campabadal, F., & Barrera, D. (2016). A new parameter to characterize the charge transport regime in Ni/HfO2 /Si-n+ -based RRAMs. Solid-State Electronics, 118, 56–60. DOI: 10.1016/j.sse.2016.01.007

[Villena2017] Villena, M. A., Roldán, J. B., Jiménez-Molinos, F., Miranda, E., Suñé, J., & Lanza, M. (2017). SIM^2RRAM: a physical model for RRAM devices simulation. Journal of Computational Electronics, 16(4), 1095-1120. DOI: 10.1007/s10825-017-1074-8

[Villena2017b] Villena, M. A., Roldán, J. B., García-Fernández, P., & Jiménez-Molinos, F. (2017). Effects of the extension of conductive filaments, a simulation approach. Journal of Vacuum Science & Technology B, Nanotechnology and Microelectronics: Materials, Processing, Measurement, and Phenomena, 35(1), 01A105. DOI: 10.1116/1.4971384

[Voter2007] Voter, A. F. (2007). Introduction to the kinetic Monte Carlo method. In Radiation effects in solids (pp. 1-23). Springer, Dordrecht.

[Vourkas2015] Vourkas, I., Batsos, A., & Sirakoulis, G. C. (2015). SPICE modeling of nonlinear memristive behavior. International Journal of Circuit Theory and Applications, 43(5), 553-565.

[Walczyk2009] Walczyk, C., Wenger, C., Sohal, R., Lukosius, M., Fox, A., Dąbrowski, J., ... & Schroeder, T. (2009). Pulse-induced low-power resistive switching in Hf O 2 metal-insulator-metal diodes for nonvolatile memory applications. Journal of Applied Physics, 105(11), 114103.

[Walczyk2011] Walczyk, C., Walczyk, D., Schroeder, T., Bertaud, T., Sowinska, M., Lukosius, M., ... & Wenger, C. (2011). Impact of Temperature on the Resistive Switching Behavior of Embedded HfO_2-Based RRAM Devices. IEEE transactions on electron devices, 58(9), 3124-3131.

[Wang2010] Wang, S. Y., Huang, C. W., Lee, D. Y., Tseng, T. Y., & Chang, T. C. (2010). Multilevel resistive switching in Ti/Cu x O/Pt memory devices. Journal of Applied Physics, 108(11), 114110.

[Wang2015] Wang, L. G., Qian, X., Cao, Y. Q., Cao, Z. Y., Fang, G. Y., Li, A. D., & Wu, D. (2015). Excellent resistive switching properties of atomic layer-deposited Al 2 O 3/HfO 2/Al 2 O 3 trilayer structures for non-volatile memory applications. Nanoscale research letters, 10(1), 1-8.

[Wang2019] Wang, Z., Li, C., Song, W., Rao, M., Belkin, D., Li, Y., ... & Strachan, J. P. (2019). Reinforcement learning with analogue memristor arrays. Nature Electronics, 2(3), 115-124.

[Waser2009] Waser, R., Dittmann, R., Staikov, G., & Szot, K. (2009). Redox-based resistive switching memories–nanoionic mechanisms, prospects, and challenges. Advanced materials, 21(25-26), 2632-2663.

[Waser2010] Waser, R., & Aono, M. (2010). Nanoionics-based resistive switching memories. In Nanoscience And Technology: A Collection of Reviews from Nature Journals (pp. 158-165).

[Waser2012] R. Waser, "Nanoelectronics and Information Technology", 3rd ed., Wiley-VCH, Berlin, 2012.

[Winslow1966] Winslow, A. M. (1966). Numerical solution of the quasilinear Poisson equation in a nonuniform triangle mesh. Journal of computational physics, 1(2), 149-172.

[Won2009] Won Seo, J., Park, J. W., Lim, K. S., Kang, S. J., Hong, Y. H., Yang, J. H., ... & Kim, H. K. (2009). Transparent flexible resistive random access memory fabricated at room temperature. Applied Physics Letters, 95(13), 133508.

[Wong2012] Guan, X., Yu, S., & Wong, H. S. P. (2012). On the switching parameter variation of metal-oxide RRAM—Part I: Physical modeling and simulation methodology. IEEE Transactions on electron devices, 59(4), 1172-1182.

[Wong2012b] Wong, H. S. P., Lee, H. Y., Yu, S., Chen, Y. S., Wu, Y., Chen, P. S., ... & Tsai, M. J. (2012). Metal–oxide RRAM. Proceedings of the IEEE, 100(6), 1951-1970.

[Wu2013] Wu, X., Cha, D., Bosman, M., Raghavan, N., Migas, D. B., Borisenko, V. E., ... & Pey, K. L. (2013). Intrinsic nanofilamentation in resistive switching. Journal of Applied Physics, 113(11), 114503.

[Xie2013] Xie, Y. (Ed.). (2013). Emerging Memory Technologies: Design, Architecture, and Applications. Springer Science & Business Media.

[Xie2013b] Xie, C., Nie, B., Zhu, L., Zeng, L. H., Yu, Y. Q., Wang, X. H., ... & Wu, Y. C. (2013). High-performance nonvolatile Al/AlOx/CdTe: Sb nanowire memory device. Nanotechnology, 24(35), 355203.

[Yan2011] Yan, Z., Guo, Y., Zhang, G., & Liu, J. M. (2011). High-performance programmable memory devices based on co-doped BaTiO3. Advanced Materials, 23(11), 1351-1355.

[Yan2015] Yan, P., Li, Y., Hui, Y. J., Zhong, S. J., Zhou, Y. X., Xu, L., ... & Miao, X. S. (2015). Conducting mechanisms of forming-free TiW/Cu2O/Cu memristive devices. *Applied Physics Letters*, *107*(8), 083501.

[Yang2009] Yang, J. J., Miao, F., Pickett, M. D., Ohlberg, D. A., Stewart, D. R., Lau, C. N., & Williams, R. S. (2009). The mechanism of electroforming of metal oxide memristive switches. Nanotechnology, 20(21), 215201.

[Yang2012] Yang, Y., Sheridan, P., & Lu, W. (2012). Complementary resistive switching in tantalum oxide-based resistive memory devices. Applied Physics Letters, 100(20), 203112.

[Yang2012b] Yang, Y., Gao, P., Gaba, S., Chang, T., Pan, X., & Lu, W. (2012). Observation of conducting filament growth in nanoscale resistive memories. Nature communications, 3(1), 1-8.

[Yang2013] Yang, Y., & Lu, W. (2013). Nanoscale resistive switching devices: mechanisms and modeling. Nanoscale, 5(21), 10076-10092.

[Yang2013b] Yang, J. J., Strukov, D. B., & Stewart, D. R. (2013). Memristive devices for computing. Nature nanotechnology, 8(1), 13.

[Yang2013c] Yang, J. B., Chang, T. C., Huang, J. J., Chen, S. C., Yang, P. C., Chen, Y. T., ... & Tsai, M. J. (2013). Resistive switching characteristics of gallium oxide for nonvolatile memory application. Thin Solid Films, 529, 200-204.

[Yao2020] Yao, P., Wu, H., Gao, B., Tang, J., Zhang, Q., Zhang, W., ... & Qian, H. (2020). Fully hardware-implemented memristor convolutional neural network. Nature, 577(7792), 641-646.

[You2014] You, T., Du, N., Slesazeck, S., Mikolajick, T., Li, G., Bürger, D., ... & Volz, K. (2014). Bipolar electric-field enhanced trapping and detrapping of mobile donors in BiFeO3 memristors. ACS applied materials & interfaces, 6(22), 19758-19765.

[Yu2011] Yu, S., Guan, X., & Wong, H. S. P. (2011). Conduction mechanism of TiN/HfOx/Pt resistive switching memory: A trap-assisted-tunneling model. Applied Physics Letters, 99(6), 063507.

[Yu2016] Yu, S., & Chen, P. Y. (2016). Emerging memory technologies: Recent trends and prospects. IEEE Solid-State Circuits Magazine, 8(2), 43-56.

[Yu2017] Yu, S. (2017). Neuro-inspired computing using resistive switching devices. Switzerland: Springer.

[Zahoor2020] Zahoor, F., Azni Zulkifli, T. Z., & Khanday, F. A. (2020). Resistive random access memory (RRAM): an overview of materials, switching mechanism, performance, multilevel cell (MLC) storage, modeling, and applications. Nanoscale Research Letters, 15, 1-26.

[Zahurak2014] Zahurak, J., Miyata, K., Fischer, M., Balakrishnan, M., Chhajed, S., Wells, D., ... & Nakazawa, K. (2014, December). Process integration of a 27nm, 16Gb Cu ReRAM. In 2014 IEEE International Electron Devices Meeting (pp. 6-2). IEEE.

[Zangeneh2013] Zangeneh, M., & Joshi, A. (2013). Design and optimization of nonvolatile multibit 1T1R resistive RAM. IEEE Transactions on Very Large Scale Integration (VLSI) Systems, 22(8), 1815-1828.

[Zhang2009] Zhang, L., Huang, R., Gao, D., Wu, D., Kuang, Y., Tang, P., ... & Wang, Y. (2009). Unipolar resistive switch based on silicon monoxide realized by CMOS technology. IEEE electron device letters, 30(8), 870-872.

[Zhao2015] Zhao, L., Clima, S., Magyari-Köpe, B., Jurczak, M., & Nishi, Y. (2015). Ab initio modeling of oxygen-vacancy formation in doped-HfOx RRAM: Effects of oxide phases, stoichiometry, and dopant concentrations. Applied Physics Letters, 107(1), 013504.

[Zhao2017] Zhao, L., Magyari-Köpe, B., & Nishi, Y. (2017). Polaronic interactions between oxygen vacancies in rutile Ti O 2. Physical Review B, 95(5), 054104.

[Zhong2014] Zhong, L., Jiang, L., Huang, R., & De Groot, C. H. (2014). Nonpolar resistive switching in Cu/SiC/Au non-volatile resistive memory devices. Applied Physics Letters, 104(9), 093507.

[Zhu2012] Zhu, W., Chen, T. P., Liu, Y., & Fung, S. (2012). Conduction mechanisms at low- and high-resistance states in aluminum/anodic aluminum oxide/aluminum thin film structure. Journal of Applied Physics, 112(6), 063706.

[Zhuravlev2005] Zhuravlev, M. Y., Sabirianov, R. F., Jaswal, S. S., & Tsymbal, E. Y. (2005). Giant electroresistance in ferroelectric tunnel junctions. Physical Review Letters, 94(24), 246802.